Background Reduction Methods and Vacuum Technology at the KATRIN Spectrometers

Zur Erlangung des akademischen Grades eines

Doktors der Naturwissenschaften

von der Fakultät für Physik des

Karlsruher Instituts für Technologie (KIT)

genehmigte

DISSERTATION

von

Dipl.-Phys. Stefan Görhardt

aus Simmern/Hunsrück

Tag der mündlichen Prüfung: 24.01.2014

Referent:	Prof. Dr. Guido Drexlin
	Institut für Experimentelle Kernphysik, KIT
Korreferent:	Prof. Dr. Ulrich Husemann
	Institut für Experimentelle Kernphysik, KIT

I declare that I have developed and written the enclosed thesis completely by myself, and have not used sources or means without declaration in the text.
Karlsruhe, 19.12.2013

. . . .
(Stefan Görhardt)

d

Abstract

To determine the absolute neutrino mass scale is one of the major challenges of (astro)-particle physics. The neutrino mass is of key importance for our understanding of the fundamental mass generating mechanisms in general and an unknown input parameter for cosmological models. A lower bound of $0.05\,\mathrm{eV/c^2}$ was provided by neutrino oscillation experiments during the last decade, and an upper limit of $2.0\,\mathrm{eV/c^2}$ was found by direct neutrino mass experiments. The **Ka**rlsruhe **Tri**tium **N**eutrino experiment (KATRIN) will observe tritium β-decay electrons and make use of the model-independent kinematics of this superallowed decay. A spectrometer based on the MAC-E filter principle will offer unprecedented accuracy and precision in β-spectroscopy. KATRIN is designed to determine the effective mass of the electron anti-neutrino with a sensitivity of $200\,\mathrm{meV/c^2}$ (90% C.L.). In order to achieve this ambitious goal an ultra-low background level is required. To minimize the background processes due to residual gas ionization in the spectrometer section, a pressure in the lower $10^{-11}\,\mathrm{mbar}$ region is needed.

This work focuses on the vacuum technology applied at KATRIN, and in particular on entrapment pumps in form of $3\,\mathrm{km}$ non-evaporable getter (NEG) material which has to maintain the ultra high vacuum condition in the spectrometer. One of the objectives of this thesis was to develop, test and implement an optimized vacuum bake-out procedure for the spectrometer vessel to minimize the outgassing behavior of the stainless steel walls. The outgassing behavior of materials both in theory and experiment is a complex subject, strongly depending on the materials used in the vacuum environment. For example, future bake-out cycles will be constrained to temperatures below $200\,^\circ\mathrm{C}$ to protected the fragile inner wire electrode system inside the spectrometer. This rather low temperature is adequate to clean the vacuum surfaces but in any case is not sufficient to properly activate the NEG pumps by thermal radiation. As part of this work a new concept of heating the getter strips by the passage of an electric current was adapted for the KATRIN NEG pumps and is currently being implemented.

Measurements at the pre-spectrometer test setup revealed ^{219}Rn emanating from the getter material, as well as ^{220}Rn coming from the vessel walls, as a major background source. As a countermeasure, a system of liquid nitrogen (LN2) cooled baffles was proposed and implemented at the main spectrometer as part of this work. The baffle system consists of LN2 cooled V-shaped blades made of copper that are blocking the direct line of sight from the NEG pump to the main volume. At LN2 temperature, the cold surfaces adsorb almost all radon isotopes while guaranteeing a sufficient NEG pumping speed for hydrogen as the dominant residual gas.

The results presented in this thesis show that a dedicated bake-out procedure and in combination with fully activated NEG pumps allows to reach the ambitious vacuum goal in the lower $10^{-11}\,\mathrm{mbar}$ region. A system of LN2 cooled baffles provides a powerful tool to eliminate almost the entire radon-induced background, which is an essential requirement for a successful neutrino mass measurement.

f

Zusammenfassung

Das Neutrino wurde 1930 von Wolfang Pauli postuliert, mit dem Ziel das beobachte kontinuierliche Energiespektrum des β-Zerfalls zu erklären. Erst im Jahre 1956 gelang einer Gruppe um die beiden amerikanischen Physiker Clyde L. Cowan und Frederick Reines der experimentelle Nachweis der Existenz dieses elektrisch neutralen und nur schwach wechselwirkenden Elementarteilchens. Reaktionen mit Neutrinos sind im Vergleich zu Prozessen der elektromagnetischen oder starken Wechselwirkung sehr selten. Das Standard Modell der Teilchenphysik kennt drei Arten (Generationen genannt) von Neutrinos als neutrale Partner der geladenen Leptonen: Elektron-, Myon- und Tau-Neutrinos sowie deren Antiteilchen. Der Nachweis von Neutrinos ist sehr aufwändig. Cowan und Reines nutzten für ihre Experimente in Los Alamos einen der ersten großen kommerziellen Kernreaktoren als künstliche Neutrinoquelle. Andere Physiker unter Leitung von Raymond Davis Jr. untersuchten Neutrinos aus dem Inneren der Sonne. Die Kernfusion dort liefert eine natürliche Quelle für Neutrinos. Jedoch betrug die am Homestake-Experiment gemessene Einfangrate mit 0.5 Neutrinos pro Tag nur etwa einem Drittel der aus den Standardmodellen der Sonne und der Elementarteilchenphysik vorhergesagten Rate. Dieses *Solare Neutrino Problem* sollte die Wissenschaft über dreißig Jahre hin weiter beschäftigen. Die Lösung des Solaren Neutrino Problems erfordert eine Erweiterung des Standard-Model der Teilchenphysik durch einen Effekt, der als Neutrinooszillation bezeichnet wird. Noch in den 1970er Jahren galten Neutrinos als masselose und Flavour-invariante Teilchen. Erst Oszillations-Experimente mit solaren, atmosphärischen und künstlichen Neutrinos zeigten, dass Neutrinos bei ihrer Propagation durch den Raum ihren Flavourzustand ändern. Somit ist die Erhaltung der Leptonenfamilienzahlen verletzt. Die Wahrscheinlichkeit einen bestimmten Flavourzustand zu messen ändert sich periodisch mit der räumlichen Ausbreitung, da sich die einzelnen Masseneigenzustände des Neutrinos mit leicht unterschiedlichen Phasen überlagern. Folglich kann sich ein als Elektron-Neutrino in der Sonne erzeugtes Neutrino auf seinem Weg zur Erde in ein Neutrino einer anderen Generation umwandeln und so von den damaligen ν_e-spezifischen Detektoren nicht mehr erkannt werden. Die von Bruno Pontecorvo 1957 theoretisch vorhergesagte Umwandlung gilt heute als bewiesen und zeigt, dass Neutrinos eine von Null verschiedene Ruhemasse besitzen müssen.

Die absolute Größe der Ruhemasse des Neutrinos gilt weiterhin als ungelöstes Rätsel der Physik. Zahlreiche Experimente versuchen mit unterschiedlichen Ansätzen dieses Rätsel zu lösen. Eine (stark modellabhängige) Obergrenze der Neutrinomasse liefert die Kosmologie: das Urknallmodell sagt ein festes Verhältnis zwischen der Anzahl der Neutrinos und der Anzahl der Photonen aus der Kosmischen Hintergrundstrahlung vorher. Modellabhängige Analyse der Kosmischen Hintergrundstrahlung, der Beobachtung von Galaxiehaufen oder von der Verteilung der Absorptionslinien im Lyman-Alpha-Wald ergeben meist Obergrenzen für ν-Massen, aber auch von

Null verschiedene Zentralwerte. Daher ist die direkte Bestimmung der absoluten Neutrinomasse in Laborexperimenten unabdingbar. Ein Ansatz hierbei ist die Beobachtung des neutrinolosen doppelten β-Zerfalls. Wenn der Nachweis eines $0\nu\beta\beta$-Zerfalls erbracht wäre, wäre das Neutrino ein Majorana-Teilchen und die Größe seiner Majorana-Masse wäre stark abhängig von theoretischen Modellrechnungen. Bis heute wurden keine Hinweise auf den neutrinolosen Doppelbetazerfall gefunden. Die aktuelle (modellunabhängige) Obergrenze für die Neutrinomasse von $2.2\,\text{eV/c}^2$ stammt aus Experimenten von Gruppen aus Mainz und Troitsk. Durch die hochpräzise Vermessung des Elektronenspektrums aus dem Tritium-β-Zerfall kann auf die Masse des Elektron-Antineutrinos geschlossen werden. Diese Methode basiert rein auf der Kinematik des β-Zerfalls und ist somit modellunabhängig.

Das **KA**rlsruher **TRI**tium **N**eutrino Experiment (KATRIN) steht für eine neue Generation von Neutrinoexperimenten. Wie seine Vorgänger aus Mainz und Troitsk ermöglicht KATRIN die direkte und modell-unabhängige Messung der Neutrinomasse durch Beobachtung der β-Elektronen aus der Kinematik des Tritium-Zerfalls mit einer bisher unerreichten Sensitivität von $200\,\text{meV/c}^2$. Der Messaufbau setzt sich zusammen aus einer fensterlosen, gasförmigen, molekularen Tritiumquelle mit anschließender differentiell bzw. kryogen gepumpter Elektronen-Transportstrecke. Die Tandem-Spektrometer Sektion analysiert die Energie der Zerfallselektronen. Beide Spektrometer arbeiten als sogenannte MAC-E-Filter (*Magnetic Adiabatic Collimation combined with an Electrostatic Filter*). Dabei werden die β-Elektronen durch eine Gegenspannung nach ihrer kinetischen Energie selektiert. Es folgt eine Detektoreinheit zum Nachweis der Elektronen. Das Erreichen einer Sensitivität von $200\,\text{meV/c}^2$ auf die Neutrinomasse erfordert unter anderem ein sehr niedriges Untergrundniveau ($< 0.01\,\text{cps}$). Zur Reduktion des Untergrunds durch Restgasionisation beim Abscannen des Gesamtspektrums von $\sim 10^{11}$ Elektronen pro Sekunde ist ein Ultrahochvakuum (UHV) in der Spektrometersektion erforderlich.

Im Rahmen dieser Arbeit wurden zentrale Beiträge zum Erreichen dieser stringenten UHV Anforderungen und der Untergrundreduktion geleistet. Als erster Beitrag wurde das Vorspektrometer in den KATRIN Aufbau integriert. Das Vorspektrometer dient als Vorfilter für β-Elektronen und wird auf einem Retardierungspotential $0 < U_0 < E_0$ betrieben, z.B. mit $U_0 \approx -18.3\,\text{kV}$. Da nur die Elektronen, deren Energie nahe an der Endpunktenergie von Tritium liegen, eine verwertbare Information zur Neutrinomasse tragen, ist es das Ziel des Vorspektrometers die Anzahl der β-Elektronen, die das Hauptspektrometer erreichen um einen Faktor 10^6 zu reduzieren. Die Anzahl der Elektronen im Hauptspektrometer ist korreliert mit dem erzeugten Untergrund durch Restgasionisation. Das KATRIN Hauptspektrometer fungiert als Hochpassfilter und analysiert hoch präzise die Energie der β-Elektronen aus der Tritiumquelle. Zwei supraleitende Spulen erzeugen hierfür ein inhomogenes Magnetfeld zur Führung. Ein elektrostatisches Retardierungspotential (direkt angelegt an den Spektrometertank) von $U_0 = 18.6\,\text{kV}$ dient als eigentlicher Filter und liefert eine Energieauflösung von $\Delta E = 0.93\,\text{eV}$. Durch die sehr große Anzahl von Restgasteilchen pro Volumeneinheit folgt, dass selbst bei einem Druck von $1 \cdot 10^{-11}\,\text{mbar}$ noch über $250\,000$ Gasteilchen pro cm^3 vorhanden sind ($T = 293\,\text{K}$). Da dieses Restgas die Messung der Neutrinomasse negativ beeinflussen kann, konzentrierte sich diese Arbeit zum einem Teil auf die Vakuumtechnologie, die benötig wird zur Erzeugung und Erhaltung eines Vakuums im $10^{-11}\,\text{mbar}$ Bereich.

h

Zum Erreichen eines Ultrahochvakuums in einem realistischen Zeitraum wird eine geeignete Ausheizphase des großen Spektrometertanks (10 m Durchmesser, 24 m Länge) benötig. Durch das Ansteigen der Temperatur beschleunigen sich Desorptionsprozesse: Wasser und andere Moleküle, die an der inner Oberfläche des Vakuumbehälters anhaften, lösen sich und können abgepumpt werden. Im Rahmen dieser Arbeit wurde daher eine optimierte Ausheizphase zum Minimieren der Ausgasrate des KATRIN Hauptspektrometers erprobt. Der gewählte Ausheizzyklus sollte die Temperatur des Spektrometers bis auf eine maximale Temperatur von $T_{\text{Tank}} = 350\,°C$ regeln und beinhaltete eine Temperaturstufe beim Abkühlen des Rezipienten von $T_{\text{Tank}} = 150\,°C$. Diese Temperaturstufe reduziert die Wasserstoffkonzentration an der Oberfläche durch Desorption ohne dieses Reservoir übermäßig mit Wasserstoff, der aus dem Vollmaterial der Wand diffundiert, nachzufüllen. Die Ausheizphase des Hauptspektrometers wurde im Winter 2012/2013 erfolgreich durchgeführt. Die gesamte Prozedur umfasste einen Zeitraum von zwei Monaten. Aufgrund von Problemen an der inneren Drahtelektrode wurde eine Maximaltemperatur von $T_{\text{Tank}} = 300\,°C$ erreicht. Nach der Ausheizphase wurde ein Druck von $p_{\text{H}_2} = 3.3 \cdot 10^{-10}\,\text{mbar}$ im Spektrometer erreicht, dominiert von Wasserstoff.

Da Gastransfervakuumpumpen und Turbomolekularpumpe technisch ungeeignet für leichte Gase wie Wasserstoff sind, hat sich die KATRIN Kollaboration zum Einsatz von Sorptionspumpen entschieden in Form von 3 km nicht-verdampfbaren Getter-Materials, um so einen Druck im UHV-Bereich während der gesamten Messzeit zu halten. Wenn das Getter-Material aktiviert wird (durch Erhitzen auf über $T > 300\,°C$) akkumuliert und absorbiert es sehr effizient Restgasmoleküle an seiner Oberfläche (Physisorption) oder über chemische Reaktionen (Chemisorption) in seinem Inneren. Nach der ersten Ausheizphase wurde die maximale Temperatur des Hauptspektrometers für zukünftige Ausheizphasen beschränkt auf $T_{\text{Tank}} < 200\,°C$, um weitere Belastungen für das inneren Drahtelektrodensystems zu verringern. Daher wurde ein alternatives Konzept zum Aktiveren des Getter-Materials benötigt. Im Rahmen dieser Arbeit wurde dementsprechend die Möglichkeit der Aktivierung der Getter-Pumpe im Hauptspektrometer durch die Wärmeerzeugung mit Strom über den Heizwiderstand des Grundmaterials (Konstantan) der Getter-Streifen erfolgreich erprobt. Die aktuellen Wartungsarbeiten am Hauptspektrometer werden genutzt, um die Getter-Pumpen entsprechend umzurüsten. Das neue Konzept ist ausgelegt für höhere Temperaturen ($T_{\text{Getter}} \approx 450\,°C$) und kann somit die Ausheizphase und den damit verbunden thermischen Stress auf alle Bauteile reduzieren.

Im zweiten großen Arbeitsthema dieser Dissertation wurden neue Untergrundunterdrückungskonzepte geplant, aufgebaut und im Rahmen mehrmaliger Testmessungen erfolgreich getestet. Messungen am Vorspektrometer-Testaufbau haben gezeigt, dass kurzlebige Radon-Isotope, die aus verschieden Materialen im Inneren des Spektrometers emanieren, tief in den Flussschlauch des Experiments eindringen können. Der Radon-α-Zerfall und die Elektronen, die diesen Prozess begleiten, sind eine der Hauptquellen für Untergrundereignisse in einem MAC-E-Filter System. Um zu verhindern, dass Radon in das Spektrometervolumen eindringt und dabei gleichzeitig die Pumpleistung der Getter-Pumpen für Wasserstoff (und Tritium) zu erhalten, wurde die Installation eines mit flüssigem Stickstoff gekühlten Baffles vorgeschlagen und im Rahmen dieser Arbeit am Hauptspektrometer umgesetzt. Der Baffle blockiert die direkte Sichtlinie zwischen der Getter-Pumpe und der Vakuumkammer.

Das System hindert emaniertes ^{219}Rn aus der Getterpumpe in den Pumpports am Eintritt in das Hauptspektrometer und friert zusätzlich ^{220}Rn fest, das aus den Wänden des Spektrometers emaniert. Eine umfassende Messkampagne wurde durchgeführt, um die Auswirkungen des Radon-induzierten Untergrunds zu untersuchen und die Effizienz des mit flüssigem Stickstoff gekühlten Baffles zu bewerten. Mit kalten Baffle konnten nahezu alle Radon-α-Zerfälle im Spektrometer verhindert werden, so dass der Untergrund im Spektrometer reduziert wird auf Untergrundprozesse durch die kosmische Strahlung oder Feldemission. Das System aus Baffle kombiniert mit einer Kühlfalle hat sich als hoch effizient im Unterdrücken von Radon-induziertem Untergrund erwiesen und ist damit ein zentrales Element in der Untergrundunterdrückung.

Die in dieser Arbeit erzielten Ergebnisse zeigen, dass das Vakuumsystem des Hauptspektrometers in der Lage ist die hohen Anforderung zu erfüllen. Wenn eine optimierte Ausheizphase wie hier vorgestellt durchgeführt wird und die Getter-Pumpen voll aktiviert sind, kann ein Druck im unteren 10^{-11} mbar Bereich erreicht werden. Die mit flüssigem Stickstoff gekühlten Baffles erzeugen einen nahezu Radon-freien Untergrund im Hauptspektrometer, dies ist essentiell für eine erfolgreiche Messung der Neutrinomasse.

Contents

l

n

List of Figures

p

r

List of Tables

t

1 Introduction

This chapter focuses on the broader scientific context of this thesis. After a brief overview of the origins of neutrino physics, the second section describes neutrinos as part of the Standard Model of particle physics. Neutrinos cast a glance beyond the Standard Model and open a window to new physics. This is due to the observation of the solar (and atmospheric) neutrino problem and the solution due to neutrino flavor oscillations which also motivates a high-sensitivity search for massive neutrinos. The chapter concludes by presenting three different approaches to determine the absolute neutrino mass scale.

1.1 Short History of Neutrino Physics

The history of neutrino physics is closely tied to the discovery of radioactive decays. In 1896 Antoine Henri Becquerel experimented with uranium salt and discovered an invisible radiation emitted from the uranium sample [1]. Ernest Rutherford and Frederick Soddy attempted to explain these observations with their work on the 'Theory of Atomic Disintegration' (1903), proposing that some elements can disintegrate into other kinds of atoms [2]. The radically new idea that an element can spontaneously change to another was backed by the radiation Becquerel discovered. Furthermore Rutherford was able to distinguish between alpha, beta and gamma radiation by positive, negative or neutral magnetic deflection. Among others, Lise Meitner and Otto Hahn studied the beta particles in more detail. An experiment performed in 1911 revealed the continuous nature of the beta spectrum [3] in contrast to the discrete spectra of the 2-body alpha and gamma decays. The law of conservation of energy and momentum appeared to be violated. In a famous letter Pauli proposed in 1930 the existence of a light neutral particle [4] in order to describe the β-spectrum as a result of a 3-body decay. This 'neutron' should be emitted during the β-decay and would take care of the conservation of energy and momentum. However, due to its light and neutral nature he noted that it would be almost impossible to observe this particle. Already two years later, in 1932, James Chadwick discovered a neutral particle which he labeled 'neutron' [5]. Yet, with its respectable mass, it disqualified as the new mysterious Pauli particle. In 1931 Enrico Fermi thus renamed Pauli's 'neutron' to 'neutrino' and three years later he also published a model of the β-decay [6] containing the neutrino. The experimental proof of the weakly interacting neutrino posed to be an ambitious challenge, but it was finally accomplished by Frederick Reines and Clyde L. Cowan [7] in 1956. The basic idea was to witness the interaction of a neutrino with a proton to produce a neutron and a positron - the antimatter counterpart of an electron (see equation 1.1). This event is called the inverse β-decay [8]:

$$\bar{\nu}_e + p \rightarrow n + e^+. \tag{1.1}$$

The positron annihilates with an electron, resulting in two detectable gamma rays. The neutron is captured by a nucleus, releasing further gamma rays. The coincidence of these events results in a unique neutrino signature. In 1962 a group around Leon M. Lederman, Melvin Schwartz and Jack Steinberger [9] discovered a second kind of neutrino: the muon neutrino (ν_μ). The detection of tau neutrino (ν_τ) [10] was finally announced in the summer of 2000 by the DONUT collaboration at Fermilab. The tau neutrino was the final lepton of the Standard Model of particle physics (see section 1.2) that has been observed, thus completing its fermionic content.

1.2 The Standard Model of Particle Physics and the Neutrino Flavors

The Standard Model (SM) of particle physics, which was continually developed throughout the 20th century, combines all known subatomic particles and their interactions. However, it is not a complete 'theory of everything' since gravitation, as described by the General Theory of Relativity, is missing.

Table 1.1: The Standard Model of particle physics, composed of fermions, their corresponding antiparticles and the gauge bosons in the forth column. The model is completed by the Higgs boson which was recently observed with 5σ evidence on July 4, 2012.

three generations of fermions	I	II	III	gauge bosons	
Quarks	u	c	t	γ	H
	d	s	b	$W^\pm$	
Leptons	e^-	μ^-	τ^-	Z^0	
	ν_e	ν_μ	ν_τ	g	

The Standard Model, as presented in table 1.1, distinguishes six quarks (up, down, charm, strange, top, bottom), six leptons (electron, muon, tau and their corresponding neutrinos) and four interaction particles (photon, $W^\pm$, Z^0, gluon) as well as the Higgs boson. All spin-½-particles are referred to as fermions and obey *Pauli's exclusion principle*[1]. Quarks interact electromagnetically, weakly and strong. They carry a fractional electric charge, weak isospin and color charge. The *color confinement* forces quarks to form color-neutral particles (hadrons) and results in quark-antiquark-pairs (mesons) and quark-triplets (baryons). The charged leptons (electron, muon, tau) interact electromagnetically and weakly, by carrying one electric charge and weak isospin. Neutrinos do not carry electric charge; they are left with the weak force for interaction. This enables neutrinos to penetrate even very dense matter such as the solar core or a supernova, and explains the difficulties of their detection. In the Standard Model of particle physics the neutrino is defined as a massless particle.

The gauge bosons (spin-1 particles) act as force carriers responsible for the interactions. The different kinds of gauge bosons are:

---

[1]No two identical fermions may occupy the same quantum state simultaneously.

- the massless photons mediate the electromagnetic force between electrically charged particles,

- the massive W$^{\pm}$ and Z^0 gauge bosons mediate the charged and neutral weak interactions and connect different flavors (all quarks and leptons carry a weak isospin). Additionally, W$^{\pm}$ bosons carry electric charge which enables a coupling via the electromagnetic interaction. Grouped with the photon the massive gauge bosons can be described by the unified theory of electroweak interactions.

- the eight massless gluons mediate the strong force. By carrying color charges they are able to also interact among themselves. These processes are described by the theory of quantum chromodynamics.

The Higgs boson is the sole spin-0 particle of the SM with neither electric nor color charge. Therefore it is not a force carrier but can be used to explain the massive nature of the W$^{\pm}$ and Z^0 gauge bosons via spontaneous symmetry breaking. The Higgs mechanism explains the mass of the gauge bosons (as well as of the quarks and charged leptons) via their interaction with the Higgs field that exists throughout space. The LHC experiments (ATLAS [11] and CMS [12]) recently reported a spin-0 particle with a mass of about $125\,\mathrm{GeV/c^2}$ which is consistent with fundamental properties of the Higgs boson.

As seen in table 1.1 the elementary particles are grouped in three generations that share similar physical behavior. The mass of the particles is increasing with each generation. Hence, only particles of the first generation (often called normal matter) are considered as stable. Particles of the second and third generation decay to the first generation, and are only produced in extremely high energetic environments (such as particle accelerators or in cosmic rays). The neutrinos form a possible exception of this rule and may acquire their mass differently (see section 1.3). Due to their small cross section the neutrinos are streaming throughout the universe and rarely interact with other particles. The number of (active) neutrino generations can be determined by observing the decay width of the Z^0 boson by the invisible Z^0-width $e^+e^- \xrightarrow{Z^0} \nu\bar{\nu}$. By combining the results of different experiments the number of light[2] neutrino generations can be determined to $N_\nu = 2.92 \pm 0.05$ [13].

1.3 Beyond the Standard Model - the Phenomenology of Massive Neutrinos

This section will focus on the discrepancy between the measured and predicted neutrino flux radiated from the sun as a first hint of new physics beyond the SM. As a natural fusion reactor the sun produces a massive amount of ν_e in the proton-proton chain reaction. However, in the past neutrino experiments on earth only observed about one third to one half of the predicted number of ν_e. The difference can be explained by flavor oscillations (see section 1.3.2) which usually implies physics beyond the Standard Model of particles physics [14] and the existence of massive neutrinos. To put the theory of neutrino oscillation into context, section 1.3.3 is

---

[2]here 'light neutrino' means neutrinos with less than half the mass of the Z^0 boson.

used to introduce different experiments with artificial neutrino sources (like reactors or particle accelerators) and to report their latest results.

1.3.1 The Solar Neutrino Problem

The sun and other stars generate their energy through nuclear fusion. In the underlying proton-proton chain reaction, hydrogen nuclei are converted into helium thereby producing energy, positrons and electron neutrinos. Contrary to the photons, neutrinos pass from the sun's core without interaction[3] to the outer layers of the sun and through to space. These neutrinos can be detected by neutrino detectors (like Homestake [15] or SNO [16]) on earth. The number of neutrinos can be predicted by calculating all the relevant processes in the sun. These calculations form the Standard Solar Model (SSM) [17] [18]. Measurements done by Ray Davis (and John N. Bahcall) in the late 1960s at the Homestake experiment showed [19] a deficit in the number of expected neutrinos. This discrepancy between measurements and theoretical number of neutrinos streaming from the sun to earth is known as *solar neutrino problem*.

To resolve this discrepancy, two solutions were proposed: Changing the SSM or to modify the Standard Model of particle physics. In order to explain the missing neutrinos, a reduction of the solar core temperature in the SSM could be required. However, helioseismic measurements did confirm the SSM [20] and no combination of adjustments of the solar model were capable to explain the data measured by the Homestake and other experiments. Hence, this left the option of a modification of the Standard Model of particle physics (see 1.2).

1.3.2 The Assumption of Neutrino Oscillation

The Standard Model of particle physics distinguishes three different neutrino flavors, see table 1.1: the electron neutrino ν_e, the muon neutrino ν_μ and the tau neutrino ν_τ. A (massive) neutrino flavor eigenstate ν_α, with $\alpha = e, \mu, \tau$ is defined as a superposition of the neutrino mass eigenstates ν_i, with $i = 1, 2, 3$:

$$|\nu_\alpha\rangle = \sum_i U_{\alpha i} |\nu_i\rangle \tag{1.2}$$

where U is the unitary Pontecorvo-Maki-Nakagawa-Sakata neutrino mixing matrix (PMNS matrix) [21] [22]. The PMNS matrix describes the probability ($|U_{\alpha i}|^2$) of a neutrino of given flavor α to be found in mass eigenstate i:

$$\begin{pmatrix} \nu_e \\ \nu_\mu \\ \nu_\tau \end{pmatrix} = \begin{pmatrix} U_{e1} & U_{e2} & U_{e3} \\ U_{\mu 1} & U_{\mu 2} & U_{\mu 3} \\ U_{\tau 1} & U_{\tau 2} & U_{\tau 3} \end{pmatrix} \cdot \begin{pmatrix} \nu_1 \\ \nu_2 \\ \nu_3 \end{pmatrix} \tag{1.3}$$

---

[3]disregarding matter effect like the Mikheyev-Smirnov-Wolfenstein (MSW) effect

The matrix is (as a mathematical transformation) parameterized by three Euler mixing angles (Θ_{12}, Θ_{23} and Θ_{13}) and one complex phase φ.

$$
U = \begin{pmatrix} 1 & 0 & 0 \\ 0 & \cos\Theta_{23} & \sin\Theta_{23} \\ 0 & -\sin\Theta_{23} & \cos\Theta_{23} \end{pmatrix} \cdot \begin{pmatrix} \cos\Theta_{12} & \sin\Theta_{12} & 0 \\ -\sin\Theta_{12} & \cos\Theta_{12} & 0 \\ 0 & 0 & 1 \end{pmatrix} \cdot
$$
$$
\begin{pmatrix} 1 & 0 & 0 \\ 0 & 1 & 0 \\ 0 & 0 & e^{i\varphi} \end{pmatrix} \cdot \begin{pmatrix} 1 & 0 & 0 \\ 0 & \cos\Theta_{13} & \sin\Theta_{13} \\ 0 & -\sin\Theta_{13} & \cos\Theta_{13} \end{pmatrix} \tag{1.4}
$$

A neutrino created in a weak decay is a mixture of flavor eigenstates (see equation 1.5). By propagating through space, the mixture of the three mass eigenstates is changing. This occurs because the three mass eigenstates evolve differently due to the differences in their masses. However, a different mixture of mass states will result in a new flavor state. Hence, a neutrino created as an ν_e will change during its travel into new flavors corresponding to its superposition of all three mass eigenstates. This quantum-mechanical effect is observable over macroscopic distances. The wave function of the neutrino mass eigenstate is given by:

$$
|\nu_i(t)\rangle = e^{-\frac{i}{\hbar}(E_i t - \vec{p}_i \cdot \vec{x})}|\nu_i(0)\rangle \tag{1.5}
$$

The mass of the neutrino is small compared to its energy ($m_\nu << E_\nu$). Hence, in the ultrarelativistic limit the speed of the neutrinos is very close to the speed of light ($v \approx c$), and the momentum p can be approximated by

$$
p = \frac{1}{c}\sqrt{E_i^2 - m_i^2 c^4} \approx \frac{1}{c}\left(E - \frac{m_i^2 c^4}{2E}\right) \tag{1.6}
$$

where E is the total energy of the particle. If L equals the distance between the source and the detector the time the neutrino travels is given by $t = L/c$. This approximation can be applied to the wave function of the mass eigenstate (equation 1.5):

$$
|\nu_i(L)\rangle = |\nu_i(0)\rangle \, e^{-i\frac{m_i^2 c^4}{2E}\frac{L}{\hbar c}} \tag{1.7}
$$

The eigenstates with different masses acquire different phases. The oscillation probability P for a neutrino [23] created in flavor α but observed in flavor β is then given by

$$
\begin{aligned}
P(\nu_\alpha \to \nu_\beta) &= |\langle\nu_\beta(0)|\nu_\alpha(L)\rangle|^2 \overset{1.2}{=} \left|\sum_{i,j} U_{\alpha i}^* U_{\beta i} U_{\alpha j} U_{\beta j}^* e^{-i\frac{m_{ij}^2 c^4}{2E}\frac{L}{\hbar c}}\right|^2 \\
&\approx \sin^2\left(\frac{\Delta m_{ij}^2 c^4}{4E} \cdot \frac{L}{\hbar c}\right) \cdot \sin^2(2\Theta_{ij})
\end{aligned} \tag{1.8}
$$

This equation shows that the amplitude of the oscillation probability $\sin^2(2\Theta_{ij})$ depends on the corresponding mixing angle Θ_{ij}, while the mass splitting Δm_{ij}^2, the energy E and traveled distance L determine the frequency of the oscillation. This solves the missing solar neutrino problem: the electron neutrinos emitted from the sun do not disappear. They change their flavor state when traveling to Earth and

therefore can not be seen by electron neutrino observatories. This effect is called *neutrino oscillation.*

The first evidence for this effect (albeit not with solar neutrinos) was given by the neutrino observatory Super-Kamiokande [24] in Japan (1998). While experimenting with GeV-scale ν_μ produced in the upper atmosphere by cosmic rays, a deficit of up going ν_μ coming through earth was discovered, while no deficit was observed for down-going ones. The ν_μ changed their flavor into ν_τ that can not (easily) be detected by Super-Kamiokande and therefore appeared to be missing. In 2001 the Sudbury Neutrino Observatory (SNO) [16] provided more convincing proof for neutrino flavor change. Focusing on solar neutrinos, SNO could not only detect solar ν_e but also ν_μ and ν_τ via neutral current (NC) reactions on deuterium. The measurements showed that about 35% of the arriving solar neutrinos are ν_e, with the remainder being ν_μ and ν_τ.

The physics underlying neutrino oscillations requires the neutrino mass eigenstates to possess non-zero masses ($\Delta m_{ij} \neq 0$) to be able to undergo flavor changes [25].

1.3.3 Experiments with Artificial Neutrino Sources and their Results

Experiments with artificial neutrino sources have further verified the existence of neutrino oscillations by studying the $\bar{\nu}_e$ created at nuclear fission reactors (like KamLAND [26], Daya Bay [27], RENO [28] or Double Chooz [29]) and by using ν_μ beams produced at particle accelerators (like MINOS [30] or T2K [31]). The basic concept of all these experiments is identical. The neutrinos are observed at two detectors, one close to where the beam is produced (near detector), and another detector which is located further downstream, in case of GeV ν_μ beams even hundreds of kilometers away (far detector). By comparing the readings of both detectors, the experiments can determine the mixing angles ($\Theta_{12}, \Theta_{23}, \Theta_{13}$) in the PMNS-matrix as well as the squared mass differences ($\Delta m_{21}^2, \Delta m_{32}^2$) of the neutrinos. However, no single experiment is sensitive to probe the full parameter space alone. By combining the experimental data, oscillation parameters can be determined, as listed in table 1.2 and plotted in figure 1.1. All oscillation experiments however only depend on the mass-squared difference Δm_{ij}^2. Therefore the absolute neutrino mass and the hierarchy of the masses are still unknown.

Table 1.2: The neutrino mixing parameters. Presented are the observed values for the mixing angles and known squared mass differences.

oscillation parameters	value	source
$\sin^2 2\Theta_{12}$	0.87 ± 0.03	KamLAND [26]
$\sin^2 2\Theta_{23}$	> 0.90, 90% CL	MINOS [32]
$\sin^2 2\Theta_{13}$	$0.092 \pm 0.016_{\text{(stat)}} \pm 0.005_{\text{(syst)}}$	Daya Bay [27], RENO [28]
$\Delta m_{21}^2 = \Delta m_{solar}^2$	$(7.59 \pm 0.20) \times 10^{-5}\,\text{eV}^2/\text{c}^4$	KamLAND [26]
$|\Delta m_{32}^2| = |\Delta m_{atmos}^2|$	$(2.32_{-0.08}^{+0.12}) \times 10^{-3}\,\text{eV}^2/\text{c}^4$	MINOS [32] [a]

[a]The sign of Δm_{32}^2 is not known at this time, the range quoted is for the absolute value.
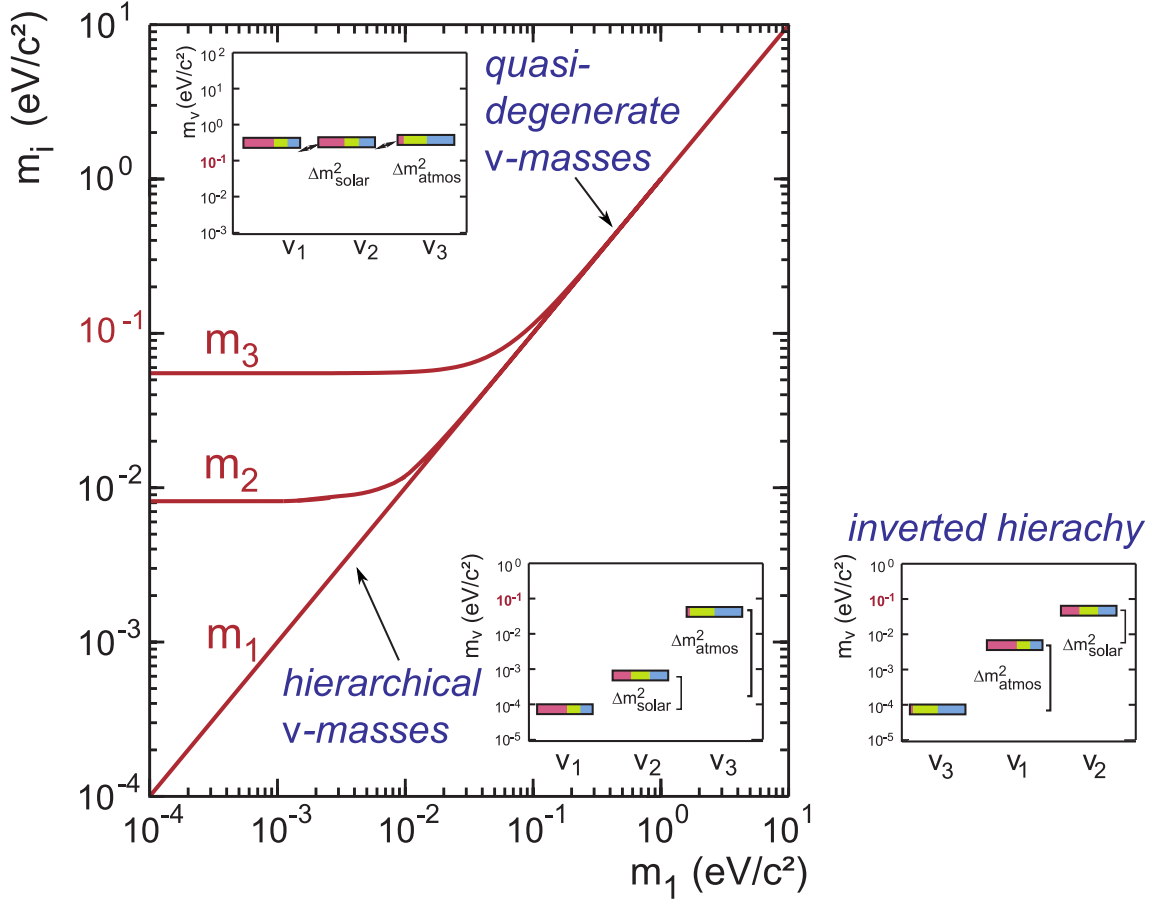
Figure 1.1: Eigenvalues of the neutrino mass eigenstates m_1, m_2 and m_3 as a function of the lightest mass state m_1 for normal and inverted hierarchy. For $m_1 > 0,1\,\mathrm{eV/c}^2$ the neutrino mass spectrum is quasi-degenerate with the mass differences Δm^2_{ij} being small compared to m^2_i. Oscillation experiments can only determine the squared mass differences, where the sign of Δm_{ij} is not known. Therefore, two hierarchical scenarios are possible: normal hierarchy (left) and inverted hierarchy (right). Additionally, the value of the lightest neutrino mass state cannot be determined by oscillation experiments, which prevents a determination of the effective mass of the other states. Figure based on [33].

1.4 Determination of the Absolute Value of the Neutrino Mass

The unknown absolute value of the neutrino mass are fundamental importance and are expected to shed light on the general mass generating mechanism in nature. This section will focus on three measurement methods to determine the absolute neutrino mass: the formation and evolution of large-scale structures (LSS) in cosmology, the neutrinoless double-β-decay ($0\nu\beta\beta$) and the kinematics of single β-decay.

1.4.1 Neutrinos in Cosmology

Cosmological investigations can provide constraints on the absolute neutrino mass by observing correlations in the distribution of galaxies. Even tiny neutrino masses in the order of a few tenths of an electron volt can have a significant effect on the formation of large-scale structures in the universe [34].

In the first second after the Big Bang at high temperature an equilibrium of photons, electrons, positrons and neutrinos ruled the Hubble expansion. However, as the universe is expanding and cooling over time, the rate of weak interaction was dropping fast and neutrinos decoupled from the cosmic plasma after one second. These relic neutrinos have no further gauge interaction with the rest of the matter. Figure 1.2 shows the possible contribution of relic neutrinos to the total energy-matter budget of the universe.
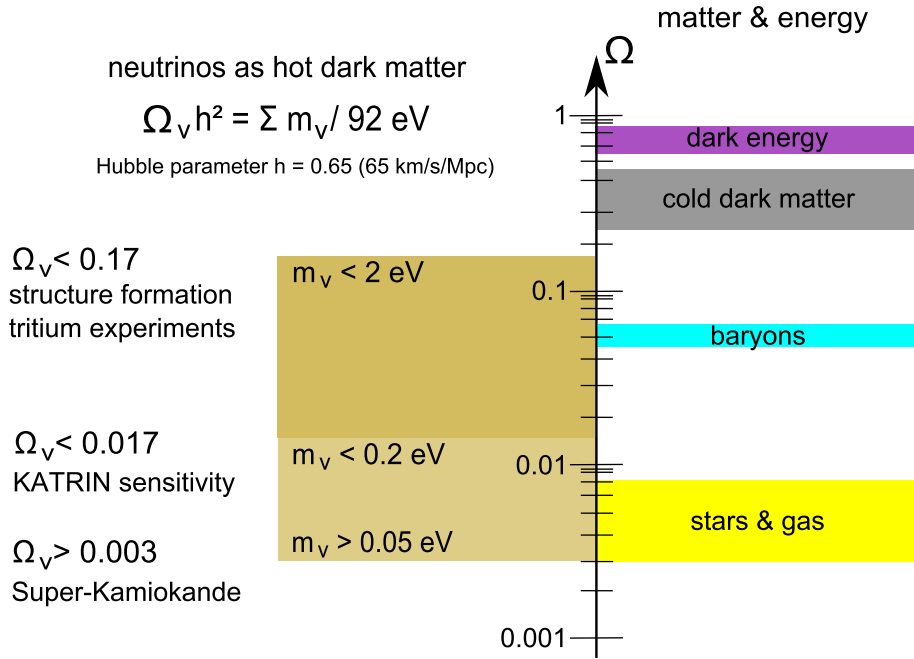
Figure 1.2: The total energy density Ω of the universe compared to a possible contribution of the neutrinos (left side). The universe is dominated by the dark energy Ω_Λ and the dark matter Ω_{DM}. The luminous matter (stars and gas clouds) is part of the baryons (Ω_b), neutrinos are classified as hot dark matter (νHDM) and are part of Ω_{DM}. The contribution of neutrinos to the masses in the universe were determined experimentally. The lower bound results from neutrino oscillation experiments, the upper bound from tritium β decay experiments and studies of the distribution of galaxies. The figure is based on [33], all values were updated.

Neutrinos are considered as 'hot dark matter' in evolution modeling as they were free-streaming at almost the speed of light in the early universe and affected the formation of large scale structures there. Neutrinos carried energy out of overdense areas with clumped matter towards areas with a lower matter density. Figure 1.3 shows how different neutrino masses can lead to different large scale structures - structures in the Mpc-range are clearly washed out by neutrinos.
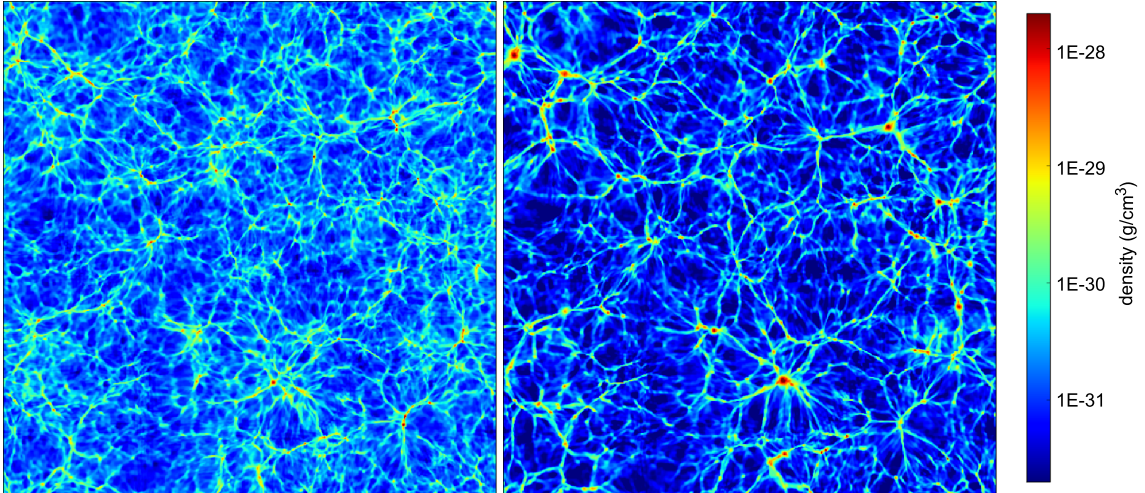
Figure 1.3: Comparison of density distributions in the universe with (left) and without (right) massive neutrinos. The maps are based on numerical simulations [35]. The colors account for the density of ordinary (baryonic) matter in one slice of the simulation box [36]. The two simulations started from the same initial conditions, with either $M_\nu = 1.9\,\text{eV/c}^2$ ($\Omega_\nu = 0.04$) (left) or $M_\nu = 0$ (right). In the massive neutrino case, matter is spread over a larger number of structures and there is less density contrast. (The unrealistically large neutrino mass of $1.9\,\text{eV}$ was chosen so as to make the comparison clear.) [37] [a]

---

[a]Illustration: Courtesy of Shankar Agarwal and Hume Feldman, University of Kansas [35]

One of the most common approaches to observe the matter density of the universe is to study the distribution of galaxies based on the 21-cm-line of hydrogen. This wavelength, created by a change in the energy state (hyperfine transition) of neutral hydrogen atoms, is within the microwave radio region and can penetrate large clouds of interstellar cosmic dust which are opaque to visible light. The galaxy redshifts surveys, like 2 degree Field Galaxy Redshift Survey (2dFGRS) [34] or MegaZ DR7 [38], are mapping the universe (more precisely hydrogen density) using the redshifts of the 21-cm hydrogen line. These measurements are called 21-cm tomography [39]. Information about the absolute neutrino mass is gained by comparing the measurements with simulations.

Methods based on observational cosmology are sensitive to the sum of all neutrino mass eigenstates:

$$m(\nu) = \sum_i m_{\nu_i}. \tag{1.9}$$

The interpretation of observations depends on the cosmological model being used and leads to a current upper limit for the neutrino mass of [40]:

$$m(\nu) < 0.28 - 2\,\text{eV/c}^2. \tag{1.10}$$

However, as a model-dependent method, the neutrino mass inferred by cosmology depends on assumptions for other parameters like baryon density, cold dark matter or the cosmological constant. The variations in the upper limit (see equation 1.10) show the crucial dependency on the input parameters and the employed data sets [34] [38].

Further constraints on the sum of the neutrino masses was reported in March 2013 by the Planck collaboration [41]. By including WMAP data (WP), high-resolution CMB data (highL) and baryon acoustic oscillation (BAO) surveys the best current constraint on the neutrino mass is:

$$m(\nu) = \sum_i m_{\nu_i} < 0.23 \, \text{eV} \quad (95\% CL; Planck + \text{WP} + \text{highL} + \text{BAO}). \quad (1.11)$$

A directly measured neutrino mass, on the other hand, is invaluable when used as a parameter to break degeneracies in different ΛCDM models.

1.4.2 Neutrinoless Double β-Decay

In specific β-decay processes where an even-even-nuclei ${}^N_Z X$ will transform into an odd-odd state problems can arise if the binding energy of the nucleus with the atomic number one higher is smaller. If the neighboring nucleus $Z + 1$ is heavier, a direct decay into the final state nuclei $Z + 2$ should be experimentally observable. In this so called two-neutrino double-beta decay ($2\nu\beta\beta$) two electrons and two neutrinos are emitted:

$$2n \rightarrow 2p + 2e^- + 2\bar{\nu}_e. \quad (1.12)$$

The observation of a neutrinoless double β-decay ($0\nu\beta\beta$) is only possible, if the neutrinos are *Majorana particles* and therefore their own anti-particles. In theory a right-handed antineutrino (positive helicity[4]) will be produced in one β-decay vertex which has to absorbed as a left-handed neutrino (negative helicity) at the inverse β-decay vertex (violating lepton number conservation). For massless particles chirality and helicity are identical while for massive particles spin and motion must be distinguished. Only if the neutrino is massive and therefore moving slower than the speed of light, there exists a Lorentz boost that reverses the direction of momentum and necessarily leaves the spin unchanged [42]. The emitted two electrons share the entire decay energy therefore a mono-energetic line at the electron energy spectrum should appear. The effective Majorana neutrino mass $m_{\beta\beta}$ is given by

$$m_{\beta\beta} = \left| \sum_{i=1}^{3} U_{ei}^2 m_{\nu_i} \right|, \quad (1.13)$$

where U_{ei} are the elements of the PMNS matrix (see equation 1.3). An observation of a $0\nu\beta\beta$ will prove the Majorana nature of neutrinos and furthermore contributing to our knowledge of the absolute neutrino mass. Several experiments are currently taking data like the GERmanium Detector Array (GERDA [43]) or EXO [44]. More experiments are proposed or planned like, Super-Nemo [45], MAJORANA [46] or CUORE [47]. At present, no evidence for $0\nu\beta\beta$ has been found and an upper limit for $m_{\beta\beta}$ in the range from $(120 - 250) \, \text{meV/c}^2$ have been established by the KamLAND-Zen Collaboration [48].

---

[4]its momentum is parallel to its spin

1.4.3 Single β-Decay

A different set of experiments focuses on a model-independent method to determine the absolute neutrino mass by observing the kinematics of the β-decay:

$$_{Z}^{N}\mathrm{X} \to {}_{Z+1}^{N}\mathrm{X} + e^- + \bar{\nu}_e. \tag{1.14}$$

The β decay is a three-body problem. The released energy is distributed statistically between the daughter nuclei, the electron and the neutrino. A theory of β-decay was described by Fermi in 1934 including the neutrino mass $m_{\bar{\nu}_e}^2$ [6]. The effective neutrino mass $m_{\bar{\nu}_e}^2$ is a superposition of the three mass eigenstates:

$$m_{\bar{\nu}_e}^2 = \sum_{i=1}^{3} |U_{ei}|^2 \, m_i^2. \tag{1.15}$$

Here, U_{ei} denote the elements of the PMNS matrix (see equation 1.3). The latest upper limit on the neutrino mass was set by experiments measuring the shape of the β-decay spectrum of tritium. The final result of the *Mainz Neutrino Mass Experiment* is the squared mass of the electron anti-neutrino:

$$m^2(\bar{\nu}_e) = (-0.6 \pm 2.2_{\mathrm{stat}} \pm 2.1_{\mathrm{syst}})\,\mathrm{eV}^2/\mathrm{c}^4, \tag{1.16}$$

deriving an upper limit of $m(\nu_e) < 2.3\,\mathrm{eV/c}^2$ (95% CL) [49]. In 2003 the *Troitsk Neutrino Mass Experiment* published the squared mass of the electron anti-neutrino

$$m^2(\bar{\nu}_e) = (-2.3 \pm 2.5_{\mathrm{stat}} \pm 2.0_{\mathrm{syst}})\,\mathrm{eV}^2/\mathrm{c}^4, \tag{1.17}$$

deriving an upper limit of $m_{\nu_e} < 2.05\,\mathrm{eV/c}^2$ (95% CL) [50]. In 2012 the *Particle Data Group* assumed an upper limit of $m_{\nu_e} < 2\,\mathrm{eV/c}^2$ (95% CL) [13].

2 The KATRIN Experiment

The goal of the KATRIN (**Ka**rlsruhe **Tri**tium **N**eutrino) experiment [33] is the direct measurement of the electron anti-neutrino mass from tritium β-decay as a model-independent method to fix the absolute ν-mass scale. KATRIN will employ a molecular gaseous tritium source and an electrostatic energy filter (MAC-E filter, see section 2.2 and [51]). By investigating the spectral shape of the tritium β decay electrons close to their kinematic endpoint (of about 18.6 keV), the experiment will determine the neutrino mass with an unprecedented sensitivity of $200 \, \mathrm{meV/c^2}$ (90% C.L.). After about three full beam years of neutrino mass data taking, corresponding to about five to six calender years of operation, KATRIN will improve the present sensitivity for the neutrino mass by one order of magnitude.
This chapter will focus on the theory of the tritium β decay, outline the concept of MAC-E filters and describe the experimental setup with its major components.

2.1 Kinematics of the Tritium β-Decay

KATRIN is going to investigate the endpoint region of the electron energy spectrum of the tritium β decay:

$$ {}^{3}\mathrm{H} \longrightarrow {}^{3}\mathrm{He}^{+} + \mathrm{e}^{-} + \bar{\nu}_e. \tag{2.1} $$

In a β^- decay of a nucleus, the weak interaction converts a neutron into a proton while an electron (e^-) and an electron anti-neutrino $(\bar{\nu}_e)$ are emitted. The energy difference between initial and final state is shared statistically between the e^- and the $\bar{\nu}_e$, disregarding the recoil energy of the nuclear parent. The energy spectrum (Figure 2.1a) can be described by [6]:

$$ \frac{d\Gamma}{dE} = \frac{G_F^2}{2\pi^3\hbar^7 c^5} \cdot \cos^2(\theta_C) \cdot |M|^2 \cdot F(Z+1, E) \cdot p \cdot (E + m_e c^2) \cdot (E_0 - E) \cdot \\ \sqrt{(E_0 - E)^2 - m_{\bar{\nu}_e}^2 c^4} \cdot \Theta(E_0 - E - m_{\bar{\nu}_e} c^2) \tag{2.2} $$

where G_F is the *Fermi constant*, θ_C the *Cabibbo angle* and M the nuclear matrix element. E denotes the kinetic energy of the electron, m_e the electron mass, p the electron momentum and $m_{\bar{\nu}_e}$ the mass of the electron anti-neutrino. E_0 corresponds to the total decay energy, $F(Z+1, E)$ is the *Fermi function* of the daughter nucleus, while the step function Θ ensures energy conservation. A more detailed description (e.g. including the final states) is given in [52]. Equation 2.2 shows that KATRIN is sensitive to the squared mass $m_{\bar{\nu}_e}^2$. Experimentally the individual mass eigenstates cannot be resolved, thus only an averaged value can be measured. To do so, shape of the β-electron spectrum (see figure 2.1a) in a narrow region close to the endpoint has to be investigated.
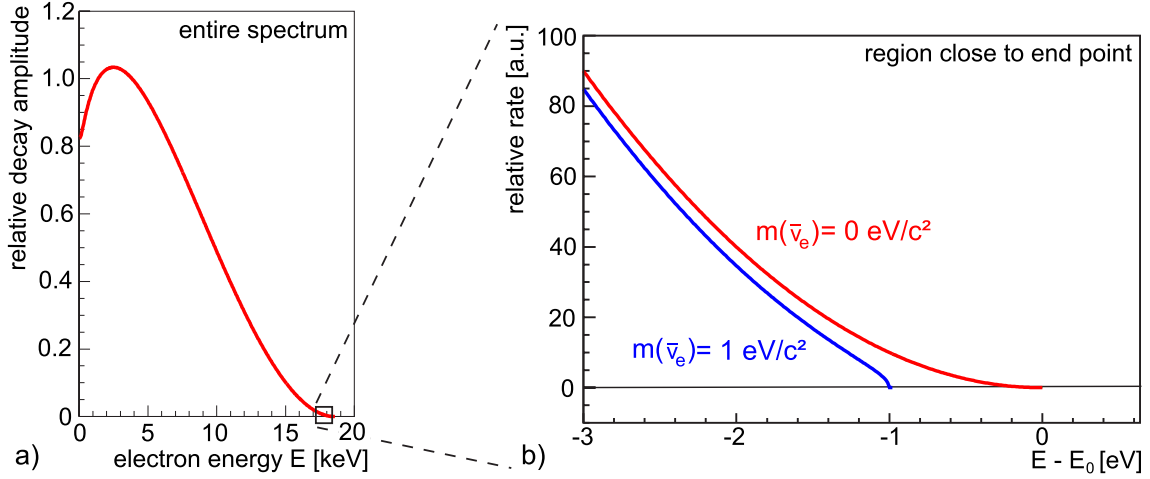
Figure 2.1: The spectrum of the tritium β-decay. a) Full tritium β decay, **b)** region close to the end point energy, two scenarios for a neutrino mass of $m_{\bar{\nu}_e} = 0$ and $m_{\bar{\nu}_e} = 1\,\text{eV}/\text{c}^2$ are plotted [33].

A non-zero neutrino mass will reduce the maximum kinetic energy of the electron since the energy for the rest mass of the neutrino will not be available. Hence, the shape of the electron spectrum is modified. Figure 2.1b shows an example of the electron spectrum with an assumed mass of the electron anti-neutrino of $m_{\bar{\nu}_e} = 1\,\text{eV}/\text{c}^2$.

Tritium as a β-emitter is ideal for neutrino mass measurements, the main advantages are [53]:

- Tritium has the second lowest[1] endpoint energy ($E_0 = 18.59\,\text{keV}$) of all elements [54], this allows to measure the β-decay electron energies in a MAC-E filter.

- Tritium has a relatively short half-life of 12.3 years, leading to a high specific activity ($3.6 \cdot 10^{14}\,\text{Bq/g}$). This allows to build a source of highest luminosity with a small amount of source material. Reducing the amount of tritium is essential to minimize inelastic scattering of β-decay electrons in the source, which also keeps systematic uncertainties as small as possible.

- Tritium, as a hydrogen isotope, has the lowest nuclear charge, hence minimizing inelastic scattering of β electrons within the source, too.

- Tritium has a simple shell configuration, therefore simplifying the *Fermi function* [55].

- The tritium β decay is a super-allowed nuclear transition. Thus, there are no energy-dependent corrections of the nuclear matrix element.

Over the past 30 years, a suite of experiments based on the kinematics of the tritium β-decay has pushed down the upper limit of the absolute neutrino mass (see section 1.4.3).

---

[1]the lowest known endpoint energy of $E_0 = 2.67\,\text{keV}$ has ^{179}Re

2.2 The MAC-E Filter Principle

As its precursor experiments in Troitsk [56] and Mainz [51], KATRIN will measure
the integrated energy spectrum of tritium β-decay by using a spectrometer based
on a MAC-E filter[2] concept [57]. In this setup, electrons are guided adiabatically by
a magnetic field and analyzed by an electrostatic filter. The MAC-E filter principle
is illustrated in figure 2.2.

Two superconducting solenoids provide a magnetic guiding field $\vec{B}$. The β-electrons
from the tritium source are guided adiabatically in the spectrometer with a starting
angle of ϑ_s with respect to the magnetic guiding field $\vec{B}$. In the ideal case, all signal
electrons with an acceptance angle of $\vartheta_s < 2\pi$ enter the spectrometer. Due to the
Lorentz force the electrons perform a circular motion around the magnetic field lines.
Hence, the momentum p of the electron is composed of a component parallel to the
magnetic field lines (carrying longitudinal energy $E_\parallel$) and a component transversal
to the magnetic field lines (carrying cyclotron energy $E_\perp$):

$$E_{\text{kin}} = E_\parallel + E_\perp. \tag{2.3}$$
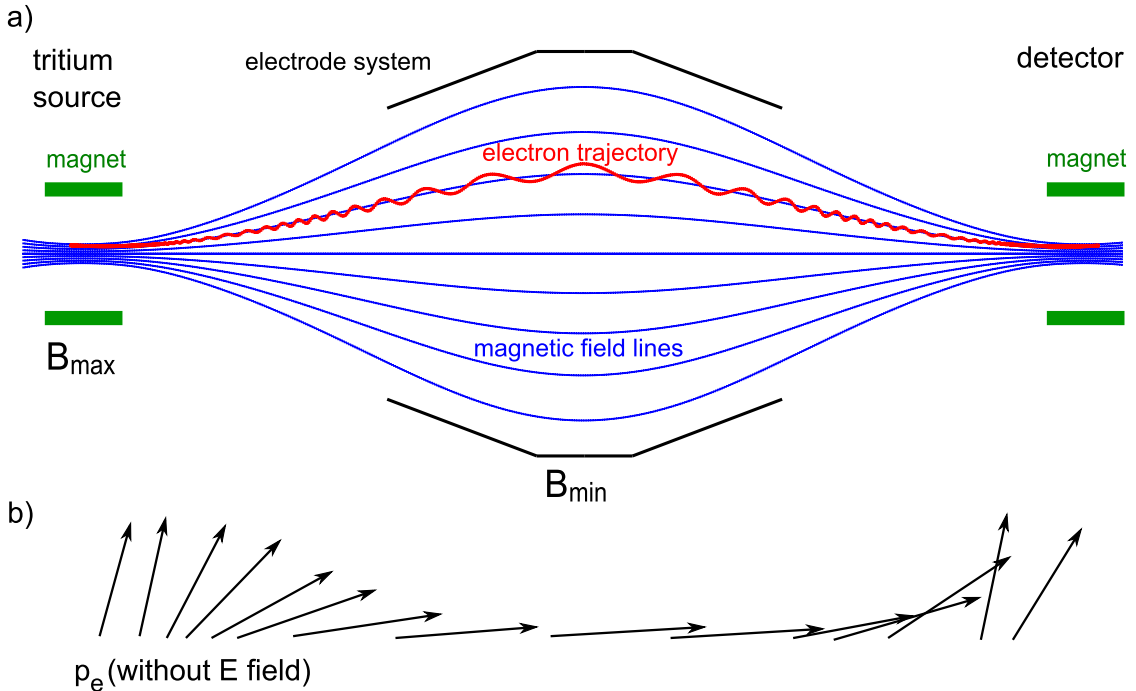
Figure 2.2: schematic drawing of a MACE-E filter. a) Two superconducting solenoids
(green) produce an inhomogeneous magnetic field. The electrons (red) are guided adiabatically
from the source to the detector in a cyclotron motion by the magnetic field lines (blue). **b)** Towards
the center of the spectrometer the magnetic field drops by many orders of magnitude. Due to the
invariance of the orbital magnetic moment μ in the inhomogeneous magnetic field the momentum p
of the electron is transformed. Most of the cyclotron energy $E_\perp$ is transferred into the longitudinal
motion $E_\parallel$.

This parallel beam of electrons is running against an electrostatic potential generated by a system
of inner electrodes. Hence, the MAC-E filter forms a high-pass filter for electrons. Electrons with
enough energy to pass this barrier are reaccelerated and collimated onto a detector. The figure is
based on [33].

---

[2]Magnetic Adiabatic Collimation combined with an Electrostatic filter (MAC-E)

In the case of KATRIN the spectrometer vessel itself is elevated on a negative potential (about $-18.6\,\text{kV}$) creating an electrical field parallel to the magnetic field lines. Hence, the electrostatic filter is only sensitive to the longitudinal component $E_\parallel$ of the kinetic energy. The signal electrons from the source are emitted isotropically and thus carry significant transversal energy. The circular energy $E_\perp$ must therefore be converted to longitudinal component $E_\parallel$ to analyze the energy of the β electron. This is achieved by the principle of the conservation of the magnetic moment μ of the electron:

$$\mu = \frac{E_\perp}{\left|\vec{B}\right|} = \text{const.} \tag{2.4}$$

In the center of the spectrometer the B-field drops by several orders of magnitude: from the maximal magnetic field B_{max} inside the magnets to the minimal magnetic field B_{min} in the analyzing plane. The magnetic gradient thus transforms the transversal cyclotron energy $E_\perp$ into longitudinal energy $E_\parallel$ (see equation 2.4). As a result the energy of the electron can be analyzed by the electrostatic filter. If the longitudinal energy component of an electron stays positive along its trajectory, it will be transmitted to the detector, otherwise it will be reflected back to be absorbed in the source. All electrons that pass the filter move from low to high magnetic field so that their longitudinal energy is transformed back into the original transversal energy state. The momentum vector (without E field) is shown in figure 2.2b. The filter width is defined as

$$\frac{\Delta E}{E} = \frac{B_{\text{min}}}{B_{\text{max}}}. \tag{2.5}$$

For a perfect filter the transmission of electrons with a kinetic energy $E \leq eU$ would be zero and for electrons with $E > eU$ maximum. In a MAC-E filter the transmission increases from zero to maximum. The width of this transition region equals the 'energy resolution ΔE' of the spectrometer. The probability for an electron to pass the spectrometer is given by the transmission function:

$$T(E,U) = \begin{cases} 0 & \text{for } E - qU < 0 \\ 1 - \sqrt{1 - \frac{E-qU}{E} \cdot \frac{B_{\text{min}}}{B_{\text{max}}}} & \text{for } 0 \leq E - qU \leq \frac{B_{\text{min}}}{B_{\text{max}}} \cdot E \\ 1 & \text{for } E - qU > \frac{B_{\text{min}}}{B_{\text{max}}} \cdot E \end{cases} \tag{2.6}$$

Only electrons with enough energy can pass the retarding potential U inside the spectrometer and are refocused onto a detector for counting by a second solenoid. Due to the *magnetic mirror effect* the maximum acceptance angle of the spectrometer for electrons from the source is given by:

$$\vartheta_{\text{max}} = \arcsin \sqrt{\frac{B_s}{B_{\text{max}}}}, \tag{2.7}$$

with the source magnetic field strength B_s and a maximum magnetic field B_{max}. The magnetic field reflects all electrons with a larger starting angle ϑ_{max}. A significant disadvantage of this MAC-E filter principle is the fact that the two solenoids of the spectrometer form a *magnetic bottle* in which charged particle can be trapped and induce background due to residual gas ionization.

2.3 The KATRIN Setup

KATRIN is the next generation tritium based neutrino experiment and currently under construction at KIT (Karlsruhe Institute of Technology). With a total length of about 70 m KATRIN will observe β-decay electrons from a windowless gaseous tritium source. The electrons will be guided adiabatically by magnetic fields from the source to the detector. To retain the injected tritium, a differential and cryogenic pumping section follows the tritium source downstream. The kinetic energy of the electrons is measured in an electro-static tandem spectrometer (both based on the MAC-E filter principle, see section 2.2). A segmented silicon detector counts all electrons that pass the electrostatic retarding potential inside the spectrometers. A schematic overview of the KATRIN experimental setup is illustrated in figure 2.3.
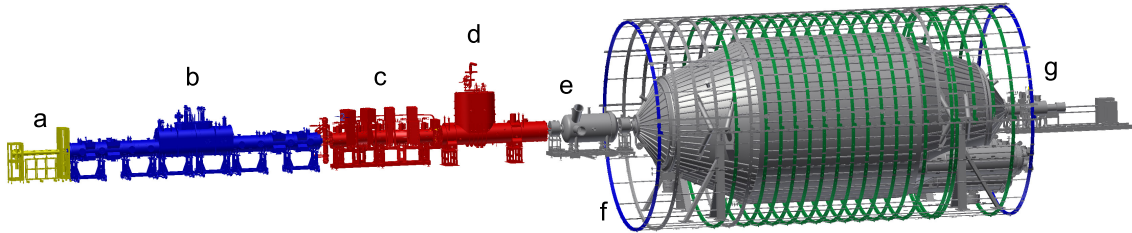
Figure 2.3: A schematic overview of the KATRIN beamline, a) rear section, **b)** windowless gaseous molecular tritium source (WGTS), **c)** differential pumping section (DPS), **d)** cryogenic pumping section (CPS), **e)** pre-spectrometer, **f)** main spectrometer, **g)** detector system.

2.3.1 Design Parameters of the KATRIN Experiment

To reach the ambitious goal of determining the neutrino mass with a sensitivity of $200\,\text{meV}/\text{c}^2$, the following design parameters were proposed [33]:

- a high tritium purity of about $\epsilon_{\text{T}} \approx 90\%$ and an extensive monitoring system.

- the signal rate of the tritium source is proportional to the ratio of the effective to free column density. Therefore the KATRIN source should reach a column density of $5 \cdot 10^{17}$ molecules/cm^2.

- the magnetic guiding field must be sufficiently high (with $B_{\text{max}} = 6\,\text{T}$) to guarantee adiabatic transport of the signal electrons.

- with a source magnetic field strength of $B_{\text{s}} = 3.6\,\text{T}$, an acceptance angle of $\vartheta_{\text{max}} = 51.7°$ is reached (see equation 2.7).

- with a retarding potential of about $U = 18.6\,\text{kV}$, and a minimal magnetic field in the analyzing plane of $B_{\text{min}} = 3 \cdot 10^{-4}\,\text{T}$, the resulting energy resolution of the main spectrometer is $\Delta E = 0.93\,\text{eV}$ (full transmission width).

- with an area of the analyzing plane of $A_{\text{A}} = 63.6\,\text{m}^2$ in the center of the main spectrometer, the maximal magnetic flux which has to be transported from the source to the detector is $\Phi = \int B \text{d}A = B_{\text{min}} \cdot A_{\text{A}} = 191\,\text{Tcm}^2$.

These features result in an improvement of the signal rate by a factor of 100 compared to the previous experiments in Mainz and Troisk.

2.3.2 Rear Section and Tritium Source

A key component of KATRIN is the windowless gaseous tritium source (WGTS) with an activity of 10^{11} Bq [58]. To ensure a high stability of the isotropic composition and to stabilize the column density of the WGTS on a 10^{-3} level, an extensive sensor instrumentation and monitor system (rear section and tritium loop system) is required.
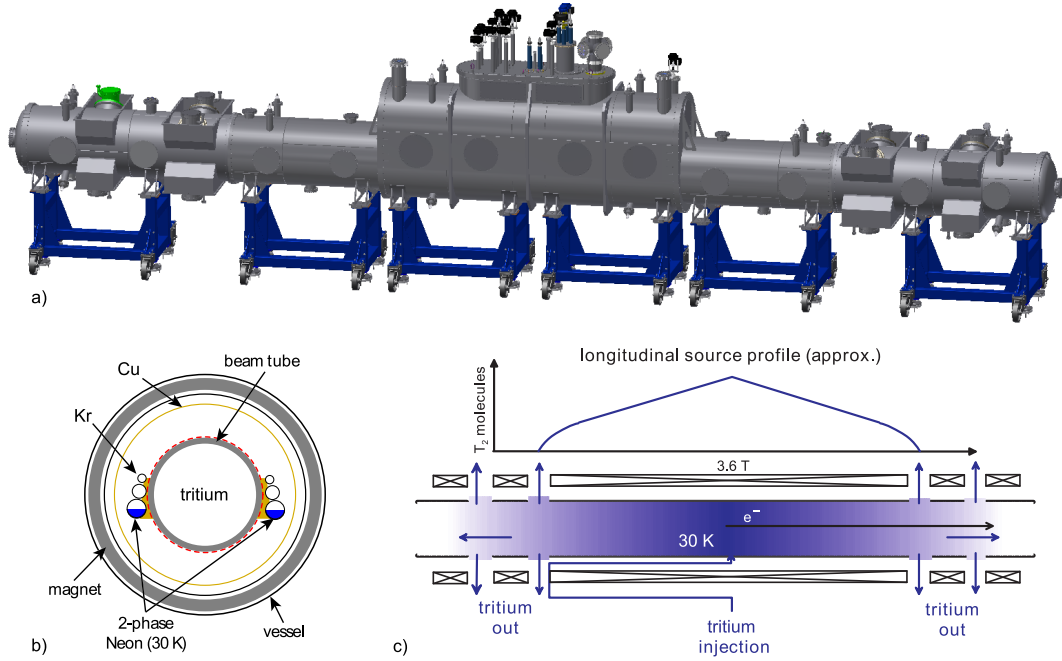
Figure 2.4: Schematic overview and principle of the WGTS. a) technical drawing of the WGTS setup. **b)** Cut through the WGTS cryostat. The source tube is cooled by two copper pipes filled with 2-phase neon^a at its boiling point (30 K). The closed neon cycle is cooled with gaseous helium at 25 K. The WGTS beam tube is surrounded by a copper shield and superconducting magnets. **c)** By continuously injecting tritium gas in the middle of the beam tube and pumping at both it ends, the density profile inside the WGTS is kept constant. The Figures are based on [58] and [33].

---

^{a}For calibration purposes the WGTS can be operated at 120 K, this temperature is obtained by exchanging the liquid neon for liquid krypton - the so-called krypton mode.

The Rear Section The rear section [59] is located at the rear end of the KATRIN tritium source. It includes a rear wall which defines the plasma potential and also monitors continuously the tritium source activity via x-rays. Furthermore the rear section is equipped with an electron source (egun) to periodically measure the column density and thus the transmission and response function of the whole KATRIN setup.

The Windowless Gaseous Tritium Source (WGTS) The windowless gaseous tritium source (WGTS) will work with a specific activity of 1.7×10^{11} Bq and is built as an open cylindrical beam tube with a diameter of $d = 90$ mm and a length of $l = 10$ m. It is surrounded by superconducting solenoids generating a homogeneous magnetic field of $B_\mathrm{s} = 3.6$ T. The tritium gas is injected in the middle (see figure 2.4b) with a pressure of $p = 3.3 \cdot 10^{-3}$ mbar. The gas is pumped out at both

ends, thus forming a constant tritium density profile inside the WGTS. The gas flow is regulated also by the beam tube temperature of about $T = 30\,\mathrm{K}$. The cooling concept [60] of the WGTS beam tube is based on two $16\,\mathrm{mm}$ evaporator tubes brazed onto the beam tube, which are partially filled with neon at its boiling point (30 K) (see figure 2.4b). The key WGTS parameters are the column density $(5.0 \times 10^{17}\,\mathrm{molecules/cm^2})$ and the composition of the hydrogen isotopologues (T_2, DT, HT, D_2, HD, H_2). If the column density is too large, the increased inelastic scattering of signal electrons will lead to systematic uncertainties deriving m_ν. Additional systematics arise from non-T_2 impurities, since different isotopologues have different recoil energies and different molecular final state distributions [58].

In its final configuration the WGTS is foreseen to be operated on a variable voltage of up to $1\,000\,\mathrm{V}$. This could be used to modify the potential difference between the WGTS beam tube and the main spectrometer.

The Tritium Inner Loop System and the Gas Composition Monitoring (LARA)
The tritium inner loop system (see figure 2.5 and [61]) is a tritium flow controller built at Tritium Laboratory Karlsruhe (TLK) which provides a constant gas injection and a stable gas composition. The injection of tritium gas in the middle of the WGTS as well as the pumping scheme on both ends of the source must be balanced (see figure 2.4b) to achieve a stable column density. For a stable injection, a constant gas flow $Q = \Delta p c$ is ensured by a constant pressure gradient (Δp) and a constant conductance (c) - monitored by a system of temperature and pressure sensors. The stable pumping rate is achieved by using turbo molecular pumps (TMPs) on both ends of the WGTS.

Tritium purity and gas composition is monitored using laser Raman spectroscopy (LARA). A particular challenge for the loops is given by the fact that a high throughput of $10\,\mathrm{kg/year}$ of high-purity molecular tritium has to circulated in the closed loop. LARA (see figure 2.5) is connected to the inner loop and enables the in-line monitoring of gas composition without contact. It is based on Raman scattering of light off the gas molecules.
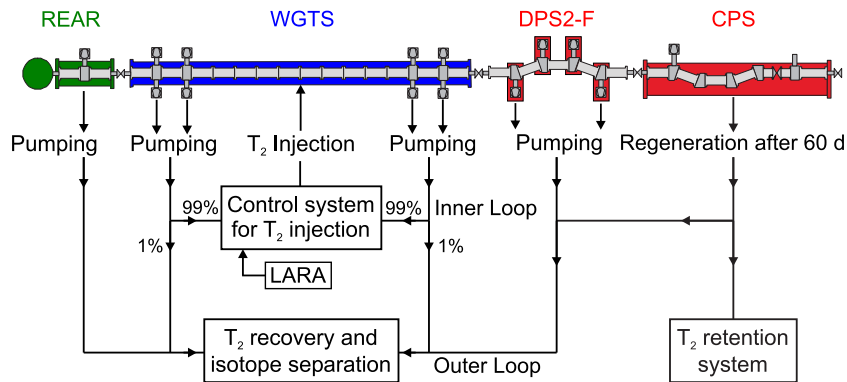
Figure 2.5: Schematic overview of the source and the transport section with the tritium management system. Shown are the rear section (green), the WGTS (blue) and the transport section (red) with the tritium loop system. A large amount of tritium is directly recycled through the inner loop system. LARA is connected to the inner loop and enables the in-line monitoring of gas composition. Lower flow rates but higher impurities are handled by the outer loop system. The figure is based on [58] and [62].

2.3.3 Transport and Tritium Retention Section

The purpose of the transport section is to adiabatically guide the β-decay electrons from the tritium source to the spectrometer section while at the same time retaining the tritium in the source. For a successful neutrino mass measurement it is crucial that the spectrometer section is essentials tritium-free ([63] and [62]). Therefore the tritium flow must be reduced from $1.8\,\text{mbar}\cdot\text{l/s}$ down to about $10^{-20}\,\text{mbar}\cdot\text{l/s}$ in the main spectrometer to provide a low background rate. KATRIN combines several pumping techniques such as differential and cryogenic pumping to achieve this.

The Differential Pumping Section (DPS2-F) The differential pumping section (DPS2-F) is based on four stages of differential pumping (see figure 2.6b), each using a *Leybold MAG W 2800* TMPs and a bended beamline. The four bends of 20° (see figure 2.6a) in the beamline are used to avoid the beaming effect of T_2 molecules from the source towards the spectrometer section. The main objectives of the DPS2-F design are [62]:

- an adiabatic transport of electrons with a magnetic flux of $191\,\text{T}\,\text{cm}^2$,

- a tritium flow reduction $> 2.5\cdot 10^4$ (this experimentally obtained value of the actual DPS2-F differs from the specified value of $1\cdot 10^5$),

- an instrumentation for beam diagnostics (FTICR) and the ion removal [64].

After a magnet safety failure of the previous DPS2-F cryostat, a new DPS concept (see figure 2.6a) foresees five superconducting magnets in a bended arrangement, fixed on a support bearing the weight and the magnetic forces. The five beam line tubs are placed in the warm bore of the magnets and are supplemented by four pumping chambers. The second containment is constricted to the beam line and the pumping chambers, suspending the magnets. The beam line instrumentation of the old DPS2-F as well as the interfaces and the peripheral equipment can be reused.
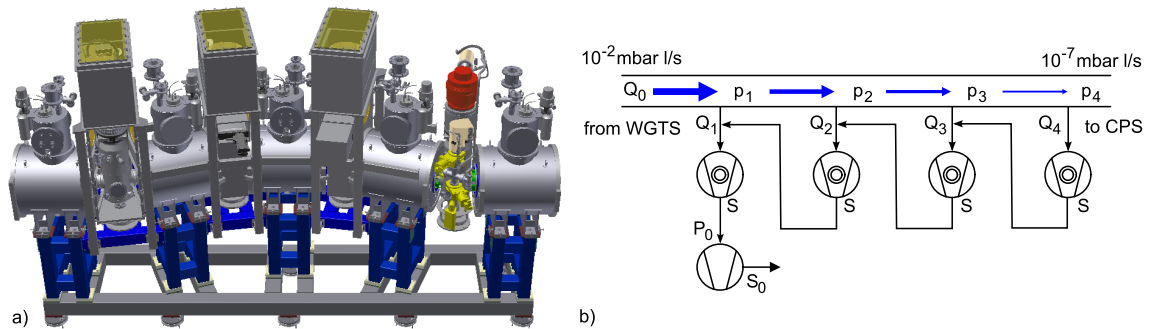
Figure 2.6: schematic overview of the Differential pumping section (DPS2-F). a) technical drawing of the new DPS2-F concept. The inner vacuum system has four bends of 20° in order to increase the pumping efficiency and to avoid transport of T_2 molecules. **b)** The tritium flow is reduced by a factor of 10^5 by differential pumping with four identical TMPs[a].

---

[a]The technical drawing was provided by V. Popov and the schematic drawings are based on [62]

The Cryogenic Pumping Section (CPS) The cyrogenic pumping section (CPS) (shown in figure 2.7) uses a similar setup: a fourfold buckled beamline surrounded by superconducting magnets ($B = 5.6\,\text{T}$ or correspondingly a magnetic flux of $\Phi_B = 191\,\text{T}\,\text{cm}^2$) guides β-electrons adiabatically into the spectrometer section.

To reduce the tritium flow by a factor of $\geq 3 \times 10^7$ the CPS setup features an argon frost pump based on cryo-sorption (see schematic drawing 2.7). The system is kept at a temperature of $3 - 6\,\text{K}$ where a layer of argon frost is deposited onto a gold-plated stainless steel pipe. Tritium molecules are passively absorbed by the argon, minimizing the tritium contamination of the beam tube. After a 60 days measuring period, the thin layer of argon frost is removed by purging with warm He gas. After purging, the adsorbed tritium gas will be reprocessed, see figure 2.5. The adsorption properties of condensed argon were simulated [65] and studied in the test experiment TRAP [66].

In the last section of the CPS the beam tube is equipped with a non-evaporable getter (NEG) pump [67]. In the standard operation mode no significant amounts of tritium should reach this section. However, in case of a system malfunction, the cold gate valve between CPS and pre-spectrometer will close within a few seconds. The getter will prevent a build-up of residual gas that could condensate and damage the valve. Furthermore the getter is the last resort if a sudden cryopumping failure occurs and excessive amounts of tritium could be released. The NEG pump will prevent a contamination of the spectrometer section with tritium until (about $t = 15\,\text{s}$) the valve is closed.
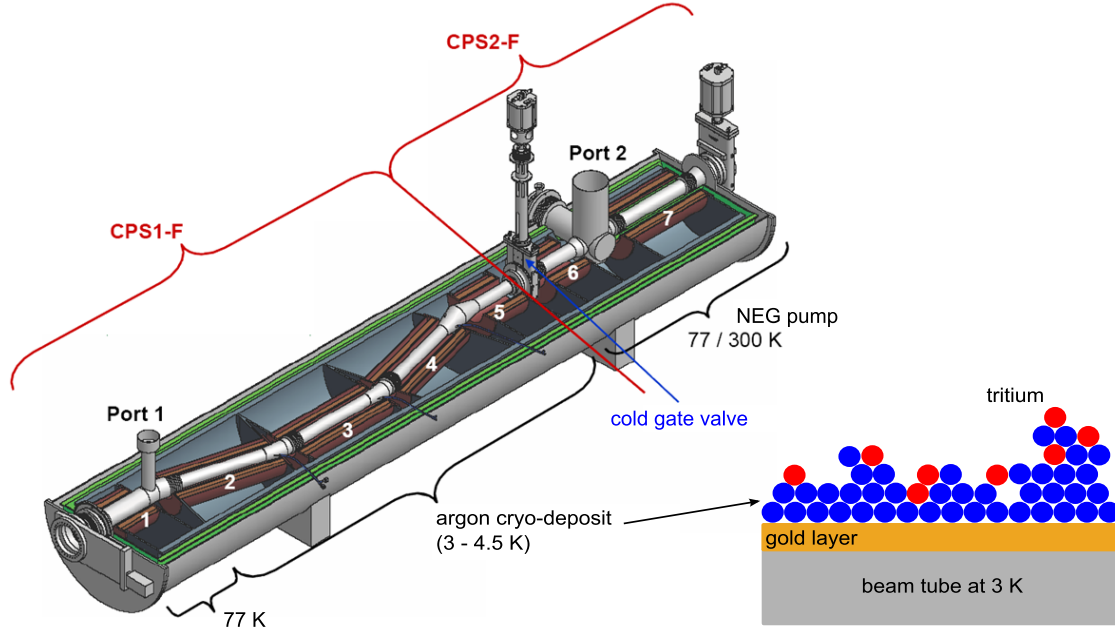
Figure 2.7: Technical drawing of the Cyrogenic Pumping Section (CPS) and schematic drawing of the argon frost pump. Section 1 to 5 is covered by a layer of argon frost. Section 7 is equipped with a non-evaporable getter (NEG) pump [67].

2.3.4 Spectrometer Section

The tandem spectrometer section forms a central part of the KATRIN experiment. The electrostatic spectrometers are based on the MAC-E filter principle (see section 2.2). The magnetic field generated by superconducting solenoids at each side of the spectrometer guides β-decay electrons adiabatically to the detector. The transversal energy of the electrons is converted to longitudinal energy due to the conservation of the their magnetic moment μ. In the analyzing plane the electrons have to pass the retarding potential applied to the spectrometer vessel. A complex system of inner electrodes is devoted to a more negative potential relative to the tank potential. This feature reduces background induced from electrons emitted from the vessel walls created by cosmic rays or radioactive decays.

In order to reduce background due to ionization of residual gas, a strict UHV regime with $p < 10^{-11}$ mbar is needed in the spectrometer section. Therefore the KATRIN vacuum setup combines a system of cascaded turbo-molecular pumps (TMP) and non-evaporable getter (NEG) pumps.

Both vessels were made of electro-polished stainless steel (316LN). To reduce the outgassing rate of the vacuum surfaces, and to activate the NEG pumps, the whole system can be heated up to $350\,^\circ$C. The goal of the vacuum technology is to reach an outgassing rate for hydrogen of about $1 \cdot 10^{-12}$ mbar l/s/cm^2 [68] [69] to maintain a final pressure of $p < 10^{-11}$ mbar.

The pre-spectrometer   The pre-spectrometer allows the option to act as a high-pass pre-filter to reduce the electron flux arriving at the main spectrometer. Based on the MAC-E filter principle, the retarding potential could be set up to $E = 18.3$ keV to reflect all electrons with smaller energies carrying no information about the neutrino mass. By decreasing the amount of electrons entering the main spectrometer the background due to residual gas ionization is minimized. In this case, however, a major Penning trap will form, so that a pre-spectrometer at 0 V is the default option.

With a diameter of 1.7 m and a length of 3.4 m and a resulting volume of 8.5 m^3 and an inner surface of 25 m^2, the pre-spectrometer is a smaller version of the main spectrometer. In β-spectroscopy, this reduced size results in an inferior energy resolution of $\Delta E \approx 70$ eV. The experimental setup of the pre-spectrometer as part of the KATRIN beamline is described in detail in chapter 3.

The main spectrometer   The KATRIN main spectrometer provides a precision energy analysis of β-decay electrons. Based on the MAC-E filter principle, the magnetic field inside the spectrometer drops by a factor of 20 000 leading to an energy resolution of $\Delta E = 0.93$ eV. With a diameter of 10 m and a length of 23.4 m, the main spectrometer forms a major component of the experiment. The recipient has a volume of $V = (1\,238 \pm 2)$ m^3 and a inner surface of $A = 690$ m^2. It is evacuated by six TMPs and three NEG pumps (each equipped with about 1 000 m *SAES St707* getter strips).

Inside the spectrometer a two layered 'massless' inner wire electrode system is mounted. The potentials of the two layers of wires are foreseen to be operated with an offset of -100 V to -200 V to the tank potential. The 24 000 wires define a

high-precision axially symmetric retarding potential of the MAC-E filter. The main spectrometer is surrounded by two air coil systems: the Earth Magnetic Field Compensation System (EMCS) to compensate the geomagnetic field over the major part of the spectrometer, and the Low Field Correction System (LFCS) for fine-tuning the magnetic flux tube. The whole experimental setup is described in detail in chapter 4.

The monitor spectrometer The former Mainz spectrometer is now being used for precise voltage monitoring [70]. With a length of 3.5 m and 1 m in diameter the spectrometer retarding potential is fed by the HV of the main spectrometer. By observing a krypton source as a nuclear standard the monitor spectrometer adds an online voltage monitoring system to KATRIN. The spectrometer scanns the monoenergetic K32 line ($E = 17.8$ keV conversion electrons) of the ^{83m}Kr decay, hence it is able to determine long-term variations of the retarding potential on a ppm scale. To cross check the results, a high-voltage divider is connected to a precise voltmeter [71].

2.3.5 Detector System

The Focal Plane Detector (FPD) at the end of the beamline is a silicon PIN-diode array with 148 pixels on a wafer with a diameter of 125 mm (see figure 2.8b). The pixels are separated by 50 μm and have a dead layer of about 100 nm.
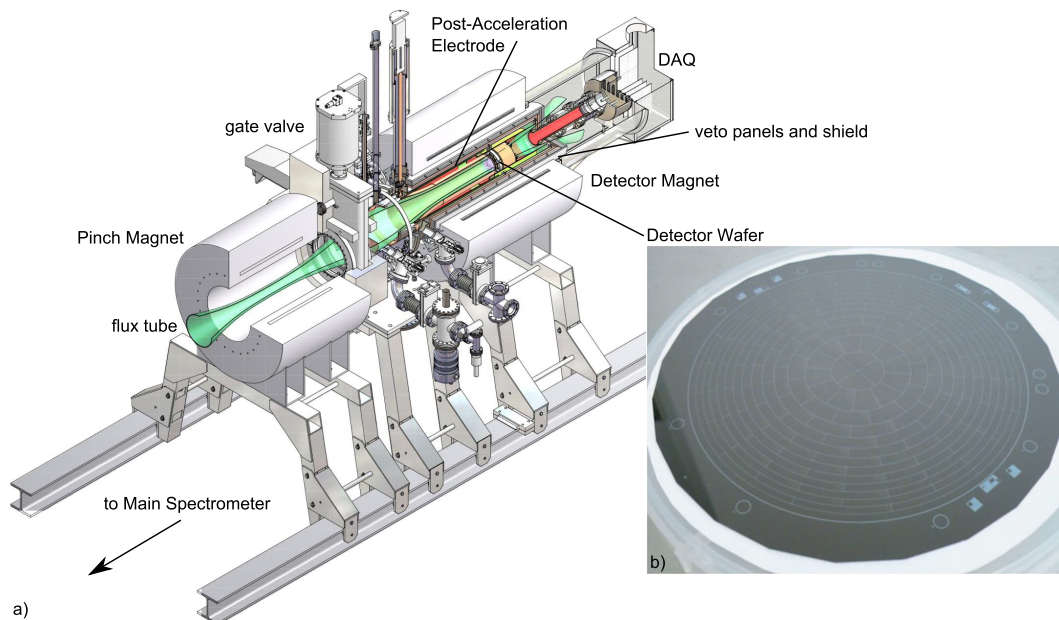
Figure 2.8: The Focal Plane Detector System. a) Shown is the FPD System as it is installed at main spectrometer. The magnet system and the flux tube carrying the signal electrons is shown as well as the actual detector, its electronics, the shielding and the muon-veto. **b)** The 148 pixels are arranged in a radial set-up consisting of twelve rings made up of twelve segments plus four pixels for the bulls eye. Each pixel is designed to encompass the same area. The segmentation with the resulting position sensitivity makes it possible to investigate inhomogeneities of the retarding potential in the source and the analyzing plane. The figure is based on [72].

The β-decay electrons are guided to the FPD by two superconducting solenoids: the pinch magnet at $6.0\,\mathrm{T}$ at the spectrometer exit and the detector magnet operating at $3.6\,\mathrm{T}$ surrounding the wafer. The detector is mounted inside the bore of the detector magnet in an ultra high vacuum (UHV) chamber that can be separated from the main spectrometer by an in-beamline valve placed in the bore of the pinch magnet. The custom made data acquisition (DAQ) electronics (manufactured by the IPE, Karlsruhe) and the cooling system are placed in a high vacuum (HV) chamber downstream of the detector.

The trumpet-shaped, post-acceleration copper electrode forms part of the boundary between the UHV (inside) and HV (outside) chambers. The electrode is brazed to a ceramic insulator and at the present can carry a $10\,\mathrm{kV}$ potential. By accelerating the signal electrons a larger input signal is created giving a better timing resolution due to their higher signal-to-noise ratio. Hence, applying a post-acceleration potential improves timing resolution without sacrificing energy resolution of the detector.

For testing and calibration purposes the detector system is equipped with a γ source ($^{241}\mathrm{Am}$ or $^{109}\mathrm{Cd}$) that can be moved into the line of sight of the FPD without breaking the vacuum and the detector can be illuminated with an ultraviolet light-emitting diode (255 nm UV LED).

The system (see figure 2.8a) was constructed by the US collaborators led by the University of Washington, Seattle.

2.4 Sensitivity of the KATRIN Experiment and Background Processes

This section gives an overview of systematic uncertainties caused by the experimental setup of the source, the transport, the spectrometer and the detector section. The background rate of the entire experiment depend on several critical parameters. For comparison, the tritium β-decay electrons arriving at the detector typically result in a signal rate of no more than $10^{-2}\,\mathrm{cps}$. In order to reach the required accuracy, the background should be less or at least of the same order of magnitude [52]. If the statistic and systematic uncertainties contribute equally, KATRIN can measure a neutrino mass of $m(\bar{\nu}_e) = 350\,\mathrm{meV}$ with 5σ significance. If no neutrino mass signed is observed, KATRIN will set a new upper limit of

$$m\left(\bar{\nu}_e\right) < 200\,\mathrm{meV}\,(90\%\,\mathrm{CL}) \tag{2.8}$$

and therefore improve the current upper limit of the neutrino mass measured by tritium β-decay experiments by one order of magnitude [33].

2.4.1 Source and Transport Section (STS)

The background properties of the KATRIN tritium source have been investigated in detail by simulation tools [73] [74] identified severed sources for systematic uncertainties (e.g. the thermal behavior of the WGTS [60]). The following effects disturb the tritium β-decay spectrum:

- The exact gas composition of the tritium source has to be known to take into account the different final states of the tritium isotopologues. The LARA

setup [75] will allow an activity monitoring of a gaseous tritium source on the 10^{-3} level in $60\,\text{s}$.

- The inelastic interactions between β-electrons and source molecules will lead to energy losses due to scattering. The tritium column density depends on the source temperature [60], the gas influx [61] and the stability of the pumping scheme [76]. So all parameters have to be known and stabilized.

- The radiative corrections due to photon emission during the β-decay process and synchrotron radiation during propagation have to be taken into account.

- The energy remaining with the daughter molecule HeT and HeD, either in excited states or in the nuclear recoil energy have to be calculated precise.

- The Doppler effect due to the thermal motion of the gaseous tritium molecules calls for excellent temperature stabilities.

- The potential stability and magnetic field variations have to be kept at a minimum.

The simulation tool KASSIOPEIA and the KASPER analysis code are essential for a better understanding of the background properties of the KATRIN source. Besides providing corrections to the tritium β-decay spectrum by detailed modeling, an important tool is intensive monitoring of the tritium source to guarantee the stability of the operating parameters.

The major source of background in the transport section is generated by tritium ions leaving the source and following the magnetic field lines. The differential pumping scheme is only effective in removing neutral molecules. To kick out the tritium ions in the transport section, a dipole potential (about $100\,\text{V}$) is applied to the DPS2-F. The ions are drifted out of the flux tube by the dipole electrode [62] thus preventing an accumulation of the ions. Otherwise the resulting plasma would influence the energy of the signal electrons flying through the transport section. A non-destructive FT-ICR[3] detection system for monitoring the ion concentration will be installed in the KATRIN beamline [64].

2.4.2 Spectrometer and Detector Section (SDS)

This work focuses on the background properties of the spectrometers. The main spectrometer was designed on general principles based on the knowledge gained by the Mainz and Troitsk neutrino mass experiments. However, the detailed layout of the main spectrometer was only obtained after completing of the successful prototype measurements with the pre-spectrometer [77] [78]. On the one hand, MAC-E filters can suppress external background due to magnetic and electrostatic shielding, on the other hand it can produce additional background. This section presents a number of known background phenomena in MAC-E filter based systems.

---

[3]Fourier Transform Ion Cyclotron Resonance

The ionization of residual gas by signal electrons can create secondary electrons in the spectrometer volume which can not be distinguished from signal β-electrons. To minimize the number of signal electrons to be scanned inside the main spectrometer, the pre-spectrometer offers the option as pre-filter reflecting most of the β-electrons created in the tritium source.

Low-energy electrons emitted from the inner surfaces of the vessel gain energy due to the electric retarding field. At the detector these electrons result in a background that also can not be distinguished from signal electrons. However, these electrons induced by cosmic rays (in particular cosmic muons), field emission or radioactive decays in the vessel wall are shielded by four orders of magnitude by the magnetic flux tube. All particles emitted from the walls are guided adiabatically by one of the outer magnetic field lines and therefore will miss the detector. Additionally KATRIN is equipped with an complex inner wire electrode system kept on a slightly more negative potential. Which form an electrostatic barrier for low-energy electrons, adding a further shielding factor of 100.

Stored high energy electrons are produced in nuclear decays of tritium [79] or radon [80] inside the spectrometer volume. The two superconducting solenoids at the ends of the main spectrometer generate a magnetic bottle. An electron with an energy of $> 1\,\text{eV}$ [63] that is emitted inside the flux tube of the spectrometer can be trapped. The stored electron will thus lose its energy by residual gas ionization and thereby create thousands of low-energy secondary electrons and background events as discussed above [81]. The storage time depends on the pressure in the recipient. A very good vacuum ($< 10^{-11}\,\text{mbar}$) inside the spectrometer section is required to suppress interactions between signal electrons and residual gas molecules. The KATRIN design foresees a tritium partial pressure of $< 10^{-20}\,\text{mbar}$. This emphasizes the importance of the differential and cryogenic transport section detain tritium in the source as well as of efficient UHV technologies in the spectrometer, as relevant for this thesis. During this work a liquid nitrogen cooled baffle system was installed in front of the NEG pumps at the main spectrometer. By blocking the direct line of sight the radon emitted from the getter material is detained in the pump ports [82]. As an addition to these passive methods, a wide range of active counteractions against background were modeled and tested at the pre-spectrometer like the ECR method [63], an electric dipole field, a magnetic pulse or a large-pin solution [83].

Background due to Penning traps inside the spectrometer e.g. between the ground electrode and the inner electrode system have been avoided by improved simulations and a specially designed anti-Penning electrode [78]. However, the pre-spectrometer and the main spectrometer with a magnet in between form a large Penning trap when both are operated at an elevated level. Although this trap is not a direct source of background, the accumulation of positively charged ions generated by ionized residual gas there can accelerate trapped electrons resulting in the creation of further tertiary electrons. To remove this trap, the pre-spectrometer can be operated on ground potential, thus passing on its filter properties, or a mechanical wire scanner can be used with both spectrometers on potential which collects the stored ions and electrons.

The primary source of background in the detector section are electrons in the energy range of the signal electrons. In particular, low-energy electrons emitted near the analyzing plane are accelerated to the detector by the electrostatic field of the MAC-E filter. Hence, background in the region-of-interest between 17 keV and 19 keV create a particularly dangerous class for the KATRIN setup. The FPD system is equipped with a post-acceleration electrode that can boost signal electrons into an energy range with lower backgrounds, but this does not mitigate this background class. Possible background sources at the detector are:

Radioactive decays from environmental radioactivity that create X-rays or low-energy γ's. All critical components of the FPD-system were carefully chosen for their radio-purity and were radioassayed at the Low Background Facility of the Lawrence Berkeley National Laboratory. Additionally, *Geant4* was used to simulate the radioactive decays of ^{40}K, the ^{238}U chain and ^{232}Th chain near the detector. The FPD system is equipped with a radiation shield consisting of two cylindrical copper shells embedded with a 3 cm thick layer of lead.

Cosmic rays, in particular cosmic-ray muons, form a non-negligible contribution to the background. While the large spectrometers cannot be vetoed by counters, a veto system surrounding the detector chamber is tagging incoming muons. A photon counter detects the light emitted in plastic scintillators.

The total background in the 90 mm-diameter detector in an optimized energy window and without post acceleration is $5.4 \cdot 10^{-3}$ cps (measured at the University of Washington) [72].

3 Pre-spectrometer as part of the KATRIN Beamline

This chapter focuses on the experimental setup of the pre-spectrometer as part of the KATRIN beamline. This component is foreseen to act as a high pass filter for electrons and is based on the MAC-E filter principle. In the experimental setup of KATRIN the pre-spectrometer offers the option of a pre-filter operating on a constant potential $0 < U_0 < E_0$. As only electrons with energies close to the endpoint energy ($E_0 = 18.59\,\text{keV}$) of the tritium-β-spectrum provide information on the neutrino mass, a retarding potential of $U_0 \approx -18.3\,\text{kV}$ reduces the number of β-electrons that reach the main spectrometer by a factor of 10^6. By decreasing the flux of β-electrons into the main spectrometer, the background there due to residual gas ionization by the signal electrons is reduced.

As the first major KATRIN component on site at KIT, the pre-spectrometer vessel was first set-up as a research and development project. Figure 3.1 illustrates the basic parts of the pre-spectrometer setup. A stainless steel vessel serves as vacuum recipient it is expanded by two pump ports. The horizontal pump port is holding a set of three turbo molecular pumps (TMPs) forming a cascading pumping scheme. Each pump port is equipped with a non-evaporable getter (NEG) pump (see section 3.1). Between September 2003 and April 2011 the pre-spectrometer was used as an invaluable prototype setup (for more details see [77] and [78]). The objectives of the test measurements were to optimize the MAC-E filter concept, to verify the ultrahigh vacuum (UHV) design and to develop the detector and data acquisition (DAQ) system both hard- and software components (like the DAQ package ORCA [78] and the simulation package KASSIOPEIA [63]), as well as to investigate background processes. For the test measurements the pre-spectrometer was extended by a photoelectric electron source (e-gun) and a 64 pixel-segmented silicon detector. Two superconducting solenoids with a magnetic field of $4.5\,\text{T}$ completed the experimental setup (see section 3.3). It was the first implementation of a novel electromagnetic approach (see section 3.2) where the high voltage was directly applied to the recipient. At the same time an inner wire electrode system was used to fine tune the retarding potential and to shield secondary background electrons induced by cosmic rays.

After the successful completion of the test measurements, the pre-spectrometer was, as part of this work, reconfigured to match its future application as a MAC-E filter between the transport section and the main spectrometer. The major upgrade includes a complete new installation of temperature sensors and heating tapes (see section 3.4), as well as a renewal of the entire insulation (*Kanstinger Ing. GmbH*[1]). Inside the spectrometer the inner wire electrode system was upgraded. Now the holding structure is capable of retaining two NEG pumps with up to $1\,\text{km}$ of ad-

---

[1]Fa. Theo Kanstinger Ing. GmbH, Postfach 1144, 76317 Pfinztal

ditional getter strips. In October 2011 the pre-spectrometer was relocated to its final position in front of the main spectrometer (*Kierdorf & Söhne GmbH*[2]). For the commissioning measurements of the main spectrometer or general maintenance work the pre-spectrometer can be shifted aside to open the beam line (see section 3.3.1). Hence, the pre-spectrometer magnet (PS2) close to main spectrometer is placed on a new holding structure and can be operated independently of the pre-spectrometer setup.

3.1 Pre-spectrometer Vessel and Vacuum System

The stainless steel vessel (type DIN1.4429 or 316LN) was manufactured by *SDMS*[3], France. This non-magnetic stainless steel type is characterized by its low hydrogen outgassing properties and later was also used for the KATRIN main spectrometer. Hydrogen outgassing from the stainless steel walls is expected to be the main source of residual gas that limits the final equilibrium pressure of the vacuum chamber. Hence, all inner surfaces are electropolished and carefully cleaned following the high KATRIN vacuum standards. The pre-spectrometer basically consists of a cylindrical shape with an inner diameter of 1.68 m, a length of 3.38 m and 10 mm thick walls. The whole recipient has a volume of about $8.5\,\text{m}^3$ with an inner surface of about $25\,\text{m}^2$. Three chimneys with diameters of 160 mm each are welded on top of the vessel. They are closed with a DN160 CF flange, each holding two CN40 CF high voltage feedthroughs which are connecting the different parts of the inner electrode system to a power supply (see section 3.8). Additionally the middle chimney is equipped with a t-piece and supplemented by a rupture disc to burst in case an overpressure is exceeding 0.5 bar (above atmospheric pressure). The cylinder is closed with a DN500 flange and a DN1680 flange combined with DN500 flange. To seal the DN500 and DN1680 flanges a set of special spring loaded gaskets [77] were produced by HTMS[4], Belgium. The DN1680 flange must be opened to install the inner electrode system. The DN500 flanges on both sides of the spectrometer are equipped with a conical ceramic insulator (*Friatec*[5], Germany) ending in a DN200 flange. The ground electrodes are connected to the DN200 part of these insulator flanges opening inside the spectrometer. To remove a Penning trap between the ground electrode and the inner electrode system a special anti-Penning electrode (operated at tank potential) is installed at the DN500 part of the insulator flanges (for details see figure 3.9a).

The pre-spectrometer vacuum system was designed to maintain a pressure of less than 10^{-11} mbar. To achieve this ambitious goal different pumping techniques are combined. At a position of 75 cm off the middle axis of the pre-spectrometer two tubes are acting as pump ports. Both pump ports have a length of 1 m and diameter of 50 cm, and are housing a NEG pump (each equipped with 100 m *SAES*[6] St707 getter strips). The pump ports are closed with a DN500 flange reduced to two DN200 and two DN63 flanges. In addition to the NEG pump the horizontal

---

[2]Kierdorf & Söhne GmbH, Schumannstraße 2, 76676 Graben-Neudorf, Germany

[3]SDMS, Les Condamines, 761 Route de Valence - CS 40004, 38160 Saint Romans, France

[4]HTMS NV - High Tech Metal Seals, Blarenberglaan 5, B-2800 Mechelen, Belgium

[5]FRIATEC AG, Steinzeugstraße 50, 68229 Mannheim, Germany

[6]Saes Getters S.p.A., Viale Italia 77, Lainate (Milan), Italy

pump port provides a two-staged cascaded pumping scheme. Each DN200 flange is followed by a *VAT*[7] DN200 full-metal gate valve (series 48), a ceramic insulator and a turbo molecular pump (TMP). The exhaust ports of the two main TMPs are connected to a third TMP, forming an intermediate vacuum. As fore-pump a scroll pump is used. The active and passive pumping scheme is described in detail in section 3.1.1 and 3.1.2.

On top of the 45° pump port a DN63 valve is mounted followed by a *Pirani* vacuum gauge. Right next to the horizontal pump port in the center of the spectrometer axis a 30 cm long side-port with a DN160 flange is welded in (see figure 3.1f). After a reduction piece, a DN63 valve connects the 'measuring cross' to the pre-spectrometer. This cross contains the UHV gauges and a residual gas analyzer (see section 3.1.3). The pumping scheme and the gauges used in the system are described in more detail in the following sections and a complete vacuum flow chart is presented in figure A.2 in appendix A.
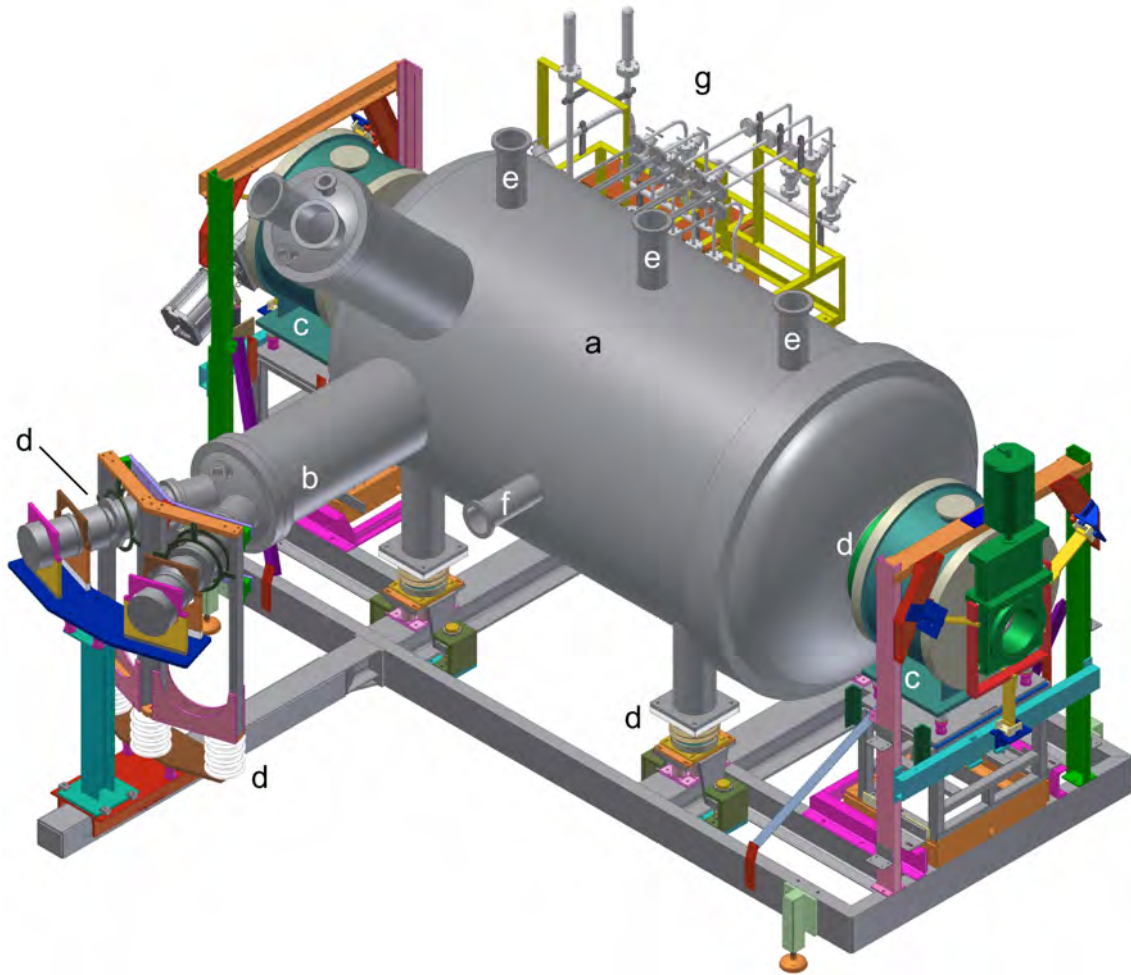
Figure 3.1: Technical drawing of the pre-spectrometer setup. a) pre-spectrometer vessel, **b**) pump port with TMPs, **c**) two superconducting solenoids, **d**) ceramic insulators for high voltage separation, **e**) port with high voltage (HV) feed through for the inner electrode system, **f**) port for 'measuring cross', holding the vacuum gauges (see section 3.1.3) and a residual gas analyzer (RGA), **g**) flow and return pipes for the thermo oil circuit.

---

[7]VAT Deutschland GmbH, Am Hochacker 4, 85630 Grasbrunn, Germany

3.1.1 Momentum Transfer and Positive Displacement Pumps

Momentum transfer pumps, here turbo molecular pumps (TMPs), operate with high speed rotating blades to push residual gas molecules out of the vacuum chamber. Positive displacement pumps (here scroll pumps) use a mechanism to repeatedly expand a cavity, thus allowing gases to flow in from the vacuum chamber, while sealing off the cavity and exhausting it to the atmosphere [84]. In general positive displacement pumps are most effective for evacuating vacuum chambers or to maintain fore-vacuums. Positive displacement pumps in combination with one or two momentum transfer pumps are a common configuration used to achieve high vacuums. Turbo molecular pumps cannot start pumping at atmospheric pressure. Hence, a scroll pump is used to obtain a fore-vacuum in the recipient before the momentum transfer pumps gain a pressure in the high vacuum regime. Mounted in a cascade, the scroll pump backs up the TMPs by evacuating to a low vacuum and thereby preventing an accumulation of displaced molecules in the TMP.

At the pre-spectrometer a two-stage cascaded set of TMPs is attached to the horizontal pump port of the vessel. Two *Leybold*[8] MAC-W-1300 TMPs are operated in parallel and form the first stage of the pumping scheme maintaining an ultra high vacuum (UHV) of about 10^{-9} mbar. At the exhaust flanges of the two main TMPs a second stage *Leybold* TW290 TMP is installed, which creates an intermediate vacuum in a pressure range of about 10^{-7} mbar. A *Leybold* Scroll fore pump forms a last stage which can operate in the $10^{-2} - 10^{-3}$ mbar region. The different pumping stages are separated by pneumatic driven valves. This cascaded pumping scheme with a intermediate pressure in the UHV range prevents a back-diffusion of gas through the first stage TMPs into the vacuum chamber. A lower pressure can be reached due to a higher H_2 compression. The system provides an effective pumping speed of $1\,000\,\ell/\text{s}$ for nitrogen.

To separate the TMPs from the vessel two full-metal DN200 gate valves are connected with bellows to the DN200 flanges of the horizontal pump port. Between the gate valve and the TMP a DN200 ceramic tube is used to insulate the pumps during the high voltage operation. A second bellow attached to the ceramic is protecting the fragile tube from vibrations caused by opening and closing the valve. By adding the length of all these components, the TMPs are about 2.8 m away from the center axis of the spectrometer.

If the superconducting magnets are operated with their standard field strength of $B = 4.5\,\text{T}$ in the center of the solenoid, the TMPs are exposed to magnetic fields (see figure 3.2a) of up to 3 mT. Magnetic fields induce eddy currents in the fast moving rotor of the TMP that causes heating of the plates. During long-term operation the heating of the rotor can lead to the destruction of the pump. The effects of the magnetic stray field caused by the two solenoids were investigated in an external setup. To replicate the effects of magnetic fields up to 50 mT, a Helmholtz coil setup (diameter: 120 cm, distance: 60 cm) was set-up at KIT [85] in the framework of this thesis. A TMP can be mounted at the center of the coils and connected to a pumping station. The temperature of the rotor is monitored in a contact-free manner by an infra-red pyrometer. A theoretical model to predict the rotor temperature over time was developed [86]. It is based on a differential equation of the power balance:

---

[8]Oerlikon Leybold Vacuum, Bonner Str. 498, 50968 Köln, Germany

$$m_{\text{rotor}} \cdot c \cdot \frac{\mathrm{d}T_{\text{rotor}}(t)}{\mathrm{d}t} = \sum_i P_i(t) = m_{\text{rotor}} \cdot c \cdot \sum_i k_i \cdot f_i(t) \qquad (3.1)$$

where the rotor mass is given by m_{rotor}, its temperature by T_{rotor} and its corresponding specific heat capacity c. The sum of the heating and cooling powers $P_i(t)$ is expanded by specific constants k_i multiplied by a function $f_i(t)$. These time-dependent functions $f_i(t)$ contain the physical parameters of the model, like the stator temperature, the motor current or the external magnetic field. For a more detailed derivation of the rotor temperature model see [87], [88] and [85].

The magnetic field compatibility tests of the pre-spectrometer TMP (*Leybold* MAC-W-1300) are presented in detail in [89]. In addition to the heating of the rotor, the stability of the magnetic bearing and the integrated electronics as well as the reliability of the controller were investigated for different field directions. The following summary and plots will focus on conditions that manifest at the place of the TMPs at the pre-spectrometer setup. The TMP was mounted in the test setup with the high vacuum flange pointing down and the Helmholtz coils were rotated that the magnetic field points upwards. Eddy currents occur only for perpendicular components of a static magnetic field.

Figure 3.3a shows an endurance test with the characteristic influence on the motor current by an increasing external magnetic field. A maximum motor current of $I_{\text{motor}} = 2.4\,\text{A}$ was reached in a vertical magnetic field of $B = 8.5\,\text{mT}$. In even higher magnetic fields the motor of the pump can not compensate further the braking torque. Hence, the rotational frequency is reduced. After switching off the magnetic field the pump stabilized at nominal rotational frequency and the motor current drops back to nominal values.
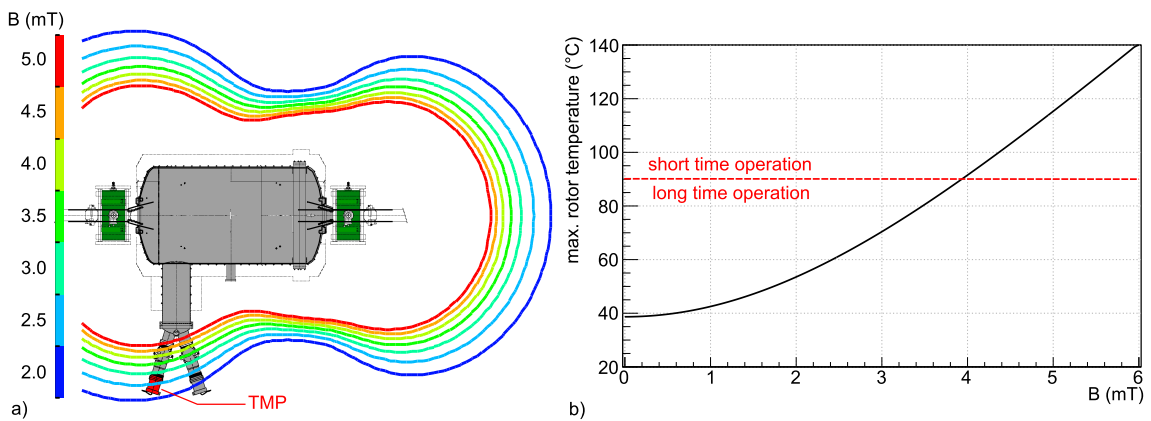
Figure 3.2: Magnetic field compatibility of the pre-spectrometer TMPs. a) magnetic field map of the pre-spectrometer generated by the superconducting solenoids operated at maximum field strength ($B = 4.5\,\text{T}$). The figure is based on [85]. **b)** Using model 1 (see text) and the measured magnetic field the maximum rotor temperature can be estimated. Shown are the calculated equilibrium temperature values at the rotor of the TMP after at least $10\,\text{h}$ operating time in a homogeneous magnetic field applied in radial direction.
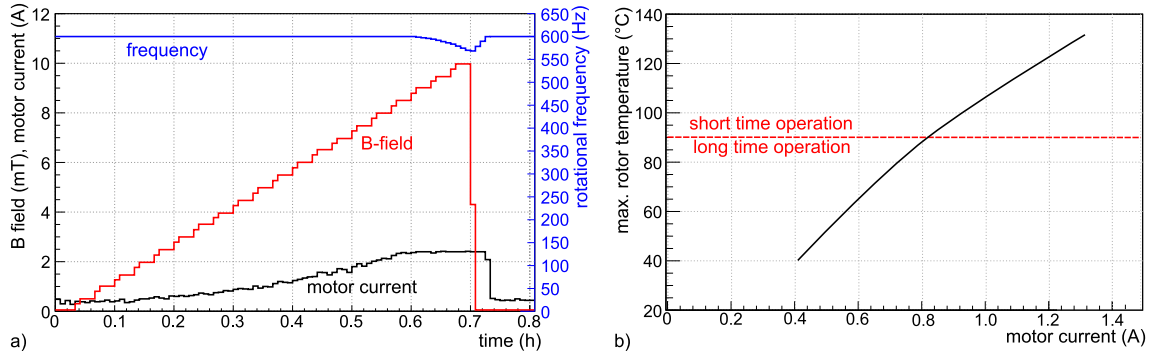
Figure 3.3: Magnetic field compatibility of the pre-spectrometer TMPs. a) Shown is an endurance test of the main pre-spectrometer TMP. Plotted are the influence of a magnetic field to the motor current and the rotational frequency of the TMP over time. **b)** Using model 2 (see text) and the measured motor current the maximum rotor temperature can be calculated. Shown are the calculated equilibrium temperature values at the rotor of the TMP after at least 10 h operating time in a homogeneous magnetic field applied in radial direction.

The theoretical models based on equation 3.1 have been fitted to the measured data. Stable long-term operation is guaranteed if the rotor temperatures of the TMP stays below a critical temperature of $T_{\mathrm{max}} = 90\,°\mathrm{C}$. Higher temperatures can reduce the lifetime of the pump. Model 1 uses a known magnetic field and model 2 is based on the monitoring of the motor current. The fit results in coefficients k_i that can be used to estimate the equilibrium temperature of the rotor during its operation. The results of the test measurements are: Model 1 predicts a maximal magnetic field of $B = 3.9\,\mathrm{mT}$ (see figure 3.2b) and model 2 leads to an upper motor current of $I_{\mathrm{motor}} = 0.82\,\mathrm{A}$ (see figure 3.3b). The prediction is based on a measured stator (housing) temperature of $T_{\mathrm{stator}} = 20\,°\mathrm{C}$ and a fore-vacuum pressure of $p = 1 \cdot 10^{-6}\,\mathrm{mbar}$.

With an active water cooling and fore-vacuum system the conditions at the pre-spectrometer thus allow a stable long-term operation of the *Leybold* MAC-W-1300.

3.1.2 Entrapment Pumps

When no vacuum leaks appear and when using a cascaded pumping scheme, the final equilibrium pressure in a vacuum chamber is dominated by hydrogen outgassing from the vessel walls. Momentum transfer pumps are less effective for light gases (like hydrogen) so that even with a vacuum bake-out cycle the final equilibrium pressure is reached already at $10^{-10}\,\mathrm{mbar}$. To improve the pressure down to the lower UHV region ($< 10^{-11}\,\mathrm{mbar}$), the KATRIN collaboration decided to use entrapment pumps in form of non-evaporable getter (NEG) material. Entrapment pumps in general capture residual gas molecules in a solid material or adsorb them on their surface. Thus, they are added to the vacuum scheme to reach an UHV level [84]. However, these passive pumps require periodic regeneration of their surfaces that trap the gas molecules. In the pre-spectrometer the non-evaporable getter (NEG) material St707 manufactured by *SAES getters* (Italy) is used. The porous alloy is a mixtures of zirconium (70%), vanadium (24.6%) and iron (5.4%). In form of a powder the getter material is firmly attached to a strip (an amagnetic constantan alloy composed of 55% copper and 45% nickel) by compression bonding, without using any type of chemical binder [90]. Its pumping principle is based on metallic

surface sorption of gas molecules. Entrapment pumps are an important tool for improving the performance of many vacuum systems.

The 1 m long getter strips are arranged in a circular geometry in a custom made cartridge that carries 100 strips (see figure 3.4). Both pump ports house NEG pumps with an effective pumping speed of about 25 000 ℓ/s for hydrogen. With no moving parts the NEG pumps adsorb mainly hydrogen by chemisorption and physisorption. For more details see section 6.1.
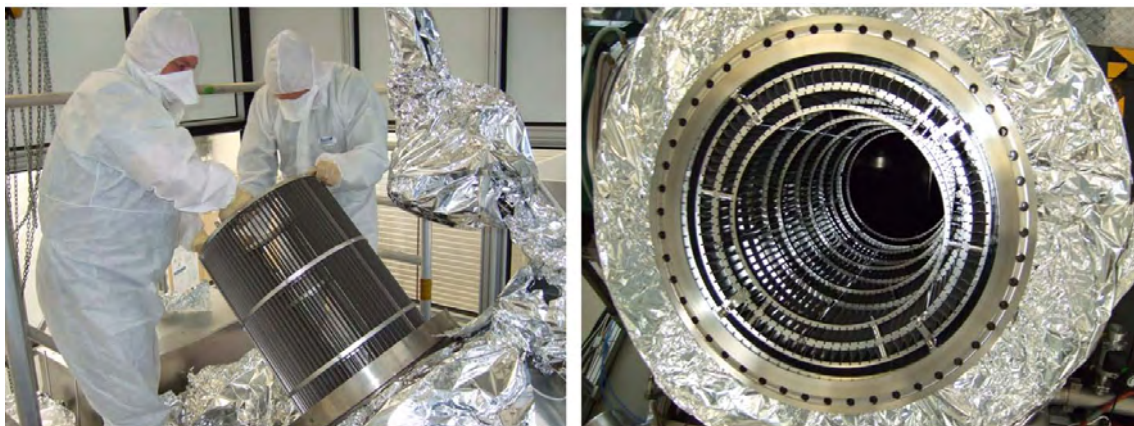
Figure 3.4: The non-evaporable getter pump at the pre-spectrometer. Left: installation into 45°-pump port. **Right:** The getter cartridge in place. The 100 strips are arranged in a circular shape [77].

The activation of the NEG pumps is achieved during the bake-out cycle of the spectrometer. The heat treatment desorbs the physisorbed gases (like hydrogen) and diffuses the passivation layer (oxides and carbides) that coveres the surface of the getter into the bulk material. The activation process is illustrated schematically in figure 6.2b). Heating tapes (`415-HEE-5-3900`[9] and `415-HEE-5-3910`) at both pump ports make it possible to heat the NEG pumps up to 350 °C, heating the thermo oil (Marlotherm LH) used at the pre-spectrometer near its upper limit of 360 °C (see section 3.4). The activation of the NEG pumps is accomplished via radiative heating over a period of about two days. The activation time increases strongly for lower temperatures (see figure 6.2a).

3.1.3 Vacuum Gauges and Residual Gas Analyzer

The vacuum monitoring system of the pre-spectrometer has to cover a wide pressure range: from atmospheric pressure down to an UHV regime ($< 1 \cdot 10^{-11}$ mbar). There are different techniques to measure the pressure, the technique typically depends on the pressure range. By combining different gauges it is possible to measure the pressure continuously. Hence, the pre-spectrometer vacuum system is equipped with several vacuum gauges listed in table 3.1).

A *Pfeiffer*[10] PPT100 vacuum gauge (based on a *Pirani* system) is mounted behind

---

[9]The name is based on the KATRIN numbering system [91] to identify all the equipment and components (e.g. sensors) by a unique label.

[10]Pfeiffer Vacuum GmbH, Berliner Strasse 43, 35614 Asslar, Germany

the scroll pump and monitors the fore-vacuum pressure. In between the TMP pumping stages the intermediate vacuum is monitored by an *MKS*[11] Series 999 Quattro. This wide range gauge combines a piezo sensor, a *Pirani* and a hot cathode ionization gauge.

The pressure in the pre-spectrometer recipient is monitored by an *MKS* Pirani 901P with a fore-vacuum gauge head combining a piezo and a *Pirani* sensor mounted at top of the 45° pump port. An *MKS* inverted magnetron (I-Mag, series 422) a cold cathode gauge uses the inverted magnetron technique and therefore is sensitive from $\gtrsim 10^{-3}$ mbar to a limit of about 10^{-11} mbar. The monitoring system is completed by a *Leybold* Extractor gauge, a hot cathode gauge (an IE 514 sensor with an Ionovac IM 540 controller) can measure a pressure down to $1 \cdot 10^{-12}$ mbar.

Table 3.1: The pre-spectrometer vacuum gauges are listed with their manufacturer and type as well with its KATRIN number and pressure range (in mbar). The different gauges are combined to enable the operator to measure the pressure in the spectrometer continuously.

gauge (manufacturer and type)	KATRIN number	range (mbar)
MKS IM422	412-RPP-3-1232	$1.33 \cdot 10^{-2} \ldots 1.33 \cdot 10^{-11}$
Leybold Extractor (IE514)	412-RPI-3-1221	$1 \cdot 10^{-6} \ldots 1 \cdot 10^{-12}$
MKS Pirani 901	412-RPH-3-1231	$1000 \ldots 1 \cdot 10^{-5}$
MKS 999 Quattro	412-RPI-3-1211	$1000 \ldots 1 \cdot 10^{-10}$
Pfeiffer PPT100	412-RPI-3-1212	$1000 \ldots 1 \cdot 10^{-4}$

To determine the composition of the residual gases in the pre-spectrometer, a quadrupole residual gas analyzer (*MKS* LM92 Microvision IP 412-RPQ-3-1252) is used. The mass spectrometer was designed for process control and contamination monitoring in vacuum systems. In addition with the *MKS* Process Eye software platform this systems allows to monitor gas composition trends.

3.1.4 Beamline Flapper Valve

To separate the pre-spectrometer from the main spectrometer, a custom-built beamline valve was manufactured. The valve is placed inside the warm bore of the second pre-spectrometer solenoid (PS2). The particularly cramped conditions there require a special valve which technically is referred to as a 'flapper' valve. A rotary feedthrough, coming from above, pushes a stem with a flapper disk towards the main spectrometer region against the valve body. The gate is sealed by a Kalrez® O-ring in a groove. The valve is operated with a manual actuator. A special gear box increases the force of the operator. A technical drawing for the cross-section and an elevation is presented in figure 3.5.

A similar beamline valve placed in the pinch magnet is used to separate the detector system from the main spectrometer. Both in-beamline valves are contributions of the University of Washington, Seattle. The beamline valves can be baked-out at temperatures up to 180 °C by custom-built heating cushions.

---

[11]MKS Instruments, 2 Tech Drive, Suite 201, Andover, MA 01810, USA
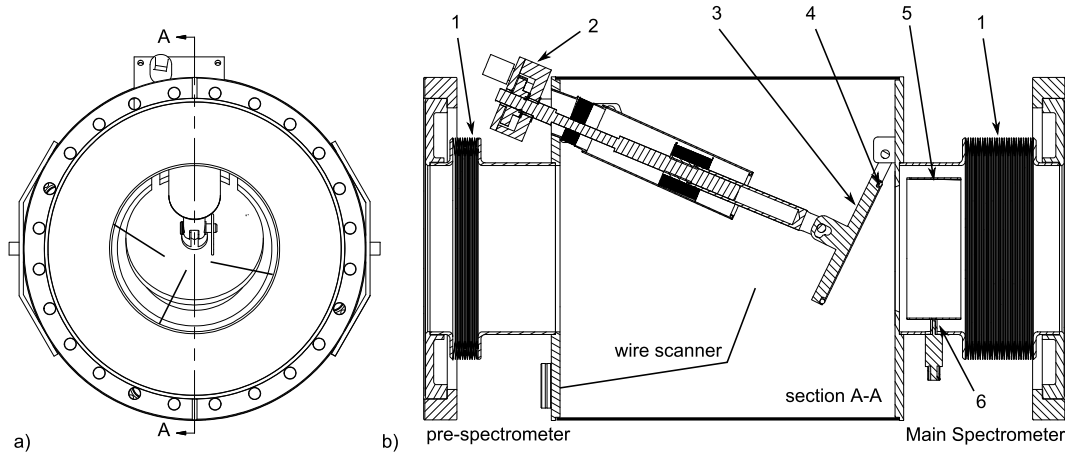
Figure 3.5: The pre-spectrometer beamline flapper valve. a) Shown is a technical drawing of the cross-section, the lines in the center illustrate three wire scanners installed to empty an electron trap inside the beamline valve. **b)** Elevation view: 1. bellows, 2. gear box, 3. flapper valve, 4. Kalrez® O-ring, 5. ion blocking ring*a*, 6. power connector of ion blocking ring. One of the three wire scanners is indicated in the picture.

---

*a*The ion blocking ring can be used to generate a dipole field to retain ions emitted from the source.

The unavoidable Penning-like trap for electrons due to the combination of the electric and magnetic fields between the pre-spectrometer and the main spectrometer is a non-negligible source of background. By sweeping a conducting wire periodically through the particle trap the stored charged particles can be removed, so that an ongoing discharge in the trap can be stopped, and the count rate measured with a detector looking at the trap is reduced [92]. The measurement of the tritium beta spectrum will take place while the sweeping wire is outside the flux tube. The principle of the wire scanner used in the beamline valve was tested at the pre-spectrometer test setup [83]. Three wire scanners are mounted in the pre-spectrometer beamline valve, see figure 3.5. The wire scanner is a contribution of the University of Münster, Germany.

3.2 Inner Electrode and High Voltage System

Both KATRIN spectrometers are based on a novel high voltage design. The retarding potential is directly connected to the vessel while an electrically separated different voltage can be applied to the inner electrode system. The advantages of this concept are:

- fine-tuning of the electrostatic field by the inner electrode to avoid Penning traps,

- decoupling of the retarding potential from noise induced to gauges, TMPs and other equipment as well as other electromagnetic interference,

- shielding of background electrons created in the vessel walls by cosmic rays or nuclear decays (monopole mode),

- active background reduction methods like the dipole mode or ECR [63].

The inner electrode system of the pre-spectrometer consists of three sets of electrodes. A quasi massless wire electrode forms the central element of the setup. About 240 wires (diameter $d = 0.5\,\text{mm}$) were tensioned and tightened evenly spaced (about $s = 2\,\text{cm}$ apart) in a frame. A vertical gap of about $5\,\text{cm}$ supported by ceramic bolts separates the wire electrode into two single half shells. The wire-electrode is a contribution of the University of Washington, Seattle. Together with two solid cone electrodes the wire electrode is mounted on a lightweight designed holding structure. This carrier is placed on ceramic ball-bearings offering a secure and simple installation of the inner electrode system (see figure 3.6). The whole system is electrically insulated with ceramic bolts against the vessel and all parts against each other (see figure 3.7). Hence, the inner electrode system can be powered with individual voltages.
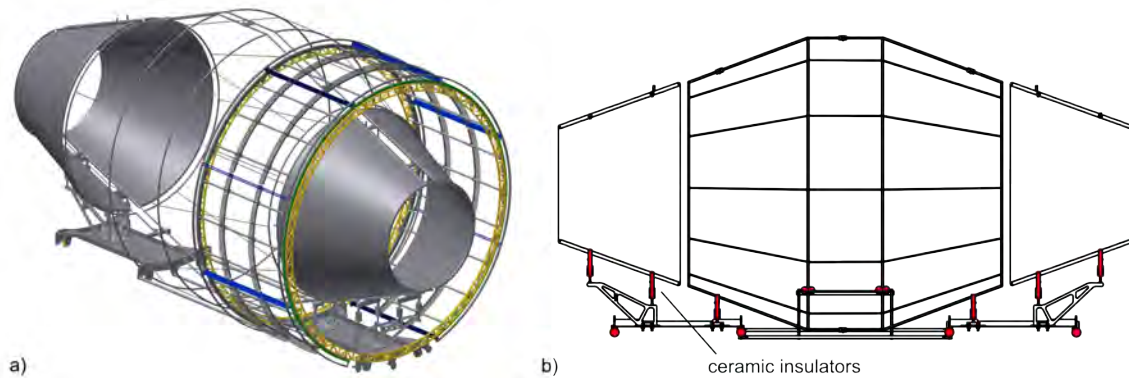
Figure 3.6: The pre-spectrometer inner electrode system. a) The technical drawing shows the inner electrode system of the pre-spectrometer: both full cones, the wire electrode and one of the possible NEG holding structures. The cylindrical holding structure for additional getter can be mounted around a full cone of the electrode system. It can hold up to $500\,\text{m}$ of getter strips. A second holding structure, mirrored at the analyzing plane, can be install, too. Adding the total amount of getter-strips to $200\,\text{m} + 2 \cdot 500\,\text{m} = 1\,200\,\text{m}$. At the moment there is no additional getter material installed, since the tritium reduction by the CPS is expected to be better than the design value [66]. **b)** Technical drawing of the cross section of the pre-spectrometer inner electrode system. The ceramic insulators are highlighted.

To apply a stable high voltage (HV) to the pre-spectrometer and its electrodes two high voltage power supplies are used (see figure 3.8). A *FuG*[12] HCN 140-35000 (the former FUG4)[13] provides a maximum voltage of $-35\,\text{kV}$ and is used to supply the pre-spectrometer vessel. An offset power supply (*ETPS*[14] NHQ 226L) is mounted in the HV rack which is connected to the tank potential and provides a voltage between $\pm 1.5\,\text{kV}$ (as an offset to the tank potential) with a precision of $0.1\,\text{V}$. This allows to adjust the voltage difference between the inner electrodes and the vessel. The voltages are available at the distribution panel inside the HV cabinet and can be distributed via pin plugs to the individual electrodes. Special potential configurations for the inner electrodes can be created (e.g. for HV dedicated measurements).

---

[12]FuG Elektronik GmbH, Am Eschengrund 11, 83135 Schechen, Germany

[13]stability: $10\,\text{ppm}/8\,\text{h}$, $350\,\text{mVpp}$ (pp = 'peak-to-peak')

[14]ETPS Ltd., Unit 14, The Bridge, Beresford Way, Chesterfield, S41 9FG, UK
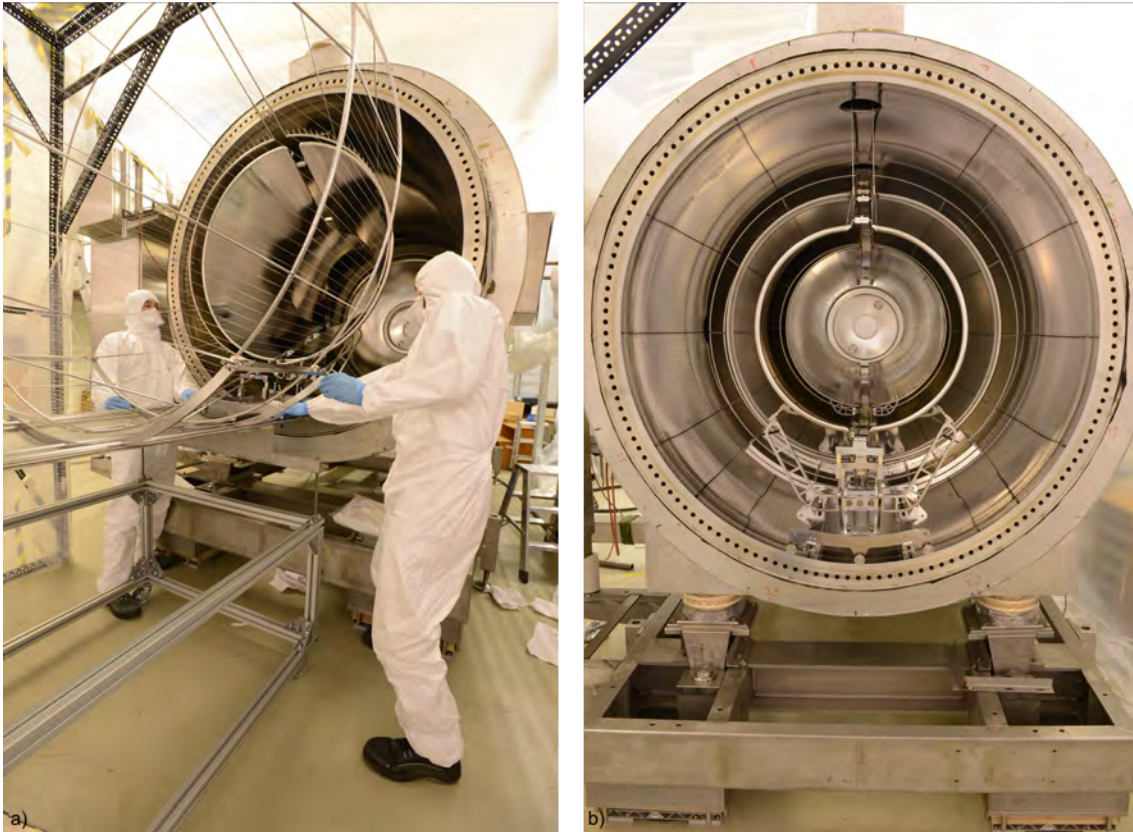
Figure 3.7: The mounting of the pre-spectrometer inner electrode system. a) Shown is the author during the installation of the fully assembled inner electrode system. As a new feature the system is placed on ceramic ball-bearings offering a secure and simple installation. **b)** Last picture before closing the DN1680 port: the inner electrode system is seen as superposed concentric circles.
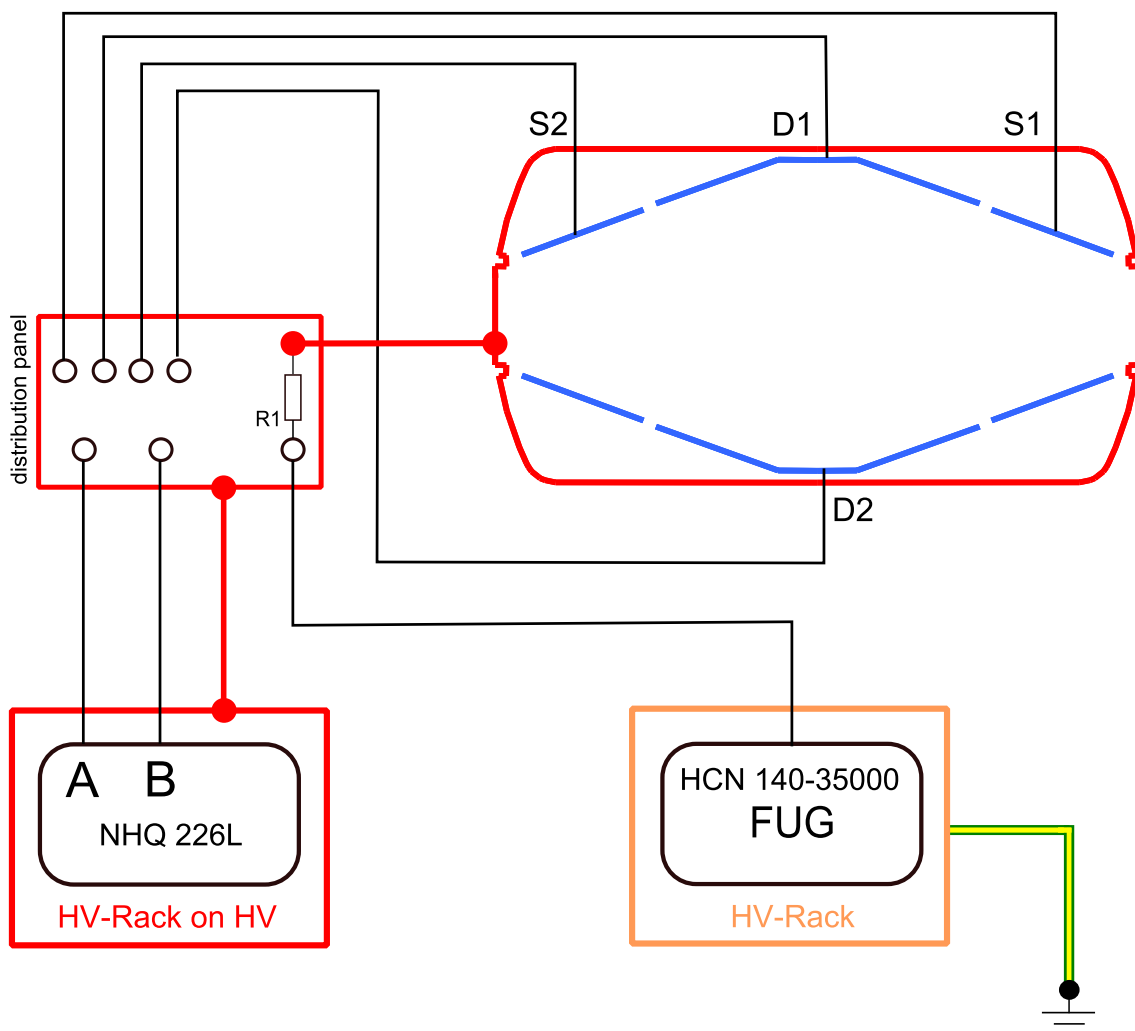
Figure 3.8: A schematic overview of the pre-spectrometer high voltage system. The pre-spectrometer vessel and the HV rack are provided with voltages by a *FuG* HCN 140-35000. Inside the HV rack a PSU[a] (*ETPS* NHQ 226L) offers an offset voltage up to $\pm 1.5\,\mathrm{kV}$. A distribution panel inside the cabinet allows via pins and plugs the distribution of the voltages to the individual electrodes. This enables the operator to fine tune the retarding potential. The figure is based on [78].

---

[a]power supply unit

The DN500 flanges on both sides of the spectrometer are equipped with conical ceramic insulators and hold the ground electrode as well as a so called anti-Penning electrode (see figure 3.9a). There the ground electrode is connected to ground potential while the anti-Penning electrode is put on tank potential [78]. To eliminate Penning traps the ground electrode is shaped to follow the magnetic field lines (see detail figure 3.9b). The ground electrode was turned on a metal lathe out of one block ultra-pure aluminum. The same approach for the ground- and anti-Penning electrode was later adapted at the main spectrometer, too.
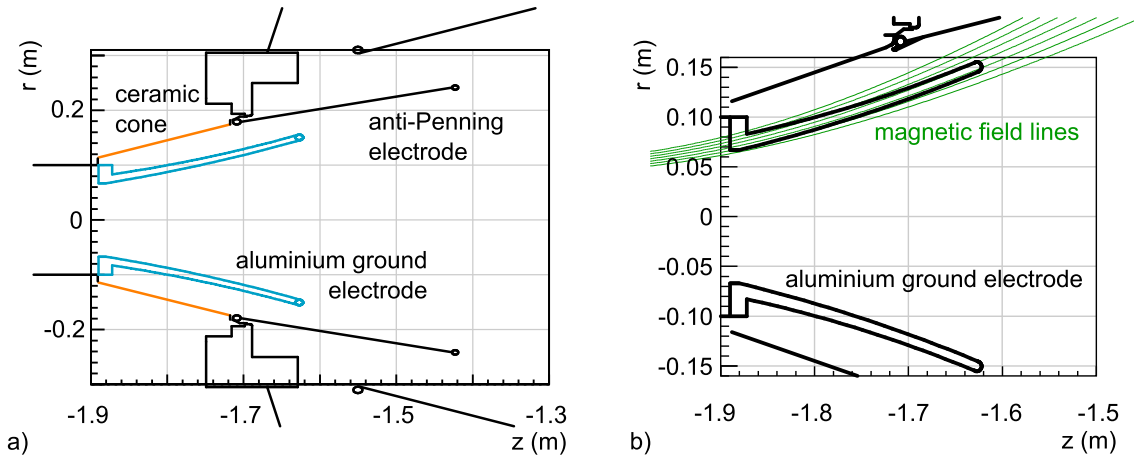
Figure 3.9: Schematic cut view of the pre-spectrometer conical ceramic insulator. a) The ultra-pure aluminium ground electrode and the anti-Penning electrode of the pre-spectrometer shown inside the ceramic cone. **b)** Detail view of the aluminum ground electrode that follows smoothly the magnetic field lines, hence avoiding any storage conditions. The figure is based on [78].

As a new feature the upgraded inner electrode holding structure is now capable of carrying up to two additional NEG pumps. The design of the getter cartridges are derived from the main spectrometer NEG pumps (see chapter 6). The getter can be mounted around the two full cones of the electrode system (see figure 3.6a). Each of the getter holding structures can carry about 500 m NEG strips. Hence, the total amount of getter in the pre-spectrometer can add up to 1 200 m. However, at pressent there is no additional getter installed, since the tritium reduction by the CPS is expected to be better than the design value [66]. The installation of an additional getter pump in the pre-spectrometer is a trade-off between reduced background from tritium and increased radon-induced background due to additional NEG strips. For more details about radon-induced background see chapter 7 and the publication [79].

3.3 Magnet System of the Pre-spectrometer

The magnetic field to guide electrons through the pre-spectrometer is created by two *Cryogen Ltd.*[15] superconducting solenoids with a free warm bore of 40 cm in diameter. Each magnet can generate a maximum magnetic field of 4.5 T measured

---

[15]Cryogenic Limited, Unit 30, Acton Park Industrial Estate, The Vale, London W3 7QE, UK

at the center of the coil at a magnet current of 157 A (the current is provided by two *FuG NTS 800-5* power supplies, the mandated ramping speed is shown in table 3.2). On each side of the pre-spectrometer a magnet is mounted with a distance of 2.15 m between the center of the magnet coil and the center of the analyzing plane ($z = 0$ m), resulting in a minimal field of $B_{\mathrm{ana}} = 0.016$ mT. In order to cool the magnets to superconducting temperatures a cryogen-free cooling system is used [93] with the advantage that no cryo-infrastructure is required. RhFe temperature sensors are placed on the relevant parts inside the cryostat to monitor the temperature of the coil. A helium cold head (*Sumitomo*[16] cryocooler) connected to a water-cooled compressor cools the superconducting coil down to < 4.2 K. Both compressor units as well as the magnet slow control system and the PSUs are placed in the basement under the pre-spectrometer stage. The coil is insulted by a two-staged thermal shield and an insulating vacuum of about 10^{-4} mbar. The basic parameters and components of the magnet system are summarized in table 3.3.

Table 3.2: The nominal ramping speed [94] of pre-spectrometer magnets [93]. The ramping speed regulates the amount of energy transfered into the coil: $E_{\mathrm{mag}} = \frac{1}{2}LI^2$. If the energy input per unit time is too high the superconducting magnet may quench.

current (A)	ramping speed (mA/s)
$0\dots120$	50
$120\dots130$	40
$130\dots140$	30
$140\dots150$	20
$150\dots157$	10

Table 3.3: Overview of the major components and important specifications of the pre-spectrometer magnets, as specified in [94].

name	PS1	PS2
location	CPS	main spectrometer
cryocooler (*Sumitomo*)	SRDK-415D s/n 3LD03 021C	SRDK-415D s/n 3LD03 030C
compressor (*Sumitomo*)	CSW-71D s/n 47D 03142D	CSW-71D s/n 47D 02A60D
power supply (*FUG*)	NTS 800-5	NTS 800-5
turns	13 707	13 617
inductance (H)	77.4	76.3
central field constant	289.559 G/A	287.74 G/A
operating current (4.5 T)	155.41 A	156.39 A

---

[16]Sumitomo Heavy Industries, Ltd. ThinkPark Tower, 1-1 Osaki 2-chome, Shinagawa-ku, Tokyo 141-6025, Japan

The system is operated in the driven mode, hence the power supplies continuously control the current input. The persistent mode, on the other hand, where the superconducting coils are short-circuited after a superconducting loop is created, is in theory more stable. In case of the pre-spectrometer magnets the stability of the magnetic field is most important making it necessary to readjust the current [77] [93]. The stability of the power supplies was investigated in detail in [95]. The measured stability of the power supplies is $< 5 \cdot 10^{-5}$ A of the current set value, and limited by the measurement equipment, favoring the driven mode.

The maintenance cycle of the system is limited to exchange of the cold heads once a year and a filter change in the compressors every two years. The warm up and cool down time of the system results in a downtime of about two weeks. The power supplies are tested annually as portable equipment according to BGV A3 (VDE 701 and 702).

The alignment orientation measurements were carried out by Dr.-Ing. Juretzko (Geodetic Institute, KIT). The measurements have revealed a deviation of about ± 1 mm in comparison to the overall KATRIN magnet installation plan.

3.3.1 Shifting the Pre-spectrometer

For maintenance purposes, such as mounting an additional NEG pump (see figure 3.6) the pre-spectrometer can be shifted out of the beam line, see figure 3.10 and 3.11. To move the spectrometer it is placed on four air cushions (newly acquired in 2013, manufactured by *DELU GmbH*[17], Germany) and guided by a double-T-beam which is anchored firmly into the floor. During the standard operation mode the first solenoid (PS1) is mounted on the pre-spectrometer holding structure while the second pre-spectrometer magnet (PS2) is placed on its own holding structure and can be operated in a standalone mode.

This feature comes in useful in particular during the main spectrometer commissioning measurements. Here, a specially designed electron source is placed between both pre-spectrometer magnets for the commissioning measurements, to determine the transmission function of the main spectrometer. The electron source is a contribution of the University of Münster, Germany.

3.4 Heating and Cooling System

In order to achieve the required pressure of $< 10^{-11}$ mbar, a bake-out procedure of the pre-spectrometer is required to artificial accelerate the outgassing processes (for more details see chapter 5). The pre-spectrometer (as well as the main spectrometer) makes use of a combination of a thermo oil circuit and heating tapes wrapped around the recipient. A thermo-oil heating unit (*Lauda*[18] KH 350L) can vary and maintain the temperature of the pre-spectrometer between -20 and about $+220\,°C$. This unit provides the basic heat output. Additional heating tapes provide extra power to activate for instance the NEG pumps ($T_{\mathrm{NEG}} > +350\,°C$). The temperature of the spectrometer is controlled and monitored by several PT100 temperature

---

[17]DELU GmbH, Gebertstraße 7, 90411 Nürnberg, Germany.
[18]Lauda Dr. R. Wobser GmbH & Co. Kg, Pfarrstraße 41/43, 97922 Lauda-Königshofen, Germany

a)

b)
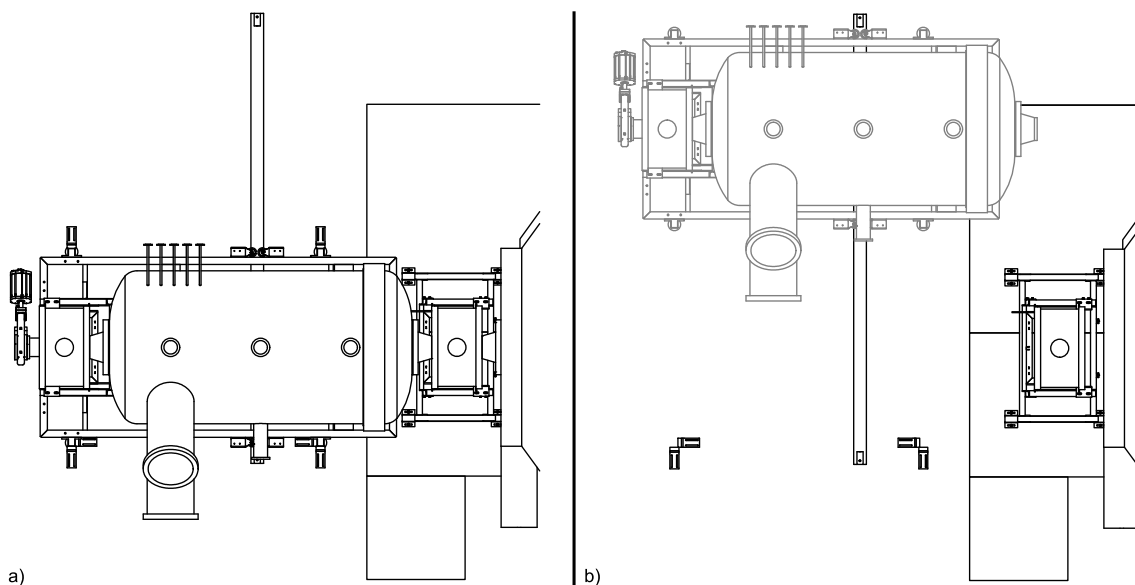
Figure 3.10: Shifting the pre-spectrometer. a) Top view of the pre-spectrometer connected to the main spectrometer before and **b)** after shifting the pre-spectrometer. The second magnet (PS2) placed near the main spectrometer can be operated in standalone mode.

Figure 3.11: Panoramic photo of pre-spectrometer setup. Photo of the shifted pre-spectrometer. For measurements with the *Münster electron source[a]* the flux tube must be contracted. Hence, in this special case both magnets are operated in standalone mode.

---

[a]In this photo the electron source is not yet installed.

sensors attached to the vessel. The whole recipient is covered in a 30 cm thick glass wool insulation enclosed with a layer of stainless steel plates.

The feature of actively cooling the pre-spectrometer can be used to reduce the outgassing rate of the stainless steel walls further and thus to reduce and also maintain the final pressure inside the pre-spectrometer.

3.4.1 Thermo Oil System

The temperature of the pre-spectrometer during bake-out procedure is controlled by a *Lauda* (KH 350L) `415-HCL-5-3401` system via circulation of thermal oil in tubes welded onto the vessel. *Marlotherm LH* (Dibenzyltoluol) is used as a heat transfer fluid. The thermal oil is stable over a temperature region between -70 and $+360\,°$C. The *Lauda* cryo-heater provides a power output of 28 kW. During the test measurements [77] the temperature of the pre-spectrometer was varied between -20 and $+220\,°$C. During the reconstruction phase additional heating tapes and an enhanced insulation were installed. These measures will increase the temperature range. A schematic drawing of the pre-spectrometer thermo oil circuit can be found in figure A.7 in appendix A.

3.4.2 Heating Tapes and Temperature Sensors

All parts of the pre-spectrometer that are not covered by the thermal oil circuit (like the valves, the measurement cross or the beamtube inside the magnets) can be baked-out by additional heating tapes or custom-designed heating pads. The electrical heating devices are controlled and monitored by PT100 temperature sensors which are screwed onto threaded rods that were spot welded onto the pre-spectrometer vessel. These measures ensure a sufficient heat transfer. Each heating tape (KATRIN number code: `415-HEE-5-xxx0`) is assigned to four temperature sensors: one sensor for regulation and one for the overheat protection, complemented by two spare sensors. The regulation sensor (`415-RTP-5-xxx1`) and the overheat sensor (`415-RTP-5-xxx2`) are placed between the heating tapes and the vessel to increase the sensibility for temperature variations. These sensors are hardwired to the KATRIN automation system (PCS7) and control the heating tapes. The spare sensors (`415-RTP-5-xxx3` and `415-RTP-5-xxx4`) are placed near the corresponding heating tape (`415-HEE-5-xxx0`) and are read-out by a slow control system (e.g. to create a 3D temperature map of the pre-spectrometer). The redundant design of the temperature sensor system prevents damages at the vacuum components due to overheating.

A map of all temperature sensors and heating tapes[19] is shown in section A.1 of appendix A.

---

[19]The heating tapes `415-HEE-5-4020`, `415-HEE-5-4030`, `415-HEE-5-4040` and the corresponding temperature sensors were installed at the pre-spectrometer but are not integrated in the PCS7 system. The three 10 m long heating tapes act as a reserve or boost system (each providing 2 kW heating power) that can be put into service if needed (e.g. to bake-out the whole system up to 350 °C).

3.4.3 Thermal Insulation

The main body of the pre-spectrometer is covered in several levels of insulation materials:

1. mineral wool in between the thermo oil piping that are welded onto the vessel,

2. a layer of stainless steel foil (reflecting the heat radiating of the thermo oil circuit back onto the vessel),

3. a 5 cm strong layer of mineral wool and a layer of aluminum foil,

4. a 20 cm strong layer of glass wool,

5. and a stainless steel casing.

All insulation works at the pre-spectrometer were carried out by *Kanstinger GmbH*, Germany.

3.4.4 Pre-Spectrometer Bake-Out Procedure

To reach a final equilibrium pressure in the UHV region a vacuum bake-out procedure of the recipient is necessary. Technically unavoidable contaminants during the assembly (like water due the humidity of air) are removed by heating the vessel up to $350\,°C$ under vacuum. During a bake-out procedure a rise in temperature accelerates the desorption of molecules adsorbed to the inner surface of the vacuum chamber so that they are removed by the vacuum pumps. The pre-spectrometer bake-out procedure includes a baking of the whole system at $200\,°C$ with a ramping speed of about $10\,°C/h$. The hydrogen outgassing rate of the pre-spectrometer was determined with the pressure rise method to about $1.2 \cdot 10^{-12}\,\mathrm{mbar}\,\ell/\mathrm{s}\,\mathrm{cm}^2$ [69]. To prevent damages of the vessel a control and monitoring system is required. If the activation of the NEG pumps is intended, both pump ports must be heated additionally with the installed heating tapes up to $350\,°C$. After the bake-out procedure and the activation of the NEG pumps the pre-spectrometer can reach a final equilibrium pressure of the order of $10^{-11}\,\mathrm{mbar}$ at room temperature [69].

4 KATRIN Main Spectrometer

The key task of the main spectrometer is to analyze the energies of β-decay electrons emitted from the KATRIN tritium source (WGTS) in an integral mode. This chapter focuses on the experimental setup of the main spectrometer and its major components. As a huge high-pass filter the spectrometer provides unsurpassed high-precision energy analysis for the tritium β-decay electrons. Two superconducting solenoids create an inhomogeneous magnetic field while an electrostatic retarding potential of $U_0 = 18.6\,\text{kV}$ is directly applied to the vessel, resulting in an energy resolution of $\Delta E = 0.93\,\text{eV}$. For a detailed description of the filter principle see section 2.2. The β-decay electrons are emitted isotropically from the tritium source and are guided in a cyclotron motion by the magnetic field lines. While the flux tube expands to a diameter of about 9 m in the analyzing plane, the magnetic field gradient transforms cyclotron motion of electrons into longitudinal motion due to the conservation of the magnetic momentum. This ensures an accurate measurement of the total kinetic energy of the signal electrons. Only electrons that pass the electrostatic barrier are re-accelerated and collimated at the detector [33].

The main spectrometer ultra high vacuum (UHV) recipient is one of the centerpieces of KATRIN and is, to our knowledge, the largest UHV recipient in the world, outperforming gravitational wave antennas or the LHC ring UHV volumes. The vessel with a diameter of about 10 m and length of about 23 m was manufactured by DWE[1], Germany. The vacuum scheme contains six turbomolecular pumps (TMPs) and three non-evaporable getter (NEG) pumps (each holding about 1 000m $SAES$ St707 Getter strips). In order to achieve a background rate of < 0.01 cps inside the vessel a complex set of a double layered inner wire electrode system was installed. This 'mass-less' wire electrode forms an electrostatic shield to block electrons emitting from the vessel walls induced by cosmic rays and allows to fine tune the retarding potential. In addition to the superconducting solenoids a set of 16 air coils are used to fine tune the magnetic field and to compensate the effects of the Earth's magnetic field.

The vessel can be baked-out at temperatures of up to 350 °C. A rise in temperature accelerates the desorption of adsorbed molecules and thereby improves the vacuum conditions. The temperature of the main spectrometer is controlled by heating tapes and a large-scale oil heating system, manufactured by HTT[2], Germany. The process is monitored by a closed-meshed net of PT100 temperature sensors spread over the vessel.

---

[1]MAN DWE GmbH, Werftstraße 17, 94469 Deggendorf, Germany
[2]HTT energy GmbH, Füllenbruchstrasse 183, 32051 Herford, Germany

4.1 Main Spectrometer Vessel and the Vacuum System

An UHV recipient comparable in size to the main spectrometer has not been manufactured before. For the stainless steel vessel the alloy type DIN1.4429 (316LN) was selected for its strength, non-magnetic properties and low radioactivity[3]. The inner diameter of the cylindrical section is 9.8 m, the total length of the vessel is 23.28 m and the thickness of the walls varies between 25 mm and 32 mm. The recipient has a total volume of about 1 240 m^3 with an inner surface of 650 m^2 and a weight of approximately 200 t. Three pump ports with a diameter of 1.7 m and a length of about 3 m are welded to the down-stream side of the spectrometer.

To obtain a high sensitivity of 200 meV/c^2 on the neutrino mass, a very low background rate of about 0.01 cps is required. Among other parameters this rate crucially depends on the pressure inside the main spectrometer. For these reasons it is designed to reach and maintain UHV conditions of 10^{-11} mbar or below during the entire lifetime of the KATRIN experiment. First prototype measurements with the pre-spectrometer (see chapter 3) and a smaller test recipient (see chapter 5) have been conducted, providing important input data on outgassing of the stainless steel (316LN) walls in the range of about $1 \cdot 10^{-12}$ mbar ℓ/s cm^2. There, the pumping concept of the system was tested successfully also [69]. Hence, the pumping scheme of the main spectrometer foresees a combination of entrapment, momentum transfer and positive displacement pumps. Each of the three pump ports contains about 1 000 m of *SAES* St707 NEG strips resulting in a combined pumping speed for hydrogen of 10^6 ℓ/s. The 1 m long NEG strips are mounted in a custom-made stainless steel holding structure with a diameter of 1.7 m and a length of 2 m (see figure 4.1c). The pumping concept of the NEG material as well as a closer look on the design of the NEG pumps is given in section 6.1.

After investigating the properties of radon-induced background in the pre-spectrometer test set-up, the use of a liquid nitrogen (LN2) cooled baffle was proposed and successfully tested [82]. As the NEG material and the bulk material of the vessel contain traces of primordial α-decay chains, they produce radon atoms (^{219}Rn and ^{220}Rn) as part of the decay chains. As a neutral noble gas radon atoms leave the source material and emanate in the main spectrometer. There, the subsequent radon α-decay generates high-energy electrons. Due to residual gas ionization, the radon emanation forms a non-negligible background [78]. On the one hand, the LN2-cooled baffle prevents the emanation of radon isotopes from the NEG pumps into the main spectrometer vessel, by blocking the direct line of sight between NEG pump and recipient (see figure 4.1b). On the other hand radon emanating from the vessel walls is also trapped to the cold surface of the baffle. The concept and development processes of the LN2 cooled baffle is presented in detail in chapter 7.

 The outer two pump ports (pump port II and III) in addition hold a cascaded TMP pumping scheme, similar to the vacuum system of the pre-spectrometer. After the initial pump down with a *Leybold* SP 630 dry screw pump (with a pumping speed for nitrogen of about 630 m^3/h) to a fore-vacuum level of about 10^{-2} mbar, six *Leybold* MAG-W-2800 turbo-molecular pumps (TMP) take over (with a combined pumping

---

[3]Radioactive decays inside the spectrometer are one possible background source, see section 2.4.2.
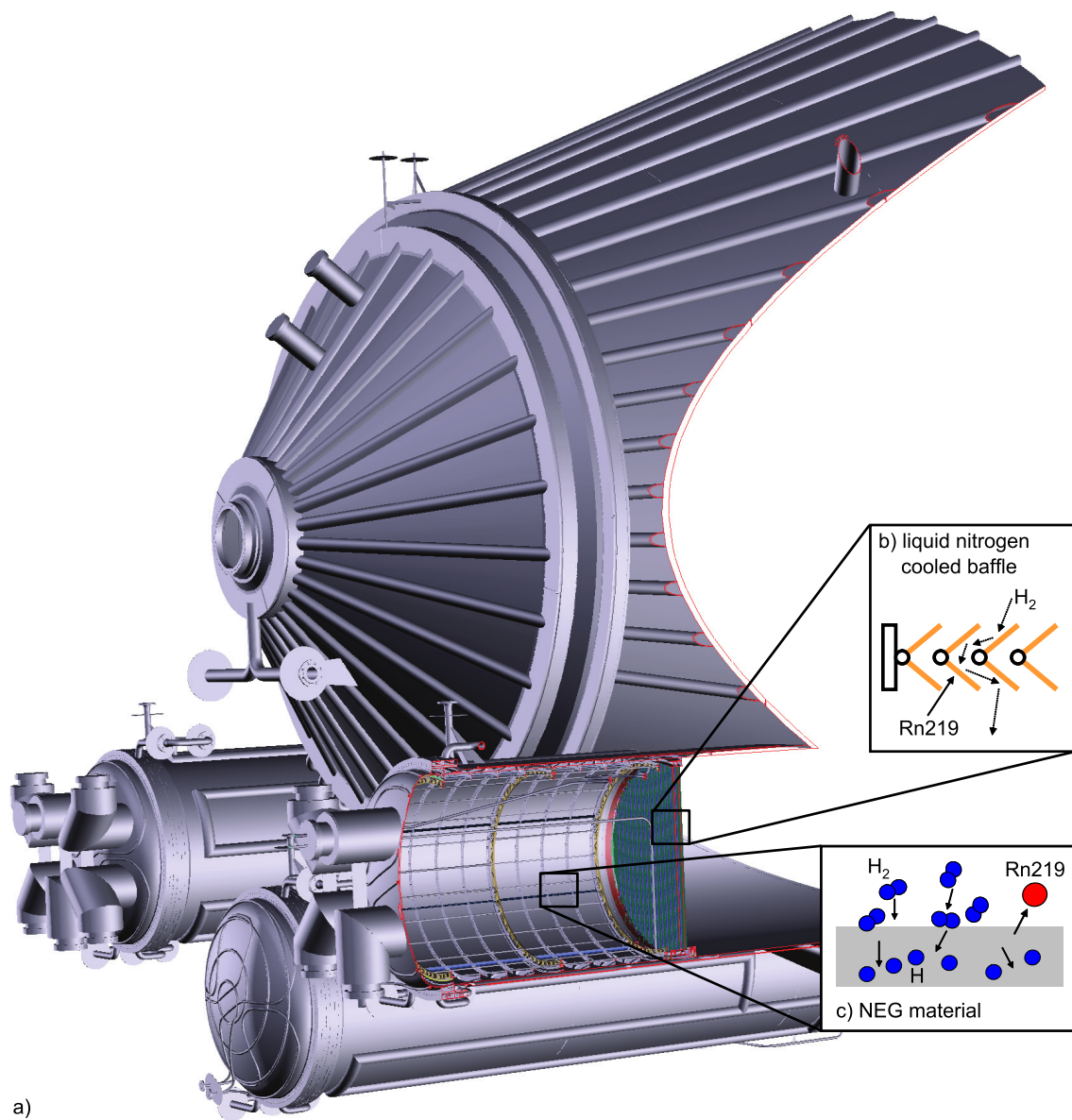
Figure 4.1: The non-evaporable getter (NEG) pump and the LN2 cooled baffle system of the main spectrometer. a) Technical drawing of the main spectrometer. **b)** The LN2 cooled baffle blocks the direct line of sight between the NEG pump and the recipient. Radon emanating from the getter material freezes to the cold surfaces of the baffle. **c)** The NEG material adsorbs residual gas molecules (mainly hydrogen) from the evacuated recipient. Therefore it is capable of maintaining a UHV regime. However, the getter material contains traces of uranium. Through a natural decay chain a small amount of radon is produced. The noble gas emanates from the material and enters the spectrometer. Electrons generated by the radon α-decay are one possible source for background (see chapter 7).

speed for hydrogen of about $S_{6xTMPs}(H_2) = 10^4 \, \ell/s$), thereby reducing the pressure to a level of approximately 10^{-8} mbar. To backup the main pumps a second stage TMP (*Pfeiffer* Hi Pace 300P) is used followed by a scroll pump (*Leybold* SC30 D) at the outer pump ports generate an intermediate vacuum. The cascaded TMP setup provides a high enough compression ratio for hydrogen to reach the required pressure regime. This setup was successfully tested at the pre-spectrometer test setup. Eddy currents induced by the magnetic guiding field can cause heating of the fast moving rotors of the TMPs. In the long-term operation the heating of the rotor may eventually lead to the destruction of the pump. The magnetic compatibility of the KATRIN TMPs was successfully tested in [85] at the Helmholtz coil setup (compare with subsection 3.1.1).

For monitoring purposes the vacuum system of the spectrometer is equipped with several vacuum gauges. Two extractor UHV gauges form the center of the vacuum readout system with one gauge at pump port III and the other one on top of the vessel (at port 0090) (see figure 4.2). An inverse magnetron gauge is installed at pump port II to monitor the transition from UHV to the intermediate vacuum region at a pressure above 10^{-5} mbar. This feature is required during the pump-down or the venting of the system. In between the cascaded pumping scheme two gauges monitor the intermediate vacuum: an *MKS 999* (multi range gauge) and an *MKS Pirani 901* for the fore-vacuum pressure. All gauges with their respective KATRIN number [91] and location are presented in table 4.1.

Both extractor gauges have been factory-calibrated ($\pm 10\%$) with nitrogen. If not mentioned otherwise, pressures values are given as measured with the nitrogen calibration factor. The gas correction factor ($K_{gas=H_2} = 0.46$) for hydrogen is used only when explicitly mentioned in the text. The inverted magnetron gauge was last calibrated in 2006, and served mainly as a crosscheck (e.g. during the bake-out cycle). To determine the residual gas composition a residual gas analyzer (RGA) by *MKS* (type: Microvision II, 435-RPQ-3-3310) is mounted at pump port III. The RGA ionizes the residual gas atoms and separates the ions according to their mass-to-charge ratio. Magnetic fields can disturb the operating principle of the device. Due to the proximity of the RGA to the detector solenoids, it is magnetically shielded with a sheet of mu-metal. For the RGA the factory calibration factors are used. However, these values should rather be seen as relative gas compositions, which have to be adjusted using the absolute pressure measured with an extractor gauge.

Table 4.1: The main spectrometer vacuum gauges. All gauges operate in different pressure ranges. Hence, different gauges are combined to measure the pressure in the spectrometer continuously. The main gauges are shown in figure 4.2, too.

gauge (manufacturer and type)	KATRIN number	location
MKS inv. Magnetron (IM422)	435-RPP-3-2320	pump port II
Leybold Extractor (IE514)	435-RPI-3-3110	pump port III
Leybold Extractor (IE514)	435-RPI-3-0096	downstream flat cone
MKS 999 Quattro	435-RPI-3-x045	intermediate vacuum
MKS Pirani 901	435-RPH-3-x080	fore-vacuum
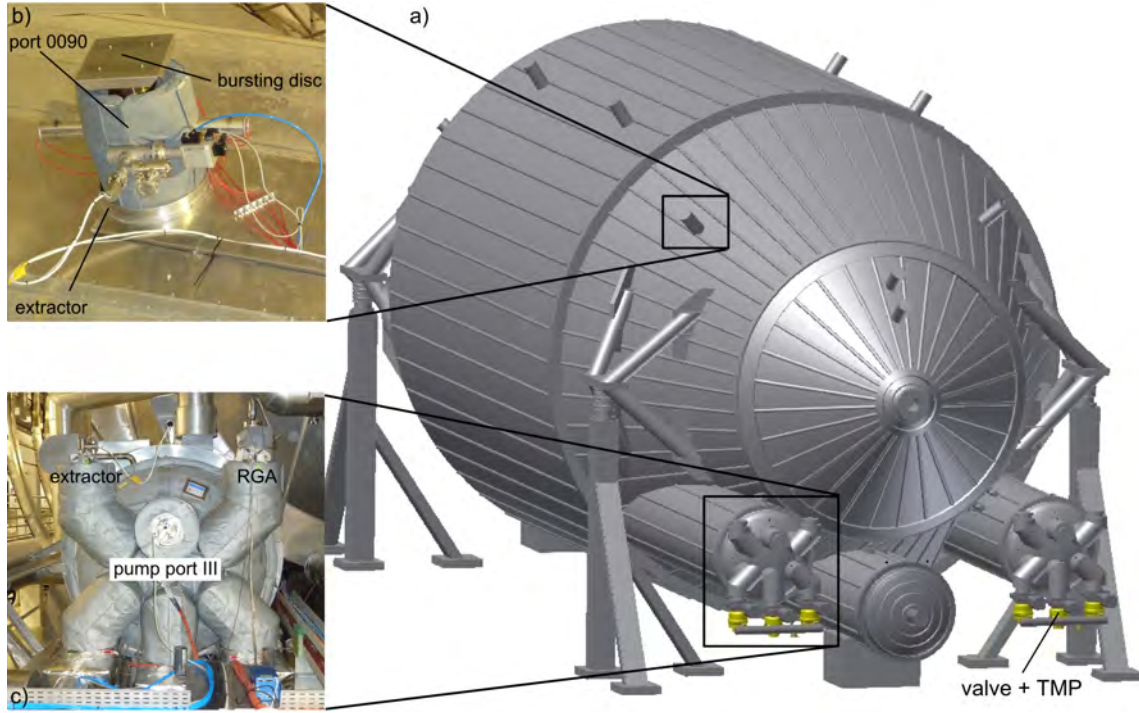
Figure 4.2: The main spectrometer vacuum system. a) Technical drawing of the KATRIN main spectrometer. Shown are the six *Leybold* MAG-W-2800 main TMPs, each separated from the main spectrometer by a *VAT* DIN250 full-metal gate valve. The exhaust port of the TMPs is connected to an manifold. **b)** Port `0090` is equipped with an extractor gauge `435-RPI-3-0096` and a bursting disc. **c)** Pump port III is equipped with an extractor gauge `435-RPI-3-3110` and an *MKS* residual gas analyzer `435-RPQ-3-3310`.

All gauges are placed behind gate valves to separate them during the measurement phase. The filaments in the gauges generate background by emitting electrons or even radon (^{220}Rn) due to the thorium decay chain. Background generated by vacuum gauges was one major issue at the pre-spectrometer test setup [78] [82]. The beam of signal electrons will enter the main spectrometer on axis trough a 500 mm flange attached to a ceramic insulator at the pre-spectrometer side. Eleven DN250 CF flanges on top of the main spectrometer hold the electric feedthroughs for the inner wire electrode system, generating the retarding potential. Port `0100` on top of the spectrometer is connected to a UV LASER to generate secondary electrons during the commissioning phase. Finally, the detector at the north side follows with a 500 mm flange separated with another ceramic insulator. Furthermore, the recipient is placed on six ceramic insulators, and its insulation resistance was tested successfully up to 50 kV.

A detailed vacuum flow chart is presented in section A.2 in appendix A.

4.2 Inner Electrode and High Voltage System

The KATRIN design foresees a high voltage (HV) supply directly connected to the wall of the spectrometer vessel, see figure 4.4. This novel approach was successfully tested hat the pre-spectrometer test setup [77] [78]. This feature is superior to the approach of the Mainz spectrometer [96] (now the KATRIN monitor spectrometer [70]) where the HV is connected to a set of inner electrodes while the

recipient is grounded. To suppress low-energy electrons, all KATRIN spectrometers are equipped with a nearly massless inner wire electrode. This inner electrode system can be put on a slightly more negative potential compared to the spectrometer to repel electrons emitted from the walls, see figure 4.3. The dominant shielding mechanism is the magnetic shielding, however.

4.2.1 Inner Wire Electrode System

The purpose of the nearly massless inner wire electrode is to prevent low-energy electrons from the inner surface of the vessel (induced by cosmic muons [97]) to penetrate into the volume of the transported flux tube, see figure 4.3. In addition the wire electrode is used to fine-tune the electrostatic field to be homogeneous and axially symmetric in the analyzing plane. This measure avoids Penning traps and optimizes the adiabatic transmission properties of the MAC-E filter [77]. Furthermore the inner electrode decouples the retarding potential from electric noise (due to electronic instruments like gauges and TMPs or other interferences) of the spectrometer vessel.
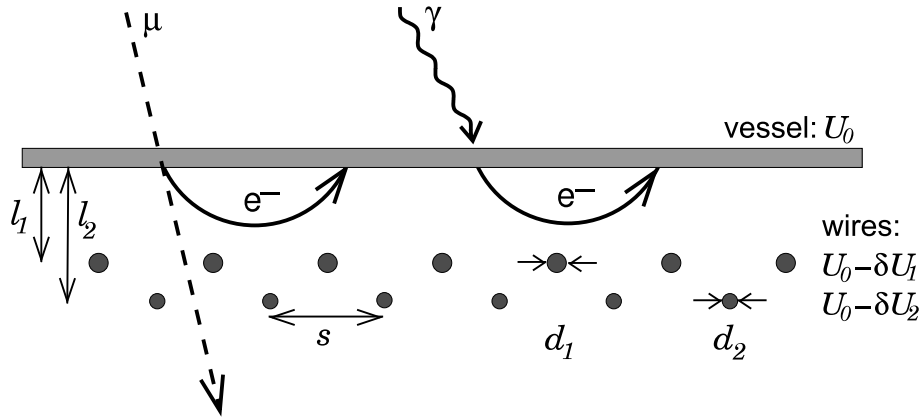
Figure 4.3: Principle of electrostatic background shielding (dimensions not to scale). The main parameters of the two-layered wire electrode are indicated: wire diameter $d_1 = 0.3\,\mathrm{mm}$ and $d_2 = 0.2\,\mathrm{mm}$, wire spacing $s = 25\,\mathrm{mm}$, layer spacing to vessel $l_1 = 150\,\mathrm{mm}$ and $l_2 = 220\,\mathrm{mm}$, wire potential offset $\delta U_1 = 100\,\mathrm{V}$ and $\delta U_1 = 200\,\mathrm{V}$ (values given for the cylindrical section of the main spectrometer). The mounting structures are not included. The figure is based on [98].

The design of the main spectrometer inner wire electrode system follows a pioneering concept successfully tested at the pre-spectrometer. The recipient is acting as a 'guard electrode' and the inner electrode system allows a more precise adjustment of the retarding potential. In particular the two-layered inner electrode system ensures a small geometrical coverage while at the same time providing a very stable retarding field, for example to compensate the not perfectly cylindrical vessel. During the neutrino measurements, the electrode will be operated in the standard monopole mode. The rings of the inner electrode are however split into two half shells that can be put on different potentials. Electrons passing through this dipole region will experience a drift perpendicular to the electric dipole field $\vec{E}$ and to the magnetic field $\vec{B}$. This effect is based on the $\vec{E} \times \vec{B}$-drift [99]. This special dipole mode can be used to remove trapped electrons. The inner wire electrode system is a contribution of the University of Münster, Germany.

The measurements at the pre-spectrometer test setup have initially revealed the presence of storage conditions for charged particles (*Penning traps*) as a major background source [78]. A careful electromagnetic design, an accurate manufacturing and a precise installation of the inner wire electrodes has avoided the formation of Penning traps. Even small deviations of the optimized shape may increase the background. Thus, the knowledge gained at the pre-spectrometer measurements was included in the design of the main spectrometer conical ground-electrodes and anti-Penning electrodes. The working principle of these electrodes is shown in figure 3.9. The main spectrometer commissioning measurement in summer 2013 have confirmed the proper operation, represanting a major milestone for KATRIN.

4.2.2 High Voltage System - General Design and Function

Figure 4.4 shows schematically the high voltage (HV) layout of the main spectrometer. The absolute voltage of $U_0 = -18.6\,\text{kV}$ must be stable on the 1 ppm level. This ambitious goal is achieved by two precise voltage dividers with an independent monitoring device and a second calibration beamline. This section provides a brief insight into the complex HV design. For a detailed description of the various subsystems see [100], [101], [71] and [102].

The main spectrometer recipient (including the main TMPs) is placed upon ceramic insulators for electrical insulation, and can be put on HV of up to $-35\,000\,\text{V}$. The fore-vacuum, the LN2 cooled baffles as well as the heating/cooling system are connected via ceramic or PVC/GRP[4] insulators. A precision high voltage system (see figure 4.4) will feed the outer vessel as well as the inner wire electrode with the required voltages.

To fine-tune the electrostatic retarding potential, the inner wire electrode (23 000 wires) is powered by a separate high voltage supply. This measure guarantees a stable, precise and homogeneous electric retarding potential. A high voltage switch allows to apply a voltage offset of up to $-1\,\text{kV}$ for each ring separately (the east and west dipole half shell are split up). This dipole mode can be used as an active background reduction method. For the standard operation mode (monopole mode) each ring can be provided with an additional offset (up to $+500\,\text{V}$). Thereby the inner and outer layers are controlled separately, and this feature enables the operator to fine tune the electrostatic retarding potential of the MAC-E filter system.

For precise high voltage monitoring the high voltage design foresees two approaches:

- **Two voltage dividers** K35 [100] and K65 [71] were developed and used to convert the potential to a measurable value. KATRIN will use an 8.5 digits multimeter (*Fluke*[5] 8508 A), that will be calibrated weekly with a 10 V calibration voltage.

- **The monitor spectrometer** as a voltmeter [70]. By observing the decay of $^{83}\text{Rb}/^{83m}\text{Kr}$ (a nuclear standard), or more precisely the quasi mono-energetic K-32 conversion-electron[6], the monitor spectrometer acts as second and independent HV monitoring device. To do so, it is electrically connected to

---

[4]glass fiber reinforced plastic

[5]Fluke Deutschland GmbH, In den Engematten 14, 79286 Glottertal, Germany

[6]32 keV gamma rays from K-shell generating conversation electrons with an energy of $17\,824.3\,\text{eV}$
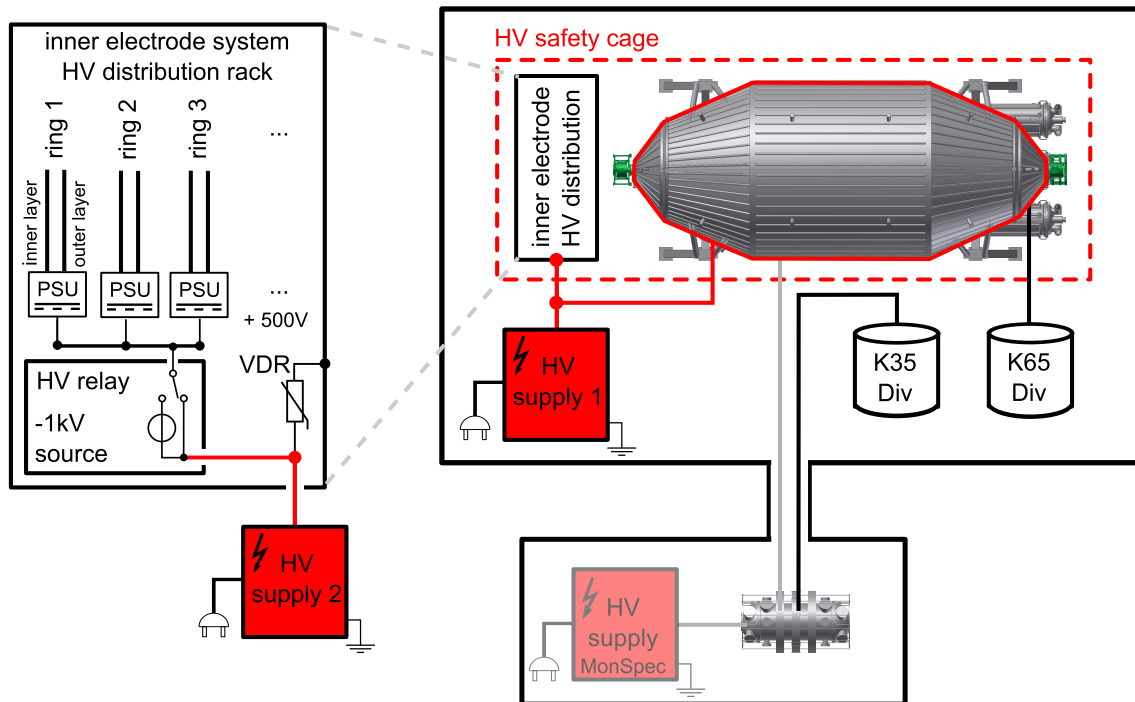
Figure 4.4: A simplified scheme of the main spectrometer high voltage supply system.
The HV supply 1 provides up to $-35\,\text{kV}$ to the vessel and HV distribution rack. The parts are interconnected to be laid to a common electrical potential. A second HV supply feeds the inner electrode system. The east and west part of the wire electrode system is split up. A high voltage switch allows to apply a voltage difference between both electrode half shells of up to $-1\,\text{kV}$. This feature is used for the dipole mode. For fine tuning the retarding potential each electrode ring (inner and outer layer are controlled separately) can be powered by an additional offset device $(+500\,\text{V})$.

For the precise high voltage monitoring two approaches are followed: 1) Two voltage dividers (K35 and K65) convert the potential of the spectrometer to a measurable value. 2) The KATRIN monitor spectrometer (right now with its own HV supply) will be connected to the main spectrometer high voltage system. As a MAC-E filter system the monitor spectrometer observes a $^{83}\text{Rb}/^{83m}\text{Kr}$ decay (as a nuclear standard). Any change in the supply voltage results in a distortion or a displacement of the measured electron spectrum.

If the voltage increases beyond the limits a VDR (voltage dependent resistor) protects the hardware.

the main spectrometer. By using the same electrostatic retarding potential, a change in the main spectrometer HV will be result in a change of the measured electron spectrum at the monitor spectrometer. This information can be used to calibrate the HV system on rather short time scales and to observe long-term drifts.

A complex safety system takes care that the allowed voltage differences do not exceed the given limits. Furthermore, it shuts down the voltage in a controlled way in case of an emergency. The whole spectrometer is locked up in a high voltage cage, secured with an interlock system at each door. In case of a blackout or any security breach a grounding switch powered by a compressed air storage conducts the electrical charges of the spectrometer to earth. If the voltage increases beyond given limits a VDR (voltage dependent resistor) protects the hardware.
In the standard operation mode the vessel is kept on $-18.5\,\text{kV}$ by one power supply. The second HV supply is used to feed the inner wire electrode system with an offset of $-100\,\text{V}$ respectively $-200\,\text{V}$ on the outer and inner layer.

4.3 The Magnet System of the Main Spectrometer

The magnetic flux tube of the spectrometer and detector section is defined by four superconducting solenoids. Together they form the magnetic guiding field for the MAC-E filter system. The first two solenoids are placed at the pre-spectrometer site: the PS1 and PS2 solenoids ($B_{\max} = 4.5\,\text{T}$), manufactured by *Cryogenic Ltd.*, London, UK (see table 3.3). To fine tune the magnetic flux tube and to compensate Earth's magnetic field, a set of 16 air coils frame the main spectrometer vessel, see section 4.3.1, is used. Another set of superconducting solenoids is placed at the detector site: the pinch and the detector magnets, both manufactured by *Cryomagnetics Inc.*[7], USA. Contrary to the pre-spectrometer magnets these solenoids are operated in the persistent mode. After energizing the magnets the windings are short-circuited with a superconductor forming a superconducting loop. The power supply can be switched off and the solenoid will preserve its field. However, the magnetic field slowly decays due to a small residual resistance in the superconducting joints. With a nuclear magnetic resonance (NMR) probe placed inside the warm bore of the pinch magnet, a maximum field drift of about 0.0015% per month[8] was determined [103]. The pinch magnet provides a $B = 6\,\text{T}$ field and thus generates the strongest magnetic field in the KATRIN beam line. It thus defines the accepted solid angle from the source. In combination with the PS2 solenoid the pinch magnet forms a MAC-E filter system with an asymmetric effect (the PS2 magnet is operated at $B = 4.5\,\text{T}$), forcing trapped electrons inside the main spectrometer to escape more likely towards the source. The detector magnet allows to map the entire analyzing plane onto the detector wafer.
During the commissioning measurements the pre-spectrometer was shifted aside (see section 3.3.1) to provide space for an electron source (e-gun). PS1 and PS2 were placed in the beamline at $z = -15.5\,\text{m}$ and $z = -15.104\,\text{m}$ (distance to the analyzing plane in the center of the spectrometer). The alignment orientation measurements

---

[7]Cryomagnetics Inc., 1006 Alvin Weinberg Drive - Oak Ridge, Tennessee 37830, USA
[8]KATRIN design goal: 0.1% per month

by Dr.-Ing. Juretzko (Geodetic Institute, KIT) show a deviation of about $\pm 1\,\text{mm}$ in comparison to the KATRIN magnet installation plan. A simulation of the resulting magnetic flux tube is shown in figure 4.5.
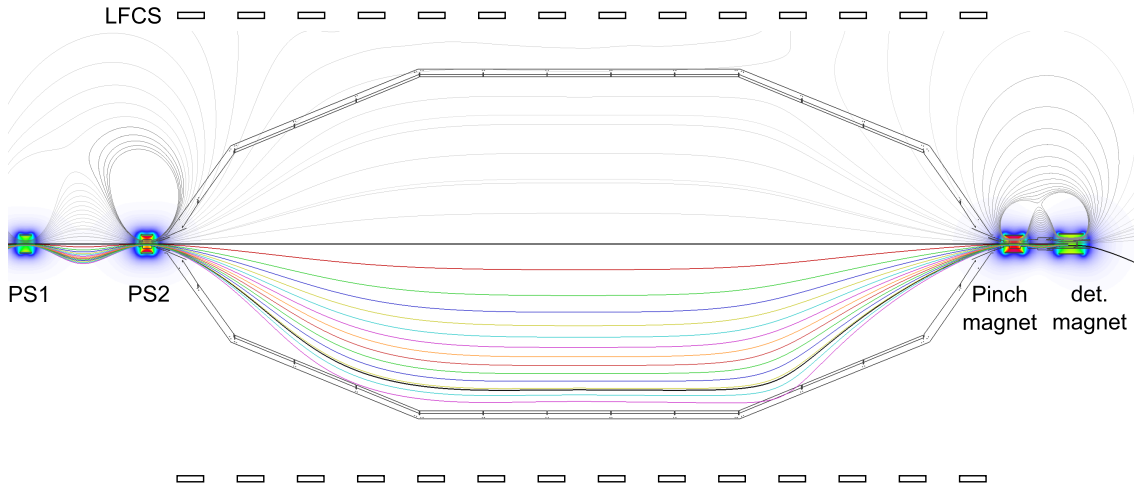
Figure 4.5: The simulated magnetic field of the main spectrometer during the commissioning measurements. Shown is the $3.8\,\text{G}$ setting according to table 4.2. The upper half of the figure shows some field lines, the lower half shows field lines corresponding to the rings of the detector[a].

---

[a]figure generated by Dipl.-Phys. J. Behrens, 2013.

Knowing the exact magnetic field is crucial for understanding background processes and also for optimizing the energy resolution of the spectrometer. However, Earth's magnetic field or ferromagnetic materials near the spectrometer can disturb the homogeneity. The monitoring of the magnetic field is thus performed by two separate systems:

- **The mobile magnetic sensor units (MobSU):** These units will move along the inner rails of the air coil support structure. Hence, thus allow a magnetic field sampling in areas that are otherwise difficult to access. A detailed description of the system can be found in [105]. The MobS units are a contribution from the University of Applied Science in Fulda, Germany.

- **The permanent magnetic field monitoring:** The main challenge in setting up permanent magnetic field sensors is to measure their exact position, in particular if the system changes (e.g. expanding during the bake-out cycle). A net of magnetic measurement units (MMUs) are thus placed at the hull of the main spectrometer and on the four surrounding pillars. A LASER box at each unit allows an easy and fast calibration of the position and orientation of the MMUs [106].

4.3.1 The Air Coil System

To fine-tune the magnetic guiding field in the low field region provided by the stray fields of the superconducting solenoids the main spectrometer is surrounded by 16 air coils. The homogeneity of the magnetic field in the analyzing plane is essential

Table 4.2: Common main spectrometer magnetic field settings. Present are the optimized currents used for the main spectrometer commissioning phase. The name of the setting correlates with the simulated magnetic field value in the center of the analyzing plane [104].

setting	'3.8 Gauss' current (A)	'9.0 Gauss' current (A)
PS1	103.8	103.8
PS2	149.7	149.7
LFCS		
1	28.6	95.2
2	24.0	99.8
3	17.3	48.9
4	22.1	98.8
5	33.5	100.0
6	36.4	74.0
7	35.8	98.2
8	54.1	96.6
9	10.2	80.9
10	52.1	90.4
11	32.0	61.3
12	20.1	99.0
13	29.8	97.6
14	-51.8	-36.2
EMCS		
vertical	50.0	50.0
horizontal	9.0	9.0
pinch	72.6	72.6
detector	54.6	54.6

for background reasons and also for a high energy resolution of the spectrometer. However, at this level the Earth's magnetic field is not negligible and electron trajectories are disturbed. Two separate air coil systems were designed and built around the main spectrometer vessel: The Earth Magnetic Field Compensation System (EMCS) to compensate the effects of the geomagnetic field, and the Low Field Coil System (LFCS) to fine tune the magnetic field gradient. To provide a very homogeneous field inside the volume of the main spectrometer a set of 14 LFCS coils and two EMCS coils was installed. As conductor a $70 \, \mathrm{mm}^2$ aluminum cable was used to reduce the weight of the system. Each coil is connected to its own power supply (SM3000 Series PSU from *Delta Elektronika*[9]) allowing a more flexible adjustment of the magnetic field [106].

4.4 Heating and Cooling System

For temperature control of the spectrometer vessel an $0.5 \, \mathrm{MW}$ oil heating system is used, manufactured by *HTT*, Germany. As a heat-transfer medium *Marlotherm* has been selected, that can be used in the temperature range from $10 \, ^\circ \mathrm{C}$ up to $350 \, ^\circ \mathrm{C}$. The thermo-oil was successfully used at the pre-spectrometer already. The main spectrometer is heated via two independent oil circuits: one for the main vessel and one for the three pump ports. A simplified flow chart is presented in figure A.12 in the appendix A.

The pump ports and their end caps, as well as all the ports on top of the spectrometer are additionally equipped with electrical heating tapes. All valves are packed in custom-made heating pads. The heating and cooling system is monitored by hundreds of PT100 temperature sensors: 326 sensors are placed at the vessel of the main spectrometer, 12 sensors in each pump port at the cryo baffles and the NEG pump and 4 sensors at the inner wire electrode system (in the cylindrical section).

In order to operate and control the vacuum system as well as the heating and cooling system a *Siemens*[10] PCS7 based control system has been developed and installed. The PCS7 process control is an embedded computer system, which ensures state-of-the-art industrial safety with its inherent system and component control as well as hard- and software interlock states. In parallel, all values of the control system are transmitted to the database (ZEUS) via the OPC[11] server and are available through an online interface (ADEI) for the whole KATRIN collaboration. The ZEUS database and the ADEI interface are a contribution of the Institute for Data Processing and Electronics (IPE), KIT, Germany. Concerning the bake-out control, the PCS7 heating control system has been upgraded with a dedicated cascaded feedback control with which the temperature ramping speed is directly coupled to the temperature of the inner electrode.

The PCS7 baking control interface panel is shown in figure 4.6. This panel provides easy access to the key values for the control of the temperature ramp including safety limits. Based on the entries in this panel, the control system generates a feed-line temperature set point T_{HTT} for the HTT oil heating system, which is based on the inner electrode temperature T_{IE} and an operator adjustable temperature difference

---

[9]Delta Elektronika B.V., Vissersdijk 4, 4301 ND Zierikzee, Netherlands
[10]Siemens AG, Wittelsbacherplatz 2, 80333 Munich, Germany
[11]Object Linking and Embedding (OLE) for Process Control

ΔT_{set}. In parallel, an independent ramp speed limit is set directly at the HTT ramping controller. Here, the maximum ramping speed of the feed-line itself can be set by the operator as specified by the heat transfer calculations.

The control system monitors the temperature difference between tank and inner electrode $\Delta T_{\text{Tank}-\text{IE}}$ permanently. In case that the temperature difference between tank and inner electrode exceeds a value of $1\,^\circ\text{C}$, the HTT feed-line temperature difference will be reduced automatically from $100\%\ \Delta T_{\text{set}}(f = 1)$ at $\Delta T_{\text{Tank}-\text{IE}} = 1\,^\circ\text{C}$ to $0\%\ \Delta T_{\text{set}}(f = 0)$ at $\Delta T_{\text{Tank}-\text{IE}} = 2\,^\circ\text{C}$ in a linear manner:

$$T_{\text{HTT}} = T_{\text{IE}} + f \cdot \Delta T_{\text{set}} \tag{4.1}$$

where $f = 2 - \Delta T_{\text{Tank}-\text{IE}}$ if $\Delta T_{\text{Tank}-\text{IE}} > 1\,^\circ\text{C}$. Thus, the ramping speed will be reduced and $\Delta T_{\text{Tank}-\text{IE}}$ can never exceed $2\,^\circ\text{C}$, simply because $f \cdot \Delta T_{\text{set}} = 0$. Based on this method, $\Delta T_{\text{Tank}-\text{IE}}$ can be kept stable even if the heat transfer efficiency should change. The setting of the feed-line offset temperature ΔT_{set} directly influences the resulting temperature gradient. Since this dynamic limit is hard-coded in the control system, it provides the maximum safety for the inner electrode but full edibility for the operators.
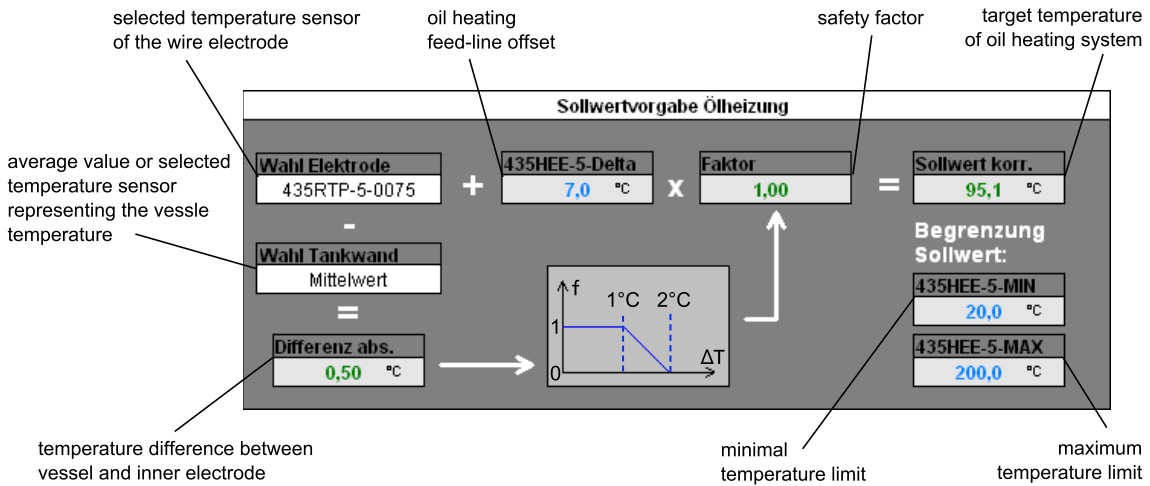
Figure 4.6: PCS7 interface of HTT oil heating system. This interface panel enables the operator to change the setpoint input of HTT oil heating system and its safety limits.

For the thermal insulation the vessel manufacturer *DWE* (respectively the sub vendor for the thermal insulation work) calculated a thickness of $160\,\text{mm}$ to ensure the specified maximum heat loss of $150\,\text{W/m}^2$ to the ambient air. To have a large safety margin with respect to heat losses the thickness of the insulation was extended to $240\,\text{mm}$. As insulation material rock wool *ISOVER MD 2* attached to a wire netting made of stainless steel was used, with an outer aluminum plate coating.

5 Vacuum Conditioning of the KATRIN Main Spectrometer

This chapter covers important fundamentals of vacuum physics which are of relevance for the later background considerations, and outlines the basic concepts of working within a stringent UHV environment [84]. After evaluating the vacuum performance of the KATRIN main spectrometer in theory, corresponding measurements at the test recipient were performed to find an optimized bake-out procedure for the spectrometer. By baking-out a recipient the vacuum conditions are improved [107]. In addition to the bake-out procedure the optimal activation of the non-evaporable getter (NEG) pumps at $350\,°C$ was investigated. The main objective of this chapter is to develop a concept to reach a final equilibrium pressure of about 10^{-11} mbar in the main spectrometer.

5.1 Fundamentals of Vacuum Physics

When enclosed within a volume V, a gas is uniformly distributed, and gas particles are constantly moving and striking the walls of the vessel (recipient). The exerted force F on the inner surface A defines the pressure p:

$$p := F/A. \tag{5.1}$$

A vacuum is defined as a state of a gas at which its pressure is lower than that of the ambient surrounding atmosphere. A real gas is composed of different types of gas species. The total pressure equals the sum of the partial pressures exerted by the corresponding gas types. The gases types present in a recipient as well as their composition can be detected with a residual gas analyzer (RGA).

The pressure of a gas in a closed volume changes if the temperature T is varied. The *ideal gas law* describes the state of a gas as a function of pressure, temperature and volume:

$$pV = Nk_{\mathrm{B}}T, \tag{5.2}$$

where N is the number of particles (or molecules) and k_{B} is the *Boltzmann constant*. Due to the high number of molecules per unit of volume at standard conditions ($T = 293\,\mathrm{K}$), it follows that even at a pressure regime of $1 \cdot 10^{-12}$ mbar about $25\,000$ molecules per cm^3 will still be present. For such small pressure values the mean free path of a gas particle greatly exceeds the dimensions of the recipient. Hence, the thermal motion of the particles is independent of each other. This situation is called *molecular flow*.

The gas flow plays an important role in vacuum technology. The pV flow q_{pV} follows equation 5.2 and is defined as transported gas per unit time:

$$q_{pV} = \frac{pV}{t} = \frac{Nk_{\mathrm{B}}T}{t}. \tag{5.3}$$

The right-hand side of the equation shows that a constant number of particles is moved at a constant temperature T. When a vacuum vessel is evacuated the volume flow rate $q_V = q_{pV}/p = \dot{V}$ equals the the pumping speed S of the vacuum pump:

$$S := \frac{\mathrm{d}V}{\mathrm{d}t} \qquad [S] = \ell/\mathrm{s}. \qquad (5.4)$$

Vacuum pumps have, as a general rule, a constant pumping speed and are independent from the pressure. However, momentum transfer and entrapment pumps are more effective on some gases than others. Hence, their average pumping speed depends on the chemical composition of the gases remaining in the recipient. Multiplying the pumping speed by the inlet pressure yields the mass flow rate q_m which refers to the throughput of a pump:

$$q_m := p \cdot S = p \cdot \frac{\mathrm{d}V}{\mathrm{d}t} \qquad [q] = \mathrm{mbar}\,\ell/\mathrm{s}. \qquad (5.5)$$

As the pressure in the recipient drops the volume contains fewer particles and thus less mass. Although the pumping speed remains constant, the throughput of the pump (or mass flow rate) drops exponentially. If a volume V is evacuated with a pumping speed S the pressure-time relation is given by:

$$V \cdot \frac{\mathrm{d}p(t)}{\mathrm{d}t} = -S \cdot p(t) \qquad (5.6)$$

$$\text{solution}: \quad p(t) = p_0 \exp\left(-\frac{S}{V}t\right) \qquad (5.7)$$

where p_0 is the pressure at the beginning of the pumping and V/S can be considered as the time constant τ of the system. On an $\ln(p)$ versus time plot the pressure decreases linearly. However, in a real vacuum system gas evolves within (outgassing) or enters the volume (leaks) of the recipient. As a mass flow the gas load Q is used interchangeably with the throughput. However, it is preferable to reserve throughput as a pump property and gas load as a chamber property. The final pressure p in a vacuum system is determined by the total gas load Q and the system pumping speed S:

$$p = \frac{Q}{S}. \qquad (5.8)$$

In order to achieve UHV conditions with a pressure regime well below 10^{-7} mbar, it is required to follow some basic principles:

- clean and careful work, all parts must be cleaned after protocol and installed with clean, powder-free gloves,

- use of stainless steel vacuum components (due to low outgassing rates [108]),

- only metallic seals (CF flange connections) are allowed,

- an appropriate pumping scheme, e.g. a combination of positive displacement (like scroll pumps), momentum transfer (like turbomolecular pumps) and entrapment pumps (like cryo- or getter-pumps),

- leaks must be avoided, e.g. by using helium leak detectors.

In an ideal leak-free vacuum system the gas load is dominated by outgassing processes originating from two different sources [107]:

1. Molecules which have been adsorbed previously (e.g. during venting of the recipient) that desorb while pumping down the vacuum chamber.

2. Molecules diffusing through the bulk material of the vacuum chamber, entering the surface and desorbing from it.

Both effects lead to the same consequence: the lowest achievable pressure is limited. The concept of sorption processes is schematically shown in figure 5.1b. Atoms from a gas phase that are impinging on a solid surface are referred to as adsorbed. They remain on the surface with a sticking probability $\alpha \leq 1$. A distinction is made between physisorption (e.g. van der Waals forces) and chemisorption (e.g. covalent linkage). Bonds due to chemisorption are approximately ten times stronger than bonds produced by physisorption. For particles to desorb a certain amount of energy E_{des} is required. Adsorbed particles can diffuse in the solid, this process is named absorption. The penetration of a gas through a solid is called permeation.

A vacuum chamber that has previously been exposed to atmospheric pressure contains adsorbed gas on its inner surfaces which desorb only slowly under vacuum. The rate of desorption as well as the out-diffusion depends on the binding energies of the various gases and the temperature of the recipient. To release the adsorbed gases from the surface in the recipient, the kinetic energy of the particles E_{kin} must exceed the desorption energy E_{des} [108]. The (concentration) density of particles at the inner surface of the vacuum chamber is proportional to the residence time. The mean residence time τ_{mean} that a molecule will spend on the surface before it desorbs into the gas phase and into the volume of the recipient is proportional to the desorption energy E_{des} [84]:

$$\tau_{mean} \propto \exp\left(\frac{E_{des}}{k_B T}\right). \tag{5.9}$$

For a stainless steel recipient at room temperature the desorption energy of some molecules is so small that they disappear quickly from the surfaces. On the other hand for large values of E_{des} the residence time is so long that the corresponding molecules are also unproblematic. Troublesome are those gas species that cannot be removed from the vacuum chamber in a practical amount of time. Unfortunately this process is dominated by water sticking to the surface of the recipient. The desorption energy of water on stainless steel surfaces lies in the range of 80 to 92 kJ/mol [107] making it the dominant residual gas even after days or weeks of pumping. To remove the adsorbed molecules the vacuum chamber has to be heated to accelerate this process. The temperature and the length of the vacuum bake-out cycle depends on the ultimate pressure that is desired after the procedure and the cool down to room temperature. Figure 5.1a shows a successful bake-out cycle up to 350 °C (held for about 90 h) of an UHV vacuum system. The bake-out procedure improved the pressure inside the recipient by one order of magnitude.
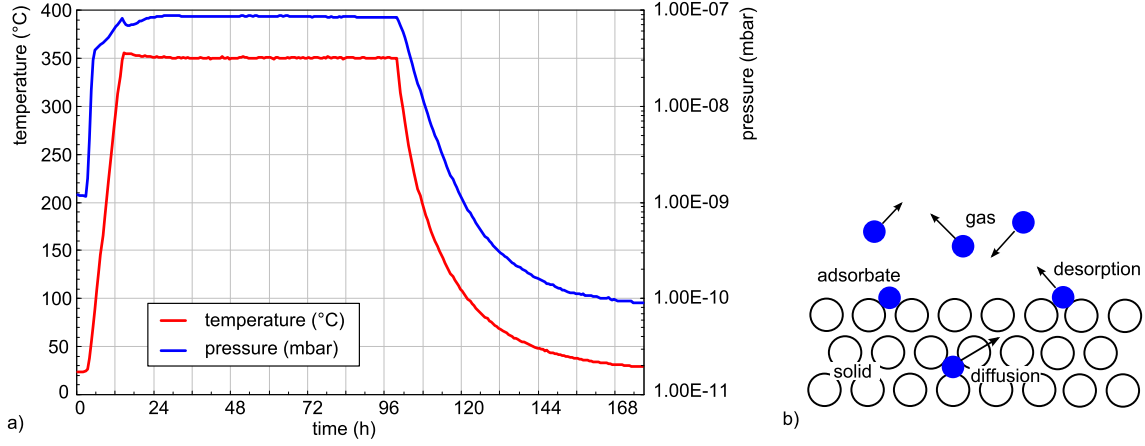
Figure 5.1: The basic concept of baking-out a vacuum system a) Measured data from a bake-out procedure at the test recipient with temperatures up to 350 °C. Plotted are the temperature and the pressure over time. The bake-out cycle (duration: 90 h) improved the vacuum in the recipient by one order of magnitude. **b)** Fundamental concepts of sorption processes. The white circles represent atoms in the solid. The gas atoms or molecules (blue circles) are impinged on the surface and are adsorbed, diffused (become absorbed) or desorbed (released from the surface). The figure is based on [84].

Hence, the final pressure in the vacuum chamber is essentially correlated to a proper bake-out cycle. The effectiveness of the procedure depends on the bake-out temperature and the duration of the process, as well as the material of the vessel (in particular the surface conditions and possible pre-treatments) and the gaskets. After a bake-out cycle one can assume that all physisorbed and chemisorbed molecules have been desorbed and the surface is 'cleaned'. As a consequence, the concentration of hydrogen is lower at the surface of the vacuum chamber than in the bulk material. Now, the second mechanism of outgassing is dominant: The diffusion of dissolved hydrogen atoms out of bulk material[1] of the vessel walls. The diffusion process is a thermally driven movement of atoms in a solid resulting in a transport of atoms following the concentration gradient. The particle flow rate j_{diff} (or diffusion flux) can be approximated by *Fick's first law*:

$$j_{\text{diff}} = -D\frac{\partial C}{\partial x}, \tag{5.10}$$

where $\frac{\partial C}{\partial x}$ represents the concentration gradient. The temperature dependent diffusion coefficient D is proportional to the activation energy[2] E_{diff} of the diffusing particles [84]:

$$D \propto \exp\left(-\frac{E_{\text{diff}}}{k_B T}\right). \tag{5.11}$$

Individual hydrogen atoms diffuse inside the bulk material of the vessel walls but desorb only as a hydrogen molecule from the surface. Therefore a hydrogen atom reaching the surface requires a second hydrogen atom to form a molecule to desorb (see schematic drawing in figure 5.2b). The recombination of hydrogen at the

---

[1]The hydrogen was dissolved during the steel production process from the surrounding atmosphere (air contains about $5.5 \cdot 10^{-5}\%$ hydrogen).
[2]The activation energy was defined by ARRHENIUS as the minimum of energy that is required to start a reaction.

surface thus limits the outgassing rate of stainless steel [109]. A higher bake-out temperature will increase the surface diffusion of single hydrogen atoms, so that the surface density of single hydrogen atoms will rise. This enhances the likelihood of recombination to molecular hydrogen which enables desorbtion from the surface as gaseous H_2, as now the desorption energy is rather low. In a quasi-static equilibrium there will be a constant net flow of hydrogen atoms to the vacuum surface which then desorb in the vessel [107]. Hence, the temperature of the bake-out procedure determines the concentration profile of hydrogen.

In theory the bake-out temperature determines the diffusion coefficient and the average surface residence time of hydrogen at the inner surface of the recipient which is then 'frozen-in' at room temperature. Figure 5.2a shows the qualitative course of the diffusion coefficient (see equation 5.11), the average surface residence time (see equation 5.9) and the resulting surface density of hydrogen as a function of the temperature in arbitrary units. The hydrogen surface density corresponds to the outgassing rate. A rise in temperature accelerates the desorption rate. Hence, the mean residence time of hydrogen molecules on the stainless steel surface of the recipient drops. Concurrently the diffusion rate increases at higher temperatures, with more and more hydrogen being released from the inner surfaces of the vessel walls.
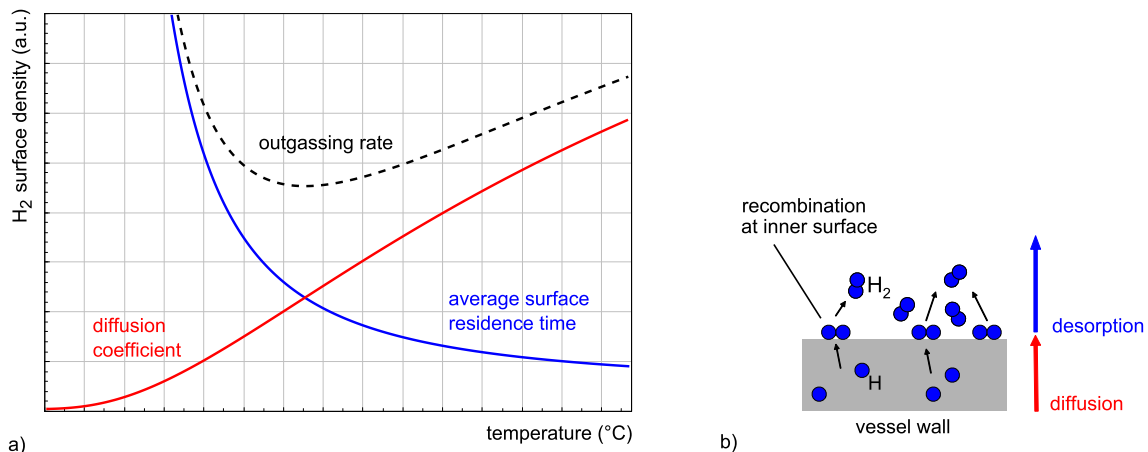
Figure 5.2: Shown is the characteristic dependence of the outgassing rate of a stainless-steel recipient. a) Qualitative course of the average surface residence time (see equation 5.9), the diffusion coefficient (see equation 5.11) and the resulting surface density of hydrogen that is corresponding to the outgassing rate over the temperature (in arbitrary units). **b)** Schematic drawing: The individual hydrogen atoms diffuse inside the bulk of the vessel walls but desorb only after their recombination as gaseous hydrogen molecules from the surface.

5.2 Expected Vacuum Performance of the Main Spectrometer

This section defines the parameters to analyze the vacuum performance of the main spectrometer. A detailed overview of the vacuum system of the main spectrometer can be found in section 4.1 and a complete vacuum flow chart in section A.2 in appendix A. The measured parameters (like the pressure readings of the gauges)

are subdivided into parameters that are unknown and yet to be determined (like the effective pumping speed of the NEG pump or the total outgassing rate of the vessel).

Effective pumping speed: The main spectrometer is equipped with a cascaded TMP pumping scheme and furthermore with three NEG pumps. The expected pumping speed of the individual components are estimated by information from the manufacturer and simulations:

- **6x TMP** *Leybold* MAG-W-2800 (`435-PTM-3-xy20`). Three TMPs are mounted at pump ports II and III, and are backed by a cascaded TMP and a scroll pump which generates an intermediate or fore-vacuum. The compression effect for hydrogen is multiplied by the sequential mounting of several pump stages. In combination these pumps reach a pumping speed for hydrogen of about $S_{\mathrm{6xTMP}}(\mathrm{H_2}) = 10^4\,\ell/\mathrm{s}$.

- **3x** $1\,000\,\mathrm{m}$ **NEG** *SAES* type St707 (`435-PNG-3-x010`). Each of the three main spectrometer pump ports is equipped with NEG material. However, the pumping speed of the NEG pump is reduced by the conductance of the baffle C_{B} (see figure 5.3). To determine the effective pumping speed $S_{\mathrm{NEG}}^{\mathrm{eff}}$ of the NEG pump the influence of the baffle is taken into account:

$$\frac{1}{S_{\mathrm{NEG}}^{\mathrm{eff}}} = \frac{1}{S_{\mathrm{NEG}}} + \frac{1}{C_{\mathrm{B}}} \tag{5.12}$$

$$C_{\mathrm{B}} = -\frac{S_{\mathrm{NEG}}^{\mathrm{eff}} \cdot S_{\mathrm{NEG}}}{S_{\mathrm{NEG}}^{\mathrm{eff}} - S_{\mathrm{NEG}}} = 272\,000\,\ell/\mathrm{s}, \tag{5.13}$$

where $S_{\mathrm{NEG}} = 334\,000\,\ell/\mathrm{s}$ is the theoretical[3] pumping speed of the NEG pump without baffle and $S_{\mathrm{NEG}}^{\mathrm{eff}} = 150\,000\,\ell/\mathrm{s}$ is the simulated (see section 7.3.2 and [82]) effective pumping speed of NEG pump with baffle.

Total outgassing: The equilibrium pressure $p = Q/S_{\mathrm{eff}}$ in the recipient depends on the effective pumping speed S_{eff} and the gas load Q of the system. The total gas load results from different effects, with the main sources contributing:

- **vessel:** $Q_{\mathrm{out}} = j_{\mathrm{H_2}} \cdot (A_{\mathrm{vessel}} + A_{\mathrm{electrode}})$. In an accurately baked-out vacuum vessel the outgassing is dominated by hydrogen followed by $\mathrm{H_2O}$, CO and $\mathrm{CO_2}$. The inner surfaces of the main spectrometer comprise the inner surface of the vessel walls ($A_{\mathrm{vessel}} = 690\,\mathrm{m}^2$) and the surface of the inner wire electrode system ($A_{\mathrm{electrode}} = 460\,\mathrm{m}^2$).

- **NEG pump:** $Q_{\mathrm{NEG}} = p_{\mathrm{NEG}} \cdot S_{\mathrm{NEG}}$, with the equilibrium pressure p_{NEG} at the NEG material and S_{NEG} the pumping speed for hydrogen. The gas load Q_{NEG} equals the hydrogen desorption from the NEG pump. For a properly activated NEG pump this gas load can be neglected at room temperature. The value

---

[3]The pumping speed of the NEG pump for hydrogen is based on simulations done by Luo et.al using a sticking coefficient of $\alpha = 0.028$. The pumping speed is expected to be smaller if the NEG pump is not fully activated.
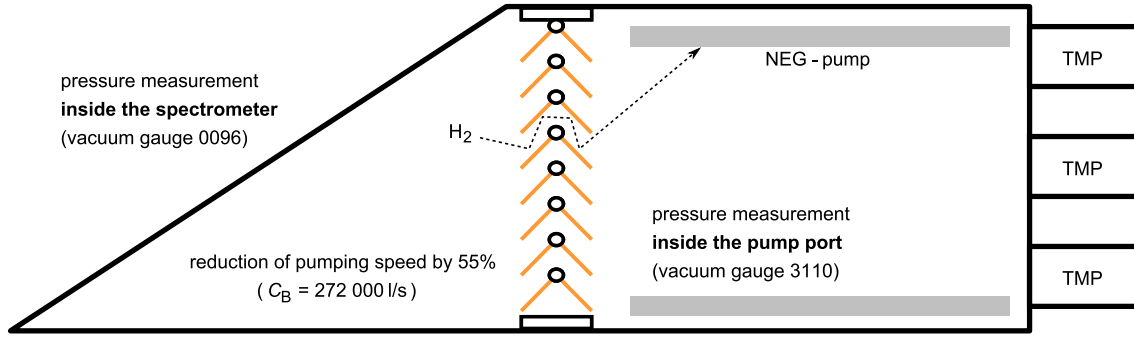
Figure 5.3: Schematic drawing of the cross-section of the main spectrometer pump port with NEG pump and liquid nitrogen cooled baffle. The pressure inside the spectrometer is given by p_{MS} resp. inside the pump port by p_{PP}, the reduction of pumping speed for hydrogen was simulated to about 55%. The conductance of the baffle $C_B = 272\,000\,\ell/s$ follows equation 5.12. For more details see chapter 7.

    depends both on the temperature and on the saturation of the NEG material (as described by *Sievert's law*, see equation 6.1).

- **leakage:** The parameter Q_{leak} equals the gas load of the air influx into the recipient through leaks. After a proper leak test (with a Helium leak detector) this effect can usually be neglected. If a leak does occur during the measurement phase, its contribution to the absolute pressure has to be identified (using a residual gas analyzer) so that it can be subtracted from the measured pressure value.

Pressure reading: The pressure in the UHV region is monitored with two extractor gauges, see figure 4.2:

- at port 0090 (`435-RPI-3-0096`) connected at a DN40 CF flange. The small volume of the port leads to a locally enhanced outgassing, resulting in a constant offset p_0 to the actual pressure value p_{MS} inside the main volume of the main spectrometer: $p_{0096} = p_{MS} + p_0$

- at knee three of pump port III (`435-RPI-3-3110`). The gauge measures the pressure p_{PP} inside the pump port, where the pressure reading is dominated by the pumping speed of the NEG pump: $p_{3110} = p_{PP}$

Thus, the measured parameters are formed by the pressure readings from the extractor gauges p_{3110} and p_{0096}. The unknown values are the offset pressure p_0 of the pressure gauge `0096`, the effective pumping speed of the NEG pumps S_{NEG}, the gas load due to outgassing of the spectrometer and the inner electrode system Q_{out}, and the outgassing of the NEG pump Q_{NEG}.

Previous bake-out measurements at the test recipient, the pre-spectrometer and the non-equipped main spectrometer (without the inner wire electrode system) all have reached an outgassing rate of about $10^{-12}\,\mathrm{mbar}\,\ell/\mathrm{s\,cm}^2$. Based on the measurements at the prototype setup, the main spectrometer pumping scheme was designed accordingly to reach a final pressure of about $10^{-11}\,\mathrm{mbar}$. Therefore, the initially planned and actual design parameters for the main spectrometer are:

Expected gas load: With a hydrogen outgassing rate of $j(H_2) \leq 10^{-12}\,\mathrm{mbar}\,\ell/\mathrm{s}\,\mathrm{cm}^2$ and a total vacuum surface inside the main spectrometer of $690\,\mathrm{m}^2$ (vessel) + $460\,\mathrm{m}^2$ (electrodes) $= 1150\,\mathrm{m}^2$ the hydrogen gas load can be approximated to a value of $Q_{\mathrm{out}} = 1.15 \cdot 10^{-5}\,\mathrm{mbar}\,\ell/\mathrm{s}$.

Theoretical pumping speed: The main spectrometer ports are equipped with $3\,\mathrm{km}$ NEG strips and six *Lebold* MAG-W-2800 TMPs resulting in a pumping speed of $S_{\mathrm{NEG}}(H_2) = 10^6\,\ell/\mathrm{s}$ and $S_{\mathrm{TMP}}(H_2) = 6 \cdot 10^4\,\ell/\mathrm{s}$, leading to a final pressure of $p = Q/S \approx 1.1 \cdot 10^{-11}\,\mathrm{mbar}$.

However, due to the LN2 cooled baffle system the effective pumping speed of the main spectrometer is reduced [82] to $S_{\mathrm{NEG}}(H_2) = 4.5 \cdot 10^5\,\ell/\mathrm{s}$, resulting in a final pressure of $p \approx 2.6 \cdot 10^{-11}\,\mathrm{mbar}$. For more details about the LN2 baffles see chapter 7. The outgassing rate now restricts the final equilibrium pressure of the main spectrometer. By optimizing the bake-out procedure the outgassing rate of stainless steel recipient can be reduced. A series of measurement at the test recipient was performed to optimize the in-situ bake-out cycle of the main spectrometer (see section 5.3).

5.3 Measurements at the KATRIN Test Recipient

The test recipient [110] was foreseen and implemented as a prototype for the vacuum system of the main spectrometer. It was built by the same manufacture (*MAN DWE GmbH* in Deggendorf, Germany) and same raw material (stainless steel 316LN) as the much larger spectrometer. Thus the test recipient is an ideal experimental setup for comparative measurements. Many aspects of the main spectrometer vacuum system can be implemented and evaluated in this smaller scaled test setup, than be scaled up and transferred to the main spectrometer.

This section focuses on measurements performed at the test recipient to reduce the hydrogen outgassing of the stainless steel vessel by optimizing the bake-out cycle. The results will be used in the planning of the bake-out procedure of the main spectrometer.

5.3.1 Experimental Setup

The test recipient (see figure 5.4) was the first prototype UHV vessel ordered for KATRIN. The vessel was manufactured by *MAN DWE GmbH* in Deggendorf, Germany. Basically it consists of a cylindrical tube with a diameter of $0.5\,\mathrm{m}$, a length of $1.42\,\mathrm{m}$ and $10\,\mathrm{mm}$ thick walls. The stainless-steel 316LN (DIN1.4429) used for the vessel is identical to the material used for the KATRIN main spectrometer. The main advantage of the non-magnetic material is its low relative permeability $\mu_r < 1.01$ and an increased structural stability against distortion caused by welding. The cylinder is closed with one DN500 CF flange at each side. Both DN500 flanges are equipped with one central DN200 CF flange and two DN63 CF flanges. On one side the vacuum gauges of table 5.1 and a *Pfeiffer* QME 200 residual gas analyzer are installed. On the opposite side a cascaded TMP pumping system is mounted, and separated from the recipient by a *VAT* DN200 bakeable all-metal gate valve (series 48). The pumping scheme of the test recipient is comparable to the pumping

scheme used at the pre-spectrometer and the main spectrometer. It is consisting of two TMPs, a *Leybold* TW70H and a *Leybold* TW290H, and completed by a *Leybold* Scrollvac SC15D used as forepump. The vacuum system of the test recipient was designed to maintain a pressure of the order of about 10^{-10} mbar. A complete vacuum flow chart[4] is shown in figure A.8 in appendix A.

Figure 5.4: Experimental setup of the KATRIN test recipient. Left (side view): 1. forepump *Leybold* Scrollvac SC15D 2. turbo molecular pumps (a. *Leybold* TW290H and b. *Leybold* TW70H) 3. *VAT* DN200 valve and heating cushion, 4. bellows with heating tape and thermal insulation 5. test recipient vessel surrounded with two 10 m long 2.18 kW heating tapes and covered with a 20 cm thick thermal insulation (insulation elements filled with mineral wool) 6. water cooling device (*Haake* TC500). **Right** (front view): 7. residual gas analyzer *Pfeiffer* QME 200, 8. *Vacom* Atmion wide range manometer, 9. *Leybold* extractor gauge, 10. all metal angle valve for venting the system.

The test recipient vessel is equipped with nine temperature sensors and two 10 m long 2.18 kW heating tapes (*Tyco Thermal Control*[5] Isopad IT-S20). Additionally, the bellows between valve and vessel are equipped with one heating tape and one temperature sensor (T_{bellows}) and the main gate valve with two electric heating jackets and one temperature sensor (T_{valve}). The thermal insulation 5.4 of the test recipient is provided by mineral wool, aluminum foil and six about 20 cm strong aluminum insulation elements filled with mineral wool. Furthermore, the vessel is surrounded with a stainless steel condenser pipe that is used for circulating a coolant fluid. A water cooling device (*Haake*[6] TC500) is used to stabilize the temperature of the experiment (nominal value $T = 20\,^{\circ}$C) during measurements.

5.3.2 Measurements to Find an Optimized Bake-out Cycle

The main objective of the measurement series was to minimize the surface density of hydrogen at the stainless steel vessel and therefore to reduce the resulting outgassing rate. A measuring plan was scheduled to repeat a bake-out cycle with a different step temperature (see figure 5.6a) and [68]). After closing and evacuating the vacuum chamber ($p \approx 10^{-7}$ mbar), the bake-out procedure was started by heating the test

---

[4]In this stage no NEG pump was installed.
[5]Tyco Thermal Controls, 7433 Harwin Drive, Houston, TX 77036, USA
[6]Thermo Fisher Scientific Inc., 81 Wyman Street, Waltham, MA 02454, USA

Table 5.1: Overview of the vacuum gauges at the test recipient with range and measurement accuracy. For the vacuum analyses the *Vacom* Atmion wide range manometer is used. The extractor gauge was mounted for calibration purposes and the pirani gauge placed in the intermediate vacuum between the TMPs is used to monitor the pump down or venting procedure. A complete vacuum flow chart is presented in figure A.8 in appendix A.

gauge	range (mbar)	accuracy
Vacom Atmion wide range manometer	$1000\ldots10^{-10}$	$\pm25\%(10\ldots10^{-2}\,\text{mbar})$
		$\pm10\%(10^{-2}\ldots10^{-8}\,\text{mbar})$
Leybold extractor gauge IE514	$10^{-4}\ldots10^{-12}$	$\pm10\%$
Balzers pirani gauge TPR 010	$1000\ldots10^{-3}$	$\pm50\%$ (at range limits)
		$\pm15\%$ (at medium range)
Balzers cold cathode gauge IKR 020	$10^{-3}\ldots10^{-11}$	$\pm50\%$ (at range limits)
		$\pm5\%$ (at medium range)

recipient up to $350\,^\circ$C and holding this temperature to desorb all adsorbed molecules from the inner surfaces. After (33 ± 3) h the temperature was lowered to a certain step temperature. The step temperature was varied between $300\,^\circ$C and $100\,^\circ$C and lowered by $50\,^\circ$C after each completed bake-out cycle as seen in figure 5.6a). The system was cooled down and held on a step temperature for (48 ± 2) h[7]. In a last step, the test recipient was cooled down to room temperature and stabilized by the water cooling device at about $20\,^\circ$C and the residual gas composition was determined by means of an RGA. The outgassing rate of the stainless steel vessel was measured with the pressure-rise (or gas-accumulation) method [107]. By closing the main gate valve, the vacuum chamber is separated from the vacuum pumps. In the closed system the pressure rises over time (see figure 5.5) due to the outgassing of the recipient. The slope of this rise in pressure is proportional to the outgassing rate of the stainless-steel if other gas loads like leaks as well as any re-adsorptions on surfaces can be neglected. After each measurement the test recipient was vented with air. This step restored the passivated layer of water and other particles to the inner surface of the vessel.

An Atmion Wide Range Manometer from *Vacom* was used as main pressure gauge. The measuring principle (Bayard-Alpert) of the Atmion Wide Range Manometer is gas-type dependent. Therefore, the residual gas composition was determined by an RGA scan revealing hydrogen as dominant residual gas (see figure 5.5). The real pressure in the recipient can be calculated by dividing the displayed value by a correction factor of $K_{\text{gas}=\text{H}_2} = 0.428 \pm 0.033$ [111] (see table 6.1). The hydrogen outgassing rate j_{H_2} is then given by

$$j_{\text{H}_2} = \frac{\text{d}p_{\text{H}_2}}{\text{d}t} \cdot \frac{V}{A}, \tag{5.14}$$

where $\text{d}p_{\text{H}_2}/\text{d}t$ equals the pressure increase over time after closing the main gate valve. The results of the measurements are summarized in figure 5.6b, where the hydrogen outgassing rate is plotted over the step temperature. A minimal measured hydrogen outgassing rate of about $j_{\text{H}_2} = 4.8 \cdot 10^{-13}\,\text{mbar}\,\ell/\text{s}\,\text{cm}^2$ was reached with a step temperature of $150\,^\circ$C.

---

[7]including the time to cool down the system.
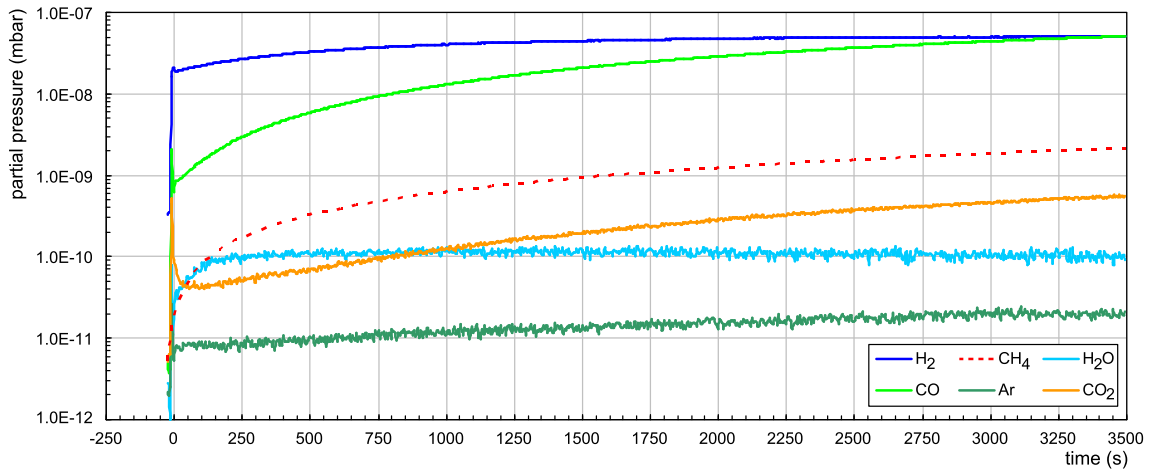
Figure 5.5: Determination of the outgassing rate of stainless steel with the pressure-rise method at the test recipient after a bake-out cycle at $T = 350\,°C$ with a step temperature of $150\,°C$. The sharp peak at the beginning of the spectrum is a result of closing the main gate valve and is disregarded for the analysis. The outgassing rate of hydrogen is gained by a linear fit of the partial pressure of H_2 between 50 and 150 s after closing the valve. The slope of the fit equals the pressure increase over time. To eliminate an overlap with atomic oxygen ($m = 16\,amu$) for methane the mass $m = 15\,amu \stackrel{\wedge}{=} CH_3$ was monitored, wighted and plotted as a 85% fraction of CH_4.
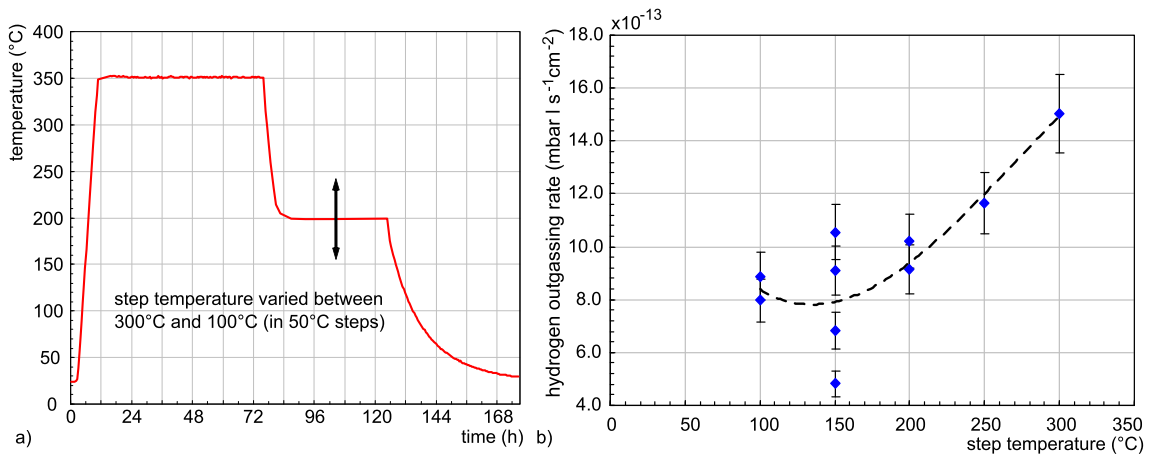
Figure 5.6: Measurement plan and result for test recipient measurement to find an optimized bake-out procedure. a) For each run the step temperature varied between $300\,°C$ and $100\,°C$ (in $50\,°C$ steps). **b)** Result of test recipient measurements. The plot shows the hydrogen outgassing rate over the step temperature. The minimum outgassing rate was measured with a step temperature of $150\,°C$. A third order polynomial fit is applied as guide for the eye. To check for reproducibility the measurements around the minimum were repeated two respectively four times. The large spreading of the data points at the minimum corresponds to slightly different initial conditions (for example due to air pressure and humidity).

5.3.3 Interpretation of Results and Conclusions for the Main Spectrometer

With an optimized bake-out procedure the test recipient reached an outgassing rate of $j(\mathrm{H_2}) = 4.8 \cdot 10^{-13}\,\mathrm{mbar}\,\ell/\mathrm{s}\,\mathrm{cm^2}$ which would result in a final pressure in the main spectrometer of about $1.2 \cdot 10^{-11}\,\mathrm{mbar}$, despite the reduced pumping speed due to the LN2 cooled baffle system. Based on these test recipient measurements a schedule for the main spectrometer bake-out cycle was worked out (see figure 5.7) [112]:

1. Slowly and steady increase of the temperature to $200\,^\circ$C with a ramping speed of $1\,^\circ$C/h while $T_{\mathrm{MS}} < 90\,^\circ$C, $1.5\,^\circ$C/h while $T_{\mathrm{MS}} < 120\,^\circ$C, $3\,^\circ$C/h while $T_{\mathrm{MS}} < 150\,^\circ$C and $5\,^\circ$C/h while $T_{\mathrm{MS}} < 200\,^\circ$C. The rather slow ramping speed ensures optimal thermal coupling of the inner wire electrode due to thermal radiation.

2. Maintain a stable temperature at $200\,^\circ$C for about two days, in order to remove most of the water bound on the stainless steel surfaces and to reduce the outgassing of hydrogen before the activation of the NEG pumps.

3. Increase of the temperature to a value of $350\,^\circ$C with a gradient of $5\,^\circ$C/h.

4. Maintain a stable temperature for at least 24 hours to activate the NEG pumps.

5. Lower the temperature to a value of $150\,^\circ$C.

6. Maintain a stable temperature at least one day or until there is no further significant pressure drop over time. This step is expected to reduce the hydrogen concentration on the surface by desorption, without replenishing the hydrogen by diffusion from the bulk (see figure 5.2 and figure 5.6).

7. Lower the temperature to $20\,^\circ$C. At this time the residual gas composition in the clean vessel is expected to be dominated by hydrogen, with only small traces of water, CO and CO_2.

8. If the final pressure is still too high, the temperature of the main spectrometer can be reduced further to $10\,^\circ$C. This should reduce the outgassing rate further and thus decrease the pressure by another factor of two.
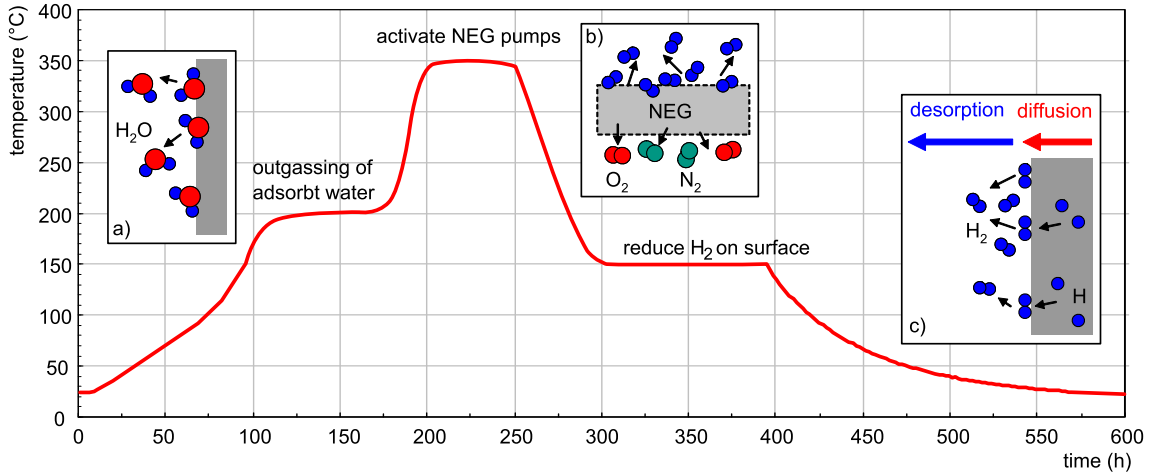
Figure 5.7: Bake-out schedule for the main spectrometer. Based on test recipient measurements an optimized schedule for the main spectrometer bake-out cycle was defined: **a)** ramp to a temperature of 200 °C to accelerate the desorption of adsorbed water molecules from the inner surfaces of the vessel, **b)** after the activation of NEG pumps at 350 °C by heat radiation **c)** decrease the temperature to 150 °C to reduce the hydrogen concentration on the surface by desorption, without replenishing the hydrogen by diffusion from the bulk. Cool down to room temperature and stabilize the temperature of the vessel at about 20 °C.

5.4 Main Spectrometer Bake-out Cycle and Resulting Vacuum Conditions

This section summarizes the events during the early 2013 main spectrometer bake-out procedure in detail. These measurements form a key element in this thesis and were intended to give a proof-of-principle, as well as to allow the subsequent commissioning measurements to be performed with excellent UHV conditions. The resulting conditions and the vacuum performance are evaluated.

5.4.1 Summary of the Main Spectrometer Bake-out Cycle

The key objective of the main spectrometer vacuum system is to reach and maintain a pressure in the lower 10^{-11} mbar regime during the entire lifetime of the KATRIN experiment. The required bake-out procedure was motivated in section 5.1 and optimized with measurements at the test recipient (presented in section 5.3.2 and in [68]). After the complete commissioning of the control and monitoring system, the system allows the operator to limit the temperature gradient by adjusting the feed-line offset temperature. It is hardwired and based on a *Siemens* PCS7 process control system. In parallel, all values of the control system are transmitted to a database (ZEUS) via the OPC server and are available thought an online interface (ADEI) for the whole KATRIN collaboration, see section 4.4.

After the initial pump down with a *Leybold* SP630 screw pump (630 m³/h) to 10^{-2} mbar, six *Leybold* MAG-W-2800 turbomolecular pumps (TMP) did take over (with a combined pumping speed for hydrogen of $10^4 \, \ell/$s), thus reducing the pressure in the recipient to approximately 10^{-8} mbar. The initial pump down was concluded with extensive helium leak tests that have been performed during summer 2012.

The final leak test showed no leaks above the sensitivity of $5 \cdot 10^{-10}$ mbarℓ/s. The main spectrometer bake-out procedure was thus performed in the winter 2012/2013. An overview of the entire bake-out cycle is shown in figure 5.8.

The main constraints for the bake-out cycle and the adapted temperature gradients resulted from the rather fragile inner wire electrode system. Hence, the most critical parameter during bake-out was and is the maximal allowed temperature difference $\Delta T \approx 5\,°C$ between the main spectrometer walls and the inner wire electrode. This parameter dictates the ramping speed. It is based on a conservative heat transfer and structural integrity calculation[8].

During the first 400 hours the vacuum and heating control systems were tested for longterm stable operation kept on a temperature of $30\,°C$. On January 4th, 2013 the temperature was slowly ramped up. With increased temperature the heat transfer (based on radiation) from the vessel walls to the inner electrode system improved. The ramping speed was adjusted as planned during the heating up to $200\,°C$. Even with increased temperature offset settings no changes of the temperature difference between tank and inner wire electrode system were observed. The smooth and parallel temperature curves of the vessel and the electrode confirmed that both are well coupled. At about $185\,°C$ the pressure inside the spectrometer dropped rapidly (see figure 5.8) and the residual gas analyzer showed a significant reduction of the water peak. After reaching the $200\,°C$ level of the temperature, the further ramping was stopped with a smooth gradient and the temperature was kept stable to remove the remaining water vapor from the getter material.

After about 90 h the ramping of the temperature was resumed. At a temperature of about $250\,°C$ the inner wire electrode monitoring system observed a short-circuit between two layers at the eastern cylindrical part. Due to the time development of the short-circuit - it took more than 10 minutes - a snap of a wire was excluded. Hence, it was decided to continue with the ramping of the temperature. Between $250\,°C$ and $300\,°C$ several sections of the inner wire electrode system developed short circuits between the two wire layers. A summary of the short-circuits can be found in [113]. The presumed cause of the short-circuits are the current leads that connect the inner electrodes to the vacuum feedthroughs (at the DN200 ports on top of the spectrometer). These current leads are made of 4 mm diameter CuBe rods. The rods lost their tensile strength at these temperatures, started to move downwards due to gravity and deformed permanently. Current photographic evidence shows that they are touching the holding structure (C-beams) of the electrode frames, thus connecting inner and outer wire layers. In order to prevent further damage the bake-out procedure of the main spectrometer had to be stopped at $300\,°C$. The temperature was kept stable over a period of 28 hours and then reduced to the step temperature of $150\,°C$.

The reduced activation time and temperature for the NEG pumps is expected to influence the effective pumping speed and the total capacity of the getter material. The nominal capacity of the pumps would have been large enough to last for the whole duration of the KATRIN experiment. With the reduced capacity additional activation cycles may be required.

During the final cool-down a major air leak opened up at a temperature of $52\,°C$ in a DN200 CF flange of port 0080 on top of the main spectrometer. To fix the leak

---

[8]Independent calculations by R. Gumbsheimer (KIT) and H.-W. Ortjohann (WWU).

the gasket would have had to be exchanged. This would have meant to vent the spectrometer, to repair the leak, to pump the system down and to repeat the bake-out-cycle again. Hence, an attempt to repair the leak was rejected and postponed to a later maintenance window. Changing the gasket to repair the leak leads to a high risk of damaging the wire electrodes underneath the flange because the current leads that supply the electrodes have to be removed in that case. For now a differentially pumped vacuum sleeve was installed around the flange and the leak. A scroll pump was mounted on top of the spectrometer to maintain the pressure and eliminate the leakage. The power supply of the pump had to be connected to the high voltage cabinet to allow its operation during high voltage measurements. Shortly thereafter the gas composition was dominated by hydrogen again. Apart from the air leak the RGA spectrum (see figure 5.9) shows only small traces of water and CO_2, as expected for a very clean vessel. An overall pressure reduction of three orders of magnitude was reached. Further information about the bake-out procedure can be found in [112].

5.4.2 Resulting Equilibrium Pressure

In general, equilibrium pressure is reached after a few times the pump down time $\tau = V_{\mathrm{MS}}/S$ (see equation 5.6). With a volume of the main spectrometer of $V_{\mathrm{MS}} = 1\,240\,\mathrm{m}^3$ and for a gas load Q dominated by hydrogen and with the NEG pumps fully activated, τ is of the order of seconds. For other gas types with lower pumping speeds the time until equilibrium is longer. However, since the processes investigated here were on a time scale of hours to days, τ can be neglected for the following analysis. Using the parameters listed in section 5.2 the equilibrium pressure in the volume of the main spectrometer can be written as:

$$p_{\mathrm{MS}} = p_{0096} - p_0 = \frac{Q_{\mathrm{out}} + 3 \cdot Q_{\mathrm{NEG}} \cdot \frac{C_{\mathrm{B}}}{C_{\mathrm{B}}+S_{\mathrm{NEG}}}}{6 \cdot S_{\mathrm{TMP}} + 3 \cdot S_{\mathrm{NEG}} \cdot \frac{C_{\mathrm{B}}}{C_{\mathrm{B}}+S_{\mathrm{NEG}}}}. \tag{5.15}$$

The numerator is composed by the sum of the gas load. The gas entering from the three pump ports is suppressed by the conductance of the baffle and the pumping speed of the baffle. The sum of the effective pumping speed forms the denominator, represented as the combined pumping speed of the six TMPs and the three NEG pumps. The pumping speed of each NEG pump is corrected for the conductance loss of the baffle. This loss was neglected for the TMPs.
The equilibrium pressure in the pump port III can be written as:

$$p_{\mathrm{PP}} = p_{3110} = \frac{1/3 \cdot Q_{\mathrm{out}} + Q_{\mathrm{NEG}}}{3 \cdot S_{\mathrm{TMP}} + S_{\mathrm{NEG}}}. \tag{5.16}$$

Only one third of the gas load from outgassing of the walls and electrodes are taken into account, reflecting the fact that there are three pump ports. The enumerator and the denominator are composed in the same way as in equation 5.15. Since the pressure gauge 3110 is placed in the pump port the conductance of the baffle was dropped.
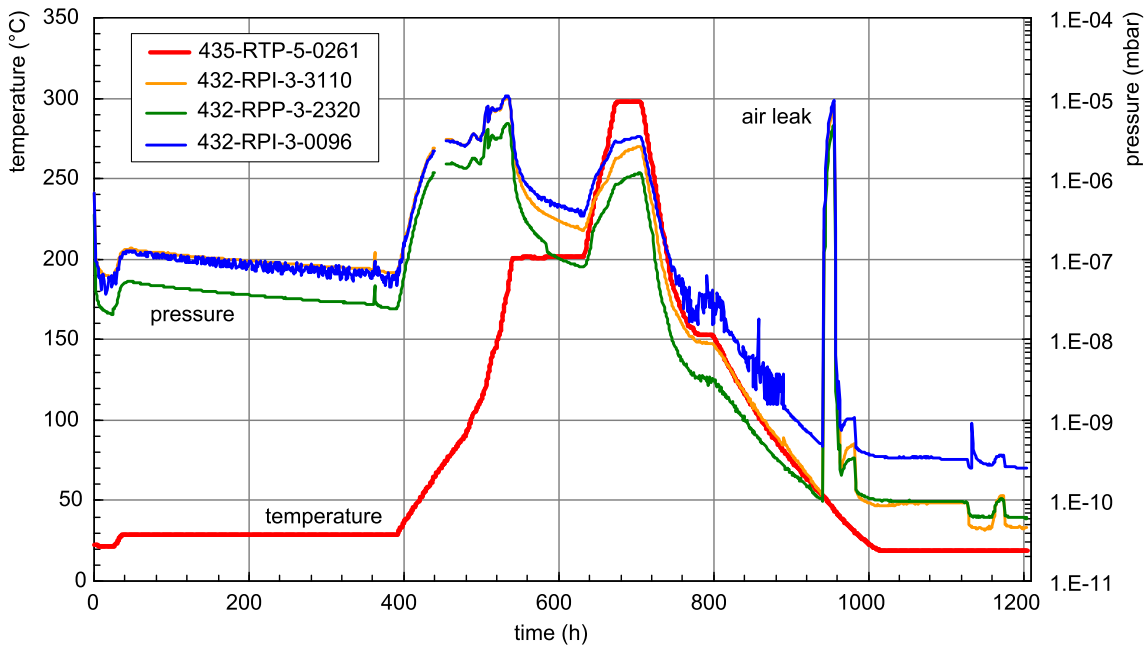
Figure 5.8: Main spectrometer bake-out procedure. Overview of pressure and temperature versus time during the baking in January 2013 of the main spectrometer. An air leak occurs in the final cool down phase at about 52 °C (leak at DN200 CF flange of port 0080).
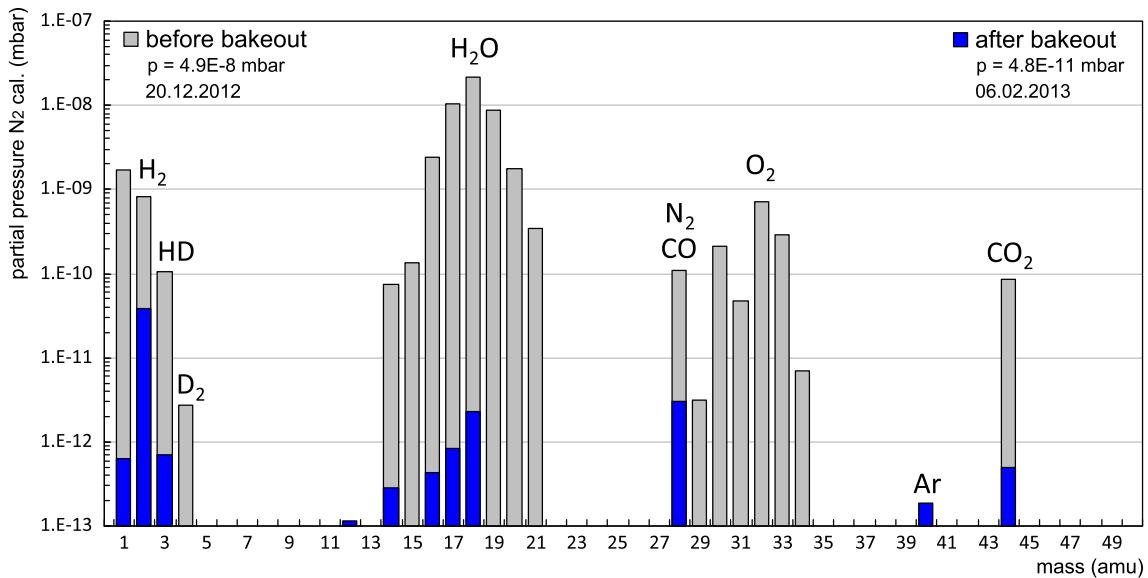
Figure 5.9: Result of the main spectrometer bake-out cycle. Shown are two residual gas spectra: one before (gray) and one after the bake-out procedure (blue). Before the bake-out cycle the pressure was dominated by water (mass = 18 amu) after the campaign hydrogen is the dominant residual gas as expected.

In principle three cases can be distinguished:

case 1: the NEG pump is not activated: $S_{\mathrm{NEG}} \approx 0\,\ell/\mathrm{s}$ and $S_{\mathrm{TMP}} \ll C_{\mathrm{B}}$. In this case it is assumed that the pumping speed of the TMPs is not affected by the conductance of the baffles. This case described the situation before starting the bake-out procedure:

$$p_{\mathrm{MS}} = p_{0096} - p_0 = p_{3110} = \frac{\sum Q_i}{6 \cdot S_{\mathrm{TMP}}} \tag{5.17}$$

where $\sum Q_i$ is the sum of all gas loads.

case 2: the outgassing from the NEG material is dominating the total gas load: $Q_{\mathrm{out}} \ll Q_{\mathrm{NEG}}$ and $S_{\mathrm{TMP}} \ll S_{\mathrm{NEG}}$. This case describes the situation during the activation process of the NEG material. The pumping speed of the turbomolecular pumps S_{TMP} can be neglected. Both gauges should measure the same pressure, disregarding the offset pressure p_0:

$$p_{\mathrm{MS}} = p_{0096} - p_0 = p_{3110} = \frac{Q_{\mathrm{NEG}}}{S_{\mathrm{NEG}}} \tag{5.18}$$

case 3: the NEG pumps are fully activated: $Q_{\mathrm{out}} \gg Q_{\mathrm{NEG}}$ and $S_{\mathrm{TMP}} \ll S_{\mathrm{NEG}}$. This case is the default case after activation of the getter material. The analyses of the vacuum performance will focus on this scenario. Equation 5.15 and 5.16 can be approximated by:

$$p_{\mathrm{MS}} = p_{0096} - p_0 = \frac{Q_{\mathrm{out}}}{3 \cdot S_{\mathrm{NEG}}} \cdot \frac{C_{\mathrm{B}} + S_{\mathrm{NEG}}}{C_{\mathrm{B}}} \tag{5.19}$$

$$p_{\mathrm{PP}} = p_{3110} = \frac{Q_{\mathrm{out}}}{3 \cdot S_{\mathrm{NEG}}} \tag{5.20}$$

$$\Rightarrow p_{0096} = p_{3110} \cdot \frac{C_{\mathrm{B}} + S_{\mathrm{NEG}}}{C_{\mathrm{B}}} + p_0 = a_1 \cdot p_{3110} + p_0 \tag{5.21}$$

$$\Rightarrow S_{\mathrm{NEG}} = (a_1 - 1) \cdot C_{\mathrm{B}} \tag{5.22}$$

If the assumptions for **case 3** are true, the slope of p_{0096} versus p_{3110} has to be $a_1 > 1$, since any gas from the main volume (outgassing or leak) has to build up a pressure gradient across the baffles before a significant amount of gas can be pumped away by the huge pumping speed of the NEG pumps.

5.4.3 Calibration of the Vacuum Gauges

For the calibration of the vacuum gauges it is assumed that in the time period before the bake-out campaign the pressure inside the main vessel equals the pressure inside the pump ports (see section 5.4.2 **case 1**), as the NEG pump was not yet activated:

$$p_{\mathrm{MS}} = p_{0096} - p_0 = p_{3110}. \tag{5.23}$$

By using the results of the fit presented in figure 5.10a one obtains: $p_{0096} = 0.971 \cdot p_{3110} - 8 \cdot 10^{-9}$ mbar. The slope of $0.971 \approx 1$ indicates very similar calibration values for both gauges (due to typical uncertainties in the measurement).

After the bake-out procedure this ratio changed, due to the large pumping speed of the NEG pumps (see section 5.4.2 **case 3**):

$$p_{0096} = p_{3110} \cdot \frac{C_\mathrm{B} + S_\mathrm{NEG}}{C_\mathrm{B}} + p_0 = a_1 \cdot p_{3110} + p_0. \tag{5.24}$$

The fit results presented in figure 5.10b $p_{0096} = 3.0023 \cdot p_{3110} + 9 \cdot 10^{-11}$ mbar compare the measured pressure between tank and pump port III. The result can be used to estimate the pumping speed of the NEG pumps (see section 5.4.5).

The calibration of the ionization gauges must be treated with caution. The gauges are very sensitive to the surrounding construction geometry (see the offset of the pressure in gauge 0096) and in particular to the chemical composition of gases that are being measured, to the corrosion of the gauge head filament or to other surface deposits. The factory calibration is given with a $\pm 10\%$ error range. The calibration shown here will be used to extrapolate the pressure over more than three orders of magnitude. Moreover the dominant residual gas changes from nitrogen to hydrogen during the bake-out procedure. Hence, the gas correction factor[9] must be adjusted from $K_{\mathrm{gas=N_2}} = 1$ (factory setting) to $K_{\mathrm{gas=H_2}} = 0.46$.
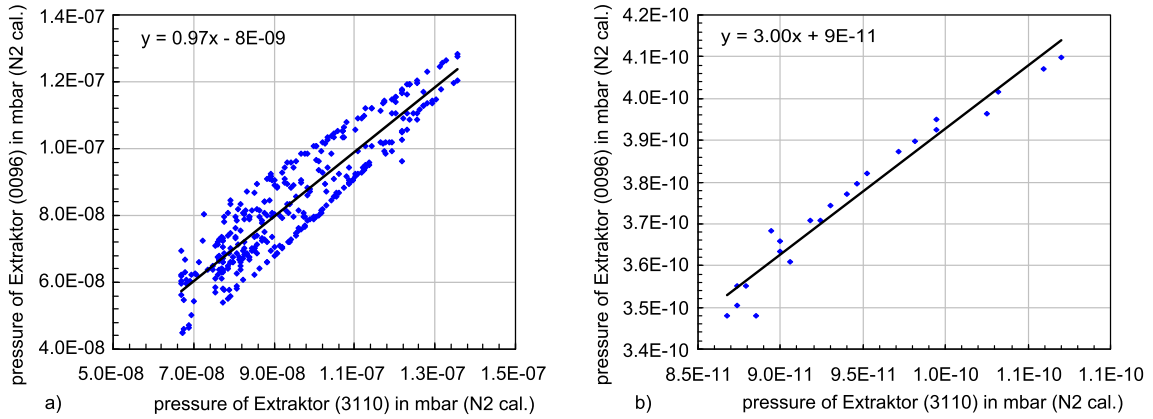
Figure 5.10: Calibration of the Vacuum Gauges. a) Measurement before the bake-out procedure (at $T = 30\,°\mathrm{C}$, dominant residual gas: water), see section 5.4.2 **case 1**. The gauges are calibrated by the manufacturer for nitrogen. The slope of 0.971 indicates as expected very similar calibration values for both gauges. **b)** After the bake-out campaign (at a temperature of $T \approx 30\,°\mathrm{C}$), see section 5.4.2 **case 3**. The slope of 3.0023 indicates the activation of the NEG pumps. However, the gauges are still calibrated for nitrogen, although the pressure in this scenario is dominated by hydrogen.

5.4.4 Air Leak at Port 0080

A reported above, during the last phase of the main spectrometer bake-out cycle an air leak opened up at one of the DN200 ports on top of the spectrometer. The lower DN200 CF flange of port 0080 leaked about $1\,\mathrm{mbar}\,\ell/\mathrm{s}$ for an interval of $10\,\mathrm{h}$ (see figure 5.8). After finding the leak the screws of the flange were tightened

---

[9]Further gas correction factor are listed in table 6.1.

($> 25\,\mathrm{Nm}$). However, only the installation of a differentially pumped vacuum sleeve (see figure 5.11) reduced the leak rate to about 10% of the total gas load. The scroll-pump (see figure 5.11c) used to evacuate the sleeve was mounted on a platform attached to the vessel. It was powered by one of the electrical cabinets on high potential and therefore could also be operated during high voltage measurements. After 'fixing' the leak, the vacuum inside the spectrometer was dominated by H_2. Figure 5.11a shows the decrease of the pressure over the temperature during the leakage. According to *Sievert's law*[10] the pressure decreases exponentially over the reciprocal temperature ($1/T$) after the activation of the NEG pump. The gauge `3110` measures the pressure inside the pump port III, and as a temperature reading one of the temperature sensors at the NEG pump is used. The extrapolation of the linear fit to $T = 20\,°\mathrm{C}$ leads to an expected pressure of $1.3 \cdot 10^{-11}\,\mathrm{mbar}$. After the installation of the vacuum sleeve the obtained pressure value was about $1 \cdot 10^{-10}\,\mathrm{mbar}$. The pressure improved slowly with the pumping time. At the end of the commissioning measurements a pressure of about $p_{\mathrm{PP}}(H_2) \approx 4.0 \cdot 10^{-11}\,\mathrm{mbar}$ was measured inside pump port III.
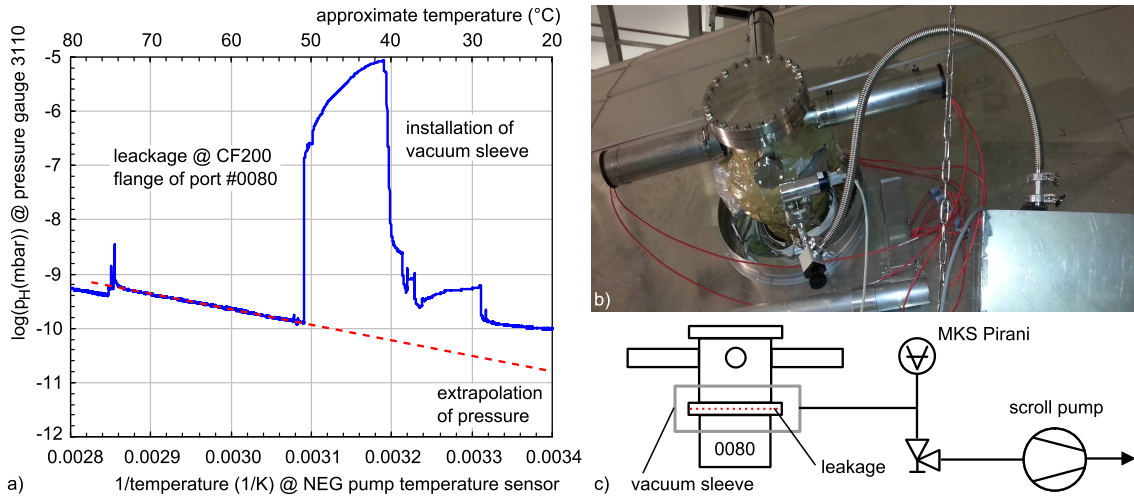
Figure 5.11: Estimation of the final pressure without the leak. a) *Sievert's law* extrapolated to $20\,°\mathrm{C}$ if the leak had not occurred. The accomplished pressure was about one magnitude above the expected value. Nevertheless, the pressure improves slowly with the pumping time. **b)** Picture of the vacuum sleeve with scroll pump at port `0080` on top of the main spectrometer. **c)** Schematic drawing and vacuum flowchart of the vacuum sleeve at port `0080`.

During a short pressure-rise measurement (presented in figure 5.15b) a continuously increasing argon pressure could be observed with the RGA. Argon and other (chemically passive) gases are only pumped by the TMPs and not by the NEG pumps. The slope of the linear fit shows a continuous increase of the ${}^{40}\mathrm{Ar}$ partial pressure with about $2.63 \cdot 10^{-14}\,\mathrm{mbar/min}$. Multiplied with the volume of the main spectrometer this corresponds to a leak rate of $5.4 \cdot 10^{-10}\,\mathrm{mbar}\ell/\mathrm{s}$. Assuming that argon has a concentration of about 1% in air the leak is estimated to about $5.4 \cdot 10^{-8}\,\mathrm{mbar}\,\ell/\mathrm{s}$. If the differential pumping resulted in a reduction of the N_2 partial pressure and therefore the leak rate by five orders of magnitude, the initial leak in the CF flange of port `0080` is estimated to about $10^{-3}\,\mathrm{mbar}\,\ell/\mathrm{s}$. The RGA spectra just before and during the leak are shown in figure 5.12.

---

[10]*Sievert's law* is presented in detail in section 6.1, see equation 6.1.
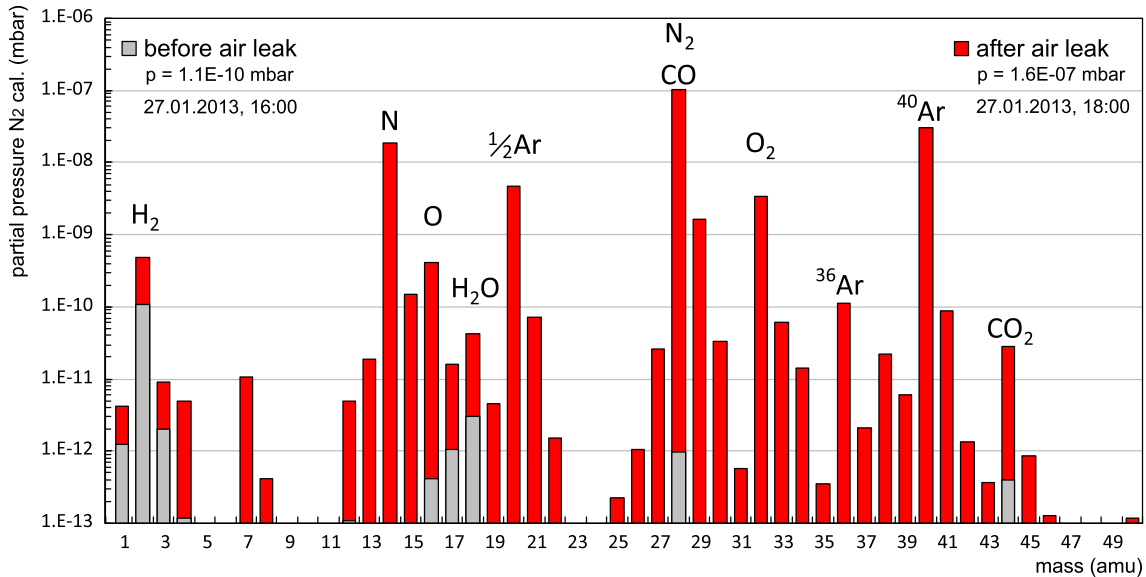
Figure 5.12: Impacted of the air leak on the vacuum performance of the main spectrometer. The residual gas spectra before (gray) and shortly after the air leak (red) at port 0080. Before the air leak the pressure was dominated by hydrogen (mass = 2 amu) during the leak nitrogen (mass = 28 amu), oxygen (mass = 32 amu) and argon (mass = 40 amu) not pumped by NEG are, as expected, the dominant residual gases.

5.4.5 Pumping Speed of the NEG Pump

For the activation of the NEG pump the manufacturer *SAES* recommends a temperature of $350\,^{\circ}$C for a duration of 24 hours [114]. Any reduction of either the temperature or the activation time can result in a reduced pumping speed and a reduced capacity for gas. The NEG activation performed during the main spectrometer bake-out campaign lasted for a period of 28 h at $300\,^{\circ}$C. The activation efficiencies for different temperatures and durations are shown in figure 6.2a. According to this plot a full activation at $300\,^{\circ}$C would have been reached only after 72 h [90]. In general, NEG pumping involves two different processes: the reversible process of binding hydrogen in the bulk material of the getter (physisorption) and the irreversible process of chemically binding active gases like N_2, O_2, H_2O, CO or CO_2 on the surface of the getter (chemisorption). During the activation process of the getter material the adsorbed hydrogen is removed by desorption. By using *Sievert's law*, a relation between temperature, pressure and hydrogen concentration inside the getter material (see equation 6.1) the degree of activation can be estimated. At the end of the maximum activation temperature of $300\,^{\circ}$C (435-RTP-5-3024) an equilibrium hydrogen pressure of $p_{3110}(H_2) = 1.9 \cdot 10^{-6}$ mbar was measured (see figure 5.13b). It is assumed that the pressure is dominated by hydrogen desorption from the NEG material and not from outgassing of the stainless steel vessel (see section 5.4.2 **case 3**). The hydrogen concentration of the KATRIN NEG pumps after the bake-out procedure is thus approximately $q = 1.36\,\text{mbar}\,\ell/\text{g}$.
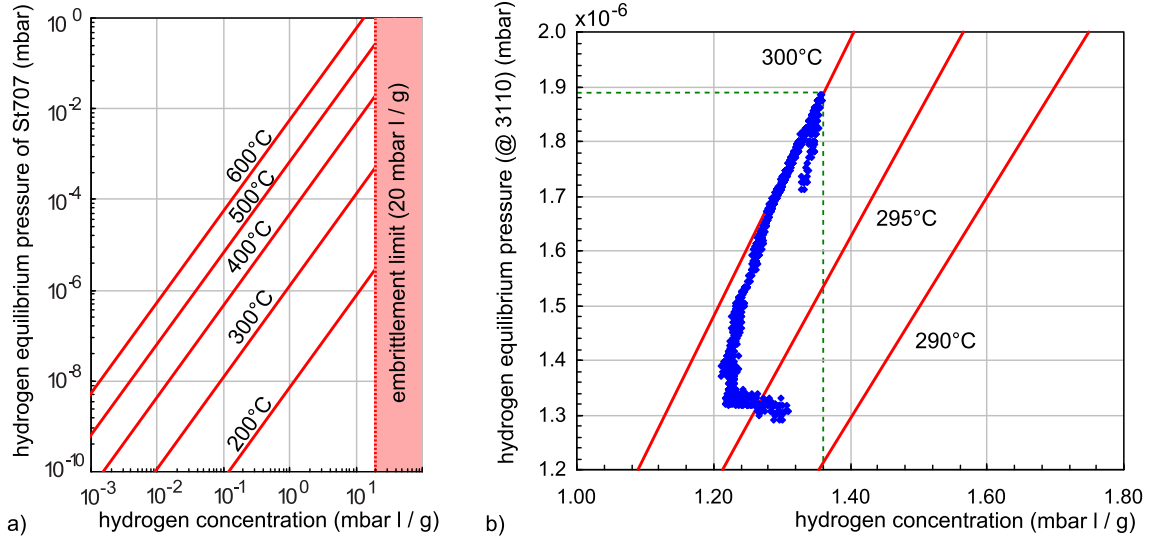
Figure 5.13: Hydrogen concentration in the NEG pumps (getter type: St707) against the equilibrium pressure in the recipient a) empirical values, based on measurements done by the manufacturer *SAES* [90]. **b)** pressure measurement at the main spectrometer during the bake-out procedure. The concentration is determined by *Sievert's law* (see equation 6.1) using the pressure gauge in pump port III (`432-RPI-3-3110`, corrected for hydrogen) and a temperature sensor at pump port III (`435-RTP-5-3024`). The measured data is plotted in blue, the red lines are calculated for fixed temperatures using *Sievert's law*.

Estimating the pumping speed of the NEG pump for hydrogen (method 1) by comparing the pressure in the main spectrometer volume with the pressure in the pump port III. Therefore equation 5.15 and equation 5.16 are approximated by:

$$p_{\text{MS}} = p_{0096} - p_0 \approx \frac{Q_{\text{out}}}{3 \cdot S_{\text{NEG}}} \cdot \frac{C_{\text{B}} + S_{\text{NEG}}}{C_{\text{B}}} \tag{5.25}$$

$$p_{\text{PP}} = p_{3110} = \frac{Q_{\text{out}}}{3 \cdot S_{\text{NEG}}} \tag{5.26}$$

The pressure in the recipient can be rewritten by combining equations 5.25 and 5.26:

$$p_{0096} = p_{3110} \cdot \frac{C_{\text{B}} + S_{\text{NEG}}}{C_{\text{B}}} + p_0 = a_1 \cdot p_{3110} + p_0 \tag{5.27}$$

$$S_{\text{NEG}} = (a_1 - 1) \cdot C_{\text{B}} \tag{5.28}$$

The linear fit of the pressure ratio p_{0096} versus p_{3110} is displayed in figure 5.10b. With hydrogen as the dominant residual gas, the offset pressure of `0096` is given by the y-axis intercept $p_0 = 9 \cdot 10^{-11}$ mbar. The slope of the straight line $a_1 = 3.00$ provides the pumping speed of the NEG pump:

$$S_{\text{NEG}} = (a_1 - 1) \cdot C_{\text{B}} = (3.00 - 1) \cdot 272\,000\,\ell/\text{s} = 545\,000\,\ell/\text{s} \tag{5.29}$$

$$S_{\text{MS}} \approx 3 \cdot S_{\text{NEG}}^{\text{eff}} = 3 \cdot S_{\text{NEG}} \cdot \frac{C_{\text{B}}}{C_{\text{B}} + S_{\text{NEG}}} =$$

$$= 3 \cdot S_{\text{NEG}} \cdot \frac{1}{a_1} = 3 \cdot C_{\text{B}} \cdot \frac{a_1 - 1}{a_1} = 545\,000\,\ell/\text{s} \tag{5.30}$$

According to equation 5.27 the start of NEG pumping can be recognized when the measured pressure values in the main spectrometer (p_{0096}) and in the pump port (p_{3110}) start to deviate. As seen in figure 5.14, the adsorption of hydrogen at the getter material in the main spectrometer started at a temperature of about 200 °C.
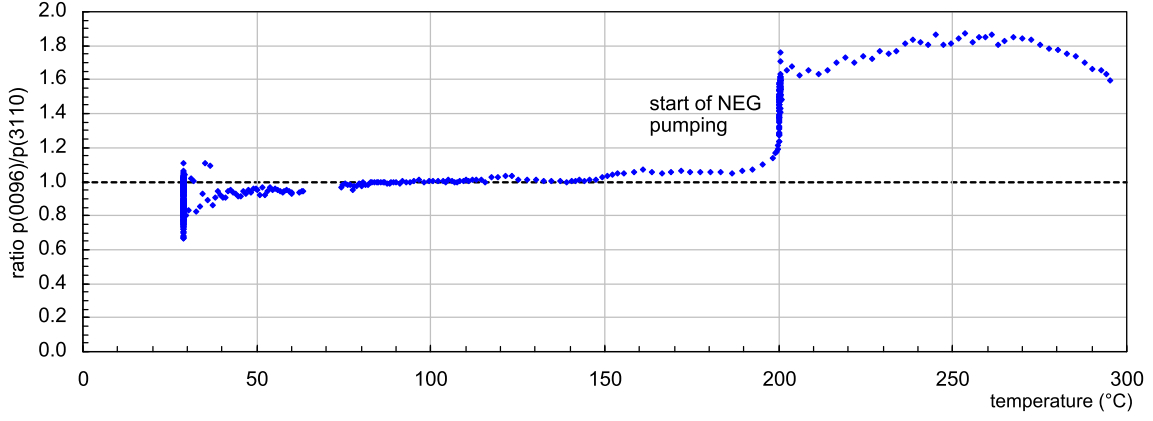
Figure 5.14: Start of the NEG activation. Ratio of the two extractor gauges p_{0096} and p_{3110}. The start of the deviation of the pressure readings indicates the start of the NEG pumping. Apparently the NEG strips started to pump already at a temperature of $200\,°\text{C}$.

Estimating the pumping speed of the NEG pump for hydrogen (method 2)   by comparing the pressure in the pump port III with and without TMPs (by closing the main gate valves). The measured data are listed in table 5.2. For this analysis the RGA peaks for hydrogen ($m = 2\,\text{amu}$) were used instead of of the absolute pressure p_{3110}, since noble gases are not pumped by the getter and the argon peak increases continuously during the measurement with all valves closed (see figure 5.15). Since the geometry of the location of the RGA is similar to the location of the extractor gauge in pump port III, and differences in the calibration are canceled in the ratio of the pressures, p_{3110} can be replaced by the RGA values without restriction.

If all valves to the TMPs are opened, the gas load Q follows the pressure difference between pump port and main spectrometer times the conductance of the baffle. With $p = Q/S$ the pressure in one pump port can be written as:

$$p_{\text{PP}}^{\text{open}} = \frac{(p_{\text{MS}} - p_{\text{PP}}^{\text{open}}) \cdot C_{\text{B}}}{S_{\text{NEG}} + 3 \cdot S_{\text{TMP}}} \tag{5.31}$$

$$\text{with} \quad p_{\text{MS}} = \frac{Q_{\text{out}}}{3 \cdot S_{\text{NEG}} \cdot \frac{C_{\text{B}}}{S_{\text{NEG}}+C_{\text{B}}} + 6 \cdot S_{\text{TMP}}} \tag{5.32}$$

$$\implies \quad p_{\text{PP}}^{\text{open}} = \frac{Q_{\text{out}} \cdot C_{\text{B}}}{(3 \cdot S_{\text{NEG}} \cdot \frac{C_{\text{B}}}{S_{\text{NEG}}+C_{\text{B}}} + 6 \cdot S_{\text{TMP}}) \cdot (S_{\text{NEG}} + 3 \cdot S_{\text{TMP}} + C_{\text{B}})}$$

If the main gate valves to the TMPs are closed ($S_{\text{TMP}} = 0$) the pressure in the pump port is dominated by the gas load of one third of the outgassing of the recipient and the pumping speed is reduced to the pumping speed of one NEG pump:

$$p_{\text{PP}}^{\text{closed}} = \frac{Q_{\text{out}}}{3 \cdot S_{\text{NEG}}} \tag{5.33}$$

Using these equations, the ratio of pressures with all valves closed and all valves open can be expressed as:

$$\frac{p_{\text{PP}}^{\text{closed}}}{p_{\text{PP}}^{\text{open}}} = \left(\frac{S_{\text{NEG}}}{S_{\text{NEG}} + C_{\text{B}}} + 2 \cdot \frac{S_{\text{TMP}}}{C_{\text{B}}} \right) \cdot \left(1 + 3 \cdot \frac{S_{\text{TMP}}}{S_{\text{NEG}}} + \frac{C_{\text{B}}}{S_{\text{NEG}}} \right), \tag{5.34}$$

by neglecting second order terms of S_{TMP}^2 (a 10^{-5} effect), the quadratic equation in S_{NEG} can be solved and provides a NEG pumping speed of

$$S_{\text{NEG}} = 231\,000\,\ell/\text{s} \tag{5.35}$$
$$S_{\text{MS}} \approx 3 \cdot S_{\text{NEG}}^{\text{eff}} = 3 \cdot S_{\text{NEG}} \cdot \frac{C_{\text{B}}}{C_{\text{B}} + S_{\text{NEG}}} = 375\,000\,\ell/\text{s}.$$

The measured pressure difference after closing all valves at one pump port was very small (see figure 5.15a). This is pointing towards higher NEG pumping speeds.
By comparing these two methods the effective pumping speed for hydrogen in the main spectrometer is in the range of

$$S_{\text{MS}}(\text{H}_2) \approx 375\,000 \ldots 545\,000\,\ell/\text{s} \tag{5.36}$$

This range is close to the simulated effective NEG pumping speed of $450\,000\,\ell/\text{s}$ (the simulations are including the effects of the LN2 cooled baffle system, see section 7.3.2). Hence, the calculations suggest three fully activated NEG pumps for hydrogen. This is an important milestone for the vacuum technology at KATRIN. However, these estimations of the pumping speed are afflicted with systematic uncertainties. The pressure measurements are carried out by two extractor gauges which have been calibrated for nitrogen (although the pressure in the spectrometer is dominated by hydrogen) by the manufacturer with an uncertainty of about 20% and the location of the gauges might lead to an additional pressure offset. Furthermore, there are uncertainties on the effective pumping speed value of the turbomolecular pump especially for gas molecules with a low mass like hydrogen. The value of the conductivity of the LN2 cooled baffle system is based on simulations (see figure 5.3). The air leak at port 0080 might also disturb the measurement more than estimated here.

Estimating the pumping speed of the NEG pump for nitrogen by using the slope of the linear fit in figure 5.16b during a small increase of the air leak (see figure 5.16a). The hydrogen contribution to the absolute pressure reading was determined by taking the mean pressures before the rise due to the leak rate, when the residual gas composition was still dominated by hydrogen. Before the linear fit the hydrogen contributions were subtracted. The evaluation of the data is based on the first method. Hence, equation 5.27 is adapted for N_2 ($m = 28\,\text{amu}$). Since the pumping speed of the TMPs can not be neglected, the total pumping speed is replacing S_{NEG}: $S_{\text{PP}}(\text{N}_2) = S_{\text{NEG}}(\text{N}_2) + 3 \cdot S_{\text{TMP}}(\text{N}_2)$ with the effective TMP pumping speed $S_{\text{TMP}}(\text{N}_2) = 1\,260\,\ell/\text{s}$.

$$p_{0096} = p_{3110} \cdot \frac{C_{\text{B}}(\text{N}_2) + S_{\text{PP}}(\text{N}_2)}{C_{\text{B}}(\text{N}_2)} + p_0 = a \cdot p_{3110} + p_0 \tag{5.37}$$

with the conductance of the baffle $C_{\text{B}}(\text{N}_2)$ calculated for N_2, using the mass dependence of the conductance:

$$C_{\text{B}}(\text{gas}) = C_{\text{B}}(H_2) \cdot \sqrt{\frac{M_{\text{H}_2}}{M_{\text{gas}}}} \tag{5.38}$$
$$C_{\text{B}}(\text{N}_2) = 73\,000\,\ell/\text{s}.$$

Table 5.2: Estimating the hydrogen pumping speed of the NEG pump (method 2).
Listed are the valve positions with the resulting pumping speeds for hydrogen as well as the partial pressures measured by the RGA in pump port III.

valve position	$\sum S_{\mathrm{TMP}}(H_2)$ in ℓ/s	mean H_2 pressure @ pump port III (mbar)
all valves open	10 000	$6.01 \cdot 10^{11} \pm 0.7 \cdot 10^{-13}$
pump port III close	5 000	$6.03 \cdot 10^{11} \pm 2.4 \cdot 10^{-13}$
pump port II close	5 000	$6.05 \cdot 10^{11} \pm 4.1 \cdot 10^{-13}$
all valves closed	0	$6.23 \cdot 10^{11} \pm 2.2 \cdot 10^{-13}$
one valve open at each port	3 333	$6.01 \cdot 10^{11} \pm 2.9 \cdot 10^{-13}$
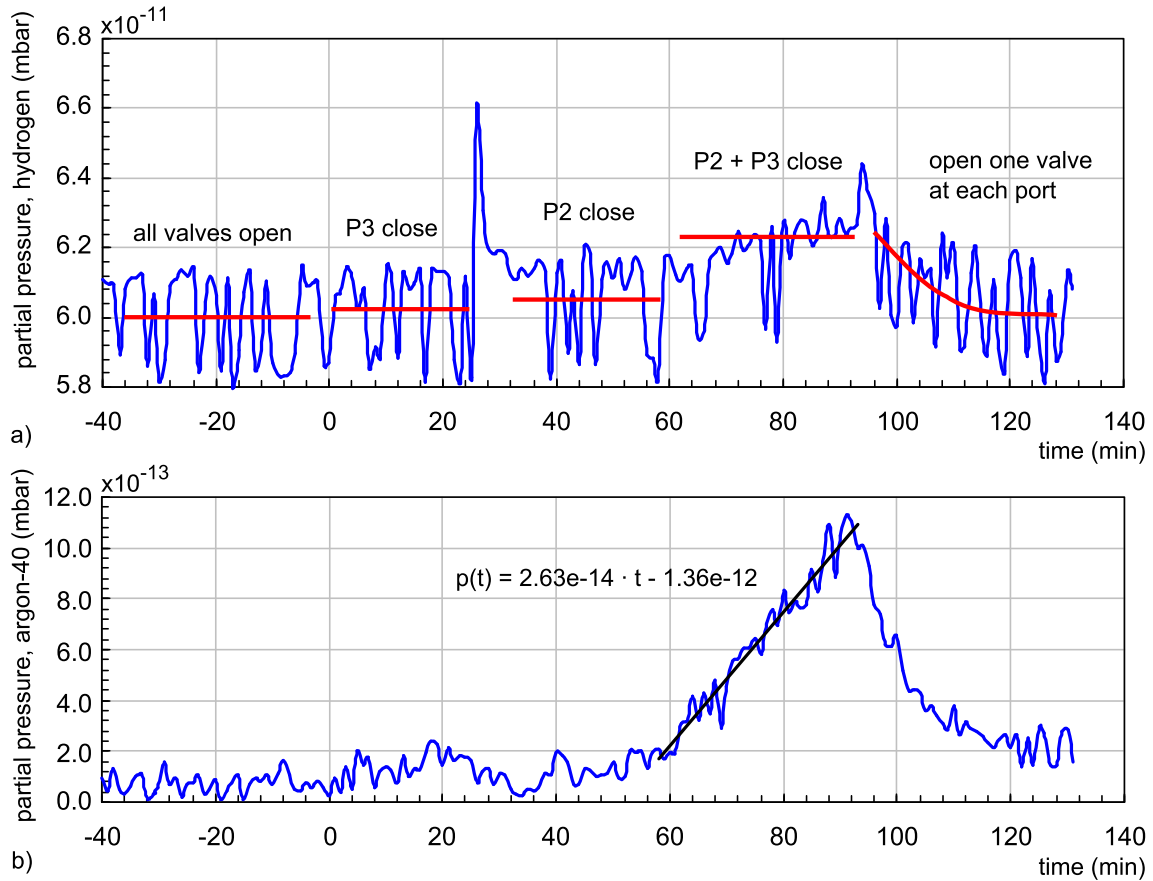
Figure 5.15: Estimating the hydrogen pumping speed of the NEG pump (method 2).
a) Development of the partial pressure of hydrogen. The valve positions are highlighted following table 5.2. **b)** Simultaneously the trend of the partial pressure of ^{40}Ar was monitored, too. Argon, as a noble gas, is not pumped by the getter material. When all valves are closed the partial pressure of argon is rising, due to the leakage at port 0080. By fitting a straight line to the measured data the impacted of the leakage can be estimated (see section 5.4.4).
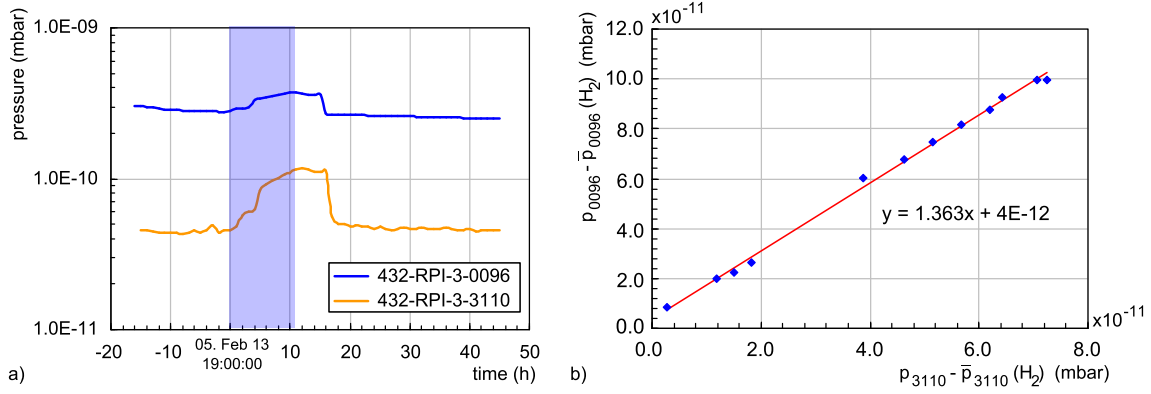
Figure 5.16: Determine the pumping speed of the NEG pumps for nitrogen. a) Small increase of pressure after 'fixing' the air leak (failure of scroll pump). **b)** Pressure ratio of the two extractor gauges during this small increase of pressure. The slope of the linear fit ($a = 1.363$) is used to estimate the NEG pumping speed for nitrogen. The contribution of hydrogen has been subtracted by using the average pressure of the respective gauge before the leak rate increased: $\bar{p}_{0096}(H_2) = 2.71 \cdot 10^{-10}$ mbar and $\bar{p}_{3110}(H_2) = 4.50 \cdot 10^{-11}$ mbar.

With the slope $a = 1.363$ from the linear fit in figure 5.16 the results are:

$$\begin{aligned} S_{PP} &= (a-1) \cdot C_B(N_2) = 26\,500\,\ell/s \quad\quad (5.39) \\ S_{NEG} &= 22\,700\,\ell/s \end{aligned}$$

The total effective pumping speed for nitrogen in the main spectrometer is thus reduced by the conductance of the baffle and the absence of TMPs in the central pump port:

$$S_{MS} \approx 56\,000\,\ell/s. \quad\quad (5.40)$$

The expected pumping speed for $S_{NEG}(N_2)$ can be estimated by using the the simulated pumping speed for hydrogen, multiplied by 15% (mass dependence of the pumping speed based on measurements performed by the manufacturer *SAES* [90] [115]): $S_{NEG}(N_2) = 350\,000\,\ell/s \cdot 0.15 \approx 50\,000\,\ell/s$. The simulated value is twice the amount measured. The measured effective pumping speed for the main spectrometer is 2/3 of the simultated value of $S_{MS}(N_2) = 92\,000\,\ell/s$.

The pumping speed of the NEG pump depends on the surface coverage and is defined by two competing effects of surface adsorption and diffusion into the bulk material of the getter [116]. In the case of hydrogen the diffusion (even at room temperature) is important for the NEG pumping speed. For nitrogen the diffusion in the bulk material is only possible at high temperatures. Hence, the pumping speed for N_2 drops rapidly with an increasing saturation of the getter material [90]. The lower pumping speed for nitrogen can be explained with a higher nitrogen coverage on the surface of the getter due to the insufficient activation temperature and duration of the process.

5.4.6 Estimating the Outgassing Rate

With equation 5.25 and 5.26 two equivalent methods exist to determine the outgassing rate per cm^2 for H_2 from the values measured by the two extractor gauges:

$$j_1 = \frac{Q_{\text{out}}}{A} = (p_{0096} - p_0) \cdot 3 \cdot S_{\text{T}} \cdot \frac{1}{A} \tag{5.41}$$

$$j_2 = \frac{Q_{\text{out}}}{A} = p_{3110} \cdot S_{\text{NEG}} \cdot \frac{1}{A} \tag{5.42}$$

The inner surface area of the stainless steel vessel and the additional surface of the inner electrode system is $A = 1\,150\,\text{m}^2$. The pressure values inside the main spectrometer and in pump port III were both dominated by hydrogen[11]. Hence, the gas correction factor for hydrogen $K_{\text{gas}=H_2} = 0.46$ is used:

$$p_{\text{MS}} = (p_{0096} - p_0) = 3.3 \cdot 10^{-10}\,\text{mbar} \tag{5.43}$$

$$p_{\text{PP}} = p_{3110} = 1.1 \cdot 10^{-10}\,\text{mbar} \tag{5.44}$$

Applying the range of the NEG pumping speed given in equation 5.36, the outgassing rate of hydrogen is in the range of

$$j(H_2) \approx (6.6 \dots 16) \cdot 10^{-12}\,\text{mbar}\,\ell/\text{s}\,\text{cm}^2, \tag{5.45}$$

assuming that the stainless steel vessel is the main source of hydrogen. Such an outgassing rate would be one order of magnitude higher than expected. Many previous measurements with the test cylinder, the pre-spectrometer and during the first commissioning of the main spectrometer (2007) have reached outgassing rates in the oder of $1 \cdot 10^{-12}\,\text{mbar}\,\ell/\text{s}\,\text{cm}^2$ or better. To explain this behavior two scenarios can be envisioned: The activation process of the NEG material could be insufficient or an additional hydrogen source exists that has not yet been identified. Possible source can be associated the inner wire electrode system (e.g. ceramics) or LN2 cooled baffle system (e.g. copper sheets). Further material tests have thus to be performed. Therefore a special UHV test setup [117] was built with the sole purpose to determine the outgassing rate of different materials.

5.5 Conclusion

In order to reach a pressure regime of about $p \approx 10^{-11}$ mbar in a very large stainless steel recipient clean work, metallic seals and an appropriate pumping scheme are required [84]. To achieve an UHV regime in a reasonable time, an optimized bake-out procedure is needed, and the following processes have to be considered: The rise in temperature accelerates the desorption processes. Water and other molecules sticking to the inner surface of the vessel are removed. After a successful bake-out cycle the pressure inside the recipient is dominated by hydrogen diffusing from the bulk material of the vessel walls. However, the outgassing behavior of materials both in theory and experiment is a complex subject, strongly depending on the materials used in the vacuum environment [107].

---

[11]neglecting the small contribution of nitrogen from the air leak

To reduce the outgassing rate of hydrogen in the main spectrometer an optimized bake-out procedure was determined at the test recipient. Build by the same manufacture (*MAN DWE GmbH*) and same raw material (stainless steel 316LN), the test recipient is an ideal experimental setup for comparative measurements. A series of bake-out cycles was executed [68] with the main objective to reduce the hydrogen concentration on the surface by desorption, without replenishing it by hydrogen atoms diffusing from the bulk material of the vessel. By comparing the resulting outgassing rates after different bake-out cycles, a minimal hydrogen outgassing rate of about $j_{\mathrm{H}_2} = 4.8 \cdot 10^{-13}\,\mathrm{mbar}\,\ell/\mathrm{s}\,\mathrm{cm}^2$ was measured.

Based on the results of these test recipient a bake-out cycle for the main spectrometer was implemented. The temperature of the spectrometer has to be slowly ramped up to $200\,^\circ\mathrm{C}$ to accelerate the desorption processes of adsorbed water molecules from the inner surfaces of the vessel. After the activation of NEG pumps at $350\,^\circ\mathrm{C}$ by heat radiation the temperature has to be decreased to $150\,^\circ\mathrm{C}$. This step temperature 'freezes' the hydrogen diffusion rate before the spectrometer is cooled down to room temperature and stabilize at $20\,^\circ\mathrm{C}$.

The main spectrometer bake-out cycle with fully installed inner electrode system as final step before the subsequent long-term commissioning measurements was performed in winter 2012/2013 [112]. The entire procedure lasted about two months. After a series of short-circuits at the inner wire electrode system developed during the ramping of the temperature above $200\,^\circ\mathrm{C}$, the maximum temperature was constrained to $300\,^\circ\mathrm{C}$. Hence, it was expected that the NEG pumps were not fully activated. However, first tests have indicated a close to full pumping speed for hydrogen. The saturation of the getter material estimated with *Sievert's law* seems rather high and the remaining capacity was unknown. During the cool-down to room temperature a leak occurred at one of the DN250 CF ports on top of the main spectrometer. The leak was fixed temporarily with a differentially-pumped vacuum sleeve with no further impact for the scheduled commissioning measurements.

The outgassing rate of hydrogen seems to be one order of magnitude higher than expected. The source has not been identified yet and further material tests need to be implemented. The residual gas analyses yield hydrogen as dominant gas, with a composition being completed by a few percent of water, CO and CO_2 (see figure 5.9). The vacuum analyses also indicate a very clean vessel. This is a direct result of the careful handling of all parts and strictly obeyed cleaning procedures for all parts installed in the recipient. Despite the air leak the pressure inside the main spectrometer reached a level of $p_{\mathrm{H}_2} = 3.3 \cdot 10^{-10}\,\mathrm{mbar}$. This value is comparable to the vacuum conditions during the measurements at the pre-spectrometer test setup. Until the leak at port 0080 is repaired, the spectrometer has to be operated with the vacuum sleeve which directly influences the stability of the pressure inside the vessel. For the background measurements presented in this work (for more details see chapter 7), the pressure level that has been achieved after the bake-out procedure suffices. Because of the short-circuits the inner wire electrode had to be operated as a single layer system. Nevertheless, even in this case it is possible to configure a working MAC-E filter setup yet with reduced background reduction factors. At present, the reduction of muon-induced background is a factor of 20 less than anticipated, but reducing the background reduction factor of the system for secondary electrons [113].

During a maintenance campaign in winter 2013/2014 several repairs and upgrades of the main spectrometer vacuum system are foreseen. The focus lies on the commissioning and optimizing of the system in order to qualify the main spectrometer for the neutrino mass measurement. The leak at port 0080 will be repaired by replacing the CF gasket with a special seal designed by *HTMS* for low leakage at low pressures. All seals that cannot be repaired after a bake-out cycle will additionally be replaced by these special gaskets. Repair options concerning the inner wire electrode system have been discussed in [113], prepared and carefully reviewed and will be implemented in a 2015 upgrade period. To protect the inner electrode system during future bake-out procedures, the maximum bake-ot temperature will be constrained to $< 200\,°C$. This may be adequate to clean the vacuum surfaces [69] but in any case insufficient to activate the NEG pumps [118] [90], so the activation process will be by Ohmic losses when feeding a current through the NEG strips.

In conclusion, the work of this thesis in vacuum technology has been instrumental in obtaining excellent UHV conditions for long-term operation of the main spectrometer, an indispensable prerequisite for successful measurements.

6 Non-evaporable Getter (NEG) Pump

This chapter gives an overview of the basic concept and the ongoing upgrade works of the non-evaporable getter (NEG) pump of the main spectrometer. After a detailed introduction of the working principle of getter material, the original design of the main spectrometer NEG pump is presented. This chapter focuses however primarily on the development of the concept of heating the getter strips by the passage of an electric current. A first prototype was built up from scratch and served as a feasibility study. The design and the implementation of this prototype is illustrated as well as the results of corresponding simulations and calculations in the framework of measurements at the KATRIN test recipient. The transfer from a second prototype to its implementation at the main spectrometer is presented, as well. The main objective of the second prototype was to refine the new design. Hence, this second prototype was developed as close as possible to the real NEG pump to allow a subsequent scaling. The measurements focused on the validation of different materials and approaches such as the electrical insulation of single NEG strips. The chapter concludes with a concept of interconnecting the NEG strips, the specification of the power input and an estimation of the electrical consumption of the upgraded main spectrometer NEG pump.

6.1 Concept and Design of the KATRIN NEG Pump

Getter materials accumulate gases by binding molecules at their surface (physisorption) or by absorbing gases into the bulk material by a chemical reaction (chemisorption). The composition of the non-evaporable getter material by $SAES$[1] (brand name St707) was crosschecked with a spectral analysis (see figure 6.1a) to include zirconium (70%), vanadium (24.6%) and iron (5.4%). As shown in figure 6.1b) the alloy forms a porous substance with a large specific surface area ($1\,500\,cm^2/g$). The NEG material is fixed as a powder on constantan (Cu 55%, Ni 45%) strips by compression bonding without chemical binders.

Getter materials can hold gases at their surface. Hence, these form an unavoidable passivating layer of oxides and nitrides when in contact with air. For storage or handling the NEG strips the manufacturer recommends to use a protective argon atmosphere. Friction (e.g. due to cutting the strips) or an exposure in air to temperature over $200\,°C$ will ignite the material. After the NEG strips are placed inside the recipient, the surface needs to be regenerated (decontamination) from physically bound gases. This activation process is done by baking the NEG material under a vacuum ($< 10^{-3}\,mbar$) or an inert gas atmosphere (like argon). At sufficiently high

---

[1]SAES Getters S.p.A., Viale Italia 77, 20020 Lainate (Milan), Italy
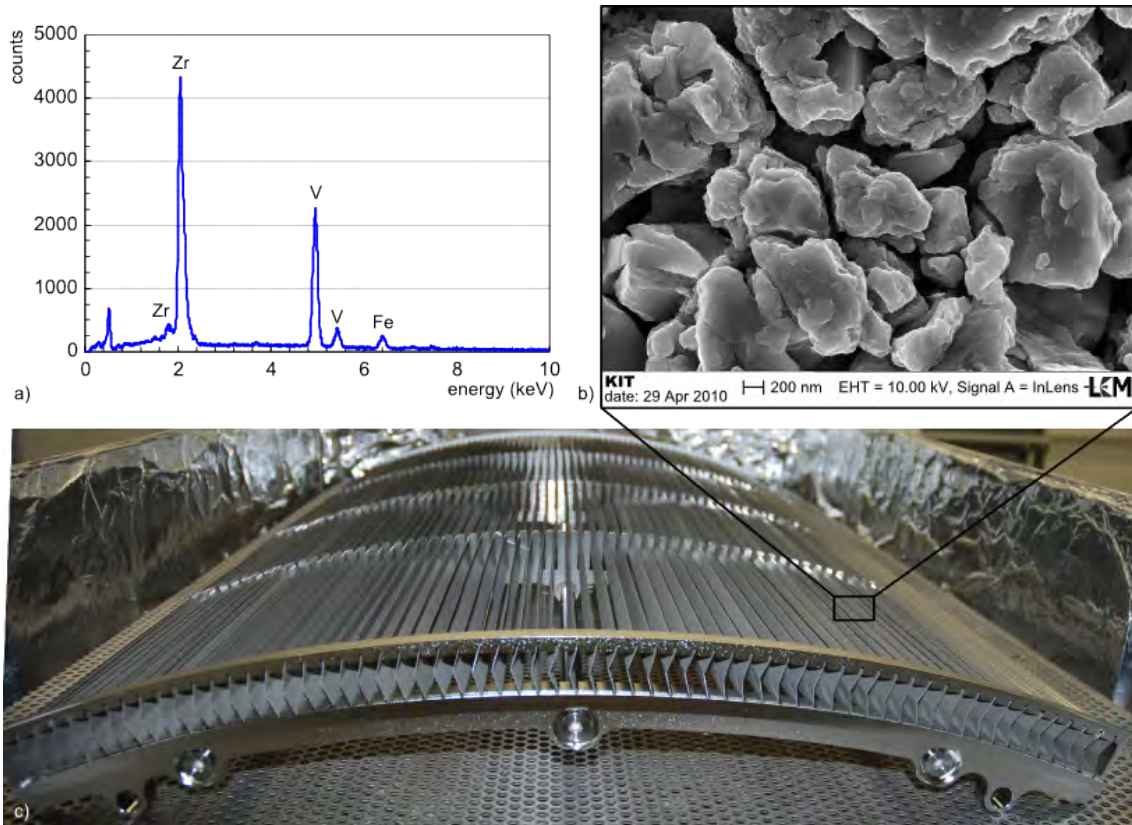
Figure 6.1: Composition of the NEG material and one module of the main spectrometer NEG pump. a) Spectral analysis[a] of the NEG material, the constituent elements are clearly visible. **b)** NEG material imaged by a scanning electron microscope (SEM). **c)** Picture of one main spectrometer NEG module. One module is holding 63 getter strips. In each of the three pump ports 16 of these modules were installed.

---

[a]Settings: Duration 199.2 s, accelerating voltage 15.0 kV, falloff angle: 34.4°. The scans were performed by the Laboratory for Electron Microscopy at the KIT.
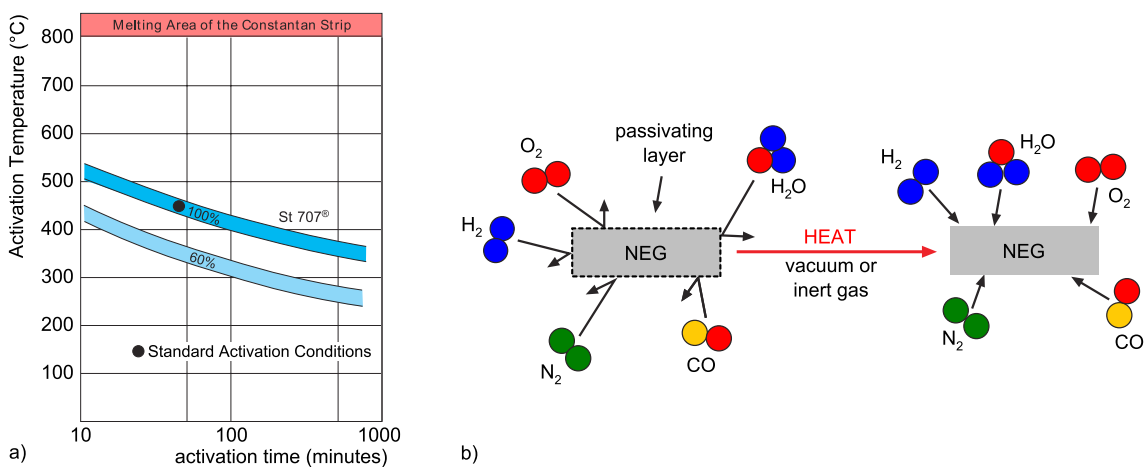
Figure 6.2: Activating NEG materials. a) Activation efficiency for St707 alloy. **b)** Schematic representation of the activation process for NEG material.

temperatures the protective layer dissolves due to outgassing or diffusion into the bulk material (see figure 6.2b). After the oxide and nitride layers have migrated into the bulk material of the getter, the surface regains its ability to bind gases. The duration of the activation process depends on the temperature (see figure 6.2a). The optimum conditions to achieve a full activation of the getter are temperatures of $(450 \pm 50)\,°\text{C}$ for a duration of about 30 min. However, these conditions are not mandatory. Lower heating temperatures of $250\,°\text{C}$ to $400\,°\text{C}$ require a longer period of time (from hours to days), to ensure full activation of the getter material. At even lower temperatures ($< 250°\text{C}$) a full activation of the NEG strips can not be reached [118] and a partial passivating layer remains on the getter surface. Hence, the sorption ability of the material will be reduced.

Once the getter material is activated it continually accumulates gases. The following list will differentiate between the different forms of sorption used by the getter material [84]:

- chemically active gases like H_2O, CO, CO_2, O_2 and N_2 react with the surface of the NEG material. In several steps the gases are dissociated. This process takes place even at room temperature or in even weaker form at lower temperatures. During a reactivation process, the produced ions (carbides, oxides and nitrides) diffuse from the surface into the bulk material of the getter. This process of chemisorbtion requires higher temperatures and is irreversible. Once sorbed, oxygen, carbon or nitrogen atoms form a strong chemical bond within the getter alloy. Hence, a reactivation is only possible until the complete saturation of the NEG material.

- chemically active gases (especially efficient for hydrogen and its isotopes) dissolve physically within the getter volume, even below room temperature. The amount of hydrogen in the volume of the getter is in a temperature-dependent equilibrium with the hydrogen partial pressure in the recipient given by *Sievert's law*, see equation 6.1. At high hydrogen concentrations, metal hydrides form and the getter material is permanently damaged by hydrogen embrittlement. Due to its high diffusability, hydrogen can move into the bulk material, thus the getter material provides a higher capacity for hydrogen as compared to other gas types between subsequent activations. The process of binding hydrogen is reversible by reactivation of the getter material.

- chemically passive or inactive gases do not react with the NEG material. Hence, hydrocarbons (like methane) and noble gases are not pumped. However, methane can react with the getter if the bonds between carbon and hydrogen are cracked near hot surfaces (e.g. filaments of gauge heads). The produced hydrogen and carbides are adsorbed by the getter material. Long-chain hydrocarbons are physisorbed to the getter surface. Getter materials can not bind noble gases. This feature can be used to purify noble gases with hot NEG cartridges.

  These filter properties of NEG material were used successfully during a gasket replacement at the main spectrometer. To vent the spectrometer, a volume of $1\,400\,\text{m}^3$ of argon 6.0^2 was purified to a 9.0 level by an *SAES* MonoTorr

---

[2]Purity is commonly expressed as a two digit number. For example, helium with a purity of

PS4-MT50. The gas purifier is based on a heated getter cartridge providing sub-ppb impurity removal. After pump down the main spectrometer NEG pumps were still activated.

During the activation process oxides and other compounds move into the bulk material by diffusion, thus freeing the surface again for further pumping. The activation procedure can be repeated between $20 - 50$ times, before the maximum capacity of the getter is reached, slowly reducing the pumping speed after each activation. Since effective diffusion of these compounds into the bulk material starts only at higher temperatures, a reduction of the pumping speed for active gases drops before the pumping speed for hydrogen is reduced. The binding of hydrogen is weaker and reversible. When heated to high temperatures hydrogen and its isotopes are released again. A given concentration of hydrogen inside the getter alloy corresponds to an equilibrium partial pressure of hydrogen, which is strongly dependent on temperature. This dependence is described by *Sieverts' Law*, given by the following expression:

$$\log(p_{\mathrm{H}}) = A + 2 \cdot \log(q_{\mathrm{H}}) - \frac{B}{T} \tag{6.1}$$

where q_{H} represents the concentration of hydrogen in the volume of the getter in mbar ℓ/g of alloy, p_{H} denotes the equilibrium partial hydrogen pressure in mbar, T is the temperature of the getter in K, and with the two material dependent constants $A = 4.67$ and $B = 6\,116$ for the St707 alloy being given by the manufacturer. The critical accumulation of hydrogen lies beyond a value of > 25 mbar ℓ/g. At rather high hydrogen concentrations the crystalline structure of the getter changes which causes an embrittlement of the material. The getter fractures, and in extreme cases can disintegrate into fine powder.

The design of the main spectrometer NEG pumps is based on Monte Carlo simulations done with ProVac3D [119] developed by Dr. X. Luo (ITEP, KIT). In a comparative study different geometric arrangements of the NEG material were simulated, and evaluated by their pumping and transmission probabilities [120]. The main constraint on the design was that the NEG pumps has to fit into the pump ports of the spectrometer. The chosen design combines an excellent vacuum performance with a simple mountability and low costs by using only commercially available standard getter strips. In a small-scale prototype the design of the NEG pump was successfully implemented in the pre-spectrometer test setup (see figure 3.4).

Figure 6.3a shows one of three getter holding structures of the main spectrometer. Each pump port is equipped with 1 006 NEG strips divided to 16 modules. One module (see figure 6.3b) holds 63 strips. Hence, the total amount of NEG material in the main spectrometer sums up to 3 018 m. Each 1 m long strip is bent by 20° to increase its stability. The single NEG strips are locked in their module. A module consists of five stainless steel combs connected by three rods. The modules at the bottom of the NEG pumps contain one strip less to allow the easy installation of the last piece of the pump.

To generate the required activation temperature of the NEG pumps the heat radiation of the surrounding pump port is used. To prevent tensions due to temperature

---

99.9996% would be described as helium 5.6 with the 5 representing the number of nines, while the 6 represents the first digit following the nines.

gradients between the vessel and the pump ports, the main spectrometer is designed to withstand a bake-out procedure up to 350 °C (see chapter 5). During the commissioning phase in winter 2012/2013, the bake-out procedure was stopped at 300 °C to avoid further damage of the inner wire electrode system (see section 5.4.1), and for future bake-out cycles the temperature is constrained to maximal 200 °C. A full activation of the getter material by exploiting the heat radiation will not be possible anymore. Measurements at a NEG test setup [67] confirmed the manufacturer's information that temperature below 250 °C are insufficient for a proper activation of the getter material [118]. A new concept of activating the NEG pump without reaching the critical temperature of 200 °C had to be developed within this thesis.
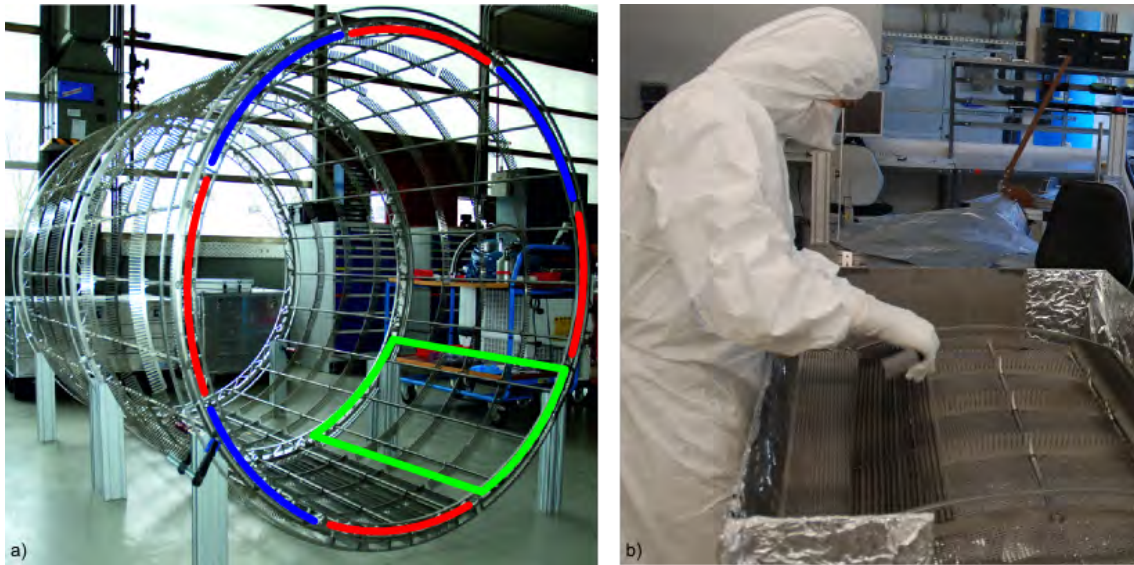
Figure 6.3: The main spectrometer NEG pump. a) The NEG module holding structure. The blue and red lines mark the single modules, whereas the green lines mark the confines of one module. **b)** The author assembling one module. The highly flammable getter material was handled with care in a tank flooded with argon forming an inert gas atmosphere. To prevent contamination of the material and injuries due to sharp edges the use of rubber finger cots and gloves is suggested.

6.2 New Concept of Electrical Heating and Prototype Development

This work proposes the activation of the NEG pump by passage of current through the constantan base material of the getter strips. The concept of activating getter material by electrical heating is not fundamentally new, however the size of the KATRIN NEG pump is unique [115]. The present work describes the path of an electrically heated NEG pump from the idea through a first feasibility study and prototyping to scaling up the model and its implementation in the main spectrometer. Apart from the energy consumption and the electrical connections, the non-conductive mounting of the single getter strips turned out to be a major obstacle. Different materials (like ceramic or a titanium dioxide coating) planned to use were tested and rated for their outgassing behavior [117], insulation resistance and hardiness. A cornerstone in these design considerations was to maintain the

high vacuum standards of the KATRIN. After calculating and simulating energy consumption values a pattern for interconnecting the strips was designed to achieve an even distribution of the generated heat over the surface of the NEG pump.

6.2.1 Design and Simulation of the First NEG Pump Prototype

The first prototype was loosely based on one module of the main spectrometer NEG pump. The purpose of this feasibility study was to prove that the concept of heating the getter strips by passing a electric current was viable indeed. The prototype has allowed to evaluate the heat distribution simulations and calculations by providing actual measured input data. By using the same getter strips[3] as installed in main spectrometer, the results of this study allow a high degree of comparability and transferability to the full-scale NEG pump.

All measurements were performed in the test recipient. As a small prototype of the main spectrometer, the test recipient is an ideal environment for feasibility studies. The overall experimental setup is describe in section 5.3.1. A full vacuum flow chart of the test recipient can be found in figure A.8 in the appendix A.

A stainless steel frame forms the holding structure of the prototype. Four ceramic pipes, each with ten 10 mm deep slits, hold the NEG strips in place and provide the necessary electrical and thermal insulation (see figure 6.4b). Each of the ten *SAES* St707 NEG strips are pierced on both ends to be connected with a stainless steel screw put in a copper jacket to ensure good conductivity (see figure 6.6b). A picture of the mounted NEG pump in the test recipient and a technical drawing (cross section) of the prototype is shown in figure 6.4.
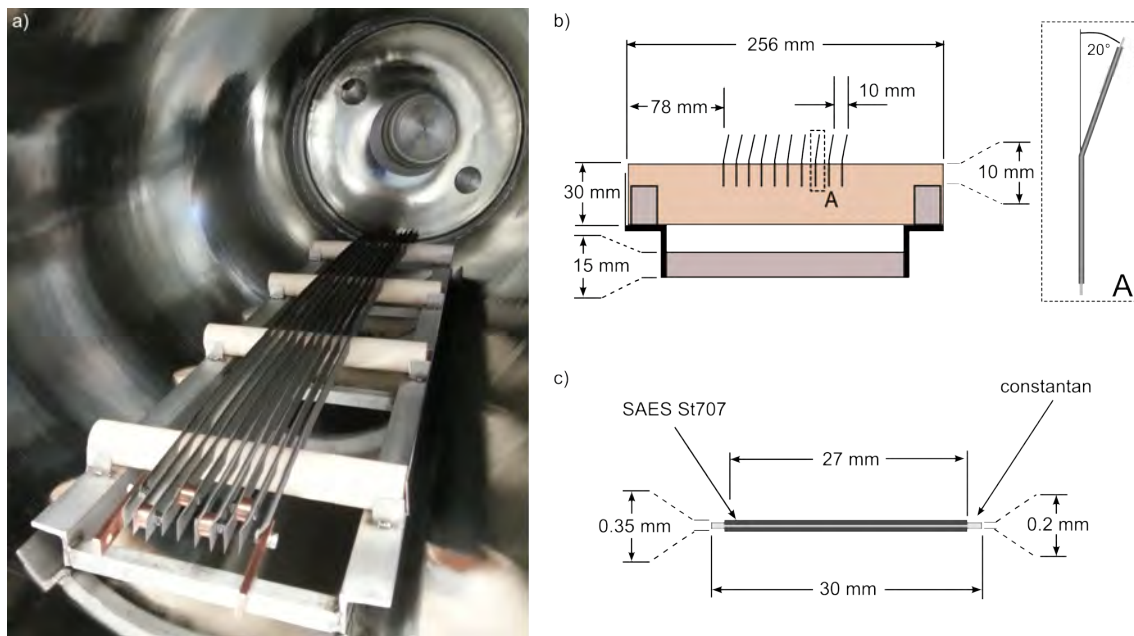
Figure 6.4: Picture and technical drawing of the first NEG pump prototype. a) The NEG pump prototype mounted in the test recipient. **b)** Technical drawing of the prototype and **c)** a cross section of a St707 NEG strip. Due to the production process the NEG material does not cover the whole surface of the strip.

---

[3]remaining stocks from the main spectrometer NEG pump assembly.

As a current feed through a DN16 CF-flange with two copper pins each with a diameter of 2.4 mm (*allectra[4]* type: 264-24CU5K-2-C16) was connected on a DN40 CF adapter flange and fully insulated with ceramic beads. The NEG pump was connected in the recipient by two 3 mm strong non-insulated copper supply lines and three ceramic blocks support the connection. As a power supply one of the PSUs of the KATRIN air coil system (*delta electronica* SM 45-70D) was used. One PT100 sensor (embedded in ceramic) was installed below the center of the prototype, see figure 6.6a). After integrating the sensor in the test recipient slow control system, the operator is enabled to monitor the temperature of the NEG pump.

After *Joule's first law*, the generated heat is proportional to the square of the current $P = RI^2$. The resistance of a 1 m long getter strip was determined by a series of measurements to $R = (0.082 \pm 0.001)\,\Omega/\text{m}$ [121]. This value is in good agreement with the literature value of constantan[5], the base material of the NEG strips.

In vacuum, the exchange of thermal energy is restricted to thermal radiation if the thermal conductivity is neglected. The *Stefan-Boltzmann law* describes the power radiated from a hot body in terms of its temperature:

$$P = \epsilon \sigma A T^4, \tag{6.2}$$

with the emissivity factor $\epsilon = 0.65$ (material constant based on manufacturer information [115]), the *Stefan-Boltzmann constant* σ and the radiating surface area A. This area must be corrected by the *view factor* $F_{A \to B}$, the proportion of the radiation which leaves surface A and strikes surface B. The power losses of self-viewing surfaces are neglected (surface-to-surface radiation). Hence, only surfaces of the NEG pump directly looking at the recipient contribute to the effective radiating area $A_{\text{eff}} = A_{\text{NEG}} \cdot F_{\text{NEG} \to \text{recipient}} = 0.15\,\text{m}^2$, with the view factor $F_{\text{NEG} \to \text{recipient}} = 0.248$. A detailed derivation this factor can be found in [121].

After the first law of thermodynamics the thermal energy $Q = m \cdot c_V \cdot \Delta T$ in a closed system is conserved. The rate of the heat flow $\dot{Q}$ between the NEG pump and the recipient is defined by the transferred heat dQ during a time interval dt:

$$\dot{Q} = \frac{dQ}{dt} = m \cdot c_V \cdot \frac{dT}{dt}, \tag{6.3}$$

with the mass of one 1 m long getter strip $m = m_{\text{NEG}} + m_{\text{constantan}} = 20\,\text{g/m} + 8.9\,\text{g/cm}^3 \cdot 30\,\text{mm} \cdot 0.2\,\text{mm} = 73\,\text{g/m}$ and the specific heat capacity $c_V = 410\,\text{JK}^{-1}\text{kg}^{-1}$ of constantan.

The prototype consists of ten NEG strips, which are electrically connected in series. The following differential equation is used to characterize the behavior of the systems:

$$\frac{dQ}{dt} = P_{\text{Joule heating}} - P_{\text{radiation}}(t) \tag{6.4}$$

$$10 \cdot m \cdot c_V \frac{dT(t)_{\text{NEG}}}{dt} = 10 \cdot R \cdot I^2 - \epsilon \sigma A_{\text{eff}}(T(t)_{\text{NEG}}^4 - T_{\text{recipient}}^4). \tag{6.5}$$

---

[4]Allectra GmbH, Traubeneichenstraße 62-66, D-16567 Schönfliess

[5]The electrical resistivity of constantan at room temperature is $R_{\text{constantan}} = 5 \cdot 10^{-7}\,\Omega\text{m}$ with a cross-section area of a getter strip of $A = 0.02\,\text{mm} \cdot 3\,\text{cm} = 6 \cdot 10^{-6}\,\text{m}^2$ the resistance per meter follows as $R = 0.083\,\Omega/\text{m}$

In order to validate the prototype under conditions as used later at the main spectrometer, the test recipient was heated up to $T_{\text{recipient}} = 200\,^{\circ}\text{C}$. This temperature was held constant during the whole activation process of the NEG pump. By solving differential equation 6.5 for an equilibrium temperature ($\mathrm{d}Q/\mathrm{d}t = 0$) at the getter strips of about $T_{\text{NEG}} = 345\,^{\circ}\text{C}$, a heating current of $I = 26\,\text{A}$ is required.

To estimate the time characteristic the differential equation 6.5 was solved with the *Euler method* (using a step size of $h = 0.05$). Additionally the problem was simulated with *Quickfield*[6]. The results of the numerical solution of differential equation 6.5 and the simulation are illustrated in figure 6.5. To obtain a more realistic impression of the temperature distribution on the surface of the NEG pump the prototype was additionally simulated using *COMSOL Multiphysics*[7], see figure 6.6.

6.2.2 Measurements at the Test Recipient

The main requirements with regard to the prototype measurements is to recreate the conditions in the main spectrometer. Therefore the measurement plan foresees a bake-out phase of up to $200\,^{\circ}\text{C}$ for the vacuum recipient. The following list summarizes the steps to be executed for all NEG prototype measurements:

1. Close the test recipient and evacuate the system.

2. Determine the pre bake-out residual gas composition of the test recipient. This step ensures a leak-proof system, before starting the bake-out phase. The RGA scan is used to determine if air peaks at $m = 28\,\text{amu}$ and $m = 32\,\text{amu}$ are in the system. These peaks must be in a ratio of 4 to 1 to verify that the peaks are real. In case of air leaks the measurement must be aborted.

3. Ramp the temperature of the test recipient to $T_{\text{recipient}} = 200\,^{\circ}\text{C}$ and hold it for about $48\,\text{h}$. A rise in temperature accelerates the desorption rate of adsorbed water molecules. The recipient is cleaned and the vacuum conditions are improved.

4. Start the electrical activation of the NEG pump for about $24\,\text{h}$ by choosing a current to reach about $T_{\text{NEG}} = 350\,^{\circ}\text{C}$. During the process stabilize the temperature of the test recipient at $T_{\text{recipient}} \approx 200\,^{\circ}\text{C}$. Measure the voltage across the resistance of the NEG pump periodically: a short-circuit in the NEG pump would change its specific resistance.

5. After the activation switch off the power supply of the NEG pump as well as of the heating tapes of the test recipient to let the whole system cool down.

6. Determine the post bake-out residual gas composition, while the temperature of the recipient is stabilized at $T_{\text{recipient}} = 20\,^{\circ}\text{C}$.

---

[6] *Quickfield* is a finite element analysis software package running on Windows platforms. Developed and distributed by *Tera Analysis Ltd.*,Knasterhovvej 21, DK-5700 Svendborg, Denmark

[7] *COMSOL Multiphysics* is a finite element analysis, solver and Simulation software package for various physics and engineering applications. Developed and distributed by *COMSOL, Inc.*, 1 New England Executive Park, Suite 350, Burlington, MA 01803, USA
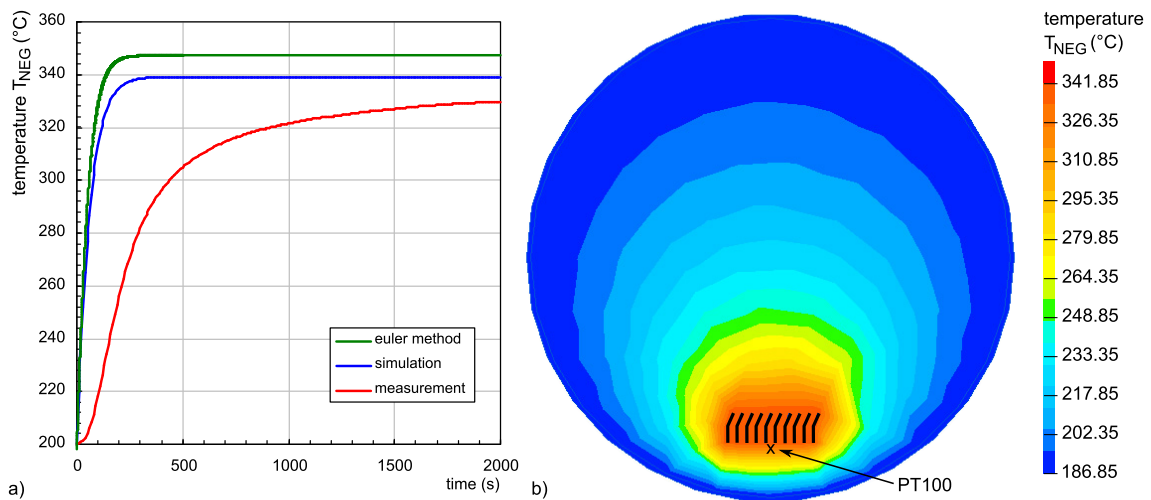
Figure 6.5: First NEG pump Prototype a) Temperature development over time: presented are the numerical solution of differential equation 6.5 (euler method), the *Quickfield* simulation (temperature reading at the marked point $x = 0$ m and $y = -0.1935$ m from the center of the recipient) and the measured temperature at the NEG pump in the test recipient. **b)** equilibrium temperature of the NEG pump with $T_{recipient} = 200\,°C$ and a current of $I = 26$ A. The position of the PT100 is marked in the figure.
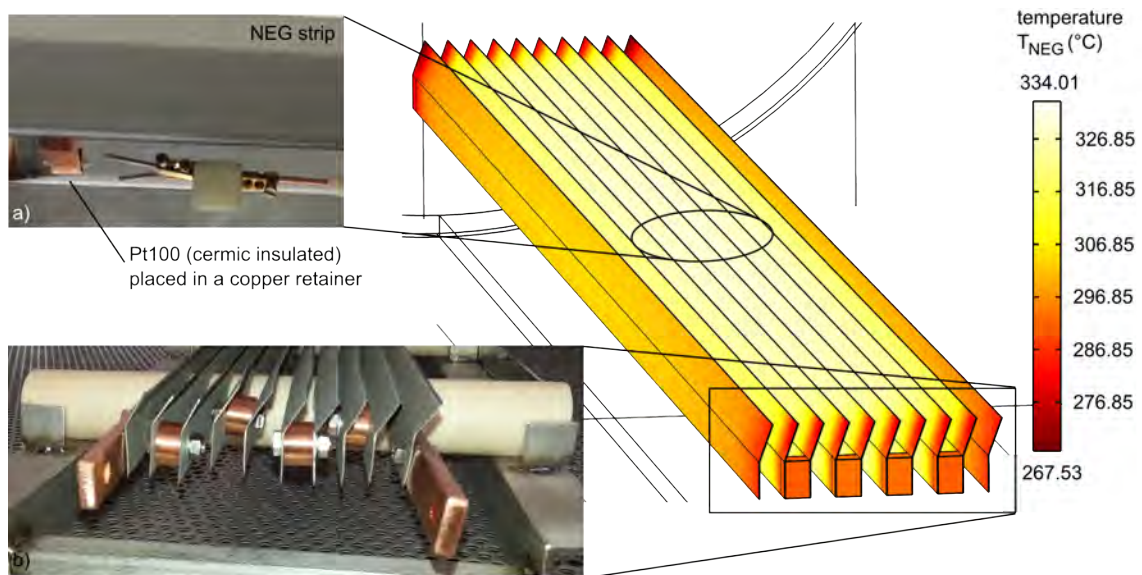
Figure 6.6: Results of *COMSOL* simulation a) A detail view of the PT100 sensor, placed in a copper retainer below the center of the NEG pump. **b)** A detail view of the electrical connection between the NEG strips. The ten strips are connected in series by using stainless steel screws in copper cylinders. **c)** Result of the *COMSOL* simulation[a]: Temperature distribution of the NEG pump prototype mounted in the test recipient, with $T_{recipient} = 200\,°C$ and $I = 26$ A.

---

[a]*COMSOL* simulation done by Dipl.-Phys. A. Jansen and Dipl.-Phys. D. Hilk, 2013.

7. Monitor the pressure and the residual gas composition, then close the main gate valve so that the recipient is separated from the TMP. If the NEG pump is activated sufficiently the pressure will remain stable or continue to decrease. The residual gas composition will show a small increase of argon (see section 6.1). Argon as a noble gas which is not pumped by the getter material.

8. Determine the residual gas composition again, before opening the main gate valve.

9. Shut down the TMPs and the fore-pump. To reset the system to its start conditions vent the test recipient (slowly) with air: fast venting the system may ignite the getter strips.

The temperature sensor T_{NEG} (see figure 6.6a) was calibrated by heating the test recipient ($T_{\text{recipient}}$) up to different temperatures. A detailed report of the calibration process can be found in [121].
The analysis focuses on the change in concentration of the following residual gas components: H_2, CH_4, H_2O, CO, CO_2 and Ar. Of particular interest is the behavior of hydrogen and argon. The measured gas dependent ion currents $I_{\text{gas,m}}$ (measured with a quadrupole mass analyzer) are corrected with the ionization probability and the relative currents of the fractal ions. The corrected ion current for each measured gas is given by:

$$I_{\text{gas}} = \frac{1}{K_{\text{ion}}} \cdot \frac{1}{K_{\text{frac}}} \cdot I_{\text{gas,m}} \qquad (6.6)$$

By comparing this corrected ion current with the absolute pressure in the recipient a gas dependent partial pressure ∂p_{gas} is calculated. As a pressure gauge a *Vacom* Atmion wide range manometer is used, in the low pressure region this device works with a hot cathode ionization gauge (Bayard-Alpert, see section 5.3.1). The pressure readings are only valid for the gas the gauge is specified for. Usually a gauge head is calibrated for nitrogen. Hence, for any other gas, a gas correction factor K_{gas} must be applied. The gas correction factors used in this work are shown in table 6.1 as well as the ionization probabilities and the relative currents of the fractal ions. The corrected gas dependent partial pressure is given by:

$$\partial p_{\text{gas}} = \frac{I_{\text{gas}}}{\sum_{\text{gas}} K_{\text{gas}} \cdot I_{\text{gas}}} \cdot p_m. \qquad (6.7)$$

Table 6.1: Gas correction factors. The values are derived by empirical methods substantiated by measurement reported in literature [122].

	K_{ion}	K_{frac}	K_{gas}
H_2	0.44	0.971	0.428
CH_4	1.60	0.436	1.517
H_2O	1.00	0.768	0.967
CO	1.05	0.900	1.067
Ar	1.20	0.813	1.125
CO_2	1.40	0.704	1.440

Before the bake-out procedure the vacuum in the test recipient was dominated by water molecules. After baking the setup for 48 h at $T_{\text{recipient}} = 200\,°C$ and after activating the NEG pump in the last 24 h with $T_{\text{NEG}} \approx 345\,°C$ the water peak was reduced by a factor of 375. To determine whether the NEG pump was sufficiently activated or not, the test recipient was stabilized at $T_{\text{recipient}} = 20\,°C$ to evaluate the pumping characteristics of the NEG pump the main gate valve was closed. If the NEG pump was activated the pressure should remain stable or even decrease. Figure 6.7 shows the partial pressure development over time during the measurement.
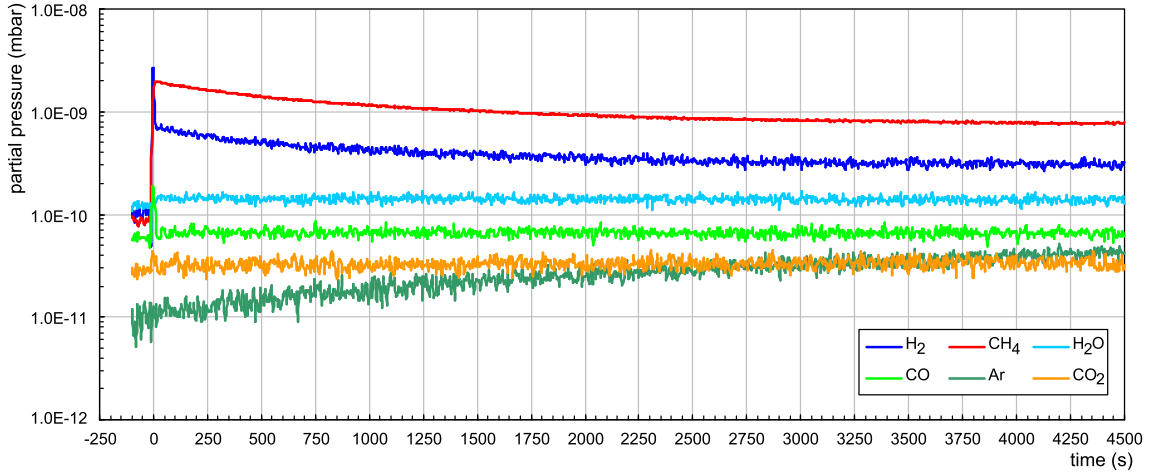
Figure 6.7: Residual gas analysis at test recipient after activating the first NEG pump prototype. During this measurement the temperature of the vessel was stabilized at $T_{\text{recipient}} = 20\,°C$. The first sharp peak in the readings is a result of closing the main gate valve. The effect of the NEG pump is obvious by comparing this measurement with a pressure rise measurement without NEG pump (shown in figure 5.5 and in figure 6.8).

The first spike in the readings is due to the closing of the main gate valve. The mechanical moving of the main gate valve will release gases in the recipient. This unavoidable effect influences in particular the overall amount of methane and hydrogen in the system. The partial pressures of H_2O, CO and CO_2 remain stable, while CH_4 and H_2 are even decreasing over time. Argon, as a noble gas, is unaffected from the NEG pump and slowly rises with a rate of $8.4 \cdot 10^{-17}\,\text{mbar}\,\ell/\text{s}\,\text{cm}^2$ due to outgassing of the stainless steel recipient and the NEG pump. To highlight the effect of the getter this measurement has to be compared to a pressure rise measurement without NEG pump (shown in figure 5.5 and as a summary in figure 6.8). About 1h after closing the main gate valve the partial pressures of hydrogen ($p_{H_2} = 7.4 \cdot 10^{-7}\,\text{mbar}$) dominates the pressure in the test recipient due to outgassing of the stainless steel vessel.

In figure 6.9 the residual gas composition is displayed as observed at the end of the measurement but before opening the gate valve again. The chemically active gases like water, CO and CO_2 react with the surface of the getter material. Their share in the residual gas composition hardly changes in comparison to the preceding measurement (see figure 6.8b). The NEG pump does not affect noble gases, hence, a rise of the argon peaks $m = 40\,\text{amu}$ and $m = 20\,\text{amu}$ (doubly ionized Argon) is expected.
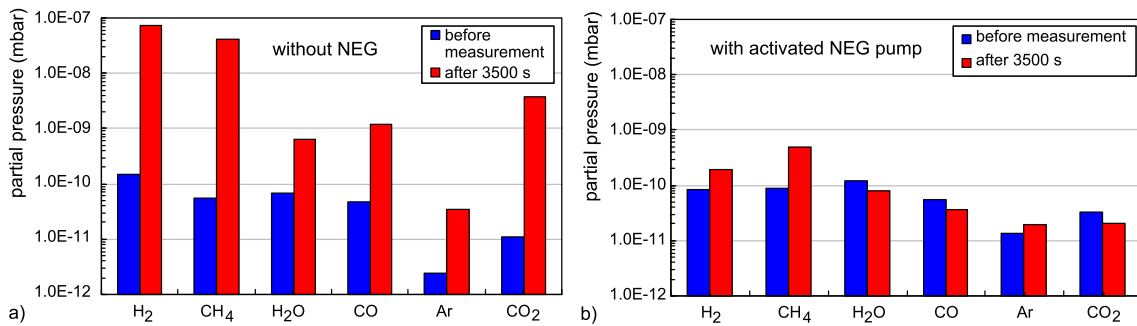
Figure 6.8: First NEG pump prototype - residual gas analyses. Presented are the readings of the RGA before and after the pressure-rise measurement. **a)** Without NEG pump: shown is the result of a 90 h long bake-out cycle of the test recipient with $T_{\text{recipient}} = 350\,°C$ followed by a step temperature of $T_{\text{recipient}} = 200\,°C$. **b)** With activated NEG pump: Here the test recipient was baked-out for 48 h with a temperature of $T_{\text{recipient}} = 200\,°C$. The NEG pump prototype was activate with a passing current of 26 A resulting in a temperature of $T_{\text{NEG}} \approx 345\,°C$. The start value of the argon peak is higher because the NEG material was stored in an argon atmosphere.
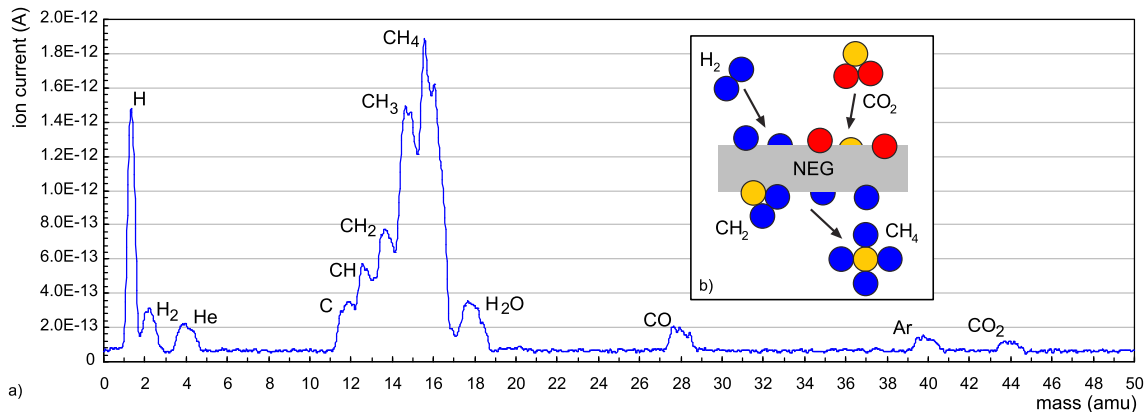
Figure 6.9: a) Detailed residual gas analysis at test recipient after the measurement with activated NEG pump. Before opening the main gate valve, still the temperature of the vessel was stabilized at $T_{\text{recipient}} = 20\,°C$. The readings are in ion current to give an impression of the residual gas composition. **b)** Catalytic effect of methane at the NEG material, shown is a schematic representation of equation 6.8.

An increase of the masses 13 amu (CH), 15 amu (CH_3) and 16 amu (CH_4) and other methane ion fragments (like carbon and atomic hydrogen) were observed in the vacuum chamber. On the other hand hydrocarbons heavier than methane have not been observed in the mass spectra. NEG material is a known catalyst for methane by dissociating hydrogen and carbon dioxide as well as carbon monoxide. The methane production is illustrated in equations 6.8 and figure 6.8b [123]. The released oxides are diffusing in the bulk material of the getter.

$$
\begin{aligned}
CO_{2\,(gas)} &\longrightarrow CO_{2\,(ad)} \longrightarrow CO_{(ad)} + O_{(ad)} \longrightarrow C_{(ad)} + O_{(ad)} + O_{(ad)} \\
H_{2\,(gas)} &\longrightarrow 2H_{(ad)} \\
C_{(ad)} + 2H_{(ad)} &\longrightarrow CH_{2\,(ad)} \\
CH_{2\,(ad)} + 2H_{(ad)} &\longrightarrow CH_{4\,(ad)} \longrightarrow CH_{4\,(gas)}
\end{aligned}
\tag{6.8}
$$
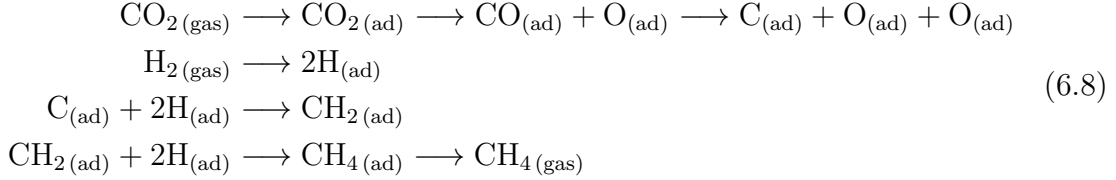
Furthermore, the influence of the ionization gauge [124] (and of the quadrupole mass analyzers) can not be neglected. The production of methane is due to surface reactions on the ion source electrodes. In the literature it is stated that chemically active gases will dissociate on the hot surfaces of the filaments (with operating temperatures of about 2 000 K). Several possible reactions are given by ALPERT [125]. The hot filaments lead to the formation of atomic hydrogen, and these active hydrogen atoms can react with carbon by forming methane:

$$
H_{2\,(gas)} + C \xrightarrow{2\,000\,K} H_{(gas)} + CH_{x\,(gas)}.
\tag{6.9}
$$
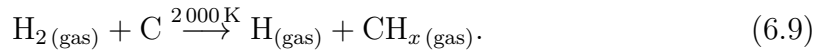
The reaction 6.9 on the filaments of the pressure gauge disturbs the measurement by leading to a detectable production of methane and atomic hydrogen. Hence, the methane pressure is linked to the hydrogen pressure. Several authors report the outgassing of methane, see for example reference [126][8]. Investigations of BENNETT et.al. showed that most, if not all, of the methane presumedly resulting from outgassing out of the stainless steel vessel was produced in the ion source of their measuring equipment. The rising of methane and its fragments was also observed during pressure rise measurements without a NEG pump (see figure 5.5).

The NEG pump thus adsorbs hydrogen (see reduction after the valve was closed in figure 6.7). The pumping speed for hydrogen in ion gauges is neglected due to the pumping speed of the NEG pump. The partial pressure of methane is linked (based on the reaction 6.9) to the partial pressure of hydrogen. The constant pressure of H_2O, CO and CO_2 as well as the slow increase of argon with a simultaneously decrease of hydrogen is interpreted as an evidence that the NEG pump was sufficiently activated by passing a current of $I = 26$ A through the base material of the strips. Hence, the principle of Ohmic heating of the NEG strips up to a value of $T_{NEG} \approx 345\,°C$ and activation of the getter material is proven to be a viable option.

---

[8]BENNETT et.al. were using a very similar experimental setup including the same vessel material (LN316), a QMA and a NEG pump. The group was confronted with the problem of gas reactions on filaments of Bayard-Alpert Ionization Gauges while measuring the outgassing rate of the vacuum vessels, too.

6.3 Transfer to Main Spectrometer NEG Pump

This section transfers the results of the feasibility study to the stage of a design prototype. This second prototype is constructed in a way to closely resemble one module of the main spectrometer NEG pump (see figure 6.1c). This small-scale implementation allows a detailed test of the various subsystems, like the getter holding structure, the electrical insulation and the electrical connections.

6.3.1 Design Prototype of KATRIN NEG Pump

The second prototype follows the geometrical framework of the main spectrometer NEG modules more closely. The objectives of the NEG upgrade are to

- meet the high vacuum standards of the KATRIN experiment.

- reuse as many parts as possible: in particular the over 3 000 NEG strips.

- guarantee a robust and maintenance-free service for the life time of the complete system.

- provide a simple and fast way to mount the pump. By accelerate the installation the work at the opened spectrometer is shortened.

A picture of the design prototype as well as a schematic drawing of one comb is shown in figure 6.10.
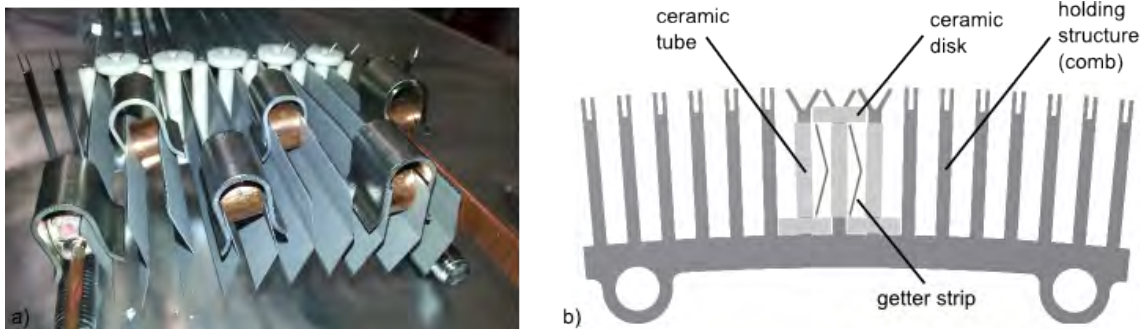
Figure 6.10: The second prototype focuses on the subsequent implementation at the main spectrometer. **a)** Picture of the prototype, including the clips and blocks to connect the getter strips. **b)** A schematic drawing of one comb. The ceramics and two getter strips are indicated.

The getter holding structure: The design of this second getter holding structure is based on the combs of the original main spectrometer NEG modules. The 1.5 mm strong comb-shaped stainless steel plates with 15 teeth and two pins on the tips were manufactured using a LASER cutter. The tips can be bent to support the installed ceramics, see figure 6.10b.
Proposal for improvement: After the electrolytic polishing of the combs some of the material wear off. The ceramic holding tips were thinned so much that their large probability for breaking during the loading of the modules with getter would create an unnecessary risk. The thickness of the tips is difficult to control during

the electrolytic polishing process and implies major uncertainties. Hence, it was proposed to rotate the pins by 90°, pierce them at the top and to use a stainless steel wire (1 mm strong, e.g. leftovers from the inner wire electrode system) to hold the ceramics in place. This method is more precise and insusceptible to malfunction or errors. The stainless steel wires are more robust and were successfully used at the inner wire electrode system (see figure 6.11a).

The electrical insulation by ceramics: In a first attempt to insulate the single NEG strips the combs were manufactured of titanium (grade 2). By processing the titanium with a thermal oxidation treatment or the *Kepla coat*[9] procedure (a plasma chemical coating), the surface of the titanium forms an insulating layer of TiO_2. However, after extensive tests the TiO_2 layers were ruled out due to their high outgassing rates. Based on the results of the first test measurements and the well known outgassing behavior of AlO_2 ceramics (e.g. thousands of these ceramics are used at the inner wire electrode system) it was decided to use ceramics for the electrical insulation of single getter strips. Furthermore, ceramics proved to be more stable and durable against friction. For the design prototype, ceramic pipes and ceramic discs are used, which are manufactured by *FRIATEC AG*, Germany.
Proposal for improvement: To prevent the getter strips to slip off the ceramic discs and connect with the stainless steel combs, the discs will be ordered larger and are made with two notches to guide the ceramic pipes to the comb, see figure 6.11a.

The electrical connections by clips and copper cylinders: For the electrical connection between the getter strips the prototype uses clips and copper cylinders. Compared to the screws in the first prototype the clips accelerate the mounting and lead to a stronger (contact pressure of about $350\,N/cm^2$) and more heat resistant connection. The design prototype uses 1 mm strong stainless steel clips and a special tool was developed (based on locking pliers) to accelerate the mounting, see figure 6.11b. The pliers can be locked, holding the clip in position by using an over-center action. One side of the handle includes a bolt to adjust the opening of the clip, the other side of the handle includes a lever to push the two sides of the handles apart to open the pliers and quick-lock the clip. The tool allows a precise and easy mounting of the clips.
Proposal for improvement: The clips will be manufactured of 1.5 mm strong *Inconel* (X-750), an austenitic nickel-chromium-based high-performance alloy. Inconel is more robust and remains stable even at high temperatures up to 700 °C. The copper cylinders are replaced by copper blocks for a more precise installation.

The new concept developed in the framework of this work reuses the original module holding structure (shown in figure 6.3) which simultaneously acts as support structure of the baffle system. All of the getter strips will be reused, as well as some parts of the modules (like rods and screws). Several new parts have already been ordered: the new combs and the ceramics, as well as the electrical connectors (*Inconel* clips and copper blocks). The upgraded concept doubles the number of temperature sensors in each pump port, thus allowing the operator an even more accurate monitoring while also increasing the redundancy of sensors in the system.

---

[9]AHC Oberflächentechnik GmbH, Coswiger Straße 16, D-12681 Berlin, Germany
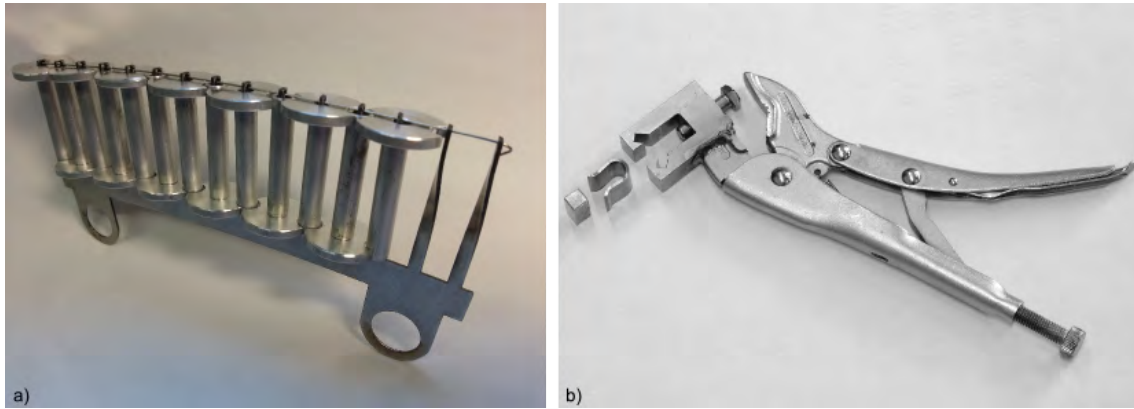
Figure 6.11: Implementation of the proposed improvements a) Picture of the improved comb with a stainless steel wire to hold the ceramics in position. As an illustrative model the ceramic pipes and discs were made of aluminium. **b)** To place the clips a special tool was developed[a].

---

[a]Idea, realization and picture by K. Mehret, 2013.

6.3.2 Simulation and Measurement with the Design Prototype

For the heat characteristics calculations the modified geometry of the design prototype must be considered. The bending of the comb increases the view factor of the NEG pump to $F_{\text{NEG}\rightarrow\text{recipient}} = 0.315$. Hence, the heat radiation calculations and simulations must be repeated using an effective area of $A_{\text{eff}} \approx 0.19\,\text{m}^2$ for the design prototype. To compensate the view factor, a current of $I = 29\,\text{A}$ was found as optimal to reach an equilibrium temperature at the getter strips of about $T_{\text{NEG}} = 345\,°\text{C}$. After baking the test recipient for about four days at $200\,°\text{C}$ the activation of the NEG pump was started. In the beginning of the activation process (the first $2\,000\,\text{s}$) the previous current of $I = 26\,\text{A}$ was chosen to observe the impact of the different view factors: according to the *Stefan-Boltzmann law* the power losses due to heat radiation are proportional to T^4. The differential equation 6.5 was solved with the Euler method (a step size of $h = 0.05$ was used). Additionally the problem was simulated using *Quickfield*. The results are illustrated in figure 6.12.

The measurement at the test recipient was analyzed in an analogous way to section 6.2.2. The progress of the residual gas composition over time after closing the main gate valve is comparable to the measurement done with the first prototype and shown in figure 6.13.

Furthermore, the design prototype was evaluated by endurance tests under very stringent test conditions. To check the high temperature compatibility of the NEG pump the test recipient was baked up to $T_{\text{recipient}} = 350\,°\text{C}$. By simultaneously applying a current of $I = 29\,\text{A}$, the getter strips were activated at $T_{\text{NEG}} \approx 435\,°\text{C}$ for about one hour. To evaluate the tolerance of high currents the test recipient was held at room temperature ($T_{\text{recipient}} = 23\,°\text{C}$), and a current of $I = 40\,\text{A}$ was applied (about 1.5 times nominal current) again for an activation temperature of $T_{\text{NEG}} \approx 435\,°\text{C}$. This value was reached and held for one hour. After dismounting the NEG prototype no visible defects or damages were observed.
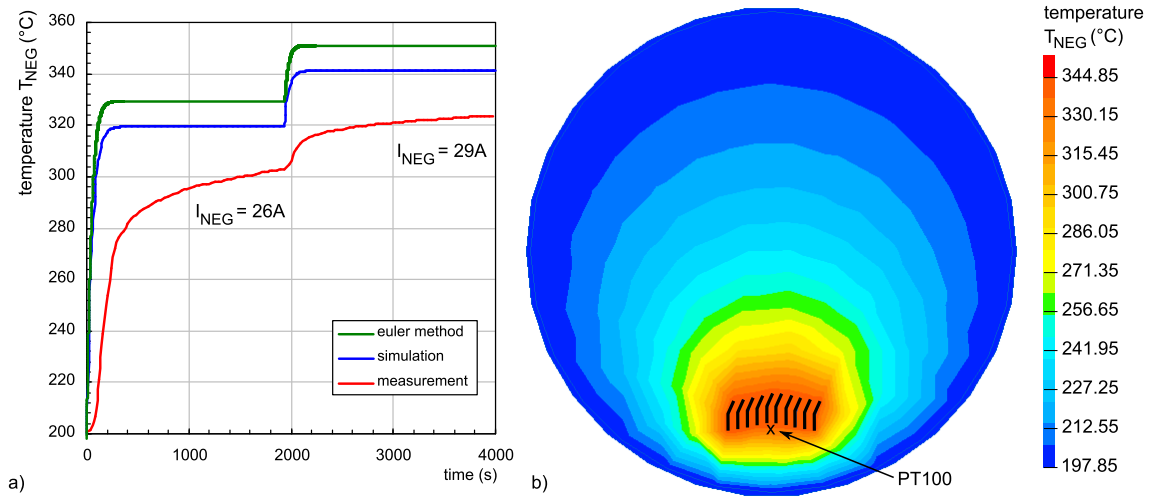
Figure 6.12: NEG pump design prototype a) Temperature development over time: presented are the numerical solution of differential equation 6.5 (Euler method), the *Quickfield* simulation (with the temperature reading at the marked point $x = 0$ m and $y = -0.18$ m from the center of the recipient) and the temperature measured at the NEG pump in the test recipient. **b)** Temperature distribution at the equilibrium temperature of the NEG pump with the vessel at $T_{recipient} = 200\,°C$ and a current of $I_1 = 26$ A resp. $I_2 = 29$ A. The position of the PT100 temperature sensor is marked in the figure.
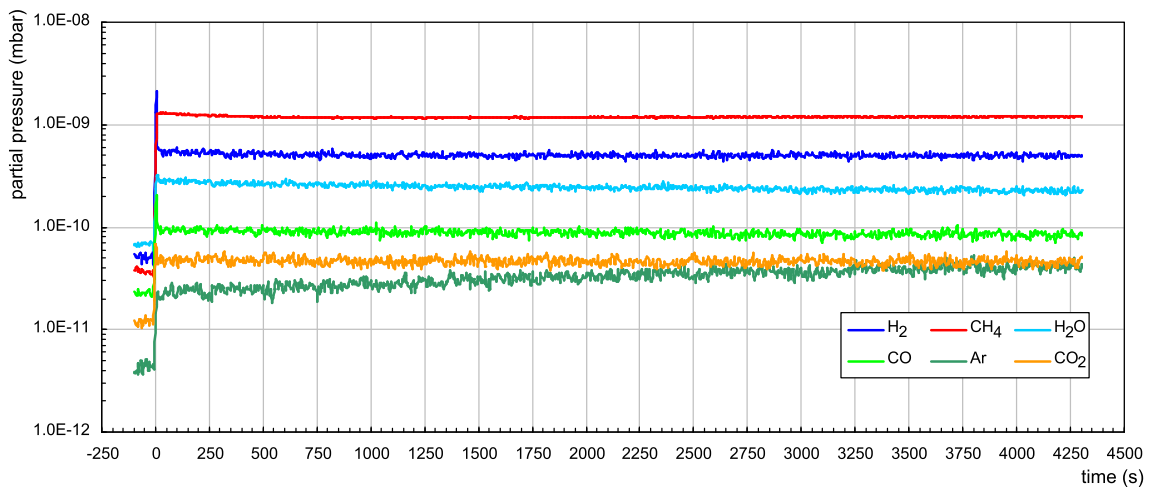
Figure 6.13: Residual gas analysis at test recipient after activating the NEG pump (design prototype). During the measurement the temperature of the test recipient was stabilized at $T_{recipient} = 20\,°C$. The first sharp peak in the spectrum is a result of closing the main gate valve.

6.3.3 Radiation Calculations of the Upgraded Main Spectrometer NEG Pump

The duration of the thermal NEG activation process depends on the specific type of getter material and the temperature. High temperatures increase the diffusion rates of oxide and nitride ions in the getter. Following the concentration gradient the ions migrate into the bulk material of the getter and the surface regains its ability to bind gases. After reaching the maximal bake-out temperature of the main spectrometer ($T_{\mathrm{MS}} \approx 200\,^{\circ}\mathrm{C}$) the upgraded NEG pumps are designed to reach the recommended activation conditions of $T_{\mathrm{NEG}} = 450\,^{\circ}\mathrm{C}$ (keep the temperature stable for a duration of 30 min). The timeframe for the whole NEG activation procedure is reduced to hours (against days in conventional activation by thermal radiation). Due to the short activation process the risk of damaging the inner wire electrode system is minimized.

In each pump port a total of 1 006 NEG strips is installed, each featuring an Ohmic residence of $R = (0.082 \pm 0.001)\,\Omega$. In order to estimate the required electrical power per pump port P_{PumpPort} to compensate power loses (due to heat radiation of the NEG material), the differential equation 6.5 was solved for the activation temperature in an equilibrium state ($\mathrm{d}Q/\mathrm{d}t = 0$):

$$P_{\mathrm{PumpPort}} = 1\,006 \cdot R \cdot I^2 = \epsilon\sigma A_{\mathrm{eff}} \left(T_{\mathrm{NEG}}^4 - T_{\mathrm{PumpPort}}^4 \right), \qquad (6.10)$$

with an emissivity factor $\epsilon = 0.65$ and an effective radiating surface area of $A_{\mathrm{eff}} \approx 15\,\mathrm{m}^2$. This area is composed of outer lateral surface ($A_1 = 10.6\,\mathrm{m}^2$) and the face surfaces of the NEG pump ($A_2 = 2 \times 2.2\,\mathrm{m}^2$). The power losses of self-viewing surfaces, like the inner lateral surface of the NEG pump, are neglected. Hence, only surfaces of the NEG pump directly looking at the pump port or the baffle are contributing to the effective radiating area. Equation 6.10 returns a required current of $I \approx 39\,\mathrm{A}$ to heat the NEG pump up to $T_{\mathrm{NEG}} = 450\,^{\circ}\mathrm{C}$. Hence, the overall power that is required to activate all three NEG pumps of the main spectrometer at the same time sums up to $P_{\mathrm{total}} = 3 \cdot P_{\mathrm{PumpPort}} = 383\,\mathrm{kW}$.

6.3.4 Concept of Electrification

To design a concept for the 'electrification' of the main spectrometer NEG pumps the number of getter strips per pump port was normalized to 1 008 NEG strips[10]. When subdivided in three groups of 336 strips each, one pump port can be operated by a three-phase power controller without a asymmetric load. As a fail-safe solution the 336 strips are grouped into three parallel groups of 112 strips that are connected in series. The resistance of one NEG strip was determined to be $R = (0.082 \pm 0.001)\,\Omega$. Hence, between two phases there are 3×112 strips resulting in a resistance of $R = 3.1\,\Omega$ with the required current of $I = 3 \times 39\,\mathrm{A} = 117\,\mathrm{A}$ (the current follows calculations and simulations done in section 6.3.3) corresponding to a voltage of about $U = 364\,\mathrm{V}$. If all three phases are connected in a delta connection the German electricity grid will limit the voltage applied to the NEGs pump to maximal 400 V between two phases. This protects the constantan strips from overheating, as

---

[10]The lower modules of each pump are equipped with one strip less. Therefore the resistance of this segment is about 2% smaller. Resulting in a tolerable error.

above 700 °C the copper could evaporate, and above 850 °C an eutectic composition of copper and zirconium would develop which could melt the getter strip [84]. A three-phase power controller (based on three single-phase thyristor units) allows to operate the NEG activation procedure from the main power grid. A thyristor is a four-layered semiconductor device that is often used to control high currents and voltages. Each pump port will thus be equipped with six high-current feedthroughs. Hence, pump port I must be equipped with an additional feed-through port. The electrical supply line for the NEG pumps in pump port II and III will be fed through existing DN250 CF flanges of the L-pieces. Each phase will be monitored by two temperature sensors plus two temperature sensors at each baffle.

It is of major importance that all three pumps are activated at once, as a consecutive activation cycle would saturate the already activated pumps.

6.4 Conclusion

For a successful neutrino mass measurement the KATRIN experiment requires a vacuum of at least in the lower 10^{-11} mbar range, and uses entrapment pumps in form of a 3 km non-evaporable getter (NEG) pump, which accumulates residual gases by binding molecules at its surface (physisorption) or by absorbing gases in its bulk material by a chemical reaction (chemisorption) after is has been activated at a temperature of $T > 300$ °C. The design of the main spectrometer NEG pump is based on a setup tested in the pre-spectrometer. Each pump port is equipped with 1 006 getter strips, mounted in 16 modules and placed in a cylindrical holding structure. In order to activate the getter material the bake-out cycle of the main spectrometer was exploited. The NEG pumps are activated via thermal radiation. However, the main spectrometer bake-out procedure has to be constrained to $T_{\text{vessel}} = 200$ °C to prevent further stress on the inner wire electrode system. Hence, an alternative concept of activating the getter material was required.

As a part of this thesis a new concept of heating the NEG pumps by passage of a current through the base material of the strips was developed and successfully tested. The upgrade of the main spectrometer NEG pumps was investigated experimentally and simulated in detail. A first prototype was developed and implemented as a feasibility study in the test recipient, which is one of the major test setups in the KATRIN vacuum lab and provides a flexible environment for realistic experiments. The performed measurements were evaluated with the help of simulations and calculations and proved the soundness and viability of the new concept. To transfer the concept to the main spectrometer NEG pump, a second prototype was constructed which was more aligned to the main spectrometer NEG pump geometry. The prototype features all intended subsystems like stainless steel combs, ceramics and clips. The main objective was to reuse as many parts of the old system in an unmodified way, such as the getter strips, the holding structure and small parts of the modules. Furthermore, endurance tests with 1.5 times nominal temperature and currents were performed successfully. With the gained experience the subsystems were improved, scaled and transfered to the main spectrometer NEG pump.

In the present 2013/2014 as well as in the next maintenance period of the KATRIN main spectrometer at the beginning of 2015 this concept will be used to upgrade the NEG pumps. The new concept is intended for higher temperatures (≈ 450 °C) while

requiring a shorter heating cycle. By concentrating the heat at the NEG pump the spectrometer will stay thermally stable at temperature below 200 °C which will be supported by the *HTT* oil heating system. The baffle system will thereby act as a thermal shield and protect the inner wire electrode from the temperature gradients. It is only be developing novel and innovative vacuum concepts such as the one presented in this chapter that the KATRIN experiment can reach its physics goals.

7 The Liquid Nitrogen Cooled Baffle System

This chapter focuses on an important background reduction technique in the KA-TRIN main spectrometer targeted at removing a major background source in form of radon α-decays. Measurements at the pre-spectrometer test setup [78] have revealed ^{219}Rn emanating from the non-evaporable getter (NEG) pump, as well as ^{220}Rn coming from the vessel walls, as a background source with the potential to seriously affect the neutrino mass measurements and influence the sensitivity of KA-TRIN. As noble gas species radon is able to penetrate deep into the spectrometer and transported flux tube volume. The α-decays of these unstable radon isotopes are accompanied by atomic or nuclear processes that generate electrons such as internal conversion or shake-off electrons. Low-energy electrons (< 100 eV) below the ionization threshold directly contribute to the background, whereas high-energetic electrons (keV-range) can be stored magnetically inside the volume of the spectrometer [80]. Depending on the electron energy and the pressure inside the spectrometer these electrons can generate thousands of secondary electrons via residual gas ionization until their storage conditions are broken. This forms a significant background source in the region-of-interest indistinguishable from signal electrons. The non-Poissonian nature of these events is especially challenging.

Based on the measurements at the pre-spectrometer test setup, the radon-induced background can be estimated to $0.3 - 1.0$ cps in the main spectrometer, with the NEG pump being considered as the dominant radon source. In order to reduce the radon-induced background, the installation of a liquid nitrogen (LN2) cooled baffle was proposed [82]. The target of the baffle is to block the direct line of sight between the NEG pumps and the main volume of the spectrometer. At the same time it maintains a sufficiently effective pumping speed of the NEG pumps for hydrogen and tritium. On the one hand the baffle prevents ^{219}Rn from entering the sensitive flux tube volume, on the other hand its cooled surface acts as a sort of cryopump for ^{220}Rn emanating from the vessel walls.

This chapter reviews first the general background production mechanism from nuclear decays in a MAC-E filter system. The earlier proof-of-principle measurements with a smaller baffle prototype at the pre-spectrometer are summarized and the radon-induced background rate at the main spectrometer is estimated based on these results. A major part of the works of this thesis was devoted to develop and implement a LN2-cooled baffle system at the main spectrometer. To evaluate the efficiency of the baffle system, a series of dedicated background measurements were performed in the framework of the first main spectrometer commissioning measurements. Furthermore a detailed radon background model was established based on fits to the measured data with the goal to determine the activity of ^{219}Rn and ^{220}Rn in the volume of the main spectrometer separately.

7.1 Radon-Induced Background in MAC-E Filters

In the process of an radon α-decay an α-particle is emitted, which result in the emission of photons and electrons (with energies from a few eV to $\sim 250\,\text{keV}$) inside the volume of the spectrometer. The α-particle, the daughter nucleus and X-rays hit the vessel walls or the inner electrode system and thus do not create further background in a measurable quantity. In some cases they may produce secondary electrons there, but these electrons are reflected by the dominant magnetic shielding of the spectrometer and are of no further concern with respect to the background analyses in this work. However, the α-particle disturbs the charge distribution within the atomic cloud (see figure 7.1) which also initiates a restructuring process of the atomic shells (like shake-off-electrons with energies of up to $80\,\text{keV}$ [127]). Furthermore, the α-particle can interact with electrons of the atomic shell to eject them, creating shell vacancies. These vacancies can be filled with electrons from a higher atomic shell number so that the released energy is emitted as X-ray fluorescence, Auger electrons or Coster-Kronig electrons (see figure 7.2). This shell reorganization electrons from the outer shells share a energy of about $230\,\text{eV}$ left after the initial perturbation [128]. In some cases, where an excited nuclear level is populated after the α-process a conversion electron can be emitted in the subsequent de-excitation process instead of radiating gamma-rays. For ^{219}Rn α-decays, the probability for emitting an internal conversion electron is about 3%, resulting mostly in electrons with $178\,\text{keV}$ (1.27%) and $254\,\text{keV}$ (0.74%) [129].
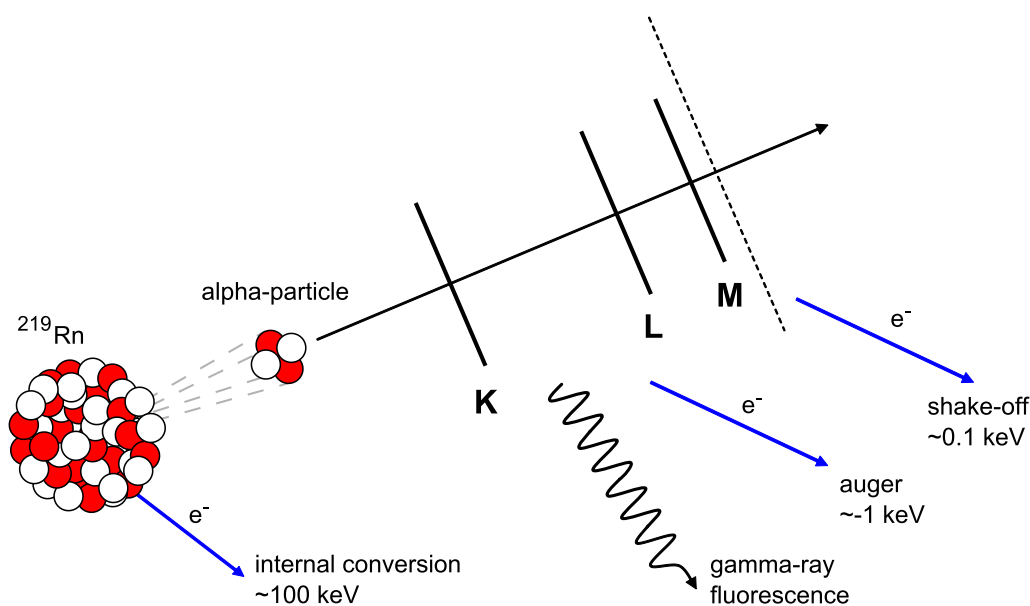
Figure 7.1: Schematic drawing of a radon α-decay and its accompanying electrons. The different electron production mechanisms during a ^{219}Rn α-decay are indicated. The details are explained in the text and in figure 7.2.

A high-energy electron will usually be trapped magnetically inside the spectrometer, see figure 7.3, due to the operating principle where the MAC-E filter forms a magnetic bottle for light charged particles. Electrons produced in the center of the spectrometer are accelerated towards the ends of the spectrometer and move from a

low magnetic field region into a high magnetic field region. Due to the conservation of the magnetic moment the longitudinal energy is transformed into transversal energy, implying that the electron is magnetically trapped until the storage condition is broken (for example by a non-adiabatic process or a scattering off residual gas) and the electron can leave the spectrometer.

The stored electrons continually lose energy due to scattering off residual gas and by emitting synchrotron radiation. If the electron is cooled down to energies of the order of few eV it is eventually released from the trap. Due to the low pressure regime of $p \approx 10^{-11}$ mbar in the recipient, the cooling time for keV electrons can take up to about 10 h. By ionizing the residual gas, a single electron can generate thousands of low-energy secondary electrons that leave the trap and reach the detector. Thus contribute to the background rate in the region-of-interest.

At the pre-spectrometer test setup these bursts in the background rate over a certain period of time (~ 1 h) were easily visible, also due to their characteristic ring-like event topologies from the magnetron motion, see figure 7.5b. Detailed information on the background patterns produced by radon-induced events is available in [80] and [79].
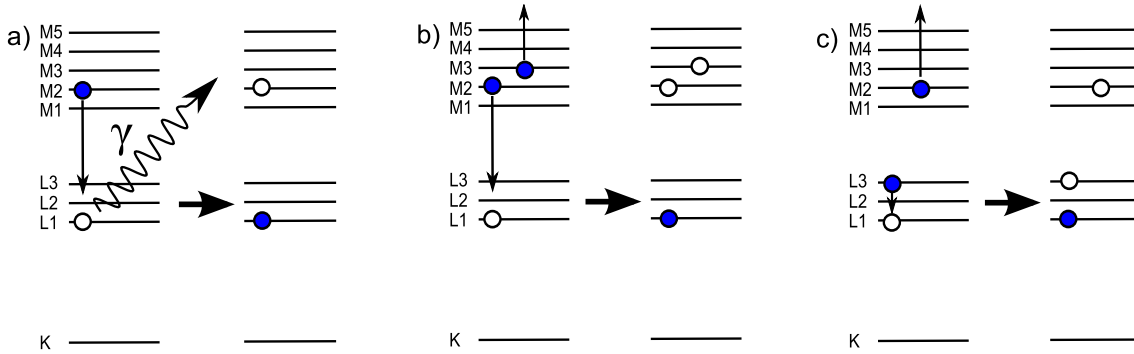
Figure 7.2: Schematic overview of processes that could follow a L shell vacancy. a) X-ray fluorescence, **b)** emission of an auger electron, and **c)** a Coster-Kronig transition. The resulting secondary vacancies are shown in each case. The figure is based on [130].

7.2 Measurements at the Pre-spectrometer

The pre-spectrometer will serve as a pre-filter (see chapter 3) in the neutrino mass measurements but previously was used as a prototype of the main spectrometer in a stand-alone mode equipped with a detector and an electron source. The objectives of the prototype setup were to optimize the MAC-E filter concept, to verify the ultrahigh vacuum (UHV) design and to develop the detector and data acquisition (DAQ) system by developing both hard- and software components. Of particular interest was the verification of the simulation package KASSIOPEIA [63], where data were analyzed and simulated in this small-scale test setup, then scaled up and transferred to the main spectrometer.

This section focuses on those measurements performed at the pre-spectrometer with the target to reduce the radon-induced background by installing a LN2 cooled baffle, as these results were instrumental in design and implement a LN2 baffle system for the main spectrometer.

7.2.1 Pre-spectrometer Test Setup

The pre-spectrometer test setup differs slightly from previously described setup of this component as part of the KATRIN beamline. To measure in a stand-alone mode the pre-spectrometer was equipped with a quadratic $16\,cm^2$ monolithic silicon PIN diode, segmented into 64 quadratic pixels for spatial resolution. The high threshold of this detector only allowed electrons with energies $> 10\,keV$ to be detected.

The vacuum pumping system consisted of two main components. First, a cascaded set of turbomolecular pumps (TMPs), attached to the horizontal pump port of the pre-spectrometer, provided an effective pumping speed of about $1000\,\ell/s$ for hydrogen. The $45°$-pump port contained the previously described (see chapter 6) non-evaporable getter (NEG) pump, here consisting of $90\,m$ of *SAES* St707 getter strips with an effective pumping speed of about $25\,000\,\ell/s$ for hydrogen. After the bake-out of the system at $200\,°C$ and activation of the NEG material at $350\,°C$ for about $24\,h$, a pressure in the range of $10^{-11}\,mbar$ was reached in the pre-spectrometer vessel at ambient temperature [69].

The getter material, being an alloy of zirconium (70%), vanadium (24.6%) and iron (5.4%) [90], contains traces of ^{235}U, so that the actinide decay chain in the material produces small amounts of ^{219}Rn. The specific activity of $90\,m$ NEG strips was measured to about $8\,Bq$ with γ-ray spectroscopy at the MPIK in Heidelberg. Due to the large surface of the material of $1\,500\,cm^2/g$ [90], and owing to its fine grained structure, radon was able to emanate into the volume of the pre-spectrometer with a released activity for ^{219}Rn of about 0.1% ($\sim 8\,mBq$) [80].

Due to the much better adiabatic properties of the pre-spectrometer, as compared to the larger main spectrometer with its lower magnetic field strength in the center, a primary keV-electron produced in a nuclear decay is trapped magnetically for several hours and generates hundreds of secondary electrons by residual gas ionization. Due to the higher B-fields in the pre-spectrometer even high-energy electrons up to $500\,keV$ were stored. A nuclear decay inside the spectrometer can be seen as typical ring structures at the detector, see figure 7.3. For the pre-spectrometer test setup an average radon-induced background due to the NEG pump was determined to be (5.4 ± 2.4) radon ring events per day (for more details see [78] and [82]).
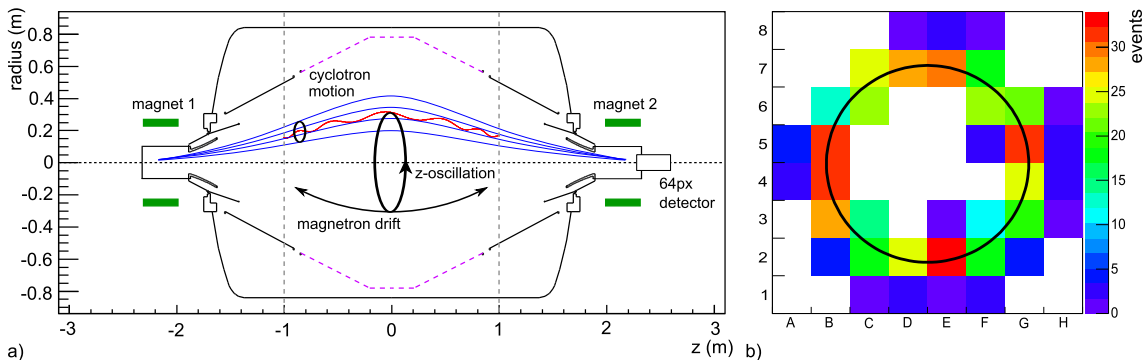
Figure 7.3: Motion of an electron trapped in the pre-spectrometer. The superconducting solenoids form a magnetic bottle for light charged particles. **a)** A trapped electron performs a azimuthal magnetron motion superimposed with an axial and cyclotron motion. Secondary electrons are produced via residual gas ionization. These low energetic electrons can leave the magnetic trap by following the magnetic field line they are created on. **b)** They arrive on a ring like distribution at the detector (simulated pixel distribution).

7.2.2 Reducing the Radon-Induced Background with an LN2 Cooled Baffle

The measurements at the pre-spectrometer test setup were instrumental in identifying ^{219}Rn atoms emanating from the NEG pump as the dominant radon background source. Also, these experiments were able to identify ^{220}Rn emanating from the bulk material of the vessel into the volume of the spectrometer. When extrapolating these results of the pre-spectrometer, the average radon-induced background rate at the main spectrometer from the NEG material is expected to be around 0.3 cps which is a factor of 30 above the nominal background level [78]. Such a large background rate would significantly reduce the sensitivity of KATRIN on $m_{\bar{\nu}_e}$ [79]. Therefore the radon-induced background at the main spectrometer needs to be drastically reduced. A simple solution would be to leave the NEG material out, so that the radon-induced background is eliminated. However, in this case the stringent UHV conditions of 10^{-11} mbar could not be reached anymore. A larger pressure would increase pressure-dependent backgrounds such as during tritium β-decay electron scanning. Furthermore, nuclear decays of tritium molecules migrating from the tritium source to the spectrometer would cause a background rate exceeding the KATRIN design limit of 0.01 cps [79]. A very attractive solution to prevent radon from entering the spectrometer - while still maintaining a significant fraction of the NEG pumping speed for H_2 and tritium - is the installation of a LN2 cooled baffle. Due to its small sticking coefficient and high mean thermal velocity hydrogen can pass the cold baffle almost unaffected. In order to test the feasibility of a LN2 cooled baffle and to determine experimentally the radon suppression efficiency, a baffle prototype was installed in the pre-spectrometer test setup, in front of the NEG pump (see figure 7.4).

The baffle for the pre-spectrometer test setup was manufactured by the company *HSR*[1]. With a diameter of 478 mm and a length of 162 mm the pre-spectrometer baffle was designed to be optically tight to block the direct flight of radon emanating from the surfaces of the NEG pump into the pre-spectrometer (see figure 7.4a). The cupreous baffle seen in figure 7.4b is connected at four points directly with the NEG pump. To generate a cold trap, about 10 ℓ/h liquid nitrogen were used to cool the surface of the baffle to trap radon isotopes and prevent them from entering the sensitive pre-spectrometer volume. An ultra high vacuum feedthrough for liquid nitrogen was build by the KIT workshop. To compensate thermal expansions a two-loop spiral was integrated in both flow and return pipe inside the pump port. The whole pre-spectrometer setup, including the baffle, can be elevated on high potential (about -18 kV). An LN2 supply in the form of a 200 ℓ cryostat was mounted on four 30 cm high ceramic insulators and connected to the pre-spectrometer high voltage. The temperature of the baffle was monitored at the exhaust pipe. The adsorption probability of radon atoms depends on the temperature of the baffle. The deposition temperature of ^{219}Rn on copper surfaces was measured to be $T_{\text{dep}} = 131$ K [131]. Consequently, the baffle should have no effect in reducing the radon background at ambient temperature.

---

[1]HSR AG, Foehrenweg 16, P.O. Box 109, 9496 Balzers, Principality of Liechtenstein
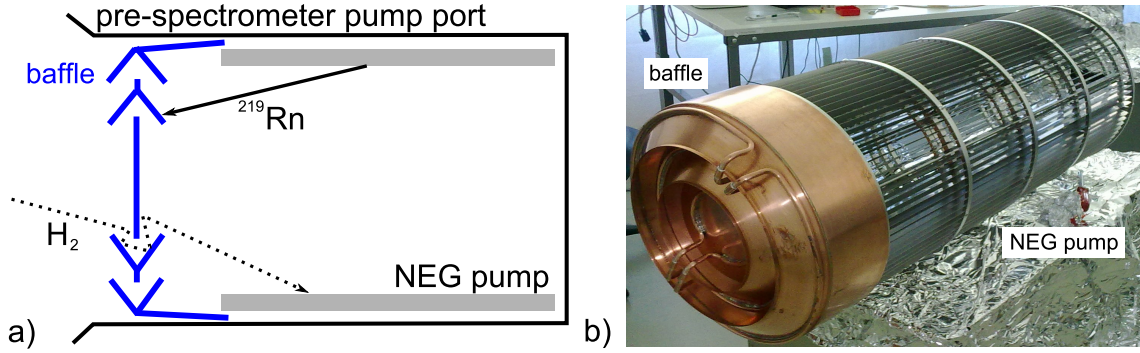
Figure 7.4: Setup of the pre-spectrometer baffle system. a) Schematic drawing of the cross-section of the pre-spectrometer pump port with NEG pump and LN2 cooled baffle. The ^{219}Rn emanating from the getter has no direct line of sight to the pre-spectrometer volume and is freezing to the cooled surfaces of the baffle. **b)** Photograph of the baffle directly attached to the NEG pump.

All measurements with baffle were performed with nominal pre-spectrometer operating parameters. The NEG pump was not activated so a pressure of about $3 \cdot 10^{-9}$ mbar was reached. A symmetric magnetic field setup was used ($B_{\mathrm{max}} = 4.5$ T inside the superconducting coil) and an electric potential of $U_{\mathrm{tank}} = -18$ kV was applied to the vessel. The inner electrodes were kept on a slightly more negative potential $U_{\mathrm{electrodes}} = -18.5$ kV to fine tune the electrostatic retarding potential [78]. Only hits in an energy region of interest between 15 and 21 keV were included in the analysis.

To validate the concept of a liquid nitrogen cooled baffle in trapping radon atoms, three measurements were performed:

- Measurement 1: baffle at ambient temperature,

- Measurement 2: baffle cooled with liquid nitrogen and

- Measurement 3: reference without NEG pump and without baffle.

Measurement 1 was taken at ambient temperature after mounting the baffle. The result is shown in figure 7.5a). Most of the time the measured rate is close to the intrinsic detector background rate of $(6.3 \pm 0.2) \cdot 10^{-3}$ cps. However, during the 120.5 h of measuring time 19 radon ring events were observed, equivalent to (3.8 ± 0.9) radon ring events per day. As expected, a baffle at ambient temperature shows no significant difference to the average background before installation.

Figure 7.6 shows the corresponding result of measurement 2. After switching on the liquid nitrogen supply the number of radon-induced events was reduced by a factor of five. In 147 h of measurement time only 4 radon-induced events were observed. This corresponds to (0.7 ± 0.3) radon ring events per day.

In measurement 3, without baffle and without NEG pump, a total of 5 radon ring events were observed in 108 h of measuring time or (1.1 ± 0.5) radon ring events per day. All results of the baffle measurements are summarized in table 7.1.
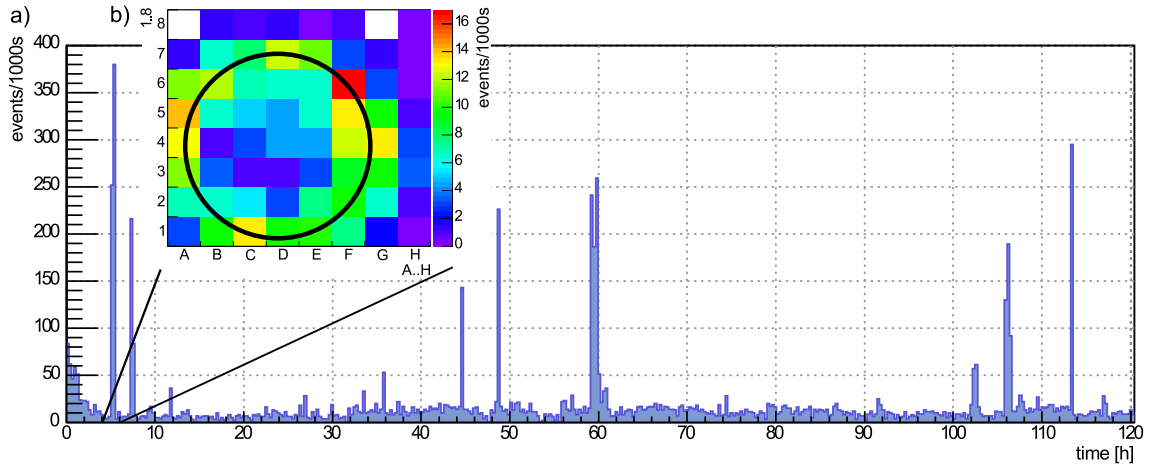
Figure 7.5: Measurement with warm baffle (measurement 1): a) Rate versus time plot for a background measurement with the pre-spectrometer standard operating conditions for a magnetic field of 4.5 T and an electric potential of $-18.5\,\mathrm{kV}$ at a pressure of about $3 \cdot 10^{-9}\,\mathrm{mbar}$ and the baffle at ambient temperature. The rates include the intrinsic detector background of $(6.3 \pm 0.2) \cdot 10^{-3}\,\mathrm{cps}$. **b)** The pixel distribution for the first time interval of elevated rate, together with a ring (radius and center resulting from a fit). The interval of elevated rate started at 4.95 h and ended at 5.5 h, it took 33 minutes, displayed are about 750 hits.
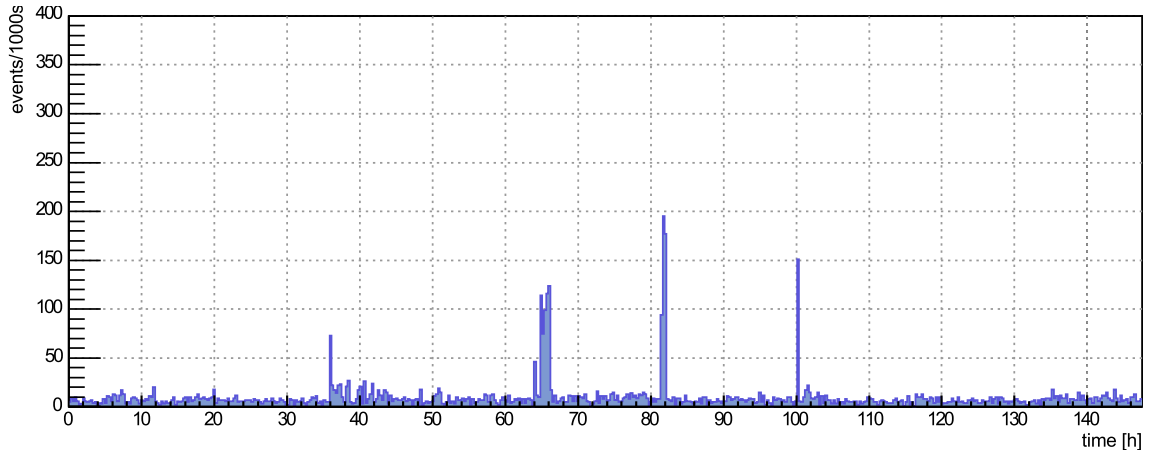
Figure 7.6: Measurement with cold baffle (measurement 2): rate versus time plot for a background measurement with the pre-spectrometer standard operating conditions for a magnetic field of 4.5 T and an electric potential of $-18.5\,\mathrm{kV}$ at a pressure of $\sim 3 \cdot 10^{-9}\,\mathrm{mbar}$ and the baffle is cooled down with liquid nitrogen. The rates include the intrinsic detector background of $(6.3 \pm 0.2) \cdot 10^{-3}\,\mathrm{cps}$.

Table 7.1: All results of the baffle measurements at the pre-spectrometer. Shown are the measurement time, the number and the rate of radon ring events (events per day). The last row shows the average radon-induced background due to the NEG pump, before mounting the baffle. The values are determined by comparing several pre-measurements described in [78] and [82].

	measurement time (h)	number of radon events	radon event rate (1/d)
1. baffle at room temperature	120.5	19	3.8 ± 0.9
2. baffle cooled with LN2	147	4	0.7 ± 0.3
3. without NEG pump and baffle	108	5	1.1 ± 0.5
with NEG pump and without baffle	from a series of measurement		5.4 ± 2.4

7.2.3 Interpretation of the Results and Extrapolation to the Main Spectrometer

The neutral radon isotopes ^{219,220}Rn emanate and quickly propagate over the entire spectrometer volume as they are not affected by the electro-magnetic shielding. Therefore the radon α-decay or more precisely its accompanied electrons form a major and uniformly distributed background source in a MAC-E filter.

By making use of a liquid nitrogen cooled baffle, ^{219}Rn emanating from the NEG pump is captured before leaving the pump port and ^{220}Rn emanating from the vessel walls is adsorbed at the cool surfaces of the baffle by the cryopump effect. The LN2 cooled baffle system can prevent radon from entering the sensitive volume of the spectrometer. The measurement 2 value of (0.7 ± 0.3) radon ring events per day is comparable with measurement 3 of (1.1 ± 0.5) radon ring events per day within the statistical uncertainties of the measurements. By comparing measurements with cold baffle to measurements with warm baffle a reduction factor of five can be estimated. The remaining radon events arise from a sources inside the spectrometer like welding seams, glass insulators or the vessel surface itself. However, the success of the baffle measurements comes at the expense of a reduced NEG pumping speed. The cryo-trapping of hydrogen (as the main component of the residual gases under these pressure conditions) is negligible. The baffle significantly reduces the pumping speed of the NEG pump in the pre-spectrometer test setup by about 76% due to the blocking of the direct line of sight between NEG pump and vacuum chamber (and therefore increasing the conductivity). This factor is based on simulations done by Dr. X. Luo with the software package *ProVac3D* [119] developed at KIT (ITEP).

7.3 Development of a Main Spectrometer LN2 Cooled Baffle System

Based on the results of the pre-spectrometer prototype measurements a baffle system to eliminate the radon-induced background in the main spectrometer was developed as one of the central parts of this work. As a starting point, the following section deals with an estimate of the radon emanation in the main spectrometer. This sets the stage for a layout of the LN2 cooled baffle system by simulations to determine

its conductance for hydrogen and its pumping speed for radon. This section concludes with a description of the technical realization of the LN2 cooled baffle system, including the LN2 supply line and the high voltage separation.

7.3.1 Estimation of Radon-Induced Background at the Main Spectrometer

Based on the results of the pre-spectrometer measurements [78] [82] the amount of ^{219}Rn and ^{220}Rn emanating in the main spectrometer can be estimated by scaling the observed radon sources:

- ^{219}Rn with a lifetime of 5.71 s is produced from the primordial ^{235}U decay chain (see appendix A.15). The dominant source of ^{219}Rn was tracked to traces of ^{231}Pa in the NEG material. The NEG pump held 90 m of NEG strips, corresponding to 1.8 kg of NEG material [114]. As a further weak source of ^{219}Rn specific vacuum gauges and other sensor equipment as well as the inner surface of the stainless steel walls were identified [82].
  The main spectrometer is equipped with a much larger pump containing about 3 000 m of NEG strips equivalent to 60 kg of NEG material. Due to the porous getter surface, as shown in figure 6.1, the noble gas ^{219}Rn emanates with a probability of 10^{-3}. The NEG material used in the main spectrometer has been pre-selected as low-activity material, for which the specific activity is a factor of two lower compared to the pre-spectrometer NEG material [78]. In a special production process most of the ^{227}Ac has been removed. Hence, ^{219}Rn that is naturally in a secular equilibrium was cut off from the ^{235}U decay chain. However, over time the α-decay of ^{231}Pa fills the reservoir of ^{227}Ac, thereby increasing the ^{219}Rn activity by a factor of 0.3 Bq/kg per year. During the SDS commissioning measurements in mid-2013 the ^{219}Rn activity of the NEG material is estimated to correspond to about 2.3 Bq/kg. With an emanation probability of 10^{-3}, the emanation rate of ^{219}Rn is expected to be about 0.14 Rn/s.
  The ^{219}Rn activity of the main spectrometer NEG material was independently measured at SNO lab, Canada [132] by Dr. J. Farine determining the ^{219}Rn emanation of the NEG material to about 0.2 mBq/m. However, due to the short lifetime of ^{219}Rn and the complex measurement setup this value should be considered as a lower limit.

- ^{220}Rn with a lifetime of 80.2 s is produced from ^{232}Th within the thorium decay chain (see appendix A.16). After removing the getter pump from the pre-spectrometer, as well as detaching all other components that were suspected to emanate radon (e.g. a thermocouple, glass windows and vacuum gauges), the remaining emanation of ^{220}Rn was assumed to be caused by the vessel walls. To estimate the emanation of ^{220}Rn from the stainless steel surfaces in the main spectrometer, the observed decays in the pre-spectrometer measurements were scaled with respected to the ratio of the inner surfaces[2]. The emanation rate of ^{220}Rn is thus expected to be about 0.08 Rn/s.

---

[2]The surface areas of the pre-spectrometer is $A_{\mathrm{PS}} \approx 25\,\mathrm{m}^2$ and of the main spectrometer $A_{\mathrm{MS}} \approx 690\,\mathrm{m}^2$.

In doing so it is assumed, that sources like the emanation of ^{220}Rn from vacuum gauges or other instrumentation as well as from welding seams, which do not scale with the surfaces can be neglected [133].

- ^{222}Rn with a lifetime of $5.51\,\mathrm{d}$ is produced from the uranium chain (see appendix A.17). The decay of ^{222}Rn, which is of special interest for low-level experiments such as GERDA [134] or Borexino [135] is not an issue for KATRIN due to its rather long lifetime. The probability for a ^{222}Rn decay inside the spectrometer can be neglected ($< 0.07\%$) due to the large pumping speed of the TMPs with a corresponding pump-out time of about $360\,\mathrm{s}$.

Despite careful radio assaying and use of low-activity components, the structural elements of the spectrometers contain small traces of elements from these decay series, which subsequently can decay into radon, thereby generating a background source which is distributed homogeneously over the entire spectrometer volume. This work will focus on the reduction and signature of background processes due to the α-decay of ^{219}Rn emanating from the NEG material, and of ^{220}Rn emanating from the walls of the stainless steel recipient.

Nuclear decays occurring in the volume of the spectrometer can produce high-energy (keV-range) electrons, which are trapped in the magnetic bottle design of the spectrometer. Due to the exceedingly long electron cool-down times, a single electron can be stored for several hours. Hundreds of secondary electrons which are created via ionization of residual gas molecules are accelerated by the retarding potential and hit the detector. This results in a background component in the region-of-interest (ROI) which is indistinguishable from signal electrons. A primary electron thus slowly cools down until its storage conditions are broken due to

- reaching a minimum energy of $E_{\mathrm{kin}} \leq 1\,\mathrm{eV}$. The electron cannot be further trapped, due to the condition $E_{\mathrm{kin}} < \Delta E$ where the strong acceleration by the electric field allows the electron to leave the spectrometer towards the source or the detector.

- a starting energy of $E_{\mathrm{kin}} \geq 180\,\mathrm{keV}$, for which the electron cyclotron radius becomes larger than the radius of the spectrometer, so that the electron hits the wall.

- non-adiabatic effects in regions of low magnetic fields.

All these processes have been simulated in detail with KASSIOPEIA [63] [81]. The simulations revealed that for any given time there will be several high-energy electrons from radon α-decays which are stored. The actual number depends on the absolute pressure (which governs the storage time). Hence, an observation of single ring events at the main spectrometer, as recorded at the pre-spectrometer test setup cannot be expected.

7.3.2 Baffle Design and Vacuum Performance Simulation

The design of the large LN2 baffle at the main spectrometer pump ports is based on the experience gained during the prototype measurements at the pre-spectrometer test setup. The baffle system blocks the direct line of sight between the NEG pump

and the main volume, thus blocking all ^{219}Rn atoms emanating from the NEG strips while at the same time cryotrapping ^{220}Rn emanating from the walls of the spectrometer with a sticking probability α. The baffles introduce an additional conductance to the NEG pump. Thereby they reduce the effective pumping speed for hydrogen. To decrease the conductance of the baffle the center disk was dropped. Hence, the inlet area for hydrogen is increased, however at the price of a larger required cooling power due to the larger surface. A technical drawing of the baffle is shown in figure 7.9. To determine the vacuum performance of the baffle one pump port including a total of $1\,000\,\mathrm{m}$ of NEG material was simulated with *ProVac3D*[3], a Monte Carlo simulation tool developed by Dr. X. Luo (ITEP) [136] based on the accumulated time-of-flight method. The simulated particles were generated at a source plane following *Lambert's cosine law*[4]. ProVac3D follows a numerical approach to simulate the transient gas flow in the free molecular flow regime. By monitoring the particles in a first simulation, the reduction of the NEG pumping speed by the conductance of the baffle can be determined. In a second simulation, the baffle pumping speed for radon is calculated. For the simulations the geometry of one pump port including the NEG pump and the baffle was created, see figure 7.7.
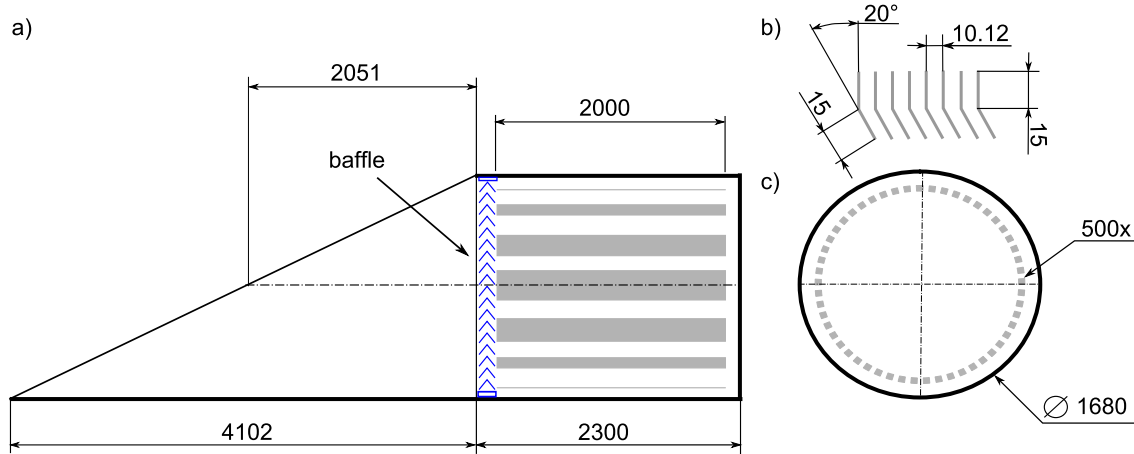
Figure 7.7: Technical drawing of one pump port of the main spectrometer. a) top view: the baffle system is indicated in blue, in the rear part of the port the NEG pump is located. **b)** Detail view of the NEG strips. Each $1\,\mathrm{m}$ long strip is bent by $20°$ to increase its stability. **c)** Cross section of the NEG pump: The $1\,006$ NEG strips are arranged in a circular shape (all values in mm).

The NEG pump was approximated by 500 strips each $2\,\mathrm{m}$ long and bent by $20°$. The surface of the NEG strips was set up as a two-sided reflector with a sticking coefficient of $\alpha = 2.8\,\%$ [138]. The rest of the pump port was treated as a diffuse reflector, with a reflection coefficient of $\Gamma = 1$. As particle source the entire opening area of the pump port was used, approximated by an ellipse with an area of $A = 5.85\,\mathrm{m}^2$. The number of particles to be simulated was set to $n = 10^7$. To calculate the pumping speed in this new setup, particles were started at the source area, from which they

---

[3]ProVac3D = Profile of the Vacuum system 3D complexities

[4]the number of particles observed from an ideal diffusely reflecting surface or ideal diffuse radiator is directly proportional to the cosine of the angle Θ between the observer's line of sight and the surface normal. A detailed test of ProVac3D and the particle generator used in the program is presented in [137].

can leave the simulation geometry by getting absorbed by the NEG pump (N) or by being reflected back into the spectrometer volume, hitting the source area. The pumping speed of the NEG pump can be calculated by determining the pumping probability P_{Ho} (referred as the *Ho factor* based on a publication by Ho in 1932 [139]). The Ho factor P_{Ho} is defined as the number of absorbed particles N divided by the number of started particles n:

$$P_{Ho} = \frac{N}{n}. \tag{7.1}$$

Hence, the pumping speed of the NEG pump S_{NEG} is given by

$$S_{NEG} = \frac{1}{4} \cdot \bar{v}(M, T) \cdot A \cdot P_{Ho}, \tag{7.2}$$

with the area of the pumping port cross section A, the pumping probability P_{Ho} and the mean thermal velocity $\bar{v}(M, T)$ (see table 7.2), which depends on the gas species mass M and the temperature T:

$$\bar{v}(M, T) = \sqrt{\frac{8RT}{\pi M}} \tag{7.3}$$

Table 7.2: Molar masses and mean thermal velocities of various gases ($T = 20\,°C$). According to equation 7.3 the thermal velocity is proportional to $1/\sqrt{M}$ at a constant temperature.

gas	molar mass (g/mol)	mean velocity (m/s)
H_2	2	1 762
HT	4	1 246
He	4	1 246
H_2O	18	587
N_2	28	471
air	29	463
Ar	40	394
CO_2	44	376
Rn	219	168

The simulations were performed both with and without LN2 cooled baffle. The dominant residual gas at $p < 10^{-11}$ mbar is molecular hydrogen. Additionally the simulation allows to cover HT as expected if extremely tiny traces amounts of tritiated molecules migrate from the WGTS to the spectrometer section. Since stored electrons from tritium β-decays in the spectrometer are a major background issue of the spectrometer [63] this inclusion of HT is of prime importance for future tritium scanning data. The Ho factor as well as the pumping speed for hydrogen and HT for one NEG pump are presented in table 7.3.

Table 7.3: Pumping speed of NEG pump with and without LN2 cooled baffle. The simulations covers one pump port with $1\,000\,m$ NEG strips. For hydrogen the baffle has a sticking coefficient of $\alpha = 1$ whether is warm or cold. Due to the production process not the whole surface of the getter strip is packed with getter material. The resulting systematic uncertainties are neglected.

	Ho factor P_{Ho} (%)	pumping speed NEG H_2 (m^3s^{-1})	pumping speed NEG HT (m^3s^{-1})
without warm baffle	12.65	325.86	230.42
with cold baffle	5.76	148.48	104.99

As a result of the extensive simulation, one finds that the pumping speed of the NEG pumps is reduced by 55%, implying in a conductance of $C_B = 272\,000\,\ell/s$ (see equation 5.12) and a reduced final equilibrium pressure in the main spectrometer of about $1.6 \cdot 10^{-11}$ mbar.

Due to the large cold surface of the baffle, the pumping speed S_B of the spectrometer for radon is increased significantly. The LN2-cooled baffles act as cryopumps, not only for the radon, but also for other residual gases such as H_2O, CH_4 or CO_2. The impact of the cooled baffles on the residual gas composition can be seen in figure 7.15 and figure 7.16. However, a noticeable improvement of the final pressure is not expected, because the pressure is still dominated by hydrogen, on which the baffle has no impact. To simulate the pumping speed of the large cryobaffles for radon, again the in-house code *ProVac3D* was used. The implemented geometry is displayed in figure 7.9. In this second simulation the NEG pump and the pump port were treated as diffuse reflectors with reflection coefficient $\Gamma = 1$. For each run the sticking coefficient α of the baffle was varied and $n = 10\,000$ particles were started at the source plane. The particles have two possibilities to leave the simulation: by being scattered back into spectrometer (hitting the source plane) or by getting adsorbed by the LN2-cooled baffle. The results of the simulation are plotted in figure 7.8. With an estimated sticking coefficient of $\alpha \approx 0.8$ [79] and by using equation 7.2 the pumping speed of the baffle is determined to $S_B(Rn) \approx (60 \pm 1)\,m^3/s$. This large number for $S_B(Rn)$, is expected to result in a quasi-perfect suppression of radon α-decays.
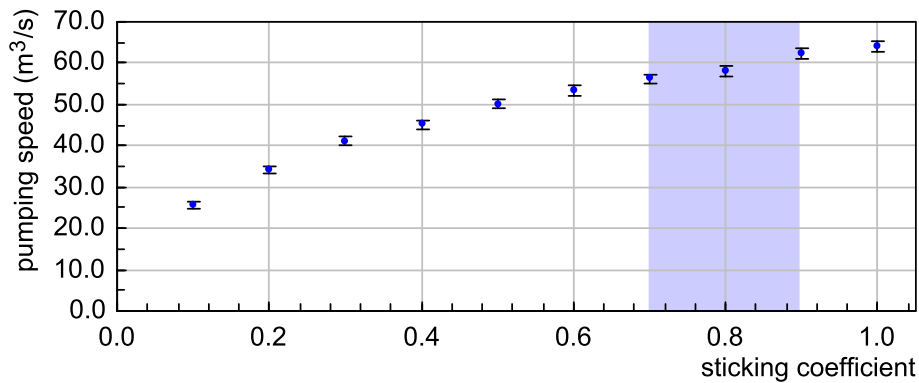
Figure 7.8: Pumping speed for radon of one baffle . The pumping speed for radon of the baffle $S_B(Rn)$ depends on the sticking coefficient α of its cold surfaces. It is estimated to $\alpha \approx 0.8$ [79] as highlighted in the plot.

7.3.3 Implementation of the LN2 Cooled Baffle System

The geometry of the LN2-cooled baffle was modelled and optimized on the basis of the above described simulation results. The technical drawing of the complete system is shown in figure 7.9. The LN2 baffles are mounted directly to the holding structure of the NEG pumps thus following the design at the pre-spectrometer (see figure 7.4). One NEG pump is composed of a cylindrical stainless steel holding structure that is loaded with sixteen NEG modules each carrying 63 NEG strips[5]. At the head end of the NEG pump the LN2-cooled baffle system is mounted. The stainless steel base parts for the LN2 supply are a parallel pipe framework welded in a ring pipe. After mounting this base part the V-shaped blades made of oxygen-free copper sheets were subsequently attached onto the pipe framework. Thus the surfaces of the cooled blades act as efficient cold trap for the radon isotopes, thus blocking (figure 7.9) the direct line of sight between the NEG pump and the volume of the main spectrometer. The system is filled from below with LN2. During the cool-down process gaseous nitrogen can escape through the return line until the baffle is completely flooded with LN2. A flexible spiral in the return line compensates any movement of the components due to thermal expansion.
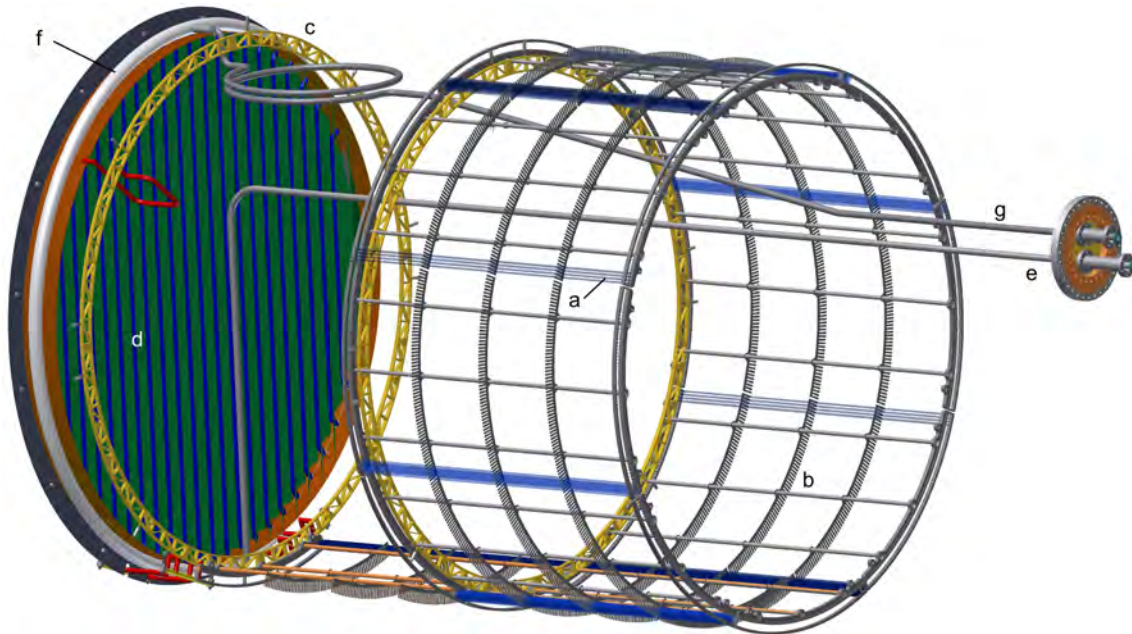
Figure 7.9: Main spectrometer Baffle setup. Baffle directly mounted to the NEG holding structure. Shown is the LN2 baffle system, a part of the NEG pump is blinded out to show the piping. In detail: **a)** NEG strip (four NEG strips are indicated at each module), **b)** NEG modules with combs to guide the strips, **c)** holding structure for NEG modules, **d)** LN2 baffle with V-shaped copper blades, **e)** LN2 flow line, **f)** LN2 ring pipe, **g)** LN2 return line with spiral to compensate movements of the components due to thermal expansion.

In combination with the NEG pump the baffles were one of the final hardware components that were mounted into the main spectrometer vessel. Figure 7.13 shows a picture of the fully assembled baffle (in pump port III). The picture was taken from the inside of the main spectrometer.

---

[5]The last module in each pump is shorter by one strip to allow the installation. Hence, the total number of NEG strips in each pump port sums up to 1 006

The large LN2 supply tank was manufactured by *Messer GmbH*[6] (see figure 7.10) and the associated control as well as the piping system was delivered by *Nexans*[7] (see figure 7.11). The vacuum insulated inner vessel of the LN2 supply tank has a volumetric capacity of $51\,550\,\ell$. A simplified flow chart for the main components is shown in figure 7.10a. To withdraw LN2 two extraction valves are available: valve number 36.1 is connected to the LN2 filling station in the monitor spectrometer building and valve number 36.2 is the LN2 supply line for main spectrometer hall (distributed by a valve box to the three baffles and a LN2 filling station at the detector platform, see next paragraph). As the baffle system requires an operating pressure of below 2 bar, the level drain valve number 30 can be used to relief pressure of the tank. To illustrate the considerable dimensions of the supply tank figure 7.10b shows the initial filling process done by two tank trucks, each with a volumetric capacity of about $20\,m^3$.
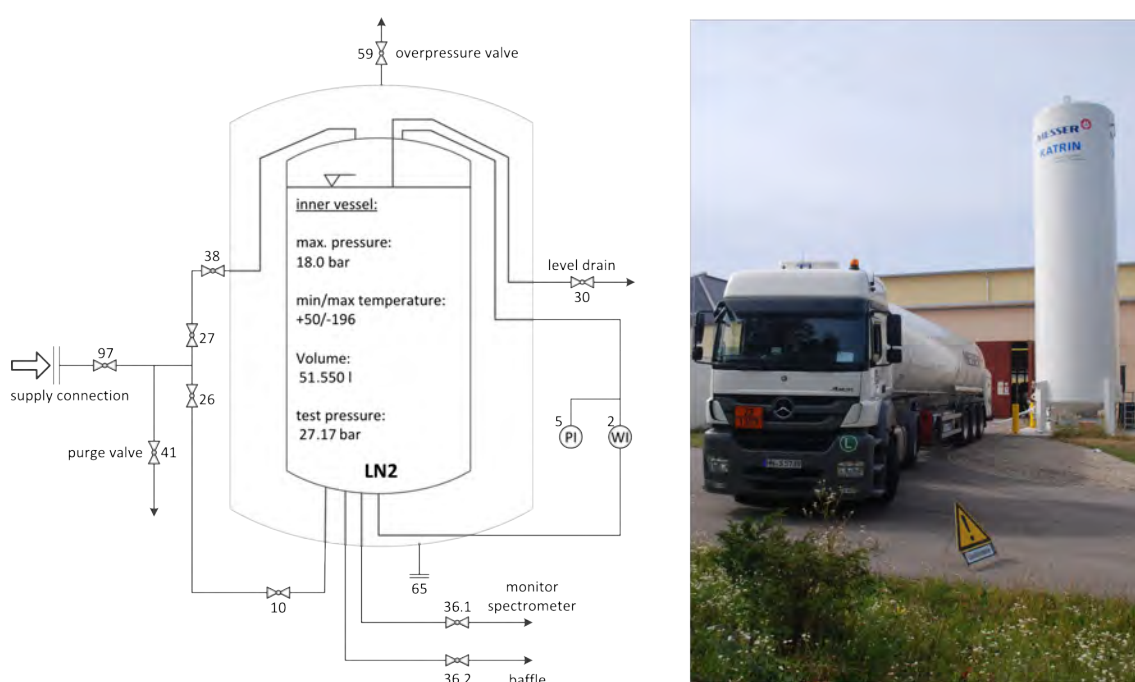
Figure 7.10: LN2 supply tank. Left) simplified LN2 flowchart of the LN2 supply tank. **Right)** To illustrate the dimensions of the supply tank the picture of the $51\,550\,\ell$ LN2 supply tank was taken during the initial filling process: *Messer GmbH* required two fully loaded tank trucks, each with a volumetric capacity of about $20\,m^3$.

The valve box for the LN2 distribution was manufactured by *Nexans*. A picture of the valve box is shown in figure 7.11a together with a simplified LN2 flowchart in figure 7.11b. The LN2 supply tank is connected with a flexible vacuum insulated pipe (*cryoflex* transfer line) to the valve box. This LN2 distribution system contains one entry flange, four remotely operated valves with an electropneumatic position controller and four exit flanges. The four valves control the baffle supply lines (B1 - B3) and the filling station at the detector platform. Flexible vacuum insulated pipes connect the valve box with the baffles via a high voltage separator, see next

---

paragraph. The same applies for the exhaust pipes. All three exhaust pipes lead out of the main spectrometer hall and each ends with a U-bend LN2 trap. During the baffle operation these bends prevent ambient air from entering the piping system. All *cryoflex* transfer lines are equipped with vacuum insulated couplings (*Johnston type*), as well as a pumping port and a rupture disk.
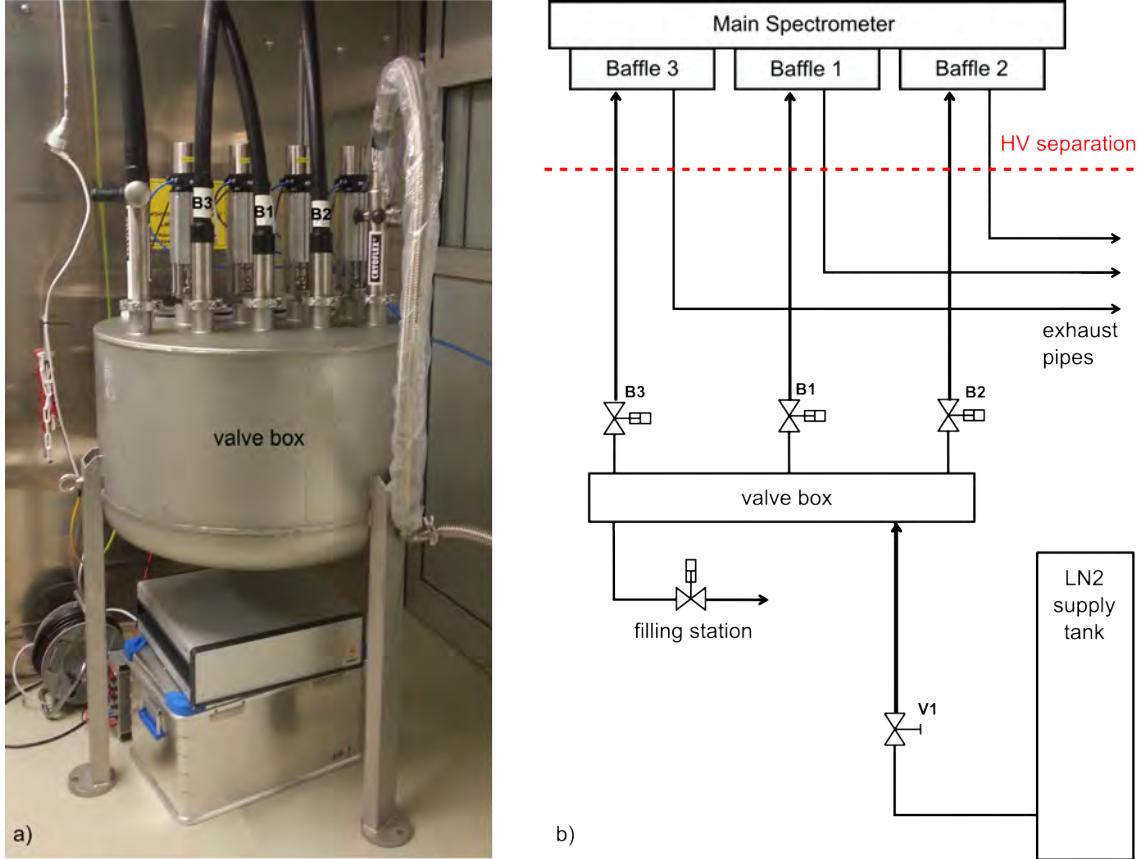
Figure 7.11: LN2 distribution scheme. a) The valve box was manufactured by *Nexans*. The LN2 connectors (from left to right) are: the LN2 supply pipe, Baffle 3, Baffle 1, Baffle 2 and indoor filling station at the detector platform. **b)** Flowchart of the baffle LN2 supply chain. The LN2 tank outside the spectrometer hall (see figure 7.10) is connected with a flexible vacuum insulated pipe with the valve box. The vacuum insulated valve box will be placed on the detector stage delivering LN2 for the baffle system and an indoor filling station at the detector platform. The flexible exhaust pipes are vacuum insulated too and equipped with a U-bend LN2 trap. During the baffle operation these bends prevent ambient air from entering the piping system.

The high voltage (HV) separator allows to connect the valve box and the exhaust pipes to the baffle system even in case of HV being applied to the spectrometer, so this connection must be electrically insulated. Liquid nitrogen has a relative permittivity of about 1.46 [140] and can therefore be used as an electrical insulating medium as long as no water or oxygen impurities are introduced into the system. The liquid nitrogen is guided through pipes which are manufactured of glass fiber reinforced plastic (GRP). To prevent icing and corresponding leakage currents these pipes are mounted in an insulating vacuum (pressure $< 10^{-3}$ mbar). The vacuum chamber is separated from ground potential by a DN150 ceramic insulator. In case of a bursting GRP pipe a safety pressure relieve valve was installed protecting the

ceramic. To enable an easy assembly extra flexible corrugated stainless steel pipes are used for the connections inside the insulating vacuum. The baffle temperature sensors are fed trough the cover flange and are connected to the HV cabinets of the main spectrometer. A technical drawing of the HV separator is shown in figure 7.12.
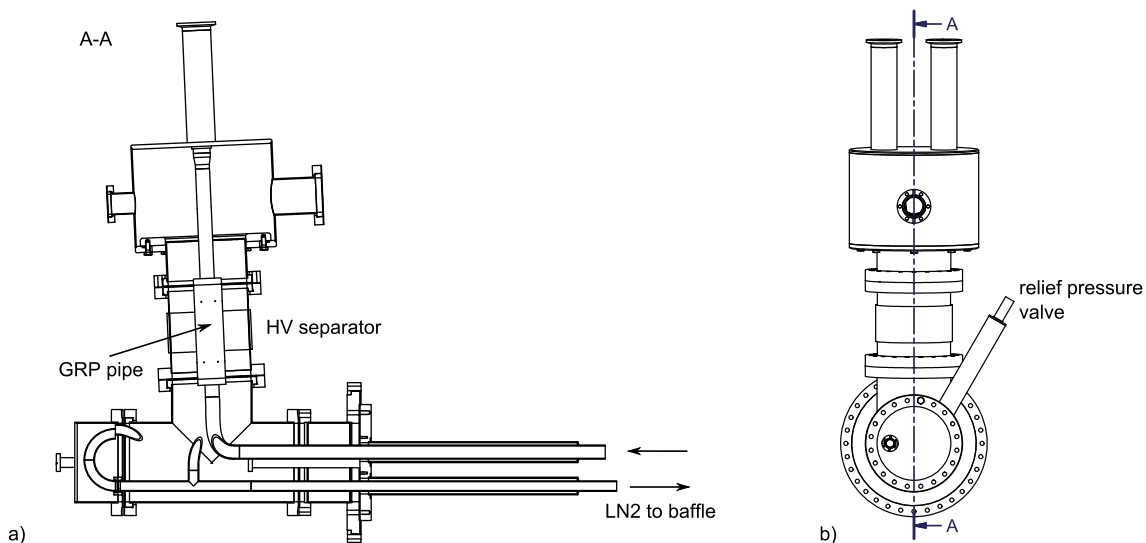
Figure 7.12: The HV separator[a] for the LN2 supply lines. **a)** Side view: a 2° bend of the top part allows a smooth connection of the LN2 pipes. Two glass fiber reinforced plastic (GRP) pipes inside of a ceramic insulator guide the liquid nitrogen. **b)** Front view: A relieve pressure valve opens in case of a LN2 leak or a sudden pressure increase.

---

[a]technical drawing by K. Vogt, 2013
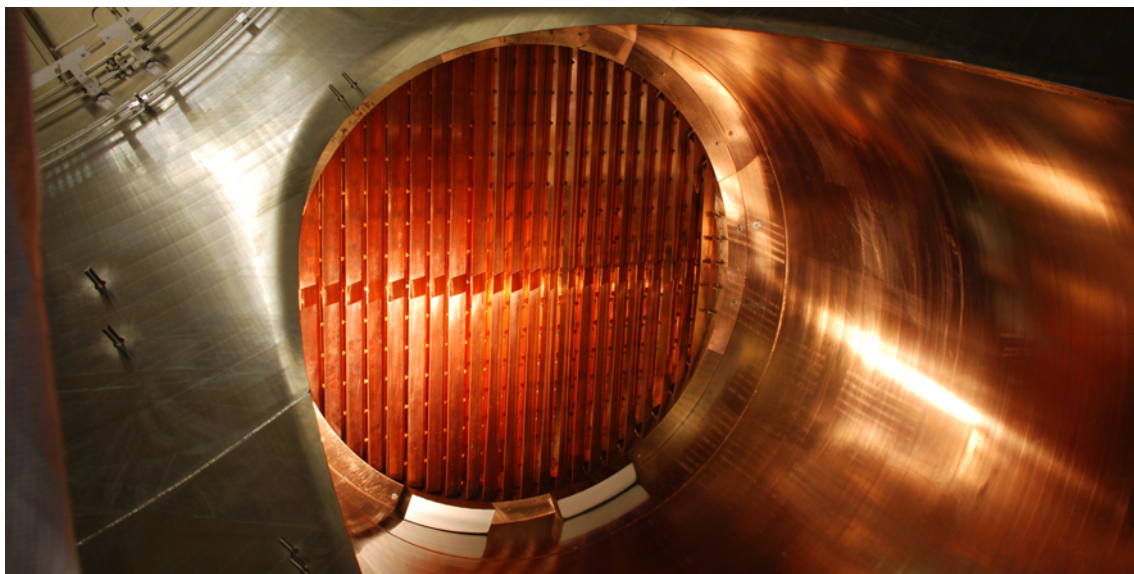
Figure 7.13: Fully assembled LN2 Baffle in pump port III, the picture was taken[a] from the inside of the main spectrometer. The V-shaped copper sheets are attached to a stainless steel pipe framework that is conducting the LN2. There is no direct line of sight between the NEG pump and the volume of the main spectrometer.

---

[a]picture taken by Dipl.-Phys. M. Zacher, 2012.

7.4 Investigation of Radon-Induced Background and the Baffle Efficiency

With the large area LN2-cooled baffle being implemented, one of the major tools of the first commissioning phase of the KATRIN main spectrometer was to test the overall functionality of the baffle system and in particular to investigate its efficiency. To do so, it is essential to set up first a detailed model of radon removal and radon emanation to guide experimental procedures as well as data analysis efforts. From these investigations and the input of independent measurements with artificially increased pressure, the activity of the different radon sources can be estimated and the removal efficiency can be deduced.

7.4.1 Main Spectrometer Radon Background Model

A prime objective of the radon background model is to successfully describe the measured electron background rate at the detector $r(i)$ as a function of the number i of cooled baffles. This budget has to include the rate $r_{\mathrm{NEG}}(i)$ due to radon emanating from the NEG pumps and the bulk material of the vessel walls $r_{\mathrm{vessel}}(i)$, as well as a constant rate $r_{\mathrm{const.}}$ due to non-radon-induced background processes such as secondary electrons or field emission from the inner electrode:

$$r(i) = (3 - i) \cdot r_{\mathrm{NEG}}(i) + r_{\mathrm{vessel}}(i) + r_{\mathrm{const.}} \tag{7.4}$$

The different rates depend on:

- the amount of radon emanating from different sources. The radon sources taken into account by this model are: ^{219}Rn emanation of the NEG pumps $E_{\mathrm{Rn219}}^{\mathrm{NEG}}$ and ^{220}Rn emanation[8] of the spectrometer vessel $E_{\mathrm{Rn220}}^{\mathrm{vessel}}$.

- the average number of electrons ϵ_{2nd} generated by a radon decay that reach the detector. This value can only be deduced from detailed KASSIOPEIA simulations.

- the probability $P_{\mathrm{Rn}}(i)$ of a radon α-decay in the spectrometer as a function of the effective pumping speed (and hence, on the number of cold baffles i) and the lifetime of the different radon isotopes.

The measured rate can thus be written as:

$$\begin{aligned} r(i) &= (3 - i) \cdot E_{\mathrm{Rn219}}^{\mathrm{NEG}} \cdot \epsilon_{\mathrm{2nd}} \cdot P_{\mathrm{Rn219}}(i) \\ &+ E_{\mathrm{Rn220}}^{\mathrm{vessel}} \cdot \epsilon_{\mathrm{2nd}} \cdot P_{\mathrm{Rn220}}(i) \\ &+ r_{\mathrm{const.}} \end{aligned} \tag{7.5}$$

with the decay probability $P_{i,\mathrm{Rn}}$:

$$P_{\mathrm{Rn}}(i) = \left(1 + \frac{\tau_{\mathrm{Rn}} \cdot (S_{\mathrm{TMP}} + i \cdot S_{\mathrm{B}})}{V}\right)^{-1} \tag{7.6}$$

---

[8]The ^{219}Rn emanation $E_{\mathrm{Rn219}}^{\mathrm{vessel}}$ of the spectrometer vessel is expected to be much smaller compared to $E_{\mathrm{Rn219}}^{\mathrm{NEG}}$ (see table 7.4) and therefore is neglected in the following.

where S_{TMP} denotes the pumping speed of the TMPs, S_{B} represents the radon pumping speed of one baffle and $V = 1.24 \cdot 10^6 \, \ell$ is the volume of the main spectrometer. The decay probability depends on the lifetime of the radon isotopes: $\tau_{\text{Rn219}} = 5.71 \, \text{s}$ and $\tau_{\text{Rn220}} = 80.2 \, \text{s}$.

The complete radon emanation and capture model is given by:

$$
\begin{aligned}
r(i) \;=\;\; & (3 - i) \cdot E_{\text{Rn219}}^{\text{NEG}} \cdot \epsilon_{\text{2nd}} \cdot \left(1 + \frac{\tau_{\text{Rn219}} \cdot (S_{\text{TMP}} + i \cdot S_{\text{B}})}{V} \right)^{-1} \\
+\;\; & E_{\text{Rn220}}^{\text{vessel}} \cdot \epsilon_{\text{2nd}} \cdot \left(1 + \frac{\tau_{\text{Rn220}} \cdot (S_{\text{TMP}} + i \cdot S_{\text{B}})}{V} \right)^{-1} \\
+\;\; & r_{\text{const.}}
\end{aligned}
\tag{7.7}
$$

leaving the emanation of radon ($E_{\text{Rn219}}^{\text{NEG}}$ and $E_{\text{Rn220}}^{\text{MS}}$) as well as the constant background rate $r_{\text{const.}}$ as free fit parameters. The table 7.4 gives a summary of the expected radon emanation rates and the calculated pumping speeds for the different radon isotopes and hydrogen.

Table 7.4: Input parameters for the calculation of the radon decay rates. Listed are the expected emanation rates of radon isotopes in the main spectrometer from the 3 000 m NEG strips as well as from the inner surface of the vessel. The values are extrapolated from measurements at the pre-spectrometer. Furthermore the table holds the calculated effective pumping speed for hydrogen and radon of the TMPs, the NEG pump and the baffles. For the cold surfaces of the baffles a sticking coefficient of $\alpha = 0.8$ is assumed. Finally the lifetime of the radon isotopes is listed. The volume of the main spectrometer is $V = 1.24 \cdot 10^6 \, \ell$.

isotope:	H_2	$^{219}\text{Rn}_{\text{NEG}}$	$^{219}\text{Rn}_{\text{vessel}}$	$^{220}\text{Rn}_{\text{vessel}}$
estimated radon activity (1/s)				
E	-	0.14 ± 0.03	0.03 ± 0.03	0.08 ± 0.06
effective pumping speed (ℓ/s)				
S_{6xTMPs}	12 010	3 510	3 510	3 500
$S_{\text{warmBaffles}}$	445 000	0	0	0
$S_{\text{3xcoldBaffles}}$	445 000	180 000	180 000	180 000
lifetime (s)				
τ	stable	5.71	5.71	80.2

7.4.2 Measurement Parameters and Standard Background Cuts

In the following first results of the KATRIN spectrometer commissioning period of mid-summer 2013 are presented. During this phase many important results on cosmic induced background and transmission properties were achieved which have validated, for example due to the complete lack of even minute Penning traps, the soundness of these spectrometer electromagnetic design (details can be found in chapter 4 and [141]).

In the following this section focuses only on those parts of the commissioning measurements which were performed in the framework of this thesis. The background

measurements of this work were split in two parts. The measurements and their parameters are summarized in table 7.5.

1. **Main spectrometer at ground potential**: In the first round of measurements no high voltage could be fed to the vessel. For these reasons a retarding voltage of 'only' up to $-600\,\mathrm{V}$ was applied to the inner wire electrode system to accelerate background electrons to the detector. Prior to their arrival there, electrons were further accelerated by a post-acceleration electrode elevated to $+10\,\mathrm{kV}$. A number of different settings were tested to increase the parameter $\epsilon_{2\mathrm{nd}}$ and therefore to amplify the radon-induced background. The baffles were sequentially cooled down with LN2. The required LN2 reservoir was provided by the supply tank and operated via the PCS7 system controlling the valve box. For the temperature change over time see figure 7.14.

2. **Measurements with high voltage $U_{tank} = -18.5\,\mathrm{kV}$**: Due to the missing HV separator for the LN2 lines (see figure 7.12) the three baffles were fed by three $200\,\ell$ LN2 cryostats which were electrically insulated by polyethylene blocks. This method has required additional safety measures and has allowed the operation of the baffles only for a limited time (a total of about $8\,\mathrm{h}$, including a $4\,\mathrm{h}$ cool-down phase). To increase the measurement time, all three baffles were cooled down in parallel, see figure 7.21. Two different magnetic field configurations were measured, and only one offset voltage of the inner wire electrode was used.

Table 7.5: Parameters used for the main spectrometer baffle measurement. The different ring segments of the inner wire electrode system were used to fine tune the electrostatic retarding potential. The magnetic field is given in the center of the analyzing plane. For the high voltage measurements $U_{\mathrm{vessel}} = -18.5\,\mathrm{kV}$ the default settings for background measurements at symmetric magnetic fields were chosen.

setting	magnetic field (Gauss)	U_{vessel} (kV)	inner electrode offset (V)			
			ring 5-13	ring 4+14	ring 3+15	ring 2+16
A	3.8	0	-600	-500	-400	-300
B	9.0	0	-600	-500	-400	-300
C	3.8	0	-30	-30	-30	-30
D	3.8	-18.5	-100	0	0	0
E	9.0	-18.5	-100	0	0	0

To analyze the data, the following software-based cuts were used. The cuts follow from experience gained during the detector standalone measurements, as well as from specific restrictions due to precision of the system alignment measurements during the main spectrometer and detector (SDS) commissioning. These second level cuts are described in [142].

- **Multipixel Cut:** In order to exclude single events that deposited their energy on two or more detector pixel at once (multipixel events), detector events with inter-arrival times of less than $2\,\mu\mathrm{s}$ are filtered out.

- **Veto Cut:** Events generated by cosmic rays (e.g. cosmic muons) in the detector region are excluded from the analysis. This is done via a coincidence measurement with the detector veto system. Events within a $\pm 2\,\mu$s coincidence window of a veto event are excluded.

- **Flapper Pixel Cut:** Since it was not possible to open the flapper (see figure 3.5) of the detector in-line beam valve completely during the SDS measurement phase, a total 21 detector pixel were shadowed by the flapper valve and do not see inside the spectrometer. These pixels lie at top quarter of the wafer and are excluded from the analysis.

- **Detector Chamber Pixel Cut:** Due to misalignments in the SDS beamline, five detector pixel look onto the walls of the detector vacuum chamber. These pixel are also excluded from the analysis.

- **Energy Region of Interest (ROI) Cut:** All SDS measurements have been performed with an electronic shaping length of $1.6\,\mu$s for each pixel read-out channel. For this shaping length the detector energy resolution is larger than $2\,$keV. Thus, the region-of-interest for the analysis of the SDS measurements has been chosen to be $5\,$keV wide. Here, an asymmetric ROI around the electron peak position is used due to the specific peak profile. The ROI is defined from $3\,$keV below the electron peak position to $2\,$keV above the peak position: e.g. for a $-18.6\,$kV potential of the spectrometer, and a $-10\,$kV post-acceleration electrode (PAE) potential, the peak position is located approximately at $-28.6\,$keV[9]. Therefore, the ROI is defined from $-25.6\,$keV to $-30.6\,$keV.

Analysis approach: to investigate the measured datasets the following standard analysis approaches were chosen to determine the background rates and their uncertainties. The mean rate r is extracted from the rate trend graph[10] provided by the KATRIN internal code package BEANS[11] by fitting a constant while the error on the rate is determined by the standard deviation of the mean: $\sigma_r = \sqrt{r \cdot t}/t$ with the duration t of the measurement.

Monitoring the Baffle temperature. The temperature of the baffle was measured by two PT1000 temperature sensors at each baffle. The sensor `435-RTP-5-X080` at top of the baffle measures the temperature of the return pipe, the sensor at the bottom of the baffle `435-RTP-5-X081` measures the temperature of the flow line. The PT1000 sensors are connected with beryllium copper (BeCu) rods. As in case of the inner wire electrode system, a deformation of the rods during the bake-out cycle was observed. As a result the monitoring system lost contact to more than half of the temperature sensors. During the ongoing upgrade of the NEG pump (see chapter 6) the BeCu rods will be replaced by copper connectors. The criterion 'cold baffle' is monitored with the temperature sensors at the return pipe of each

---

[9]shifted to lower energies due to the dead layer of the detector.
[10]if not stated different a binning of $60\,$s was used.
[11]developed by Dr. S. Enomoto at the University of Washington.

baffle with a benchmark $T_{\text{baffle=cold}} \leq 160\,\text{K}$. The whole system was flooded with liquid until LN2 was gushing out of the exhaust pipes. The monitored temperature was influenced by the position of the PT1000 sensor and the temperature of the spectrometer vessel. The actual baffle temperature is estimated to lie very close to the temperature of LN2.

7.4.3 Measurements with the Main Spectrometer at Ground Potential

In the first suite of measurements, no high voltage could be applied to the vessel, so the inner wire electrode system was used to accelerate electrons to the detector. A number of different settings were tested to amplify the radon-induced background. The most significant results were obtained with the central part of the inner wire electrode system being elevated to $-600\,\text{V}$. With each step the steep cones parts of the inner electrode system (see section 4.2) were graded by $+100\,\text{V}$ (see setting **A** and **B** in table 7.5). This potential configuration generates an *avalanche effect* [143] for background inside the main spectrometer. The secondary electrons induced by the radon α-decay are re-accelerated and trapped again when leaving the spectrometer. During this process electrons gain energy in the field gradients and ionize more residual gas molecules. Hence, the radon-induced background is enhanced.

To evaluate the effects of the baffles in this 'cascaded' field arrangement the system was sequentially cooled down with liquid nitrogen. The required LN2 was provided by the supply tank and operated with the PCS7 system controlling the valve box. For the temperature change over time see figure 7.14. This initial baffle operation consumed about $7.2\,\text{m}^3$ LN2 and took about $82\,\text{h}$.
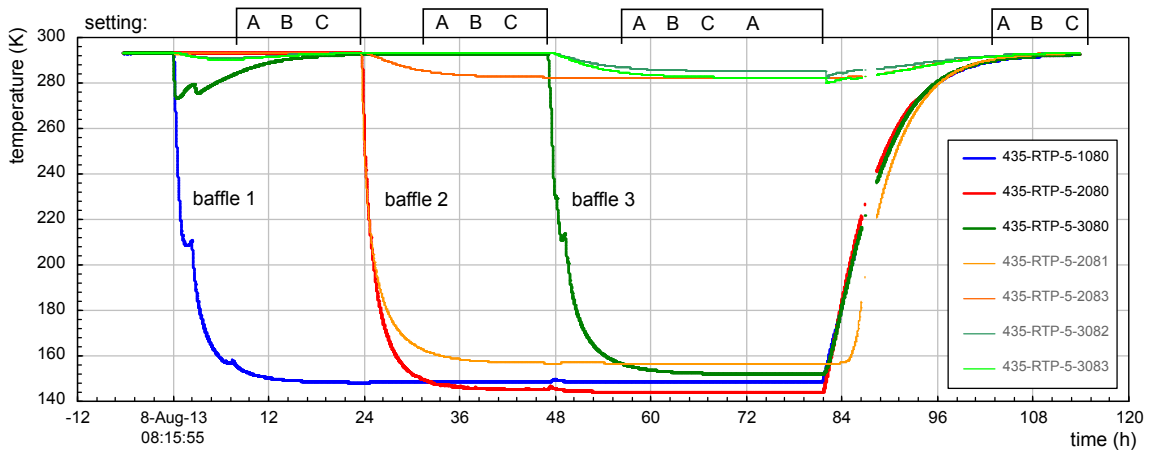
Figure 7.14: Course of the temperature inside the pump port. All measurements were performed with $U_{\text{tank}} = 0\,\text{kV}$. The different settings (for the parameters see table 7.5) are indicated at the top of the plot. Next to the temperature sensors at the return pipe of the baffle (`435-RTP-5-X080`), the temperature sensors placed at the NEG pump are listed, too.

In parallel the cool-down process was monitored with a residual gas analyzer (RGA), see figure 7.15. The partial pressure of CH_4 is an excellent marker of the baffle status, as this molecule species is correlated with the number of cooled baffles. Small steps can be seen at the beginning of the cooling of each single baffle at $t_{\text{B1}} = 0\,\text{h}$, $t_{\text{B2}} = 24\,\text{h}$ and $t_{\text{B3}} = 48\,\text{h}$. The partial pressure of nitrogen and CO_2 slowly decrease

during the measurement, pointing towards a rather small pumping speed for these gases. An effect of the baffles on H_2O molecules is only visible during the cooling of the last baffle in pump port III, interestingly the same port where the RGA is mounted. Since the latter is connected via a 40 mm diameter tube to the pump port, the removal of local outgassing of water may cause this effect. As expected, hydrogen remains the dominant residual gas, and stays unaffected from the LN2 cold surfaces of the baffle. Hence, the overall pressure remains virtually unchanged during the measurement.

As shown in figure 7.17 and figure 7.18 the measured background rate is modified if a baffle is cooled down. The large fluctuations of the rate when the baffles are at room temperature are typical for the non-Poissonian background induced by the radon α-decays. During the cool down and the defrosting setting **A** was chosen to amplify the radon-induced background. The plots show a rather fast change in the background rate at a transition temperature of $220 - 240$ K, as expected.

During the defrosting of the baffles the residual gas composition was also monitored with an RGA (see figure 7.16). After a time period of about 82 h the main valve at the LN2 supply tank was closed. At first a small increase of the partial pressure of nitrogen was observed which was followed by a major release of methane and, after a longer period of two hours, of a small increase of CO_2 (dry ice). The gas composition stabilized at the same level as before the measurement.

Before the radon emanation rates can be calculated from these numbers, the average number of secondary electrons ϵ_{2nd} generated by a single radon α-decay has to be known. The number of secondaries ϵ_{2nd} was determined by corresponding KAS-SIOPEIA [81] simulations and is defined as the average number of electrons hitting the detector over the course of a radon decay. Table 7.6 summarizes the results of the simulations. This number includes all relevant effects stemming from parameters such as different potentials at the inner wire electrode and the dependence of the visible flux tube volume to the magnetic field setting. Because of the existence of the novel avalanche effect the parameter ϵ_{2nd} strongly depends on the electromagnetic setting. A trapped high-energy electron from a radon α-decay can thus generate a particularly larger number of secondary electrons that are accelerated towards the detector and further ionize additional residual gas molecules in the distinct potential gradients.

Table 7.6: Simulated[a] number of secondary electrons ϵ_{2nd} produced by a radon α-decay. For each setting about 1 000 radon decays were simulated in the main spectrometer. By counting the electrons that hit the detector the mean number of secondary electrons ϵ_{2nd} can be determined.

setting	simulated decays	detector hits	mean number of secondary electrons
A	963	34 737	36.1 ± 1.4
B	976	17 463	17.9 ± 0.7
C	998	3 822	3.8 ± 0.2

[a]simulated with KASSIOPEIA by Dr. N. Wandkowsky
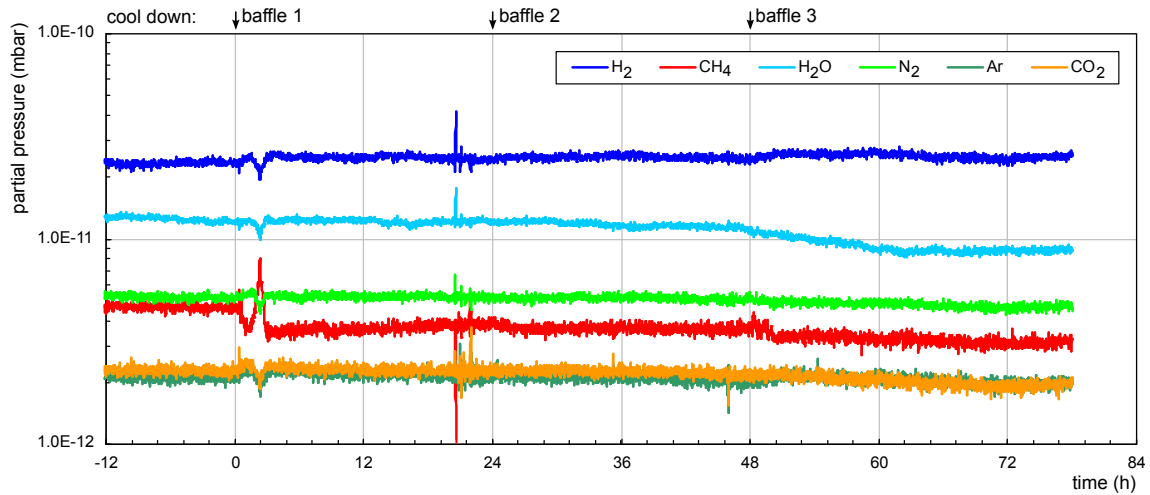
Figure 7.15: Course of the partial pressure during the cool down phase of the baffles. The baffles were cooled down sequentially at $t_{B1} = 0\,h$, $t_{B2} = 24\,h$ and $t_{B3} = 48\,h$. Hydrogen as the dominant residual gas is unaffected by the cooled baffles. A decrease of the water peak is only seen after cooling baffle 3. Small steps in the partial pressure of CH_4 are observed corresponding to the number of cool down baffles. The partial pressure of nitrogen and CO_2 are slowly decreasing during the cool down, pointing towards a small pumping speed for these gases.
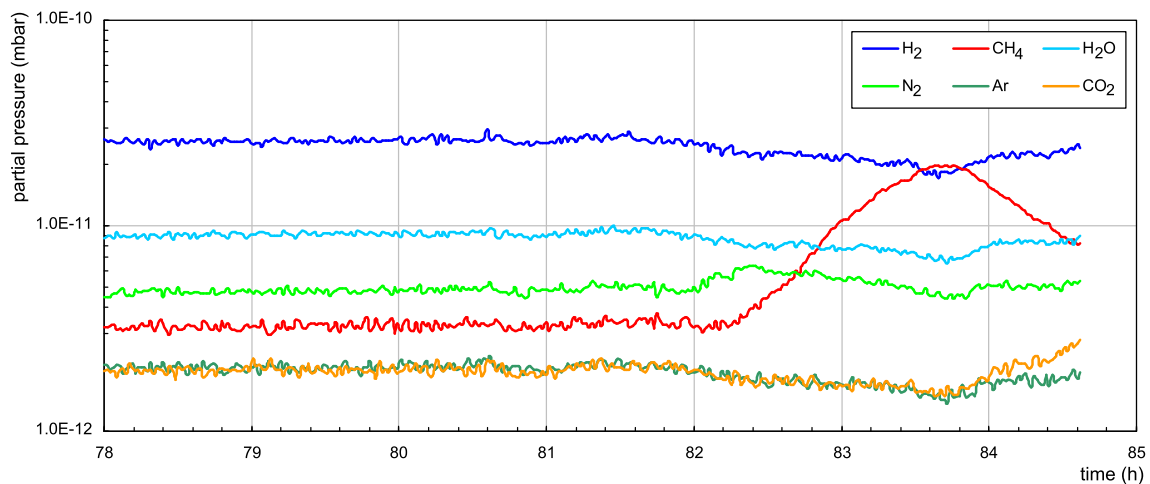
Figure 7.16: Residual gas composition during the defrosting of baffle system. The supply was cut at $t \approx 82\,h$ an increase of N_2, CH_4 and CO_2 was observed.
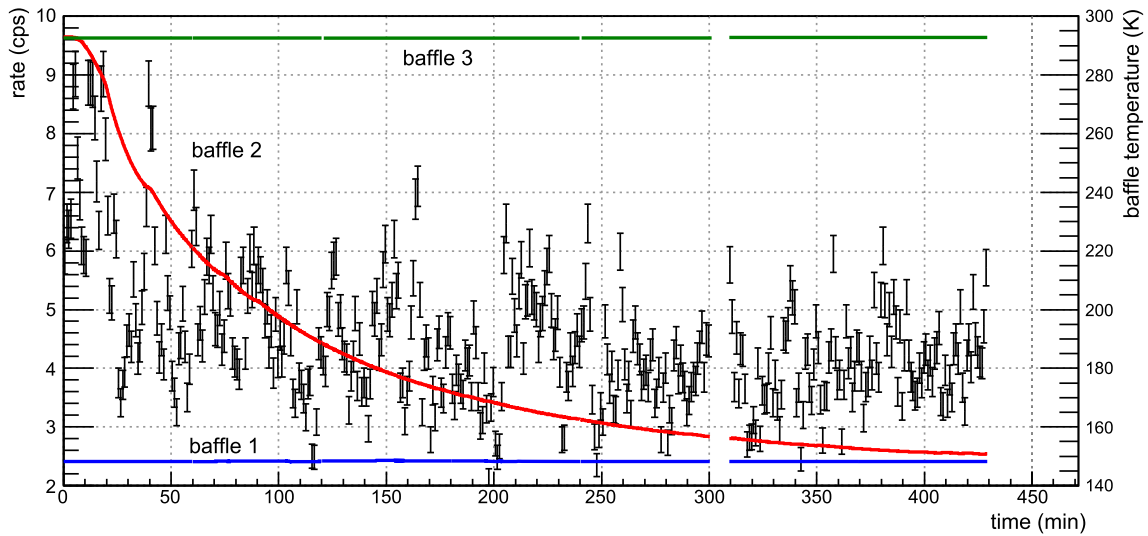
Figure 7.17: Rate over time plot during the cool down of baffle 2. Setting **A** was chosen to amplify the radon-induced background. To monitor the temperature of the baffles the following sensors at the return pipes were used: `435-RTP-5-1080` (blue), `435-RTP-5-2080` (red) and `435-RTP-5-3080` (green).
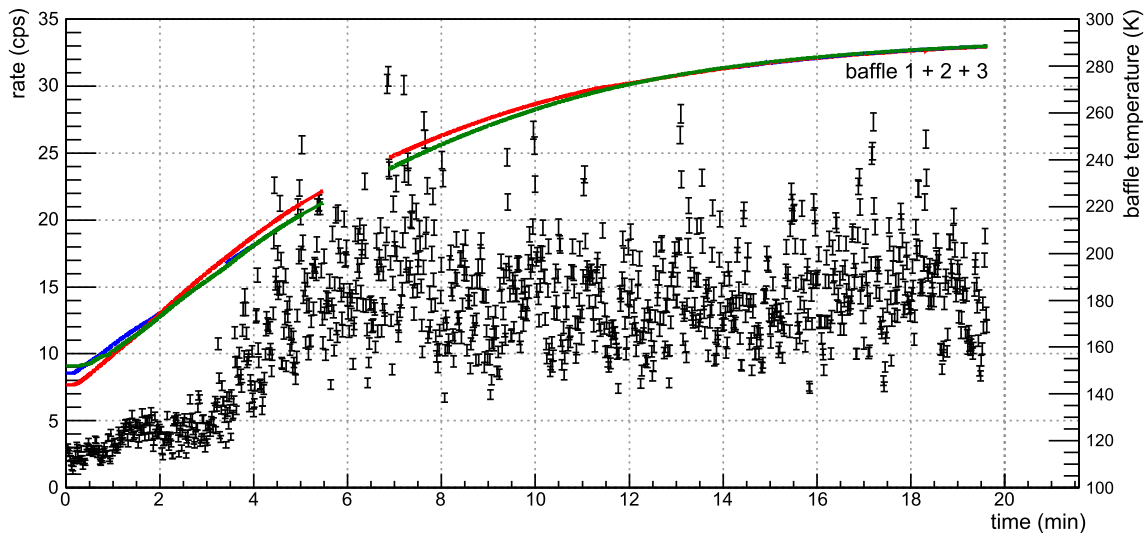
Figure 7.18: Defrosting of baffle system. Setting **A** was chosen to amplify the radon-induced background. To monitor the temperature of the baffles the following sensors at the return pipes were used: `435-RTP-5-1080` (blue), `435-RTP-5-2080` (red) and `435-RTP-5-3080` (green). The rate increasing by a factor of about 5.

133

The radon model was used to perform fits to the measured background rates with both setting **A** and **B**. As numerical minimization code the well-known computer program MINUIT2 was used, which is available as an optional package in the *ROOT* [144] release. The radon model was implemented as a subroutine into this code, thereby defining the function to be optimized. Due to the existing avalanche effect the radon decays induce a rather high mean rate in the range of a few counts per second and thus dominate the background in the spectrometer. Accordingly, the background reduction factor strongly depends on the number of cooled baffles. With all three baffles operating at nominal LN2 temperatures, setting **A** resulted in a background reduction factor of 5.7, while setting **B** yielded a factor of 8.5. The higher magnetic field strength in setting **B** reduces the visible flux tube volume and therefore focuses on the center of the spectrometer where the high-energy electrons of radon α-decays are more likely to remain stored over long periods of time. The fit results are presented in figure 7.19, figure 7.20 and in table 7.7.

The radon background model did not yield reasonable fit results in case of setting **C**. The reasons may be found in the very low retarding potential of $-30\,\mathrm{V}$:

- the simulation did not take into account non-adiabatic behavior,

- small electric dipole fields may have disturbed the measurements (especially at low retarding potentials) and

- a higher constant background rate due to unknown background components disrupt the background composition.

The mean experimental rate of setting **A** compared to setting **C** differs by a factor 100, whereas the simulated number of secondary electrons deviates only by a factor of 10. For very small retarding voltages, the background behavior is rather peculiar due to exceedingly long storage times which can exceed the measurement time so that the generic radon background model developed in this work can not be applied anymore.

Table 7.7: The following results were extracted from the radon background model after the fit to the measured rates. Shown are the radon emanation rates $E_{\mathrm{Rn219}}^{\mathrm{NEG}}$ (for all three NEG pumps) and $E_{\mathrm{Rn220}}^{\mathrm{vessel}}$ as well as the constant background rate $r_{\mathrm{const.}}$. The pumping speed of the baffle S_B was constrained to $60 \pm 1\,\mathrm{m^3/s}$ based on the results of the simulation shown in figure 7.8. The fitter is allowed to adjust this value using the 'pull'-method [145].

setting	$E_{\mathrm{Rn219}}^{\mathrm{NEG}}$ (1/s)	$E_{\mathrm{Rn220}}^{\mathrm{vessel}}$ (1/s)	$r_{\mathrm{const.}}$ (cps)	S_B (ℓ/s)
A	0.114 ± 0.005	0.326 ± 0.01	1.75 ± 0.03	$59\,246 \pm 1\,050$
B	0.067 ± 0.003	0.286 ± 0.01	0.31 ± 0.01	$60\,700 \pm\ \ 977$

When only data of electromagnetic setting **A** and **B** are compared, both fits show a rather good agreement for the expected emanation rate of ^{219}Rn (see table 7.4) which emanates dominantly from the NEG material. When comparing the fit results for the emanation of ^{220}Rn to the estimate based on the pre-spectrometer measurements a larger (factor 4) emanation rate at the main spectrometer could be deduced. However, given the rather large uncertainties of the earlier data, it is difficult to assess whether this is a statistical fluctuation only, or truly represents an unknown
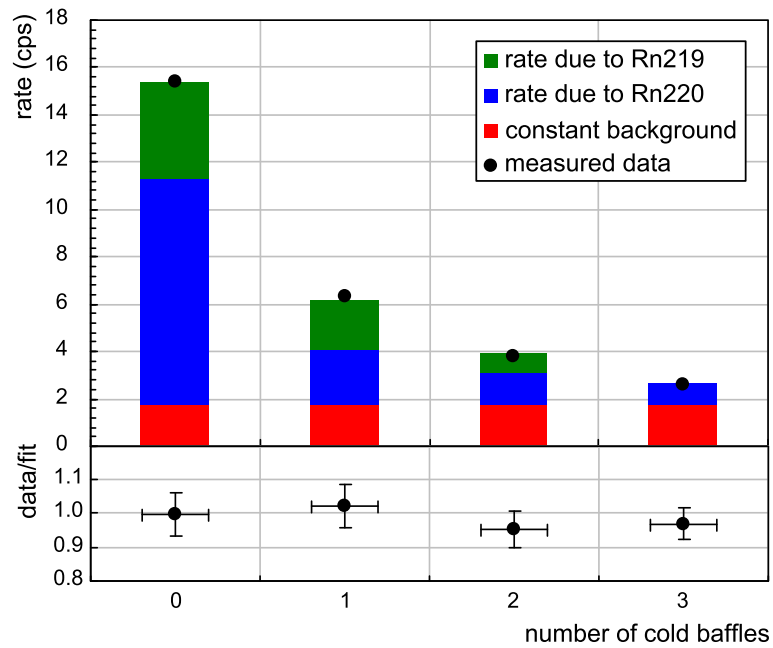
Figure 7.19: Fit of the radon background model to measured data (setting A). The resulting rates of the best fit values are indicated in the plot. By dividing the measured data by the result of the best fit the quality of the radon background model is indicated in the lower part of the figure.
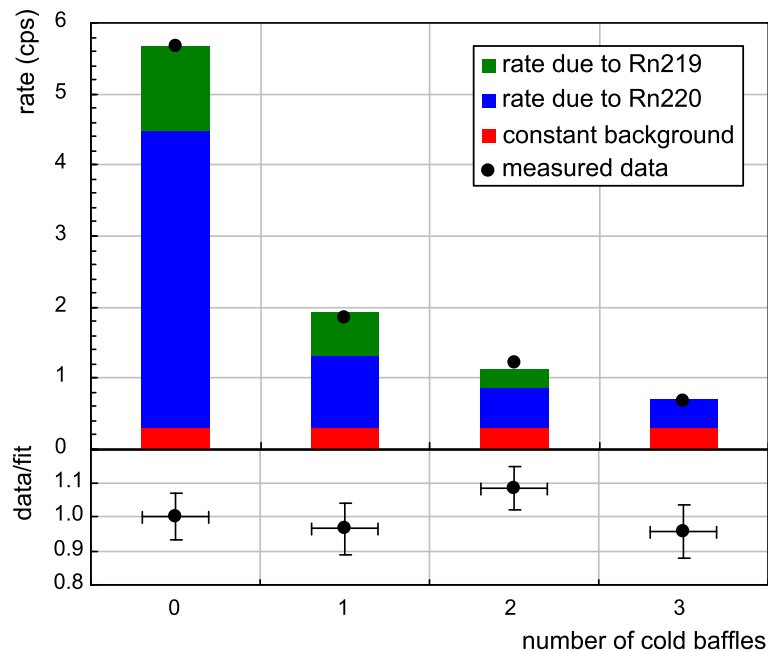
Figure 7.20: Fit of the radon background model to measured data (setting B). The resulting rates of the best fit values are indicated in the plot. By dividing the measured data by the result of the best fit the quality of the radon background model is indicated in the lower part of the figure.

additional ^{220}Rn source in the main spectrometer. Also, the fit strongly depends on the Monte Carlo simulation results the number of secondary electrons ϵ_{2nd}. By calculating the ratio of the radon activity in the spectrometer this simulation input is eliminated, see table 7.8. The activity of radon is determined by equation 7.8:

$$A_{\text{Rn}} = E_{\text{Rn}} \cdot P_{\text{Rn}} = E_{\text{Rn}} \cdot \left(1 + \frac{\tau_{\text{Rn}} \cdot S_{\text{TMP}}}{V}\right)^{-1} \tag{7.8}$$

Table 7.8: Resulting activities and their ratio. Shown are the used setting, the activity of ^{219}Rn and ^{220}Rn as well as their ratio. In the ratio of the activities the ϵ_{2nd} is eliminated. Hence, this value is free from simulation input.

setting	$A_{\text{Rn219}}^{\text{NEG}}$ (1/s)	$A_{\text{Rn220}}^{\text{MS}}$ (1/s)	$A_{\text{Rn219}}^{\text{NEG}}/(A_{\text{Rn219}}^{\text{NEG}} + A_{\text{Rn220}}^{\text{MS}})$
A	0.112 ± 0.005	0.266 ± 0.010	0.30 ± 0.01
B	0.065 ± 0.003	0.233 ± 0.082	0.22 ± 0.01

7.4.4 Baffle Measurements with High Voltage (HV) Applied

In order to obtain a better understanding of the contributions from muon-induced secondary emission electrons and stored electrons from radon decays to the overall background, measurements with nominal HV on the vessel and an operating baffle system are essential. As a standard long-term operation of the baffle was not possible during this work due to delays in the manufacturing at an industrial partner, a setup following the principle of the pre-spectrometer test setup was chosen. Therefore, each baffle was cooled with a $200\,\ell$ LN2 reservoir in a cryostat placed on a polyethylene block for electrical insulation. This approach restricts the useful measurement time with the baffle at LN2 temperature to about $4\,\text{h}$ after a $4\,\text{h}$ cool-down phase. Two different magnetic field settings were chosen as well as one inner electrode setting (**D** and **E**), see table 7.5. The temperature curve is shown in figure 7.21.
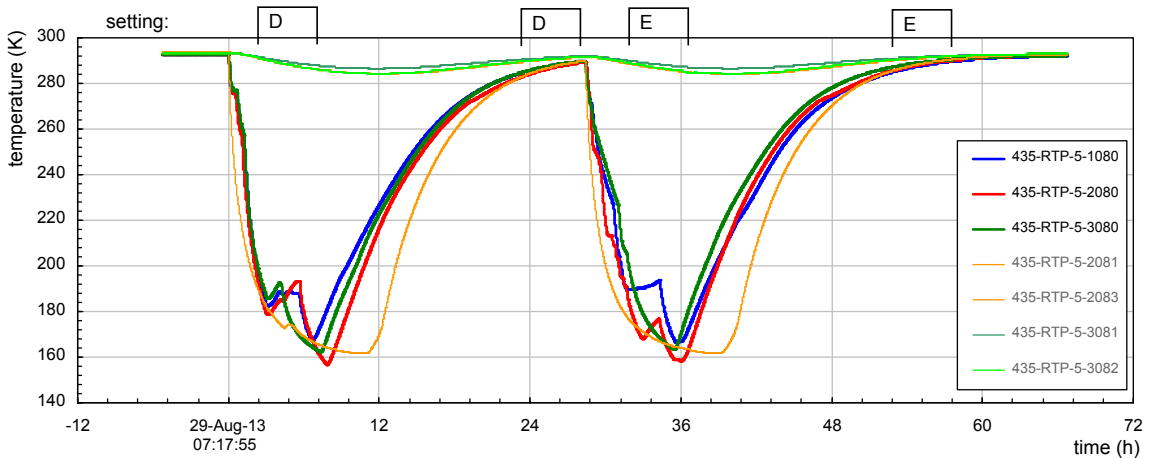
Figure 7.21: Course of the temperature inside the pump port. All measurements were performed with a retarding potential at the vessel $U_{\text{tank}} = -18.5\,\text{kV}$ and a offset of $-100\,\text{V}$ at the central part of the inner wire electrode. The different settings (for the parameters see table 7.5) are indicated at the top of the plot. Next to the temperature sensors at the return pipe of the baffle (`435-RTP-5-X080`), the temperature sensors placed at the NEG pump are listed, too.

Most of the high-energy electrons generated by the uniformly distributed radon α-decays are trapped in the center of the main spectrometer where storage conditions are favorable. Secondary electrons induced by cosmic rays or field emission are more likely visible in the region of the outer flux tube, as they have to drift into the inner part of the flux tube via rather complex $\vec{E} \times \vec{B}$ drift processes resulting from magnetic and/or electrostatic inhomogeneities. Hence, the reduction of the measured rate per flux tube volume (cps/m³) due to the cold baffles is most clearly visible at the inner radii of the analyzing plane, see figure 7.22. By increasing the magnetic guiding field, from $3.8\,\text{G}$ to $9.0\,\text{G}$, the visible flux tube volume is reduced from $V_{3.8\,\text{G}} = 851.2\,\text{m}^3$ to $V_{9.0\,\text{G}} = 391.8\,\text{m}^3$. Therefore the setting **E** allows a closer look into the central parts of the spectrometer. As shown in figure 7.23 a similar rate trend was observed. If all three baffles are operating at nominal temperatures, almost all of the ^{219}Rn atoms emanating from the NEG material should stick to the cooled surfaces of the baffle ($r_{\text{NEG}}(3) = 0$), see equation 7.4. In this case the pumping speed of the baffles for radon is maximal (see table 7.4) and the decay probability of ^{220}Rn in the main spectrometer is at its minimum:

$$P_{\text{Rn220}}(3) = \left(1 + \frac{\tau_{\text{Rn220}} \cdot (S_{\text{TMP}} + 3 \cdot S_{\text{B}})}{V}\right)^{-1} \approx 1.5\% \qquad (7.9)$$

Correspondingly, the rate induced by ^{220}Rn is given by

$$r_{\text{vessel}}(3) \propto E_{\text{Rn220}}^{\text{vessel}} \cdot P_{i=3,\text{Rn220}} \approx 0 \qquad (7.10)$$

From these results one can conclude that almost all radon decays inside the main spectrometer have been suppressed by the LN2 cooled baffle. From this it can be deduced that background rate is reduced to the level of non-radon-induced background events stemming from cosmic rays or field emission.

$$r(3) \approx r_{\text{const.}} \qquad (7.11)$$

As a major conclusion of the LN2 baffle measurements it can be assumed that the LN2 cooled baffle system is highly efficient in blocking radon-induced background. A major open issue with regard to this central outcome of this thesis remains, can one prove that the remaining level is due to cosmic rays or field emission?
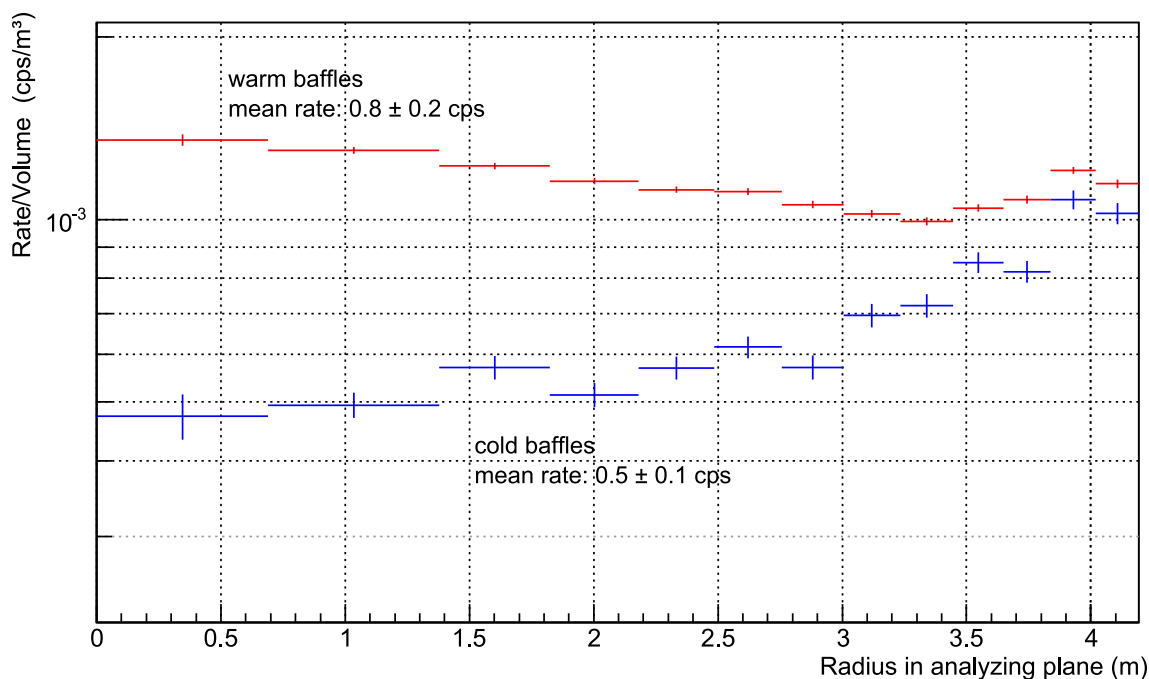
Figure 7.22: Background rate with warm baffles compared to cold baffles for $3.8\,\mathrm{G}$. Shown is the rate per flux tube volume as a function of the radius in the analyzing plane (setting **D**). In the outer flux tube volume the background is dominated by electrons induced by cosmic rays or field emission. In the center of the spectrometer the background is dominated by trapped high-energy electrons induced by radon α-decays. The baffles significantly reduce the background rate, as expected. A small reduction factor is observed at the outer flux tube. This is due to the strongly increasing muon-induced background there.
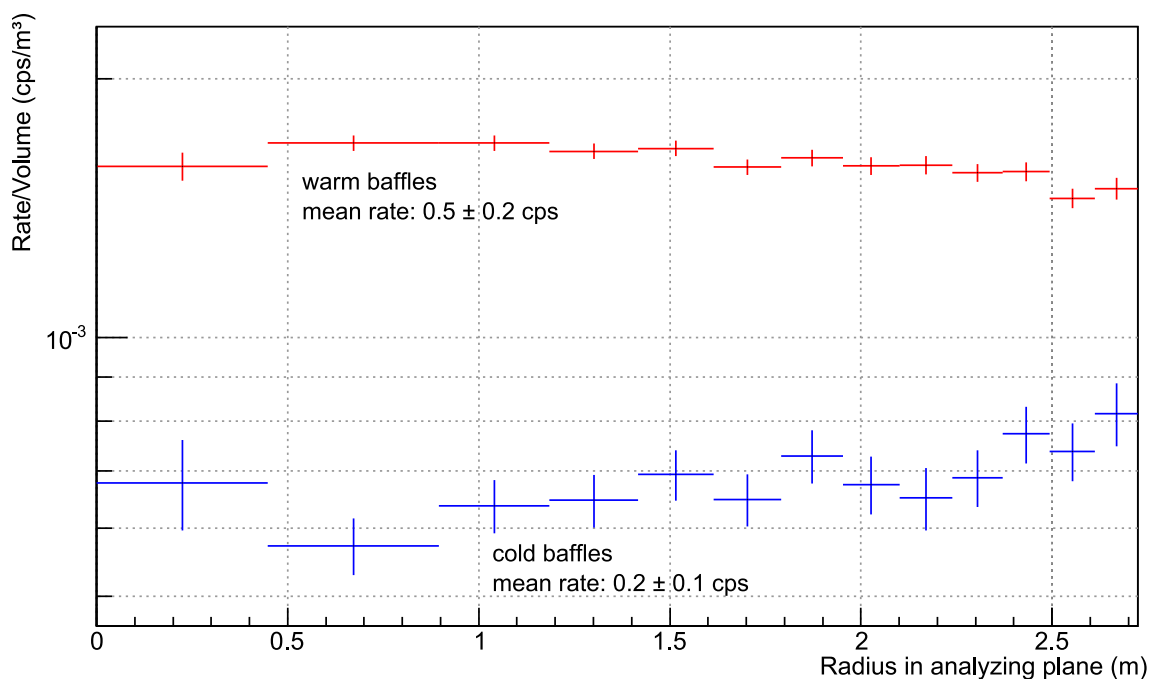
Figure 7.23: Background rate with warm baffles compared to cold baffles for $9.0\,\mathrm{G}$. Displayed are the results of setting **E**. Due to the higher magnetic field in the center of the spectrometer the detector looks at a smaller flux tube volume. The same characteristic background reduction as in figure 7.22 appears, demonstrating the excellent background reduction capabilities of the LN2 baffles.

7.4.5 Artificially Increased Pressure with Argon

A last background measurement was performed where the pressure in the main spectrometer was artificially increased to a level of about 10^{-8} mbar by injection of a constant argon flow. During this measurement the baffle system stayed at room temperature. With higher pressures in the main spectrometer, the cool-down time of the stored high-energy electrons from radon decays in the spectrometer volume decreases by many orders of magnitude to about 1 s. One high energy electron may thus generate hundreds of secondary electrons by residual gas ionization in only one second. Hence, radon α-decays are visible as 'spike-events' in the rate trend graph comparable to the earlier measurement results at the pre-spectrometer test setup (see figure 7.5 and figure 7.24). During the magnetron drift of the high-energy electron, the secondaries are generated along the circular magnetron path resulting in ring-like patterns on the detector (see figure 7.24b). Here, the electromagnetic setting **E** was used. About 7 000 radon-induced events were observed in a total of about 44 h measuring time [146].
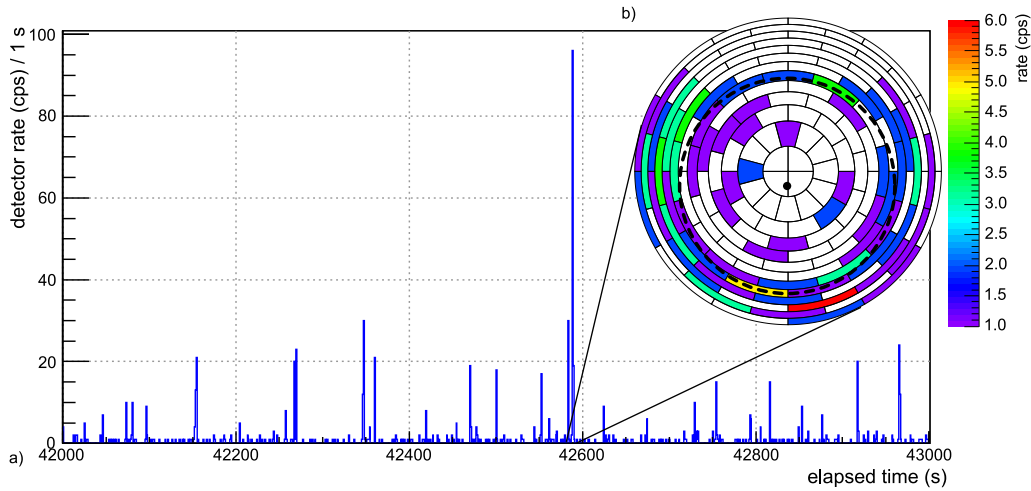
Figure 7.24: Rate trend graph over time. a) The spikes are generated by high energy stored electrons from radon α-decays. **b)** Pixel distribution of a single radon spike event with a duration of 1.3 s where the background rate soars to 117 cps. The radius (31.75 mm) and the center ($x = -0.25$ mm and $y = -4.25$ mm) of the ring was fitted and is in nice agreement with the expected position taking into account a radial displacement of the FPD with respect to the spectrometer [146].

By looking at the inter-arrival time of the electrons at the detector during the high pressure measurements (see figure 7.25), all events inside the radon-induced spikes hit the detector in less than 200 ms. This allows to discriminate between radon events ('spikes') and other background components ('single' hit events). While the total background rate has been found to be distributed in a rather strongly non-Poissonian way, the rate of events with inter-arrival times larger than 200 ms are found to be Poisson-distributed. If the LN2 cold baffles work in an effective way to eliminate practically all radon atoms in the transported flux tube, the rate distribution of single events should equal the rate distribution with cold baffles. As shown in figure 7.25b this is indeed the case. This is a central conclusion of this thesis: there is clear and irrefutable evidence that the level of radon-induced background is reduced to a level where no remaining radon-induced events can be observed.
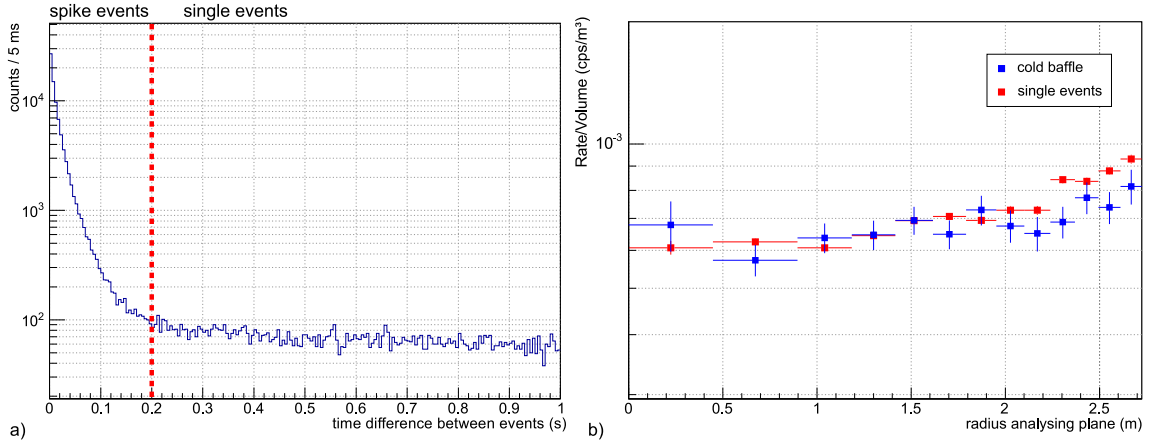
Figure 7.25: Closer look at the event structures. a) Distribution of the inter-arrival times of electrons at the detector during the high pressure measurements. All events inside a radon-induced spike hit the detector within a time difference of less than 200 ms. All other events are classified as single events and are attributed to non-radon-induced background (resulting from cosmic rays or field emission). **b)** The radial rate distribution of the single events equals the background measured with LN2 cooled baffles. This is a central result for this work.

The high pressure measurements alone can not discriminate between ^{219}Rn and ^{220}Rn as both decays generate similar spikes. However, when extrapolating the detector hits to the complete main spectrometer volume the total radon activity A_{tot} can be estimated:

$$A_{\text{tot}} = A_{\text{Rn219}}^{\text{NEG}} + A_{\text{Rn220}}^{\text{vessel}} = (0.200 \pm 0.003)\,\text{Bq}. \qquad (7.12)$$

With the radon activity ratio determined with the baffle measurements (see table 7.8), the specific activities of ^{219}Rn and ^{220}Rn can be calculated. The values are listed in table 7.9.

Table 7.9: Resulting radon activities in the main spectrometer. The total radon activity was estimated with the high pressure measurement, whereas the ratio of the radon activities was used to determine the activities for ^{219}Rn and ^{220}Rn.

setting	$A_{\text{Rn219}}^{\text{NEG}}$ (1/s)	$A_{\text{Rn220}}^{\text{MS}}$ (1/s)
A	0.060 ± 0.001	0.140 ± 0.002
B	0.044 ± 0.001	0.156 ± 0.002
mean activity	0.053 ± 0.002	0.148 ± 0.004

From these activity values the emanation rate can be determined using the following equation:

$$E_{\text{Rn}} = A_{\text{Rn}} \cdot \left(1 + \frac{\tau_{\text{Rn}} \cdot S_{\text{TMP}}}{V}\right). \qquad (7.13)$$

By combining the results of the baffle and the high pressure measurements the total radon emanation rate is found to be about $E_{\text{tot}} \approx (0.235 \pm 0.007)\,\text{Bq}$ which is in a good agreement with the estimates listed in table 7.4. From this one can conclude that radon emanation and dropping processes in the KATRIN spectrometers are well known and understood.

7.5 Conclusion

Radon isotopes which emanate from materials inside the spectrometers are able to penetrate deep into the transported flux tube. The radon α-decay releases electrons in the eV - keV range which are a major background source for a MAC-E filter system. Measurements at the pre-spectrometer test setup [78] have revealed ^{219}Rn atoms emanating from the non-evaporable getter (NEG) pump as well as ^{220}Rn coming from the vessel walls, as the dominant sources of radon. In order to achieve a final equilibrium pressure in the main spectrometer in the lower 10^{-11} mbar range, it is essential to operate a pump for hydrogen consisting of about 3 km of NEG material. By extrapolating the background results of the pre-spectrometer, the average radon-induced background rate at the main spectrometer (mainly due to the NEG material) was expected to be around 0.3 cps [80]. Such a huge background rate would significantly reduce the sensitivity of KATRIN on $m_{\bar{\nu}_e}$ [79].

To prevent radon from entering the spectrometer, while at the same time maintaining a significant fraction of the NEG pumping speed for H_2 (and tritium), the installation of a LN2 cooled baffle was proposed within this work. In the framework of a feasibility study, a prototype of an LN2 cooled baffle system was mounted in front of the NEG pump at the pre-spectrometer test setup [82]. By blocking the direct line of sight between NEG pump and vacuum chamber the baffle prevents ^{219}Rn emanating from the getter material from entering the main volume of the spectrometer. In addition, the spectrometer-facing cold surfaces of the baffle form a cold trap for ^{220}Rn emanating from the vessel walls.

Based on the results of the pre-spectrometer prototype measurements a large-scale baffle system to eliminate the radon-induced background in the main spectrometer was developed and successfully tested in this thesis. The LN2 cooled baffle system has been simulated and optimized with the software package *ProVac3D* to determine the exact conductance of the system and its pumping speed for radon. The technical realization is based on three stainless steel rings pipes (with an outer diameter of 1.68 m) which hold a framework of pipes guiding the liquid nitrogen. After mounting the rings to the holding structure of the NEG pump, the V-shape blades made of oxygen-free copper sheets were attached to these pipes. The V-shape copper blades are cooled down to liquid nitrogen temperatures, generating a cryo-trap for radon. A supply tank containing > 50 m^3 liquid nitrogen was successfully connected via an LN2 distribution system while a high voltage separator allows LN2 supply during regular runs with elevated vessel potential.

A series of measurements in the framework of the initial commissioning measurements of the spectrometer were performed to investigate the radon background level and properties at the main spectrometer, and, in particular, to evaluate the efficiency of the LN2-cooled baffle system. In a first step, a background model for radon emanation and cryotrapping was created. This contains the emanation of ^{219}Rn from the NEG pumps, the emanation of ^{220}Rn from the vessel walls and a constant background rate due to non-radon-induced background processes from cosmic rays or field emission. In a first measurement all three baffles were cooled down sequentially with LN2. During these measurements the main spectrometer was kept on ground potential, and the inner wire electrode system was used to accelerate the electrons to the detector resulting in an amplification of radon-induced background.

The radon model was used to determine the ratio of radon activities in the main spectrometer.

For the second suite of measurements the nominal settings for background measurements at symmetric magnetic fields were chosen and a high voltage of $U_{\text{vessel}} = -18.5\,\text{kV}$ was applied to the spectrometer. Since the HV separator was not yet available, three $200\,\ell$ cryostats each placed on polyethylene blocks (for the electrical insulation) supplied the baffle system with liquid nitrogen. These measurements yielded a much deeper insight into the radial dependence of the radon-induced background. The high-energy electrons released by a radon α-decay are more likely to be stored in the center of the flux tube, whereas non-radon-induced background is dominant in the outer regions of the visible flux tube. These measurements have thus provided rich and detailed insight into the storage conditions of high-energy electrons with large surplus energies. This is also of great relevance for KASSIOPEIA which has been successfully validated in the course of these investigations.

The final measurement was performed with a constant argon inflow to artificially increase the pressure inside the spectrometer to about $10^{-8}\,\text{mbar}$. Now the radon events are resolved as individual spikes (with durations about $1\,\text{s}$) in the rate trend graph and the total radon activity can be estimated. By using the ratio of the radon activities obtained in the baffle measurements, the total radon emanation in the main spectrometer can be determined to $E_{\text{tot}} \approx (0.235 \pm 0.007)\,\text{Bq}$, in good agreement with predictions.

Almost all radon decays inside the main spectrometer are prevented by the LN2 cooled baffle. The background rate is reduced to the level of non-radon-induced components only, stemming from cosmic rays or field emission. As a major conclusion of this thesis it can be emphasized that the LN2 baffle system is highly efficient in eliminating radon-induced background.

In addition to the liquid nitrogen cooled baffle system several active background suppression methods are currently being prepared, for more details see [79], [147] and [141]. Further tests of active reduction methods such as the magnetic pulse or the electric dipole in combination with a cold baffle have also been investigated in parallel to this work. Together these passive and active background reduction methods will be essential to push the background level down to the nominal value of $0.01\,\text{cps}$ as an important prerequisite for neutrino mass measurements.

8 Conclusion

The neutrino was postulated by W. Pauli in 1930 to describe the β-decay spectrum as a result of a three-body process. In 1956 C. L. Cowan and F. Reines published their first observation of this electrically neutral and only weakly interacting particle. Today the three generations of neutrinos are described in the Standard Model of particle physics and have been detected experimentally. Cowan and Reines were using a nuclear fission reactor as neutrino source. Several other experiments, such as the famous Homestake experiment were looking into the interior of the Sun as a giant natural nuclear fusion reactor. As only one third of the predicted number of electron neutrinos were detected, the solar neutrino problem was born, which would puzzle science for over thirty years. The solution of the solar neutrino problem requires physics beyond the Standard Model of particle physics in the form of neutrino flavor oscillations. Throughout most of the 1970s it was widely believed that neutrinos were massless particles. Oscillation experiments with solar, atmospheric, reactor and accelerator neutrinos have given conclusive evidence that neutrinos propagating through space are mass eigenstates which acquire quantum mechanical phases. Hence, electron neutrinos generated in the Sun can change partly into other flavors which the early experiments could not detect. Today the concept of neutrino oscillations is well-established which implies that neutrinos have a non-zero mass. To determine the absolute value of the (unknown) neutrino mass, different approaches are being explored. A rather strong upper limit of neutrino masses comes from cosmology. The Big Bang model predicts a well-defined ratio between the number of (relic) neutrinos and the number of photons in the cosmic microwave background (CMB). Comprehensive analyses of cosmological data, such as the cosmic microwave background radiation by the *Planck* collaboration, galaxy cluster surveys or the investigation of the Lyman-alpha forest yield however only model-dependent values on the neutrino masses. A number of experiments is targeted at determining the absolute neutrino mass scale directly in laboratory setups. One group focuses on the observation of neutrinoless double β-decay ($0\nu\beta\beta$) that however requires that neutrino are Majorana particles. Today the best model-independent upper limit $(2.2 \, \text{eV/c}^2)$ of the absolute electron anti-neutrino mass comes from groups in Mainz and Troitsk pioneering the MAC-E filter technique in tritium β-decay spectroscopy. The **Ka**rlsruhe **Tri**tium **N**eutrino experiment (KATRIN) opens up a new era of precision neutrino mass experiments. This next-generation setup will use a windowless gaseous tritium source with highest luminosity and stability. Several superconducting solenoids guide the β-electrons through a differential and cryogenic pumping section for tritium retention and adiabatic electron transport. A crucial element of KATRIN is the MAC-E filter principle which makes use of a precise combination of electric and magnetic fields to analyze the kinetic energy of signal electrons. The KATRIN setup features two electrostatic spectrometers, the smaller pre-spectrometer acting as pre-filter, and the larger main spectrometer acting as precision filter. A

focal plane detector system at the end counts the electrons that pass the spectrometer section. The objective of KATRIN is to determine the electron anti-neutrino mass down to a level of $0.35\,\mathrm{eV/c^2}$ at 5σ significance or $0.2\,\mathrm{eV/c^2}$ at 90% C.L. Hence, KATRIN will improve the current sensitivity of tritium β-decay experiments by one order of magnitude. The KATRIN experiment is currently under construction at the TLK at the KIT Campus North.

Within this thesis the pre-spectrometer was setup as a pre-filter for β-electrons in the KATRIN setup. In the KATRIN beamline the pre-spectrometer allows the option to use it as a pre-filter elevated to a constant potential $0 < U_0 < E_0$. This is possible as only electrons with energies close to the endpoint energy of tritium provide information on the neutrino mass. At a retarding potential of $U_0 \approx -18.3\,\mathrm{kV}$ the pre-spectrometer would reduce the number of β-decay electrons that reach the main spectrometer by a factor of 10^6. By decreasing the flux of β-electrons into the main spectrometer, the background due to residual gas ionization by the signal electrons will be reduced (albeit at the risk of igniting a Penning trap).

The main spectrometer will analyze the energies of β-decay electrons emitted from the windowless gaseous tritium source (WGTS). Acting as a huge high-pass filter, the spectrometer provides high-precision energy analysis for tritium β-decay electrons. To do so, two superconducting solenoids create an inhomogeneous magnetic field while an electrostatic retarding potential of $U_0 = 18.6\,\mathrm{kV}$ is directly applied to the vessel resulting in a energy resolution of $\Delta E = 0.93\,\mathrm{eV}$.

This work was focused on setting up and optimizing the vacuum technology for the spectrometer, the world's largest UHV recipient. A successful neutrino mass measurement with the KATRIN spectrometers will require a vacuum at least in the lower 10^{-11} mbar range, thus posing many challanges to UHV technologies.

To achieve the UHV regime in a reasonable time, a dedicated bake-out procedure is required. The bake-out process relies on a rise in temperature which accelerates desorption processes. Water and other molecules sticking to the inner surface of the vessel are thus removed. Within this thesis an optimized bake-out procedure for the main spectrometer was found which includes as a specific procedure a step temperature of $T_{\mathrm{vessel}} = 150\,^\circ\mathrm{C}$. This reduces the hydrogen concentration on the surface by desorption, without replenishing too much hydrogen by diffusion from the bulk. The main spectrometer bake-out cycle was performed in winter 2012/2013. The whole procedure took about two months. After the bake-out cycle the pressure inside the recipient was dominated as expected, by hydrogen diffusing from the bulk material of the vessel walls.

Positive displacement and momentum transfer pumps are unsuitable for light gases like hydrogen. Therefore the KATRIN collaboration decided to use entrapment pumps in form of a 3 km long non-evaporable getter (NEG) pump to maintain a pressure in the UHV region. Getter materials accumulate residual gases by binding molecules at their surface (physisorption) or by absorbing gases in their bulk material by a chemical reaction (chemisorption) after activation at a temperature of $T_{\mathrm{NEG}} > 300\,^\circ\mathrm{C}$. However, after the first bake-out cycle the maximal temperature of the main spectrometer had to be constrained to a regime $T_{\mathrm{vessel}} < 200\,^\circ\mathrm{C}$ to prevent further stress on the inner wire electrode system. Hence, an alternative concept of activating the large-scale getter material is required. As part of this work important R&D works and design optimizations for the NEG pumps were performed so

that they can be heated by the passage of a current through the base material of the strips. During the ongoing maintenance break of the main spectrometer this concept will be used to upgrade the NEG pumps. The new concept is intended for higher temperatures $T_{\mathrm{NEG}} \approx 450\,°\mathrm{C}$ requiring a shorter heating cycle.

In a second major part of this thesis novel background reduction methods against radon-induced background were planned, tested and successfully operated. Radon isotopes emanating from materials inside the spectrometers are able to penetrate deep into the flux tube. The radon α-decay can result in electrons emitted with energies ranging from the eV up to the hundreds of keV scale. Accordingly, these decay processes represent a major source of background in a MAC-E filter. To prevent radon from entering the spectrometer, while at the same time maintaining a significant fraction of the original NEG pumping speed for H_2 (and tritium), the installation of a LN2-cooled baffle was proposed. As part of this work a smaller baffle was successfully tested at the pre-spectrometer. This was the starting point to implement a much larger LN2-cooled copper baffle at the main spectrometer. By blocking the direct line of sight between NEG pump and vacuum chamber the LN2-cooled baffle prevents ^{219}Rn emanating from the getter material from entering the main volume of the spectrometer, while at the same time the cold surfaces of the baffle form a cold trap for ^{220}Rn emanating from the vessel walls. In the framework of the highly successful first commissioning measurements with the spectrometer and detector system in mid-summer 2013, a series of measurements was performed to investigate the radon background at the main spectrometer and to evaluate the efficiency of the LN2-cooled baffle system. As a major scientific conclusion of this thesis it can be stated that almost all radon decays inside the main spectrometer are suppressed by the LN2-cooled baffle. The background rate is reduced to the level of non-radon-induced background, originating from cosmic rays or field emission. The LN2-cooled baffle system is thus highly efficient in blocking radon induced background and an essential asset for the neutrino mass measurements.

The results presented in this thesis have demonstrated that the main spectrometer conditioned by a dedicated bake-out procedure in combination with fully activated NEG pumps is very well able to reach the ambitious vacuum goal of maintaining a stringent UHV regime in the lower 10^{-11} mbar. In addition a system of LN2 cooled baffles provides a powerful tool to eliminate radon-induced background which is an essential requirement for a successful neutrino mass measurement.

A Appendix

In this appendix, specific information (e.g. a detailed vacuum flow charts) are given for the pre-spectrometer, the main spectrometer (including the baffle system) and the test recipient.

A.1 Additional Information about the Pre-spectrometer and the Test Recipient

Table A.1: List of all the pre-spectrometer heating tapes. The location of the tapes is indicated in figure A.1. The part numbering is following the KATRIN numbering system. The upper half contains the heating tapes connected to a rack at ground potential, the lower half those that are connected to the HV rack.

rack	KATRIN number	location	lenght (m)	power (W)
ground	415-HEE-5-3800	diaphragm bellows		
ground	415-HEE-5-3810	diaphragm bellows		
ground	415-HEE-5-3820	PS-MS valve		
ground	415-HEE-5-3830	PS-CPS valve		
ground	415-HEE-5-3840	PS2 magnet		800
ground	415-HEE-5-3850	PS1 magnet		800
HV	415-HEE-5-3900	45°-Pumpport	10	2 000
HV	415-HEE-5-3910	90°-Pumpport	10	2 000
HV	415-HEE-5-3920	90°-Pumpport-AddOn	1.5	375
HV	415-HEE-5-3930	45°-Pumpport-AddOn	1.5	375
HV	415-HEE-5-3940	VAT gate valve 1	cushion	2×240
HV	415-HEE-5-3950	VAT gate valve 2	cushion	2×240
HV	415-HEE-5-3960	measurement cross	cushion	
HV	415-HEE-5-3970	feed through and vessel	10	2 000
HV	415-HEE-5-3980	feed through, vessel and measurement cross	10	2 000
HV	415-HEE-5-3990	feed through and vessel	10	2 000
HV	415-HEE-5-4000	end cap	10	2 000
HV	415-HEE-5-4010	head end cap	10	2 000
-	415-HEE-5-4020[a]	pre-spectrometer	10	2 000
-	415-HEE-5-4030[a]	pre-spectrometer	10	2 000
-	415-HEE-5-4040[a]	pre-spectrometer	10	2 000

[a]additional heating tape - not connected

147
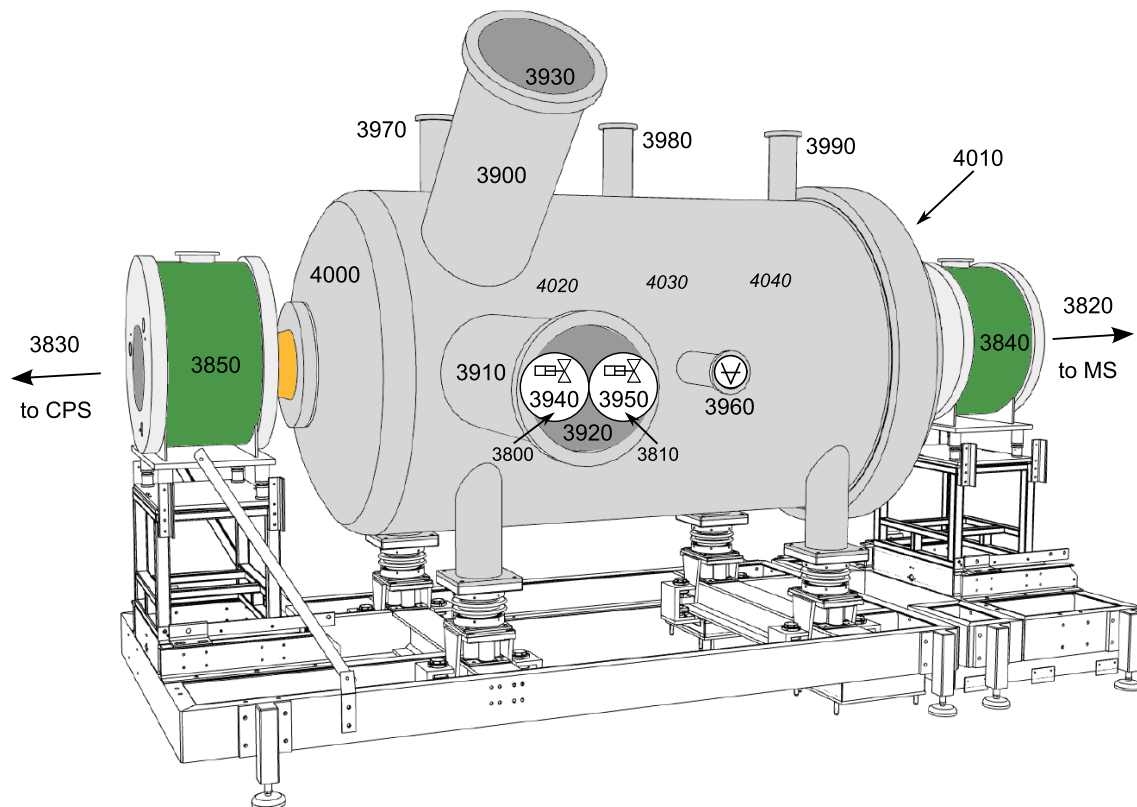
Figure A.1: Schematic drawing of the location of the pre-spectrometer heating tapes.
To improve the overview the figure only holds the fourth field (`415-HEE-5-nnnn`) of the KATRIN numbering system providing a unique four digit serial number for each component. All heating tapes are additionally listed in table A.1.
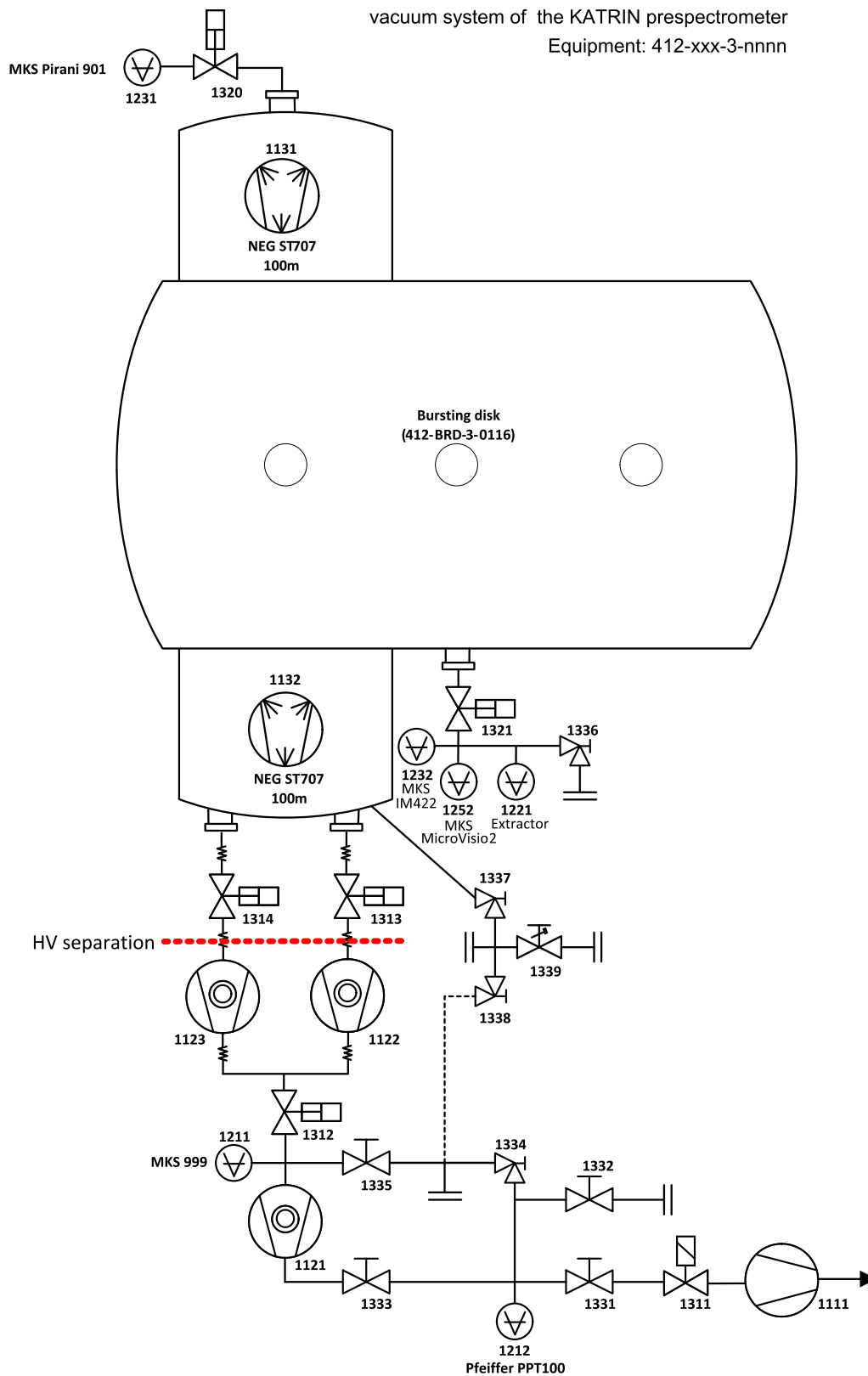
Figure A.2: Flow chart of the pre-spectrometer vacuum system. To improve the overview the figure only holds the fourth field (412-xxx-3-nnnn) of the KATRIN numbering system providing a unique four digit serial number for each component. The high voltage separation of the pumping system with ceramic tubes is indicated with a red dotted line. The exhaust ports of the main TMPs is connected to the second TMP forming a cascading pumping scheme. As a fore-pump a scroll pump is used. To maintain a vacuum in a UHV region the pre-spectrometer is equipped with entrapment pumps in form of two NEG pumps, one in each pump port. The different gauges are combined to enable the operator to measure the pressure in the spectrometer continuously. All vacuum gauges are listed with their manufacturer and range in table 3.1.
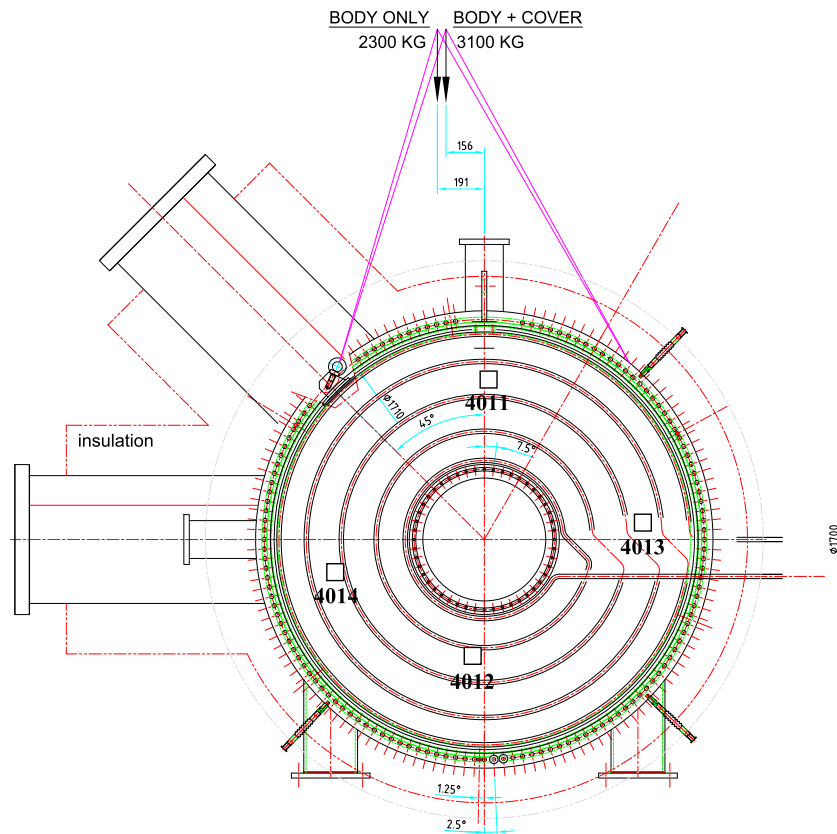
Figure A.3: Technical drawing of the location of the pre-spectrometer temperature sensors - front view. To improve the overview the figure only holds the fourth field (`415-RTP-5-nnnn`) of the KATRIN numbering system providing a unique four digit serial number for each sensor.
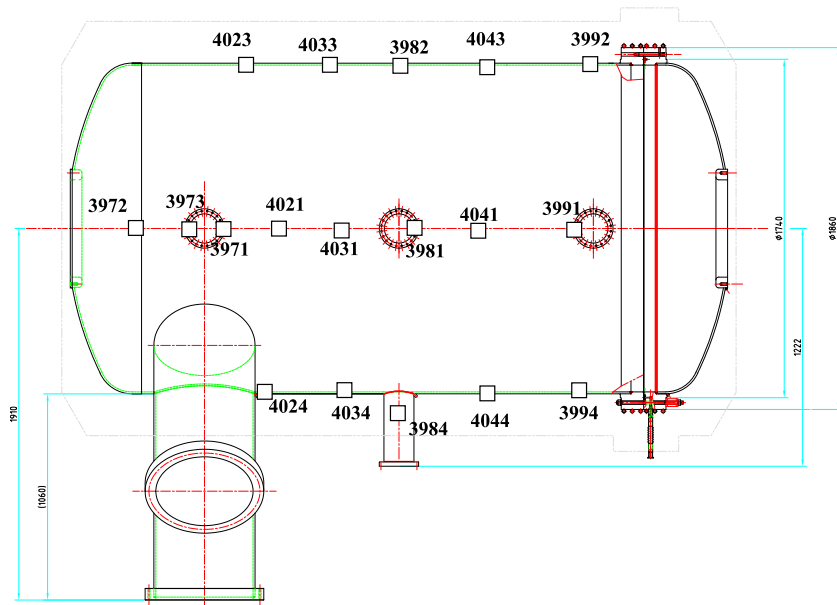
Figure A.4: Technical drawing of the location of the pre-spectrometer temperature sensors - top view. To improve the overview the figure only holds the fourth field (`415-RTP-5-nnnn`) of the KATRIN numbering system providing a unique four digit serial number for each sensor.

Figure A.5: Technical drawing of the location of the pre-spectrometer temperature sensors - back view. To improve the overview the figure only holds the fourth field (`415-RTP-5-nnnn`) of the KATRIN numbering system providing a unique four digit serial number for each sensor.

Figure A.6: Technical drawing of the location of the pre-spectrometer temperature sensors - side view. To improve the overview the figure only holds the fourth field (`415-RTP-5-nnnn`) of the KATRIN numbering system providing a unique four digit serial number for each sensor.

Figure A.7: Flow chart of the pre-spectrometer oil-heating system. To improve the overview this simplified representation only holds the fourth field (`415-xxx-5-nnnn`) of the KATRIN numbering system providing a unique four digit serial number for each component. The high voltage separation with ceramic pipes is indicated with a red dotted line. All important valves and drains are included as well as the collection container. The heart of the system is a *Lauda* KH350L kryoheater (`415-HCL-5-3401`).
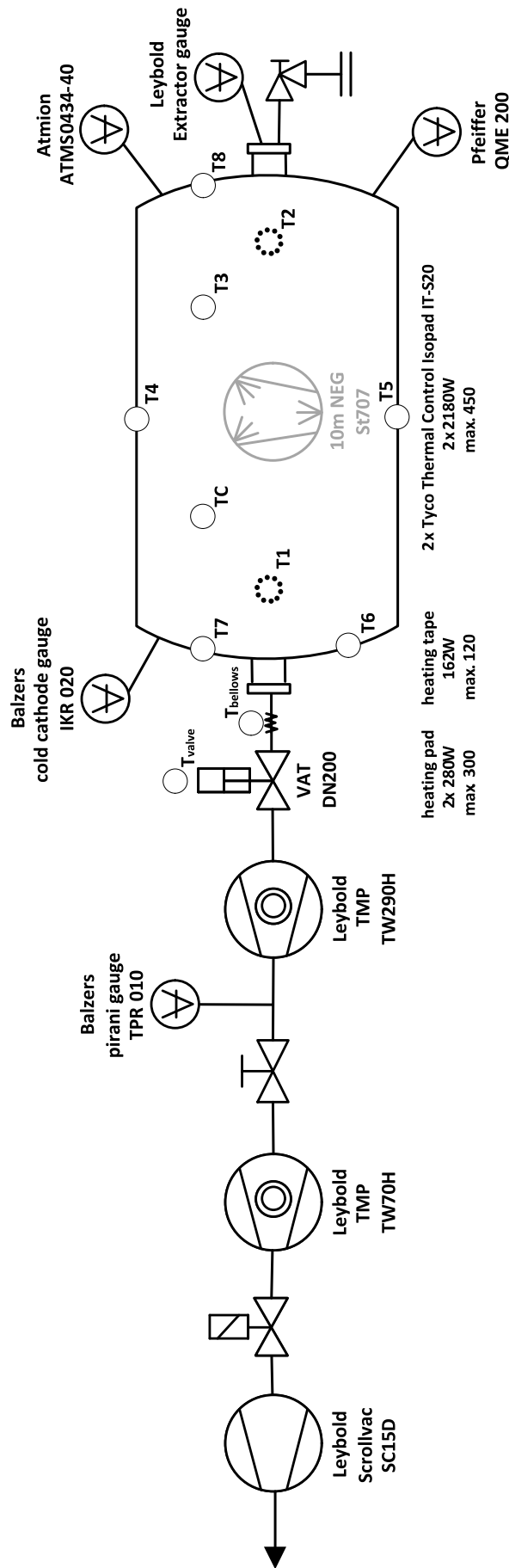
Figure A.8: Flow chart of the test recipient vacuum system. The exhaust port of the main TMP (*Leybold* TW290H) is connected to a the second TMP (*Leybold* TW70H) forming a cascading pumping scheme. As fore-pump a scroll pump (*Leybold* SC15D) is used. The different gauges are combined to enable the operator to measure the pressure in the recipient continuously. All vacuum gauges are listed with their manufacturer, range and accuracy in table 5.1. To maintain a vacuum in a UHV region the test recipient can be equipped with an entrapment pump in form of NEG material. The experimental setup is completed with ten temperature sensors and four heating tapes for a controlled bake-out of the system.

A.2 Complete Vacuum Flow Chart of the KATRIN Main Spectrometer

Vacuum System of the KATRIN Main Spectrometer
Equipment: 422-PID-2-0000-Pumpport2
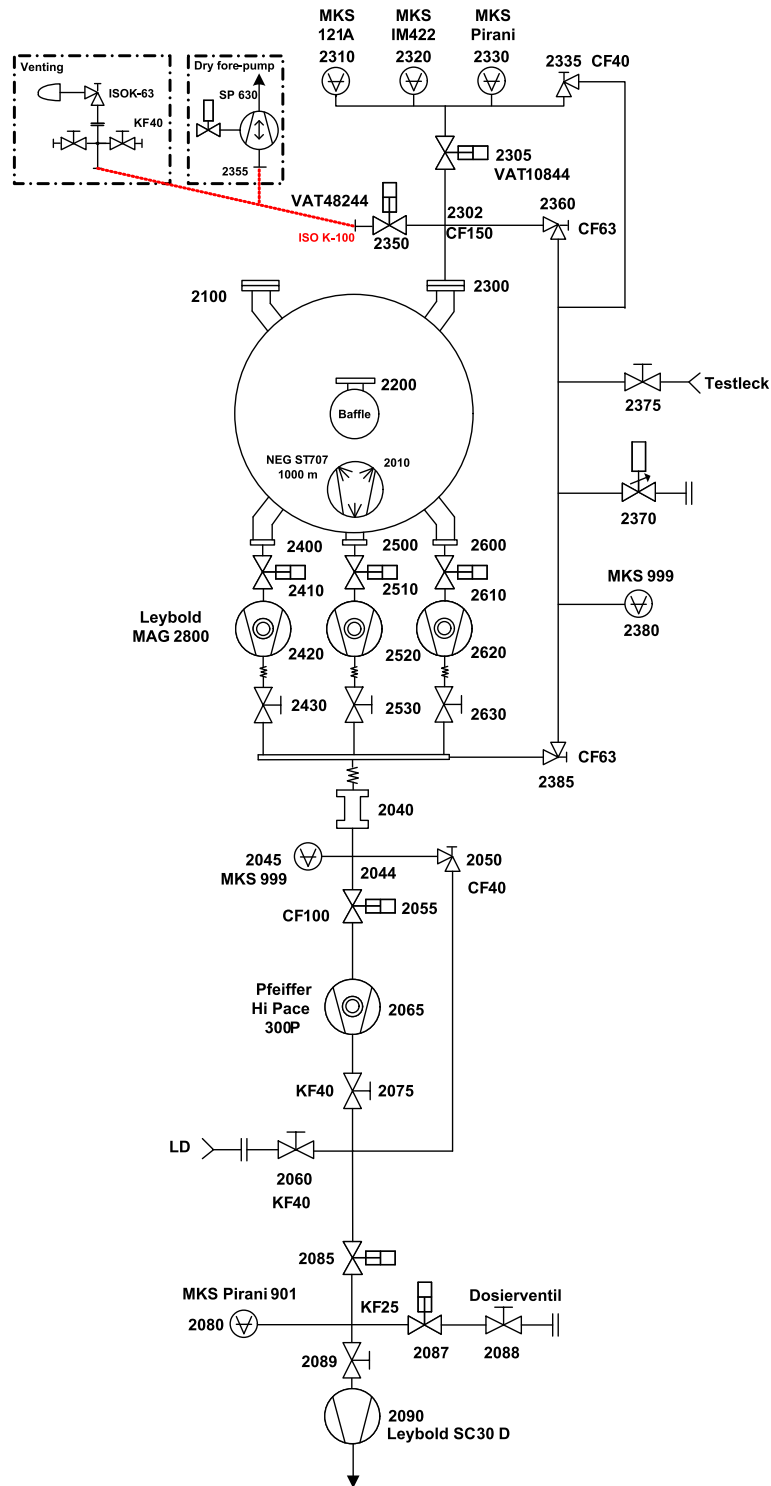
Figure A.9: Flow chart of the main spectrometer vacuum system of pump port II.
To improve the overview the figure only holds the fourth field (422-xxx-3-nnnn) of the KATRIN numbering system providing a unique four digit serial number for each component.

Vacuum System of the KATRIN Main Spectrometer
Equipment: 432-PID-3-0000-Pumpport3
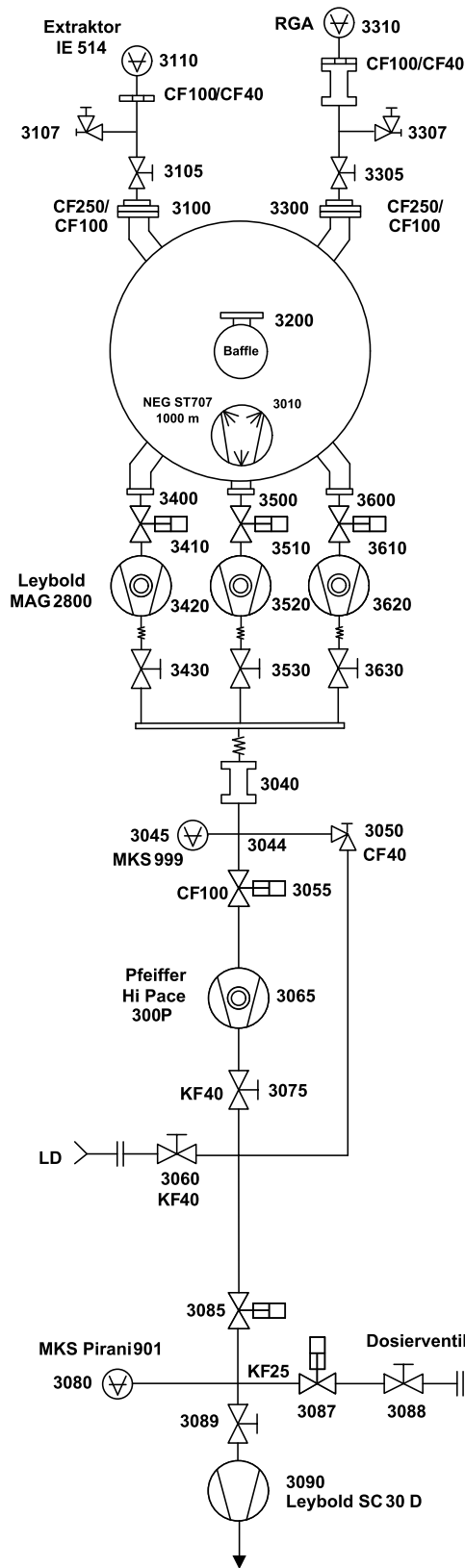
Figure A.10: Flow chart of the main spectrometer vacuum system of pump port III.
To improve the overview the figure only holds the fourth field (422-xxx-3-nnnn) of the KATRIN numbering system providing a unique four digit serial number for each component.
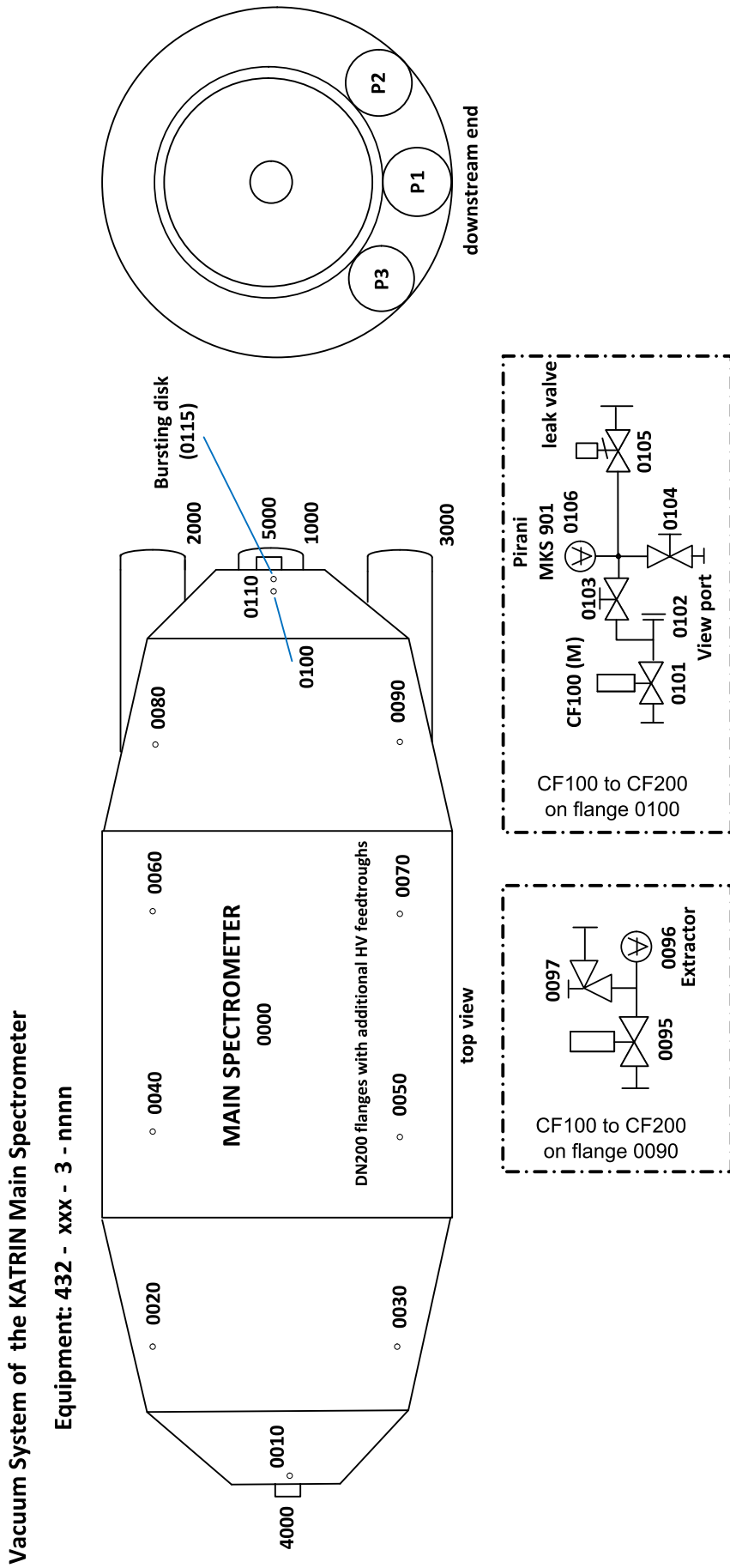
Figure A.11: Flow chart of the main spectrometer vacuum system. To improve the overview the figure only holds the fourth field (422–xxx–3–nnnn) of the KATRIN numbering system providing a unique four digit serial number for each component.

A.3 Oil heating system Main Spectrometer
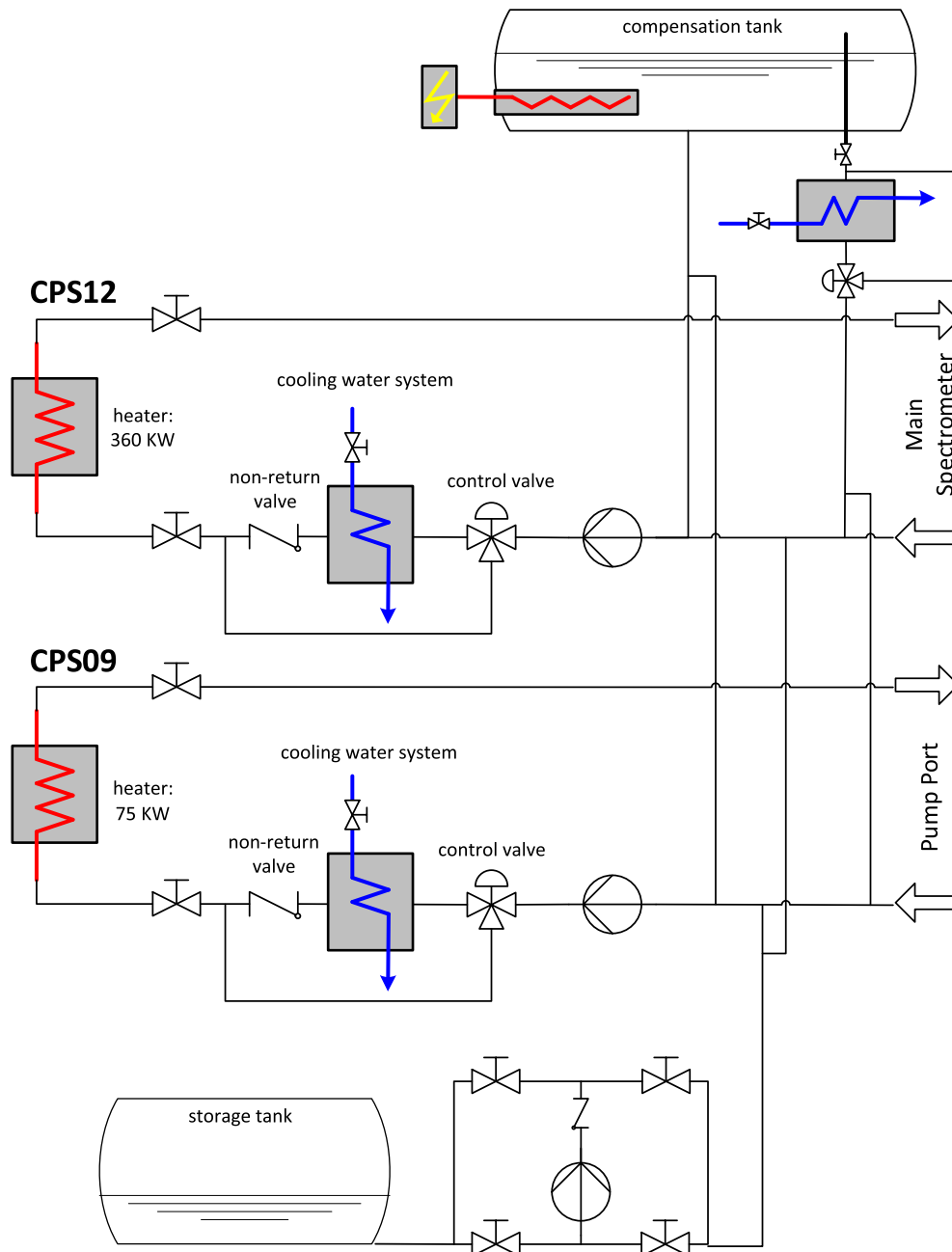
Figure A.12: Flow chart of the main spectrometer oil-heating system (HTT). To improve the overview this simplified representation only holds the central components of the complex system. All important control valves are included as well as the heating and cooling devises. The hearts of the system are the two heaters: the **CPS12** for the main spectrometer vessel (360 kW) and the **CPS09** for the three pump ports (75 kW). If the thermal oil is heated it expands into the compensation tank. To drain the whole system (in case of an emergency or for maintenance work) the entire oil can be pumped into a special storage tank.

A.4 Additional Information about the LN2 Cooled Baffle System
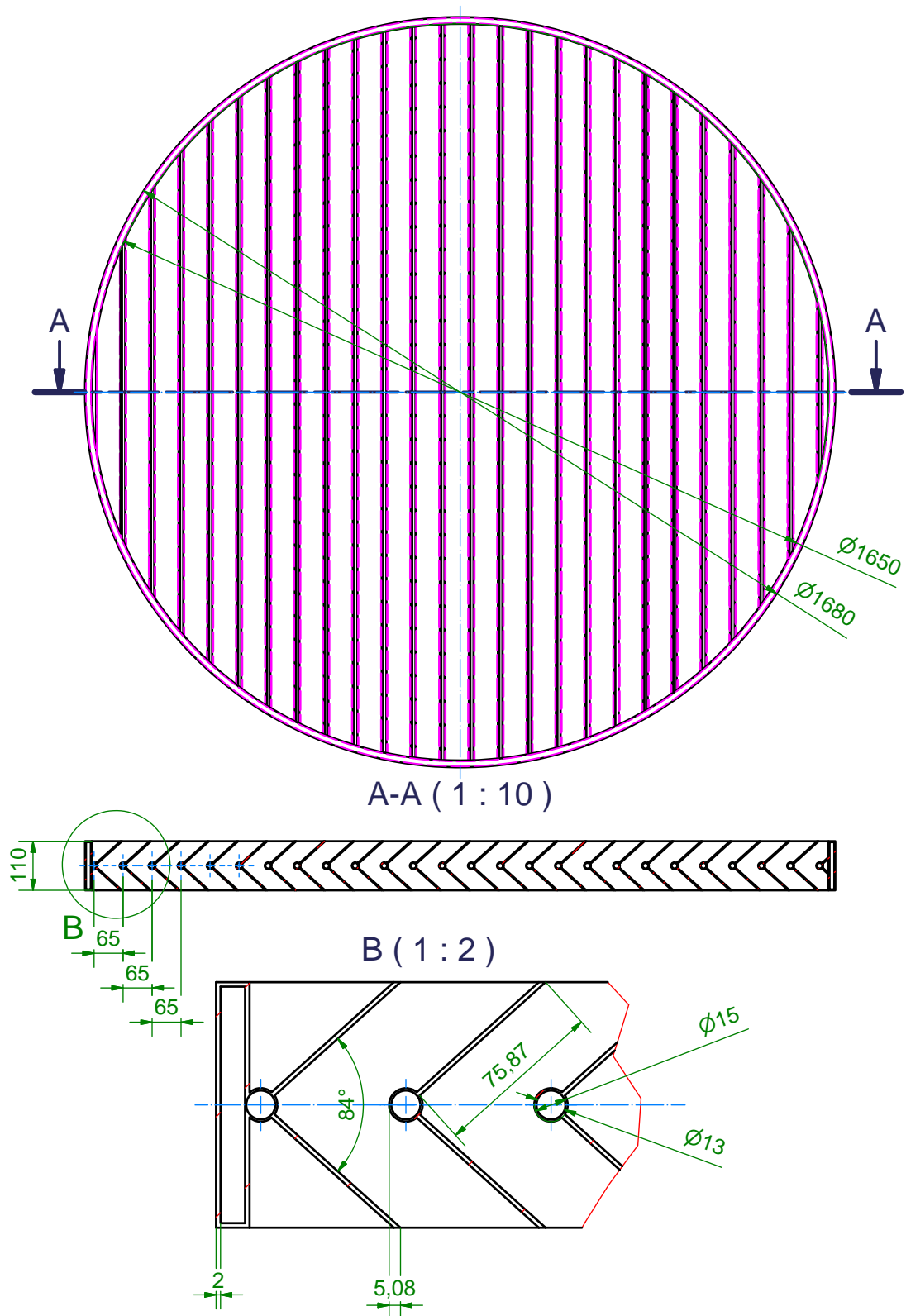
Figure A.13: Technical drawing of the LN2 cooled baffle. Shown are the V-shaped cooper plates and the stainless steel cooling pipes. All values are in mm.
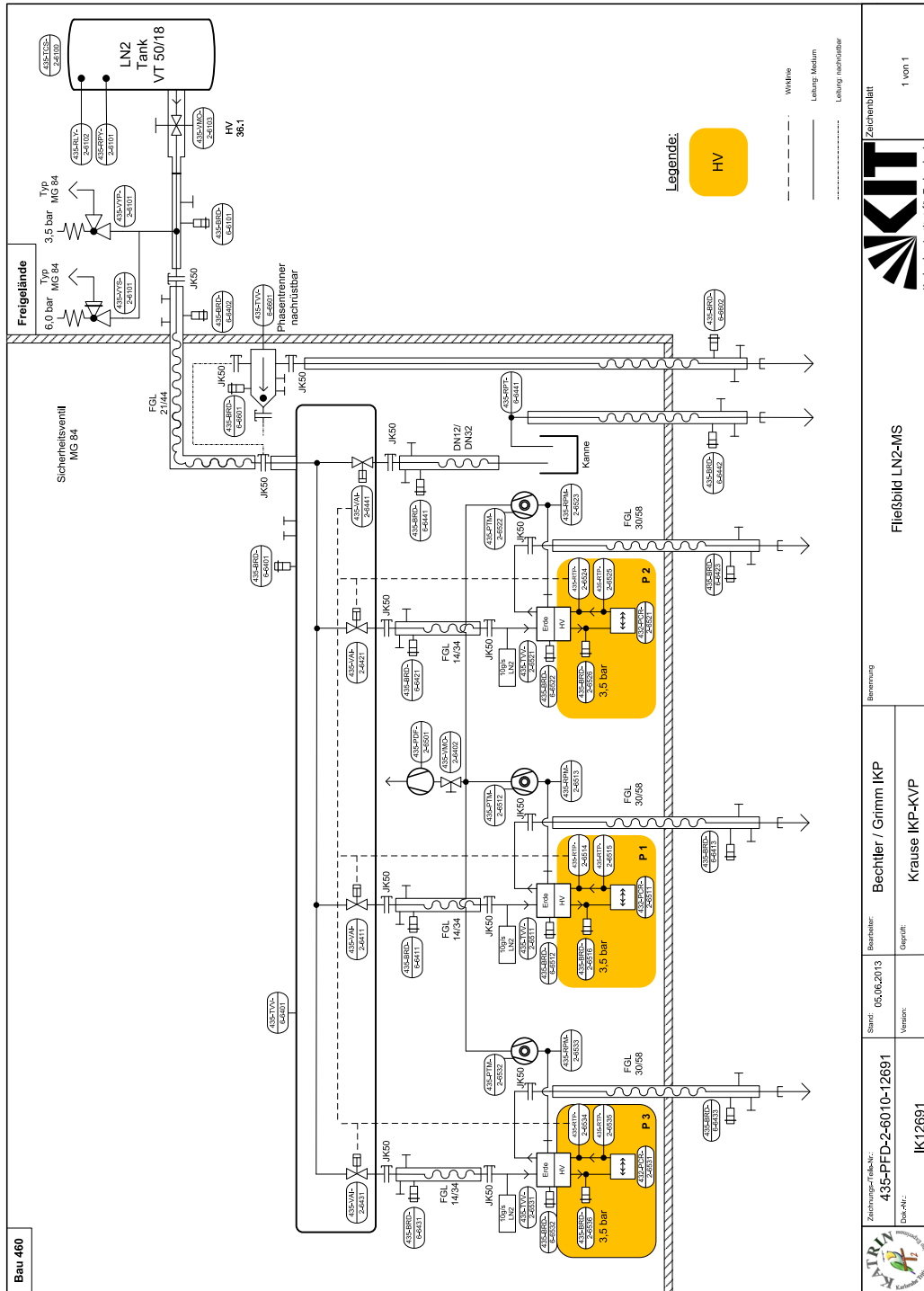
Figure A.14: LN2 flow chart of the baffle system. The LN2 distribution system (valve box), including the LN2 supply tank outside the main spectrometer building and the three baffles with their HV separation connector. The HV part is highlighted in orange. The part numbering is following the KATRIN numbering system.

A.5 Decay Chains

In nuclear science a decay chain refers to a chained series of discrete radioactive decay products. Commonly four decay chains (so called families) are observed in nature:

- thorium series, starting isotope ^{232}Th, ending isotope ^{208}Pb ($A = 4n$)

- neptunium series, starting isotope ^{237}Np, ending isotope ^{205}Tl ($A = 4n + 1$)

- radium series, starting isotope ^{238}U, ending isotope ^{206}Pb ($A = 4n + 2$)

- actinium series, starting isotope ^{235}U, ending isotope ^{207}Pb ($A = 4n + 3$)

The neptunium series ($A = 4n+1$), is already extinct in nature, except for the final rate-limiting step, the decay of ^{209}Bi[1]. Hence, this decay chain will not be considered any further.
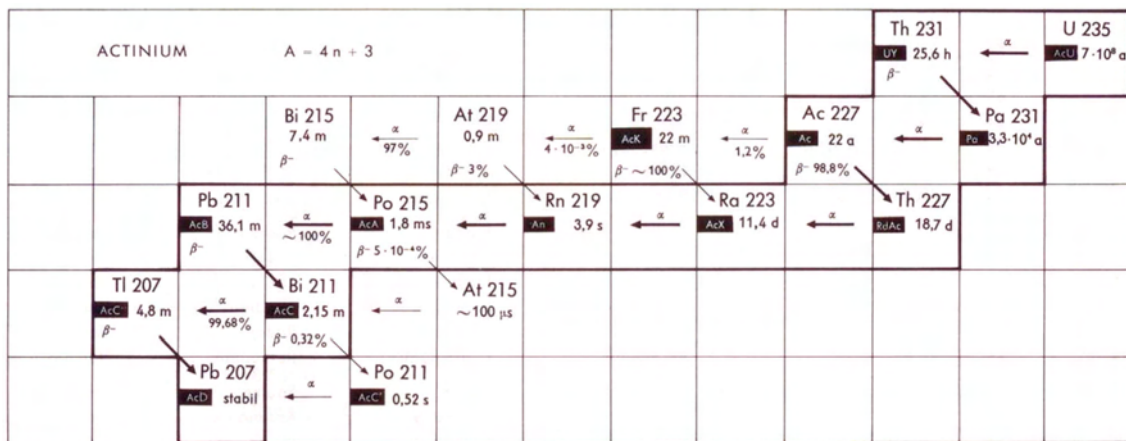
Figure A.15: Shown is the actinium series beginning with naturally occurring ^{235}U. As an intermediate step ^{219}Rn is produced with a half-life of $3,96$ s. The figure is based on [148].
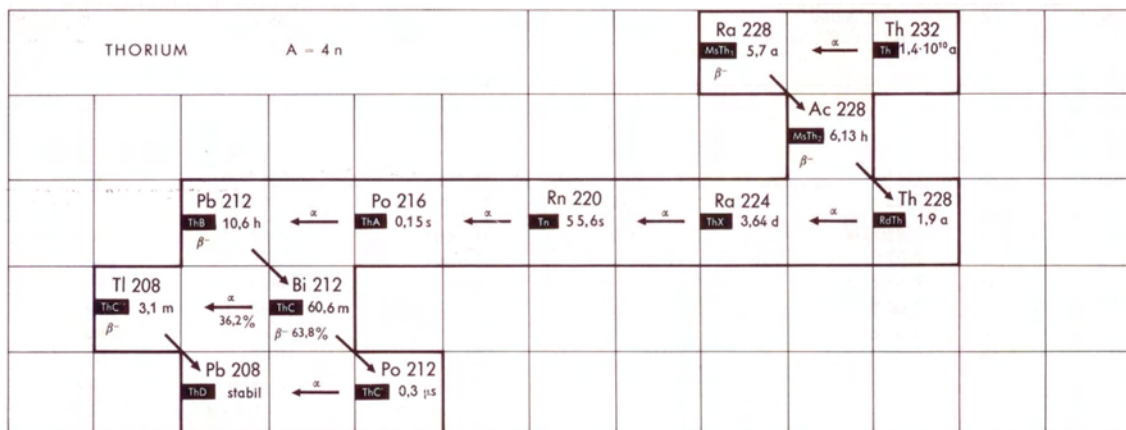
Figure A.16: Shown is the thorium series beginning with naturally occurring ^{232}Th. As an intermediate step ^{220}Rn is produced with a half-life of $55,6$ s. The figure is based on [148].

---

[1]Some older sources give the final isotope as ^{209}Bi with a half-life of $1.9 \cdot 10^{19}$ a.
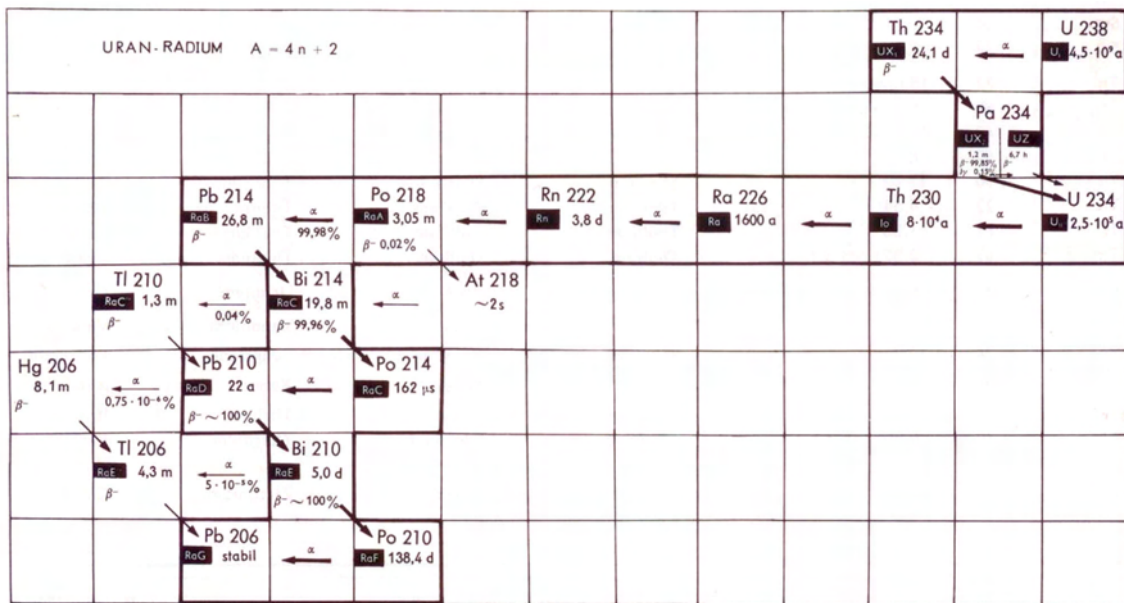
Figure A.17: Shown is the radium series beginning with naturally occurring ^{238}U. As an intermediate step the most stable radon isotope ^{222}Rn is produced with a half-life of 3.823 days. The figure is based on [148].

Bibliography

[1] H. Becquerel. Sur les radiations invisibles emises par les corps phosphorescents. *Comptes Rendus*, 122:420–421, 1896.

[2] E. Rutherford and F. Soddy. Die Ursache und Natur der Radioactivitaet I. *Zeitschrift für physikalische Chemie*, 42:81–109, 1902.

[3] L. Meitner, O. von Baeyer, and O. Hahn. Über die Beta-Strahlen des aktiven Niederschlags des Thorium. *Phys. Z.*, 12:273, 1911.

[4] W. Pauli. Offener Brief an die Gruppe der Radioaktiven bei der Gauvereins-Tagung zu Tübingen. Dez 1930.

[5] J. Chadwick. Possible Existence of a Neutron. *nature*, 129:312, 1932.

[6] E. Fermi. Versuch einer Theorie der beta-Strahlen. I. *Zeitschrift fuer Physik A: Hadrons and Nuclei*, 88(3):161–177, 1934.

[7] F. Reines and C. L. Cowan. Detection of the Free Neutrino. *Phys. Rev.*, 92(3):830–831, Nov 1953.

[8] F. Reines and C. L. Cowan. Free Antineutrino Absorption Cross Section. I. Measurement of the Free Antineutrino Absorption Cross Section by Protons. *Phys. Rev.*, 113(1):273–279, Jan 1959.

[9] G. Danby et al. Observation of High-Energy Neutrino Reactions and the Existence of Two Kinds of Neutrinos. *Phys. Rev. Lett.*, 9(1):36–44, Jul 1962.

[10] DONUT Collaboration. Observation of tau neutrino interactions. *Physics Letters B*, 504(3):218–224, 2001.

[11] ATLAS Collaboration. Combined search for the Standard Model Higgs boson using up to 4.9 fb-1 of pp collision data at sqrt(s) = 7 TeV with the ATLAS detector at the LHC. *Physics Letters B*, 710(1):49 – 66, 2012.

[12] CMS Collaboration. Combined results of searches for the standard model Higgs boson in pp collisions at sqrt(s) = 7 TeV. *Physics Letters B*, 710(1):26 – 48, 2012.

[13] J. Beringer et al. Review of Particle Physics (RPP). *Phys.Rev.*, D86:010001, 2012.

[14] P. Ramond. Neutrinos: A glimpse beyond the standard model. *Nuclear Physics B - Proceedings Supplements*, 77(1-3):3–9, 1999.

[15] Raymond Davis. Solar Neutrinos. II. Experimental. *Phys. Rev. Lett.*, 12:303–305, Mar 1964.

[16] SNO Collaboration. Measurement of the Rate of $\nu_e + d \rightarrow p + p + e^-$ Interactions Produced by ^{8}B Solar Neutrinos at the Sudbury Neutrino Observatory. *Phys. Rev. Lett.*, 87:071301, Jul 2001.

[17] John N. Bahcall. Solar Neutrinos. I. Theoretical. *Phys. Rev. Lett.*, 12:300–302, Mar 1964.

[18] John N. Bahcall, M. H. Pinsonneault, Sarbani Basu, and J. Christensen-Dalsgaard. Are Standard Solar Models Reliable? *Phys. Rev. Lett.*, 78:171–174, Jan 1997.

[19] Bruce T. Cleveland, Timothy Daily, Jr. Raymond Davis, James R. Distel, Kenneth Lande, C. K. Lee, Paul S. Wildenhain, and Jack Ullman. Measurement of the Solar Electron Neutrino Flux with the Homestake Chlorine Detector. *The Astrophysical Journal*, 496(1):505, 1998.

[20] John N. Bahcall, Sarbani Basu, and M.H. Pinsonneault. How uncertain are solar neutrino predictions? *Physics Letters B*, 433(2):1–8, 1998.

[21] Ziro Maki, Masami Nakagawa, and Shoichi Sakata. Remarks on the Unified Model of Elementary Particles. *Progress of Theoretical Physics*, 28(5):870–880, 1962.

[22] B. Pontecorvo. Neutrino Experiments and the Problem of Conservation of Leptonic Charge. *Soviet Journal of Experimental and Theoretical Physics*, 26:984, May 1968.

[23] S. M. Bilenky, C. Giunti, and W. Grimus. Phenomenology of neutrino oscillations. *Progress in Particle and Nuclear Physics*, 43(0):1 – 86, 1999.

[24] Super-Kamiokande Collaboration. Evidence for Oscillation of Atmospheric Neutrinos. *Phys. Rev. Lett.*, 81:1562–1567, Aug 1998.

[25] V. Gribov and B. Pontecorvo. Neutrino astronomy and lepton charge. *Physics Letters B*, 28(7):493 – 496, 1969.

[26] KamLAND Collaboration. Precision Measurement of Neutrino Oscillation Parameters with KamLAND. *Phys. Rev. Lett.*, 100:221803, Jun 2008.

[27] Daya Bay Collaboration. Observation of Electron-Antineutrino Disappearance at Daya Bay. *Phys. Rev. Lett.*, 108:171803, Apr 2012.

[28] RENO Collaboration. Observation of Reactor Electron Antineutrinos Disappearance in the RENO Experiment. *Phys. Rev. Lett.*, 108:191802, May 2012.

[29] Double Chooz Collaboration. Indication of Reactor $\overline{\nu}_e$ Disappearance in the Double Chooz Experiment. *Phys. Rev. Lett.*, 108:131801, Mar 2012.

[30] MINOS Collaboration. Improved Measurement of Muon Antineutrino Disappearance in MINOS. *Phys. Rev. Lett.*, 108:191801, May 2012.

[31] T2K Collaboration. First muon-neutrino disappearance study with an off-axis beam. *Phys. Rev. D*, 85:031103, Feb 2012.

[32] MINOS Collaboration. Measurement of the Neutrino Mass Splitting and Flavor Mixing by MINOS. *Phys. Rev. Lett.*, 106:181801, May 2011.

[33] KATRIN Collaboration. KATRIN Design Report 2004. *Wissenschafliche Berichte des FZK*, 2004.

[34] Ø. Elgarøy, O. Lahav, W. J. Percival, J. A. Peacock, D. S. Madgwick, S. L. Bridle, C. M. Baugh, I. K. Baldry, J. Bland-Hawthorn, T. Bridges, R. Cannon, S. Cole, M. Colless, C. Collins, W. Couch, G. Dalton, R. De Propris, S. P. Driver, G. P. Efstathiou, R. S. Ellis, C. S. Frenk, K. Glazebrook, C. Jackson, I. Lewis, S. Lumsden, S. Maddox, P. Norberg, B. A. Peterson, W. Sutherland, and K. Taylor. New Upper Limit on the Total Neutrino Mass from the 2 Degree Field Galaxy Redshift Survey. *Phys. Rev. Lett.*, 89:061301, Jul 2002.

[35] Shankar Agarwal and Hume A. Feldman. The effect of massive neutrinos on the matter power spectrum. *Monthly Notices of the Royal Astronomical Society*, 410(3):1647–1654, 2011.

[36] Matthew Turk. Analysis and Visualization of Multi-Scale Astrophysical Simulations Using Python and NumPy. In Gaël Varoquaux, Travis Vaught, and Jarrod Millman, editors, *Proceedings of the 7th Python in Science Conference*, pages 46 – 50, Pasadena, CA USA, 2008.

[37] Julien Lesgourgues. Galaxies weigh in on neutrinos. *Physics*, 3:57, Jul 2010.

[38] Shaun A. Thomas, Filipe B. Abdalla, and Ofer Lahav. Upper Bound of 0.28 eV on Neutrino Masses from the Largest Photometric Redshift Survey. *Phys. Rev. Lett.*, 105:031301, Jul 2010.

[39] Yi Mao, Max Tegmark, Matthew McQuinn, Matias Zaldarriaga, and Oliver Zahn. How accurately can 21cm tomography constrain cosmology? *Phys. Rev. D*, 78:023529, Jul 2008.

[40] Steen Hannestad. Neutrino physics from precision cosmology. *Progress in Particle and Nuclear Physics*, 65(2):185 – 208, 2010.

[41] Planck Collaboration. Planck 2013 results. XVI. Cosmological parameters. 2013.

[42] Andrea Giuliani and Alfredo Poves. Neutrinoless Double-Beta Decay. *Advances in High Energy Physics*, 2012:38, Oct 2012.

[43] S. Schoenert et al. The GERmanium Detector Array (GERDA) for the search of neutrinoless $\beta\beta$ decays of 76Ge at LNGS. *Nuclear Physics B - Proceedings Supplements*, 145(0):242 – 245, 2005.

[44] M. Auger et al. Search for neutrinoless double-beta decay in ^{136}Xe with EXO-200. *Phys. Rev. Lett.*, 109:032505, Jul 2012.

[45] R. Arnold et al. Probing new physics models of neutrinoless double beta decay with SuperNEMO. *The European Physical Journal C*, 70:927–943, 2010.

[46] J F Wilkerson et al. The Majorana Demonstrator: A Search for Neutrinoless Double-beta Decay of Germanium-76. *Journal of Physics: Conference Series*, 375(4):042010, 2012.

[47] C Arnaboldi et al. CUORE: a cryogenic underground observatory for rare events. *Nuclear Instruments and Methods in Physics Research Section A: Accelerators, Spectrometers, Detectors and Associated Equipment*, 518(3):775 – 798, 2004.

[48] A. Gando et al. Limit on Neutrinoless beta beta Decay of Xe-136 from the First Phase of KamLAND-Zen and Comparison with the Positive Claim in Ge-76. *Phys. Rev. Lett.*, 110:062502, Feb 2013.

[49] Ch. Kraus, B. Bornschein, L. Bornschein, J. Bonn, B. Flatt, A. Kovalik, B. Ostrick, E.W. Otten, J.P. Schall, Th Thümmler, and Ch Weinheimer. Final results from phase II of the Mainz neutrino mass searchin tritium β decay. *The European Physical Journal C - Particles and Fields*, 40:447–468, 2005.

[50] V.M. Lobashev. The search for the neutrino mass by direct method in the tritium beta-decay and perspectives of study it in the project katrin. *Nuclear Physics A*, 719(0):C153 – C160, 2003.

[51] A. Picard, H. Backe, H. Barth, J. Bonn, B. Degen, Th. Edling, R. Haid, A. Hermanni, P. Leiderer, Th. Loeken, A. Molz, R.B. Moore, A. Osipowicz, E.W. Otten, M. Przyrembel, M. Schrader, M. Steininger, and Ch. Weinheimer. A solenoid retarding spectrometer with high resolution and transmission for kev electrons. *Nuclear Instruments and Methods in Physics Research Section B: Beam Interactions with Materials and Atoms*, 63(3):345 – 358, 1992.

[52] Ernst Otten. Searching the absolute neutrino mass in tritium beta-decay-interplay between nuclear, atomic and molecular physics. *Hyperfine Interactions*, 196:3–23, 2010.

[53] B. Bornschein. Determination of Neutrino Mass from Tritium Beta Decay. *Fusion Science and Technology*, 54(1):59–66, July 2008.

[54] Sz. Nagy, T. Fritioff, I. Bergström, K. Blaum, M. Suhonen, A. Solders, and R. Schuch. High-precision mass measurements for fundamental applications using highly-charged ions with SMILETRAP. *Journal of Physics: Conference Series*, 58(1):109, 2007.

[55] Natasha Doss, Jonathan Tennyson, Alejandro Saenz, and Svante Jonsell. Molecular effects in investigations of tritium molecule β decay endpoint experiments. *Phys. Rev. C*, 73:025502, Feb 2006.

[56] V.M. Lobashev and P.E. Spivak. A Method For Measuring The Anti-electron-neutrino Rest Mass. *Nucl.Instrum.Meth.*, A240:305–310, 1985.

[57] P. Kruit, H. G. Muller, J. Kimman, and M. J. van der Wiel. Relation between 'above-threshold' ionisation probabilities and continuum-continuum matrix elements. *Journal of Physics B: Atomic and Molecular Physics*, 16(13):2359, 1983.

[58] M. Babutzka, M. Bahr, J. Bonn, B. Bornschein, A. Dieter, G. Drexlin, K. Eitel, S. Fischer, F. Glück, S. Grohmann, M. Hötzel, T. M. James, W. Käfer, M. Leber, B. Monreal, F. Priester, M. Röllig, M. Schlösser, U. Schmitt, F. Sharipov, M. Steidl, M. Sturm, H. H. Telle, and N. Titov. Monitoring of the operating parameters of the KATRIN Windowless Gaseous Tritium Source. *New Journal of Physics*, 14(10):103046, 2012.

[59] B. Monreal and M. Beck. KATRIN Rear Section conceptual design report. KATRIN internal document v1.1, KATRIN rear section working group, September 2011.

[60] S. Grohmann, T. Bode, M. Hötzel, H. Schön, M. Süßer, and T. Wahl. The thermal behaviour of the tritium source in KATRIN. *Cryogenics*, 55-56(0):5–11, 2013.

[61] M. Sturm. *Aufbau und Test des Inner-Loop-Systems der Tritiumquelle von KATRIN*. PhD thesis, KIT, Karlsruhe, Deutschland, 2010.

[62] A. Kosmider. *Tritium Retention Techniques in the KATRIN Transport Section and Commissioning of its DPS2-F Cryostat*. PhD thesis, KIT, Karlsruhe, Deutschland, 2012.

[63] S. Mertens. *Study of Background Processes in the Electrostatic Spectrometers of the KATRIN Experiment*. PhD thesis, KIT, Karlsruhe, Deutschland, 2012.

[64] M. Ubieto Diaz. *Off-line commissioning of a non-destructive FT-ICR detection system for monitoring the ion concentration in the KATRIN beamline*. PhD thesis, Ruprecht-Karls-Universität and MPIK, Heidelberg, Deutschland, 2011.

[65] X. Luo and Ch. Day. Test particle Monte Carlo study of the cryogenic pumping system of the Karlsruhe tritium neutrino experiment. *Journal of Vacuum Science and Technology A: Vacuum, Surfaces, and Films*, 26(5):1319–1325, 2008.

[66] O. Kazachenko, B. Bornschein, L. Bornschein, F. Eichelhardt, N. Kernert, and H. Neumann. TRAP - a cryo-pump for pumping tritium on pre-condensed argon. *Nuclear Instruments and Methods in Physics Research Section A: Accelerators, Spectrometers, Detectors and Associated Equipment*, 587(1):136 – 144, 2008.

[67] Felix Bachmann. Aufbau und Inbetriebnahme des CPS-Testaufbaus. bachelor thesis, KIT, Karlsruhe, Deutschland, 2012.

[68] Max Renschler. Pressure Rise Measurements at the KATRIN Testzylinder. bachelor thesis, KIT, Karlsruhe, Deutschland, 2013.

[69] L. Bornschein, Ch. Day, F. Habermehl, X. Luo, and J. Wolf. Outgassing measurements with a prototype for a large UHV spectrometer. *AIP Conference Proceedings*, 837(1):200–209, 2006.

[70] Moritz Erhard. Untersuchung der Langzeitstabilität des nuklearen Standards für die Energieskala des KATRIN-Experiments. Master's thesis, KIT, Karlsruhe, Deutschland, 2012.

[71] Stephan Bauer. Aufbau und Inbetriebnahme des zweiten Präzisionsspannung-steilers bis 65 kV für das KATRIN-Experiment. Master's thesis, Westfälische Wilhelms-Universität, Münster, Deutschland, 2010.

[72] A. Beglarian et al. Prototype focal-plane detector system for the KATRIN experiment. *internal KATRIN document*, 2012.

[73] W. Kaefer. *Sensitivity studies of the KATRIN experiment.* PhD thesis, KIT, Karlsruhe, Deutschland, 2012.

[74] M. Hoetzel. *Simulation and analysis of source-related effects for KATRIN.* PhD thesis, KIT, Karlsruhe, Deutschland, 2013.

[75] Magnus Schlösser, Simone Rupp, Hendrik Seitz, Sebastian Fischer, Beate Bornschein, Tim M. James, and Helmut H. Telle. Accurate calibration of the laser Raman system for the Karlsruhe Tritium Neutrino Experiment. *Journal of Molecular Structure*, 1044(0):61 – 66, 2013.

[76] F. Priester. *Tritiumtechnologie für die fensterlose Quelle WGTS von KATRIN.* PhD thesis, KIT, Karlsruhe, Deutschland, 2013.

[77] F. Habermehl. *Electromagnetic Measurements with the KATRIN Pre-Spectrometer.* PhD thesis, KIT, Karlsruhe, Deutschland, 2009.

[78] F. M. Fraenkle. *Background Investigations of the KATRIN Pre-Spectrometer.* PhD thesis, KIT, Karlsruhe, Deutschland, 2010.

[79] S. Mertens, G. Drexlin, F.M. Fränkle, D. Furse, F. Glück, S. Görhardt, M. Hötzel, W. Käfer, B. Leiber, T. Thümmler, N. Wandkowsky, and J. Wolf. Background due to stored electrons following nuclear decays in the KATRIN spectrometers and its impact on the neutrino mass sensitivity. *Astroparticle Physics*, 41(0):52 – 62, 2013.

[80] F.M. Fraenkle, L. Bornschein, G. Drexlin, F. Glueck, S. Goerhardt, W. Kaefer, S. Mertens, N. Wandkowsky, and J. Wolf. Radon induced background processes in the KATRIN pre-spectrometer. *Astroparticle Physics*, 35(3):128 – 134, 2011.

[81] N. Wandkowsky. *Study of background and transmission properties of the KATRIN spectrometers.* PhD thesis, KIT, Karlsruhe, Deutschland, 2013.

[82] Stefan Görhardt. Reduktion der durch Radon induzierten Untergrundprozesse in den KATRIN Spektrometern. Master's thesis, KIT, Karlsruhe, Deutschland, 2010.

[83] B. Hillen. *Untersuchung von Methoden zur Unterdrückung des Spektrometeruntergrunds beim KATRIN Experiment.* PhD thesis, Univ. Münster, Münster, Deutschland, 2011.

[84] K. Jousten. *Handbook of Vacuum Technology.* John Wiley & Sons, 2008.

[85] Alexander Jansen. Modellierung der Rotortemperatur von Turbomolekularpumpen in Magnetfeldern mit unterschiedlichen Gasflüssen. Master's thesis, KIT, Karlsruhe, Deutschland, 2012.

[86] J. Wolf, B. Bornschein, G. Drexlin, R. Gehring, R. Größle, S. Horn, N. Kernert, S. Riegel, R. Neeb, and A. Wagner. Investigation of turbo-molecular pumps in strong magnetic fields. *Vacuum*, 86(4):361 – 369, 2011.

[87] R. Größle, N. Kernert, S. Riegel, and J. Wolf. Model of the rotor temperature of turbo-molecular pumps in magnetic fields. *Vacuum*, 86(7):985 – 989, 2012.

[88] Sebastian Riegel. Die Erwärmung von Turbomolekularpumpen in verschiedenen Betriebszuständen. Master's thesis, KIT, Karlsruhe, Deutschland, 2011.

[89] Jan Bondy. Modeling and measurement of the rotor temperature of a turbomolecular pump in an external magnetic field. bachelor thesis, KIT, Karlsruhe, Deutschland, 2013.

[90] C. Benvenuti and P. Chiggiato. Pumping characteristics of the St707 non-evaporable getter (Zr70-V24.6-Fe5.4). *J. Vac. Sci. Technol. A*, 14(CERN-MT-95-10 SM):3278–3282. 18 p, Oct 1995.

[91] B. Bornschein. *KATRIN numbering system for equipment, components and related documents.* KIT, 4 edition, May 2008.

[92] M. Beck, K. Valerius, J. Bonn, K. Essig, F. Glück, H.-W. Ortjohann, B. Ostrick, E.W. Otten, Th. Thümmler, M. Zbořil, and C. Weinheimer. Effect of a sweeping conductive wire on electrons stored in a Penning-like trap between the KATRIN spectrometers. *The European Physical Journal A*, 44(3):499–511, 2010.

[93] R. Gehring, J. Bonn, B. Bornschein, B. Flatt, K.P. Juengst, H. Neumann, A. Osipowicz, and J. Pitel. The KATRIN magnet system. *Applied Superconductivity, IEEE Transactions on*, 14(2):589 – 591, june 2004.

[94] Cryogenic Limited. 4.5Tesla Cryogen-Free Magnet System. Job number: 2054, United Kingdom, 2003.

[95] Thiemo Schmelzer. Stability measurements to determin the magnetic field at prespectrometer-magnet I at the KATRIN experiment. bachelor thesis, KIT, Karlsruhe, Deutschland, 2013.

[96] B. Flatt. *Voruntersuchungen zu den Spektrometern des KATRIN-Experiments.* PhD thesis, Johannes Gutenberg University, Mainz, Deutschland, 2004.

[97] F. Schwamm. *Untergranduntersuchungen für das KATRIN-Experiment.* PhD thesis, KIT, Karlsruhe, Deutschland, 2004.

[98] K. Valerius. The wire electrode system for the KATRIN main spectrometer. *Progress in Particle and Nuclear Physics*, 64(2):291 – 293, 2010.

[99] Benjamin Leiber. Non-axially symmetric field and trajectory calculations for the KATRIN-experiment. Master's thesis, KIT, Karlsruhe, Deutschland, 2010.

[100] T. Thümmler. *Präzisionsüberwachung und Kalibration der Hochspannung für das KATRIN-Experiment.* PhD thesis, Westfälische Wilhelms-Universität, Münster, Deutschland, 2007.

[101] Robin Größle. Konzeptionierung und Systematik der Hochspannungsversorgung für das KATRIN-Experiment. Master's thesis, KIT, Karlsruhe, Deutschland, 2010.

[102] Marcel Kraus. Kalibration und Entwicklung von Komponenten für das KATRIN Präzisions-Hochspannungs-System. Master's thesis, KIT, Karlsruhe, Deutschland, 2012.

[103] Johannes Fischer. Analysen zur Langzeitstabilität und den Betriebsmodi des KATRIN Pinch-Magneten. bachelor thesis, KIT, Karlsruhe, Deutschland, 2012.

[104] Nils Stallkamp. Optimierung und erste Messung der Transmissionseigenschaften des KATRIN-Hauptspektrometers. Master's thesis, KIT, Karlsruhe, Deutschland, 2013.

[105] A. Osipowicz, W. Seller, J. Letnev, P. Marte, A. Müller, A. Spengler, and A. Unru. A mobile magnetic sensor unit for the KATRIN main spectrometer. *Journal of Instrumentation*, 7(06):T06002, 2012.

[106] J. Reich. *Magnetic Field Inhomogeneities and Their Influence on Transmission and Background at the KATRIN Main Spectrometer.* PhD thesis, KIT, Karlsruhe, Deutschland, 2013.

[107] Karl Jousten. Thermal outgassing. In *CAS - CERN Accelerator School: Vacuum Technology*, pages 111–125, Snekersten, Denmark, June 1999.

[108] Inkyu Chun, Boklae Cho, and Sukmin Chung. Outgassing rate characteristic of a stainless steel extreme high vacuum system. *Journal of Vacuum Science Technology A: Vacuum, Surfaces, and Films*, 14(4):2636–2640, 1996.

[109] Boude C. Moore. Recombination limited outgassing of stainless steel. *Journal of Vacuum Science and Technology A: Vacuum, Surfaces and Films*, 13(3):545–548, 1995.

[110] J. Wolf. Manufacturing of the test cylinder at DWE. Technical report, KIT, February 2002.

[111] VACOM. ATMION - Wide Range Manometer. Technical report, D-07743 Jena, 2000.

[112] S. Goerhardt, V. Hannen, Th. Thuemmler, J. Wolf, and M. Zacher. Vacuum Conditioning of the KATRIN Main Spectrometer. Technical report, KIT, March 2013.

[113] Volker M. Hannen et al. Status of the inner wire electrode after baking and EMD consequences of the electrical shortcuts, 2013. KATRIN internal report.

[114] SAES Getters S.p.A., Viale Italia 77, Lainate (Milan), Italy. *St707 - non evaporable getters activatable at low temperatures.*

[115] Paolo Manini. personal communication, at the IVC-19 in Paris, France, 2013. (Business Manager, SAES Getters S.p.A.).

[116] R. J. Knize and L.M. Cecchi. Theory of bulk gettering. *Journal of Applied Physics*, 54(6):3183–3189, 1983.

[117] Max Zanner. Implementing and measuring outgassing rates of UHV set-up. bachelor thesis, KIT, Karlsruhe, Deutschland, 2013.

[118] Carsten Roettele. Optimization of the activation temperature of the CPS getter pump in the KATRIN experiment. bachelor thesis, KIT, Karlsruhe, Deutschland, 2013.

[119] X. Luo, M. Dremel, and Ch. Day. ProVac3D and Application to the Neutral Beam Injection System of ITER. In *RAREFIED GAS DYNAMICS: Proceedings of the 26th International Symposium on Rarefied Gas Dynamics*, volume 1084, page 1099. Springer, July 2008.

[120] Ch. Day and V. Hauer. Investigations into the getter strip geometry to be used for the KATRIN pre-spectrometer. *Interner Bericht*, September 2002. Katrin Document Number 30-ME-5001-2.

[121] Uwe Kraemer. Simulation and Measurement with a Prototype of an Electric Activatable NEG Pump at the KATRIN Testrecipient. bachelor thesis, KIT, Karlsruhe, Deutschland, 2013.

[122] Robert L. Summers. Ionization Gauge Sensitivities As Reported in the Literature. Technical Note TND5285, NASA, Lewis Research Center, June 1969.

[123] J. Miertusova and F. Daclon. Theoretical and experimental study of sorption processes on nonevaporable getters St707. In *Particle Accelerator Conference, 1993., Proceedings of the 1993*, pages 3873–3875 vol.5, 1993.

[124] G. Moraw. The influence of ionization gauges on gas flow measurements. *Vacuum*, 24(3):125 – 128, 1974.

[125] D. Alpert. New Developments in the Production and Measurement of Ultra High Vacuum. *Journal of Applied Physics*, 24(7):860–876, 1953.

[126] J.R.J. Bennett, S. Hughes, R.J. Elsey, and T.P. Parry. Outgassing from stainless steel and the effects of the gauges. *Vacuum*, 73(2):149 – 153, 2004. Proceedings of the European Vacuum Congress Berlin 2003, 23-26 June 2003, featuring the 8th European Vacuum Conference, 2nd Annual Conference of the German Vacuum Society.

[127] M. S. Rapaport, F. Asaro, and I. Perlman. K-shell electron shake-off accompanying alpha decay. *Phys. Rev. C*, 11:1740–1745, May 1975.

[128] J. S. Hansen. Internal ionization during alpha decay: A new theoretical approach. *Phys. Rev. A*, 9:40–43, Jan 1974.

[129] E. Browne. Nuclear Data Sheets for A = 215,219,223,227,231. *Nuclear Data Sheets*, 93(4):763 – 1061, 2001.

[130] Ch. Theisen, A. Lopez-Martens, and Ch. Bonnelle. Internal conversion and summing effects in heavy-nuclei spectroscopy. *Nuclear Instruments and Methods in Physics Research Section A: Accelerators, Spectrometers, Detectors and Associated Equipment*, 589(2):230 – 242, 2008.

[131] R. Eichler and M. Schaedel. Adsorption of Radon on Metal Surfaces: A Model Study for Chemical Investigations of Elements 112 and 114. *The Journal of Physical Chemistry B*, 106(21):5413–5420, 2002.

[132] Jacques Farine and SNO Collaboration. Assay of Radon and Radium in Water: Techniques Developed at SNO. *AIP Conference Proceedings*, 785(1):199–208, 2005.

[133] Volker M. Hannen. Results of additional test measurements of the main spectrometer electrode modules, 2008. Slides of a talk given at 15th KATRIN collaboration meeting.

[134] H. Simgen. Ultrapure gases for GERDA. *Progress in Particle and Nuclear Physics*, 57(1):266–268, 2006. International Workshop of Nuclear Physics 27th course Neutrinos in Cosmology, in Astro, Particle and Nuclear Physics Ettore Majorana Center for Scientific Culture.

[135] H. Simgen, C. Buck, G. Heusser, M. Laubenstein, and W. Rau. A new system for the 222Rn and 226Ra assay of water and results in the Borexino project. *Nuclear Instruments and Methods in Physics Research Section A: Accelerators, Spectrometers, Detectors and Associated Equipment*, 497(2):407–413, 2003.

[136] Xueli Luo, Thomas Giegerich, and Christian Day. Transient gas flow studied by a test particle Monte Carlo approach with ProVac3D. *AIP Conference Proceedings*, 1501(1):857–863, 2012.

[137] Marcel Krause. Simulation of the test setup for a getter vacuum pump. bachelor thesis, KIT, Karlsruhe, Deutschland, 2013.

[138] Ch. Day, X. Luo, A. Conte, A. Bonucci, and P. Manini. Determination of the sticking probability of a Zr–V–Fe non-evaporable getter strip. *Journal of*

Vacuum Science & Technology A: Vacuum, Surfaces, and Films, 25(4):824–830, 2007.

[139] T. L. Ho. Speed, Speed Factor and Power Input of Different Designs of Diffusion Pumps, and Remarks on Measurements of Speed. *Physics*, 2(5):386–395, 1932.

[140] J. C. McLennan, R. C. Jacobsen, and J. G. Wilhelm. Dielectric Constants of Liquefied Gases. *Proceedings and transactions of the Royal Society of Canada*, 24(3):37–46, 1930.

[141] KATRIN Collaboration. Results of the first KATRIN SDS measurement Phase. Technical report, KIT, WWU, MIT, UW, December 2013.

[142] F. Harms and J. Schwarz. Standard SDS Background Analysis Cuts. Technical report, KIT, September 2013.

[143] Nikolaus Trost. Background generation due to stored electrons at the KATRIN main spectrometer. Master's thesis, KIT, Karlsruhe, Deutschland, 2013.

[144] Rene Brun and Fons Rademakers. ROOT - An Object Oriented Data Analysis Framework. In *AIHENP'96 Workshop, Lausane*, volume 389, pages 81–86, 1996.

[145] M. Haag. *PhD thesis in preparation*. PhD thesis, KIT, Karlsruhe, Deutschland, 2014.

[146] J. Schwarz. *PhD thesis in preparation*. PhD thesis, KIT, Karlsruhe, Deutschland, 2014.

[147] S. Mertens, A. Beglarian, L. Bornschein, G. Drexlin, F.M. Fränkle, D. Furse, F. Glück, S. Görhardt, O. Krömer, B. Leiber, K. Schlösser, T. Thümmler, N. Wandkowsky, and S. Wüstling. Stochastic heating by ECR as a novel means of background reduction in the KATRIN spectrometers. *Journal of Instrumentation*, 7(08):P08025, 2012.

[148] G. Pfennig, H. Klewe-Nebenius, and W. Seelmann-Eggebert. *Karlsruher Nuklidkarte*. Marktdienste Haberbeck, 6. a. edition, 1995.

176

Acknowledgment

I would like to thank all the people that supported me during my PhD thesis, in particular:

- Prof. Dr. Guido Drexlin for giving me the opportunity to work at KATRIN and for his invaluable supervision and support.

- Prof. Dr. Ulrich Husemann for accepting to be the second reviewer of this thesis.

- the senior scientific staff: Dr. Lutz Bornschein, Dr. Joachim Wolf, Dr. Thomas Thümmler, Dr. Klaus Schlösser, Dr. Ferenc Glück and Dr. Rainer Gehring.

- our young and strong scientific group: Dr. Florian Fränkle, Dr. Susanne Mertens, Dr. Nancy Wandkowsky, Dr. Jan Reich, Dr. Udo Schmitt, Johannes Schwarz, Fabian Harms, Stefan Groh, Benjamin Leiber, Marco Haag, Marcel Kraus, Moritz Erhard, Alexander Jansen, Daniel Hilk and all other colleges of the institute of experimental nuclear physics and the TLK.

- the engineering staff for mechanic: Rainer Gumbsheimer, Steffen Lichter, Rolf Rinderspacher, Karin Vogt, Sabine Büsch and Holger Krause; for electric: Dr. Sascha Wüstling Armen Beglarian and Thomas Höhn; and of course safety: Martin Mark.

- the technical staff for mechanic: Siegfried Horn, Holger Frenzel, Martin Jäger, Alan Kumb and the trainees: Kevin, Dennis and Mario; for electric: Heike Bolz, Georg Prokott and Arne Felden; for vacuum: Luisa LaCascio, Hans Skacel and Norbert Kernert; and cryo: Siegfried Holzmann.

- Raphael Bechtold and Bernard Bender for provide valuable support.

- Berno Stark and Peter Plischke for their experience.

- my indispensable army of bachelor students: Thiemo Schmelzer, Maximilian Zanner, Felix Bachmann, Max Renschler, Jan Bondy, Uwe Krämer, Carsten Röttele and Marcel Krause.
  I hope you have learned as much from me as I've learned from you.

- my elite team of indestructible HIWI students: Moritz Erhard, Benedikt Maier, Anton Huber and Moritz Hackenjos.

- Klaus Mehret for his friendship.

Thank you all for the nice working atmosphere. I would like to thank all other people who helped me make it through my time as a PhD student even if they are not named here.

Lastly I would like to thank my parents, my little sister Anne and my stunning girlfriend Michaela for all their support.